Degenerate quantum gases of strontium

dissertation

by

Simon Stellmer

submitted to the Faculty of Mathematics, Computer Science and Physics of the University of Innsbruck

in partial fulfillment of the requirements
for the degree of doctor of science

advisors:
Univ. Prof. Dr. Rudolf Grimm,
Institute of Experimental Physics, University of Innsbruck,
Institute for Quantum Optics and Quantum Information
of the Austrian Academy of Sciences

Dr. Florian Schreck,
Institute for Quantum Optics and Quantum Information
of the Austrian Academy of Sciences

Innsbruck, January 2013

Summary

The exploration of the quantum world is a fascinating and very active field of current research. Experiments with gases of ultracold atoms are building on a long history of precision measurements and have been particularly successful in reaching ever lower temperatures. The first Bose-Einstein condensate was created about two decades ago and ignited the investigation of quantum-degenerate samples. But for a few exceptions, these experiments have utilized alkali atoms, which have a relatively simple electronic structure.

Alkaline-earth atoms, on the other hand, carry two valence electrons and exhibit a rich electronic structure of singlet and triplet states, connected by narrow intercombination lines. Such transitions of mHz-width are driven in optical clock experiments, which are outperforming microwave clocks by orders of magnitude. The unique properties of these elements are at the basis of recently proposed schemes of quantum simulation, targeted at the investigation of quantum magnetism and spin models. The proposed experiments rely on the availability of quantum-degenerate gases, and require a supreme control over all relevant parameters.

This thesis is aimed to provide a solid foundation for such experiments, choosing strontium as the atomic species. We report on the first Bose-Einstein condensation of this element, choosing the isotope ^{84}Sr for its favorable scattering properties. This achievement received widespread recognition, and we are able to attain condensates of the two other bosonic isotopes, ^{86}Sr and ^{88}Sr, as well.

The proposed schemes of quantum simulation require isotopes with nonzero nuclear spin, sparking considerable interest in the fermionic isotope ^{87}Sr, which has a large nuclear spin of $I = 9/2$. We develop a set of experimental techniques to control the spin composition of an atomic sample, and we present deeply-degenerate Fermi gases with a variable number of spin states.

Dipolar quantum gases are another active field of research. Diatomic molecules in their internal ground state, made up of an alkali and an alkaline-earth atom, possess both an electric and a magnetic dipole moment. Magnetic Feshbach resonances, which are commonly used to associate bi-alkali molecules, are absent or very weak in bi-alkaline-earth and alkali/alkaline-earth systems. We develop a novel technique of molecule association, demonstrated for the homonuclear case of Sr_2. This approach uses atoms on doubly-occupied sites of an optical lattice as the starting point for a coherent optical transfer into the molecular state.

Finally, we expand the capabilities of laser cooling to reach a long-standing goal: Bose-Einstein condensation without evaporative cooling, purely by laser cooling and thermalization within the atomic gas. This work holds prospects for the generation of a continuous atom laser.

Zusammenfassung

Die Untersuchung von Systemen, deren Verhalten von den Gesetzen der Quantenmechanik bestimmt wird, ist ein faszinierendes und lebendiges Gebiet aktueller Forschung. Experimente mit Gasen von ultrakalten Atomen sind dabei ausgesprochen erfolgreich und blicken zurück auf eine lange Geschichte von Präzisionsmessungen, bei denen immer tiefere Temperaturen erreicht wurden. Die ersten Bose-Einstein Kondensate (BECs) wurden vor etwa 20 Jahren erzeugt und eröffneten die Möglichkeit, quantenentartete Materie zu studieren. Bis auf wenige Ausnahmen wurden diese Versuche mit Alkaliatomen durchgeführt, da diese eine relativ einfache elektronische Struktur aufweisen.

Die elektronische Struktur von Erdalkaliatomen hingegen ist dank ihrer zwei Valenzelektronen sehr viel reichhaltiger und zeichnet sich durch Singlett- und Triplettzustände sowie schmale Interkombinationsübergänge aus. Solche Übergänge werden etwa in optischen Uhren verwendet; diese erreichen eine um Größenordnungen bessere Genauigkeit als Atomuhren, deren Funktionsweise auf einem Mikrowellenübergang beruht. Die einzigartigen Eigenschaften der Erdalkaliatome ermöglichen neuartige Verfahren für Quantensimulationen. Die hierzu vorgeschlagenen experimentellen Studien, etwa von Quantenmagnetismus und Spinmodellen, erfordern sowohl quantenentartete Gase von Erdalkaliatomen, als auch eine sehr genaue Kontrolle aller relevanten Parameter.

Das Ziel dieser Dissertation ist es, eine experimentelle Grundlage für diese Untersuchungen zu schaffen. Als Atomsorte wurde dazu das Element Strontium ausgewählt. Wir präsentieren die erste Bose-Einstein Kondensation dieses Elementes, wobei hierfür das Isotop ^{84}Sr auf Grund seiner günstigen Eigenschaften ausgewählt wurde. Dieser Erfolg sorgte für weltweite Anerkennung, und bald darauf konnten auch BECs der beiden anderen bosonischen Isotope, ^{86}Sr und ^{88}Sr, erzeugt werden.

Die angesprochenen Vorschläge zur Quantensimulation basieren auf einem Isotop mit von Null verschiedenem Kernspin und wecken daher Interesse am fermionischen Isotop ^{87}Sr, welches einen vergleichsweise großen Kernspin von $I = 9/2$ besitzt. Wir demonstrieren eine Reihe experimenteller Techniken, mit Hilfe derer sich die Besetzung der Spinzustände in einem atomaren Ensemble kontrollieren lässt, und erreichen tiefentartete Fermigase mit einer frei einstellbaren Anzahl von Spinkomponenten.

Dipolare Quantengase sind ein weiteres hochaktuelles Forschungsthema. Zweiatomige Moleküle, bestehend aus einem Alkali- und einem Erdalkaliatom, besitzen in ihrem Grundzustand sowohl ein elektrisches als auch ein magnetisches Dipolmoment. Magnetische Feshbach-Resonanzen, wie sie üblicherweise zur Assoziation von Bialkali-Molekülen verwendet werden, sind in Bi-Erdalkali- oder Alkali-Erdalkali-Systemen jedoch nicht vorhanden oder ausgesprochen schwach. Aus diesem Grunde haben wir eine neuartige Methode der Molekülassoziation

entwickelt und dokumentieren diese am Beispiel des homonuklearen Moleküls Sr_2. Unsere Herangehensweise nutzt als Ausgangspunkt zwei Atome auf einem doppelt besetzten Platz eines optische Gitters, um diese durch einen kohärenten optischen Transfer in einen molekularen Bindungszustand zu überführen.

Abschließend wenden wir uns einem seit langem bestehenden Ziel zu: der Erzeugung von Bose-Einstein Kondensaten nicht durch Verdampfungskühlung, sondern nur durch Laserkühlung und gleichzeitiger Thermalisierung zwischen den Atomen. Wir erreichen dieses Ziel mit Hilfe fein abgestimmter, räumlich strukturierter Dipolpotentiale. Dieses Verfahren könnte für die Erzeugung eines kontinuierlichen, kohärenten Atomstrahls verwendet werden.

Contents

Chapter 1

Introduction

The condensation of particles into a single macroscopic quantum state at low enough temperatures was predicted by S. Bose and A. Einstein some 90 years ago. This work, based on a purely statistical argument, awaited experimental realization for 70 years, and it was not until the 1990's that both the required technology and the experience in the cooling of atoms had matured to a degree that allowed for the creation of Bose-Einstein condensates in atomic vapors [Ing99]. Today, the study of ultracold gases has evolved into a large and diverse field of research that continues to expand at a breathtaking pace.

The early experiments explored the coherence properties and superfluidity of the condensate, demonstrating the interference of matter waves, the nucleation of vortices, and the atom laser. Ground-breaking studies on the mean-field behavior, collective excitations, and superradiance have been performed. In the past ten years, studies have moved from the investigation of the degenerate matter itself towards the creation of novel and more involved systems, using degenerate gases as building blocks. These studies include the realization of the famous Bose-Hubbard model in optical lattices and the demonstration of the metal to Mott-insulator transition, the study of dipolar and magnetic systems, the investigation of one- and two-dimensional systems, the observation of Anderson localization, and the exploration of few-body phenomena, such as the Efimov-effect, and of many-body systems, such as strongly interacting gases.

The first creation of degenerate Fermi gases in 1999 extended the coherence properties and supreme control to the realms of fermionic systems. The building blocks of matter are fermions, and the behaviors of many important physical systems, such as the one of electrons in a metal, of quarks in a plasma, or of neutrons in dense stars, are of fermionic character. Quantum gas experiments have realized the Fermi-Hubbard model, studied the BEC-BCS crossover, and reached the strongly interacting regime [Ing08].

Today, we witness an ambitious development: quantum-degenerate gases are no longer the object of study themselves, but lend their capabilities to the exploration of other fields of research. One of two prominent examples is the connection to chemistry through the creation of diatomic molecules in the rovibrational ground state, starting from ultracold atoms. The other one is the quantum simulation of various solid state systems in general and of quantum magnetism in particular, using atoms confined in an optical lattice.

The reason for the tremendous success of this research lies in the extraordinary degree

of control and large tunability of all relevant properties of the system, such as the sample size, its temperature and density, spin composition, interaction strength, dimensionality, and coherence time. Nonetheless, the range of possible experiments is constrained by the properties of the atomic species used. Reversely, the availability of degenerate samples of a new species has triggered proposals and subsequent experiments that employ the unique characteristics that this element brings about. The broad Feshbach resonance in Cs and the dipolar character of Cr serve as beautiful examples.

Almost all quantum gas experiments to date work with alkali atoms, which have a comparatively simple electronic structure. Alkaline-earth elements however, atomic species with two valence electrons, feature a handful of remarkable properties not found in the alkalis: metastable states, narrow intercombination lines, and ground states free of any magnetic moment. These properties have encouraged a wealth of proposals for experiments that reach beyond of what is feasible with alkali systems. These proposals, mainly addressing schemes of quantum simulation, either require or could greatly benefit from the availability of (fermionic) degenerate gases.

The first of these proposals appeared about four years ago and triggered an avalanche of further theoretical work. At that time, quantum degeneracy in Yb had already been achieved. Optical clock experiments had gathered extensive knowledge about optical cooling techniques and scattering properties of Ca and Sr, bringing degeneracy in these two elements into reach. It seemed like a good starting time for the present thesis.

The aim of this thesis is the creation and investigation of bosonic and fermionic degenerate gases of Sr, and to establish the foundations necessary for the realization of unique quantum simulation experiments with strontium. Some of the proposed experiments are described in the following, namely those headed into the direction of quantum simulation using the nuclear spin of the fermionic isotope (Sec. 1.1) and those targeted at the creation and use of polar open-shell molecules (Sec. 1.2). Afterwards, we will briefly glance at the basic concepts of bosonic and fermionic degeneracy and introduce the relevant terminology used throughout this thesis (Sec. 1.3). An outline of this thesis is given in Sec. 1.4.

1.1 Quantum simulation

Many-body systems are ubiquitous in Nature, and the description and understanding of their properties is an essential topic in many areas of physics, most prominently in solid state physics. Let us consider a system of N spin one-half particles. The quantum description of this system requires 2^N complex amplitudes, a number that grows exponentially with system size and rises beyond all comprehensible values for about 300 particles. Computation of larger systems on a classical computer is fundamentally impossible. A solution to this dilemma was proposed by R. Feynman in 1981: artificial, fully controlled quantum systems are to be used to *simulate* the quantum system of interest, rather than to *compute* its properties and dynamics [Fey82, Llo96]. It is the degree of control and the specific properties of this quantum simulator (also called "special task quantum computer") that determine the scope of problems that can be investigated. Quantum simulation might address problems in systems that are experimentally hard to investigate, such as distant neutron stars, hard

to tune, such as solid state systems, or continue to resist a theoretic description, such as the phenomenon of high-temperature superconductivity. The modeling of phenomena that have not yet been observed in Nature, such as topological insulators or non-abelian anyons, seems intriguing as well. The simulation might be implemented on various platforms, such as ultracold atoms or trapped ions, photons, superconducting circuits, and possibly more; see Ref. [TE12] for a recent review.

Ultracold gases of neutral atoms are a natural choice to simulate many-body systems [Blo12], such as the bosonic [Blo08] and fermionic [Ess10] Hubbard models. Here, an optical lattice can be used to mimic the periodic structure of an ion crystal in a solid material. The defect-free lattice potential is formed by the interference of laser beams, where the atoms are confined to individual lattice wells to assume the role of electrons in the solid state analogue [Gre02, Blo05]. Many experiments are performed on such a lattice geometry, emulating solid state phenomena (e.g. [End12, Tar12]) or probing classical and quantum magnetism (e.g. [Tro08, Str11]). A number of sophisticated techniques have been developed to achieve supreme control over the quantum system, the precise tuning of the interaction strength [Chi10] being a prominent example. Diagnostic tools such as band mapping [Gre01], measurement of the doublon fraction [Jör08] and of noise correlations [Föl05], and fluorescence imaging of individual lattice sites [Bak09, She10] are now available, while also complex lattice structures have been implemented, such as spin-dependent [Man03], non-cubic [Bec10, Jo12], and double-well lattices [Föl07]. The minimum entropy reached in most experiments today is just on the edge of allowing for antiferromagnetic ordering, and techniques of entropy removal or re-distribution are currently developed both theoretically end experimentally (e.g. [Med11, McK11, Bon12]). As a last aspect, we mention an apparent drawback of neutral gases: the absence of an electric charge, which would be necessary for the generation of the Lorentz forces found in quantum Hall systems. Recent experiments have used carefully designed laser fields to generate artificial magnetic fields, in which the neutral atom experiences a Lorentz-like force [Lin09, Dal11], thereby successfully simulating an entirely different system.

To date, all of such experiments have been performed with alkali atoms (but for [Tai12]). Alkaline-earth systems, such as Sr, possess unique properties that allow for new types of experiments. Besides practical advantages, the properties are (i) the existence of long-lived metastable states, and (ii) the almost perfect decoupling of the nuclear spin from the electronic structure in the ${}^1S_0$ and ${}^3P_0$ states [Boy07c]. These two properties have stimulated a number of proposals relevant for quantum simulation [Caz09, Gor10, Man11, Wu03, Wu06, FF10, Her09, Xu10, Hun11, Ger10, Coo11b, Bér11, Gór11a, Dal08, Gor09], some of which will be discussed in the following.

SU(N) magnetism

The decoupling of the nuclear spin from the electronic structure renders the scattering between atoms independent of their nuclear spin, aside from constraints imposed by Fermi statistics. This increases the symmetry of the underlying Hubbard model from SO(N), common to alkali systems, to SU(N) [Wu03], where N is the number of spin states involved and can be chosen to be as high as $2I + 1 = 10$ in strontium. This increased symmetry

leads to a highly degenerate energy spectrum, and the nature of the ground state of such a spin system is a subject of active theoretical investigation [Caz09, Gor10, Man11, Wu03, Wu06, FF10, Her09, Xu10, Hun11, Bér11]. The ground state will be increasingly frustrated for $N > 2$ and might take the form of exotic quantum phases such as a chiral spin liquid or a valence bond solid, depending on the value of N; see Ref. [Gor10] and references therein. Such phases might possess topological order, a property studied in only very few quantum systems so far.

Alkaline-earth systems are envisioned to simulate a vast number of different SU(N) spin Hamiltonians, among them the Kugel-Khomskii model, which includes orbital degrees of freedom and is relevant for the description of transition-metal oxides, as well as the Kondo lattice model, used to describe heavy-fermion materials [Gor10]. Magnetic ordering usually requires the entropy of the lattice system to be on the superexchange scale (t^2/U, where t is the tunneling energy and U is the onsite interaction energy in the well-known Fermi Hubbard Hamiltonian), which is challenging to access experimentally. Theoretical studies have elucidated the N-dependence of the sample temperature T/t after adiabatic loading into the lattice [Haz12, Bon12]. Quite surprisingly, the temperature in the lattice becomes significantly smaller for increased value of N [Tai12], reaching a difference of around ten between the extreme cases of $N = 2$ and $N = 10$ for typical initial temperatures. This behavior is encouraging for the experimental investigation of SU(N) quantum magnetism.

Artificial gauge fields

It seems tempting to expand the capabilities of cold gases to the simulation of quantum many-body systems of charged particles, such as a two-dimensional electron gas. The unique properties of this system arise from the Lorentz force acting on the charged particles and are manifest in the fractional quantum Hall effect. The realms of quantum Hall physics still hold unchartered territory, and a simple connection to ultracold gases is hindered by the obvious absence of electric charge. Alluring to the conceptual equivalence of the Lorentz and the Coriolis force, pioneering experiments have imparted angular momentum to a BEC and observed the nucleation of vortices [Mat99, Mad00]. To reach quantum Hall physics, however, the number of vortices must be on the order of the number of atoms. This is technically challenging in the experiment, as the centrifugal force has to be balanced by the confinement [Sch04].

More recent experiments [Lin09] have taken a new approach: instead of using rotation, synthetic magnetic fields are realized by properly designed optical fields, which couple the atoms' ground- and excited states. Atoms moving adiabatically through the spatial variations of the field acquire a phase, very similar to the Berry's phase. The phase expresses itself in the formation of vortices. This scheme can be extended to include spin-orbit coupling [Lin11]. These approaches rely on the scattering of many photons in rather intense light fields, leading to considerable heating rates.

The imprinted phase can be increased substantially by operating on a lattice geometry [Jak03, Ger10, Gór11a, Blo12]. This approach requires two long-lived states $|g\rangle$ and $|e\rangle$ (hyperfine states or ideally the clock states of alkaline-earth atoms), which can be trapped in species-selective optical potentials. For simplicity, we will consider a 2D geometry. One

lattice axis is formed by light on the magic wavelength, and atoms can tunnel along this direction in a standard way. The orthogonal axis holds light on the anti-magic wavelength, such that atoms in the $|g\rangle$ and $|e\rangle$ states are trapped on alternating sites. A so-called coupling laser (operated on the clock transition for the case of alkaline-earth atoms) drives transitions $|g\rangle \leftrightarrow |e\rangle$ and allows atoms to interchange between adjacent sites of the anti-magic lattice. The phase accumulated by an atom moving in a loop around one plaquette is then comprised of four contributions: two from the tunneling along the magic-wavelength lattice, which are identically zero, and two from the interchange along the anti-magic wavelength lattice, which add up to a nonzero phase. The amplitude of the phase can be adjusted through the angle of the coupling beam with respect to the 2D plane. This phase is then analogous to the phase experienced by a charged particle moving in a magnetic field. The simulated flux, however, is staggered, as atoms moving around adjacent plaquettes accumulate phases of opposite sign [Aid11]. Rectification of the flux yields a scenario identical to the one of the famous Hofstadter's butterfly [Hof76].

The above proposal considers lattice-confined atoms in the tight-binding limit and require an intricate rectification of the flux. By contrast, recently proposed "optical flux lattices" imprint a periodic magnetic flux density with nonzero mean [Coo11b, Coo11a], and do so with a rather shallow lattice. These proposals are particularly well suited for alkaline-earth atoms and generate sufficient flux to reach the fractional quantum Hall regime.

Quantum computation

Closely related to the field of quantum simulation is the field of quantum information processing. In alkali atoms, two hyperfine states of the ground state manifold are usually used as qubit states, connected by an RF transition. The straightforward adaptation in alkaline-earth systems would be the use of the $^1S_0$ and $^3P_0$ clock states of bosonic isotopes. The separation between these two qubit states is in the optical domain, which might have technical advantages [Häf08] and allows for faster operations [Sto08].

The real beauty of alkaline-earth systems, however, rests in the possibility to encode the qubit in the nuclear spin of the fermionic isotopes. Given the decoupling between nuclear and electronic structure, optical transitions can be employed for very well-controlled manipulation of the atom without influencing the qubit. In addition, the nuclear magnetic moment is about three orders of magnitude smaller than the electron magnetic moment, such that the quantum information is well-protected from decoherence induced by collisions or magnetic field noise.

The $^1S_0 - {}^3P_0$ clock transition would be used to coherently transfer atoms between the $^1S_0$ and $^3P_0$ states. Two state-dependent lattices would be used for storage ($^1S_0$) and transportation ($^3P_0$) of the atoms, e.g. to perform phase gates via the interaction of two atoms on a common lattice site. Single-site addressing can be achieved by transfer of atoms into the $^3P_2$ state via a coherent Raman transition from the $^3P_0$ state, or directly from the $^1S_0$ state. The $^3P_2$ state exhibits a large Zeeman-shift, and a sufficiently strong magnetic field gradient ramped across the sample splits the energy of atoms on neighboring lattice sites to enable site-selective transfer. Fluorescence read-out could then be performed on a (quasi-) cycling $^3P_2 - {}^3D_3$ transition [Dal08]. Generally, site-selectivity could also be achieved

by use of a quantum gas microscope with sufficient resolution.

Further proposals elaborate on the implementation of scalable quantum networks using registers and a suitable coupling between lattice sites [Gor09], gate operations [Hay07], and sub-wavelength lattices [Yi08]. All of these proposals on quantum information processing appeared about four years ago and evoked a wealth of further theoretical studies. The experimental realization, however, is technically challenging as it involves a number of delicate lattices, precisely-tuned Raman and clock lasers, and well-controlled magnetic fields. Certain issues, such as the stability of two atoms on a common lattice site or the feasibility of fluorescence read-out, still await experimental verification.

1.2 Polar open-shell molecules

The usual *s*-wave interaction between ultracold atoms is isotropic and short-range. Much richer systems can be created by introducing dipolar interactions, which are anisotropic and long-range, allowing for the study of a variety of novel quantum phases, among them crystalline structures, checker-board phases, topological phases, spin liquids, and supersolids [Gór02, Bar02, Yi07, Bar08]. The orientation of the dipoles can be influenced by an external field. Dipolar interactions come in two flavors: magnetic and electric.

The magnetic dipole-dipole interaction (DDI) is induced by the magnetic moment of the atoms, which is $1\,\mu_B$ for alkali atoms and can be larger for atoms with partially filled shells, e.g. $6\,\mu_B$ for Cr, $7\,\mu_B$ for Er, and $10\,\mu_B$ for Dy. Here, $1\,\mu_B$ is the Bohr magneton. Quantum degeneracy of these species has been achieved [Gri05, Lu11a, Aik12], and impressive dipolar effects such as the anisotropic *d*-wave collapse have been observed [Lah08]. These systems, however, are just on the edge of the strongly dipolar regime, in which the DDI dominates over the spherical *s*-wave interactions.

Electric dipole moments are found in heteronuclear molecules in their rovibrational ground state, where the difference in electronegativity between the two constituting atoms induces an asymmetric charge distribution within the molecule. The interaction between such molecules can be influenced by the trapping geometry, static electric fields, and microwave fields, forming a rich system that has been proposed to be used for the generation of novel quantum phases [Pup, San00, Büc07, Mic07, Gor08, Coo09] and quantum information applications [DeM02, And06, Yel06]. There are two concepts to create such molecules: direct laser [Shu10] and evaporative [Stu12] cooling of thermal molecules, or assembly from ultracold atoms. The latter approach relies on magneto- or photoassociation of weakly bound molecules from two free atoms, and a subsequent fully coherent transfer into the rovibronic ground state using a technique called stimulated Raman adiabatic passage (STIRAP). Such molecules have been produced in KRb [Ni08], and dipolar effects have been investigated. Heteronuclear molecules have dipole moments of up to a few Debye, e.g. $\sim 0.6\,\mathrm{D}$ in KRb.

The DDI of such dipolar molecules can be much stronger than that of magnetic atoms: The dipole potential induced from an electric dipole of 1 D equals that of a hypothetical magnetic dipole moment of $108\,\mu_B$. Molecules of 1 D are therefore a factor of about 10-times more dipolar than the most magnetic atom, dysprosium, and a factor of 100-times more dipolar than alkali atoms. The strength of the DDI scales as μ^2, rendering dipolar effects in

heteronuclear molecules 100-times stronger than in the most magnetic atoms.

Heteronuclear bi-alkali molecules have a strong electric, but no magnetic dipole moment due to the pairing of the two valence electrons[1]. This is different for molecules comprising one alkali and one alkaline-earth atom, which have one unpaired electron and a magnetic moment of $1\,\mu_B$. These molecules combine both flavors of DDI, and they can be influenced by both electric and magnetic fields. The additional spin degree of freedom leads to a spin-dependent DDI, a valuable ingredient that allows for quantum simulation of lattice spin models [Mic06, Bre07]. In short, molecules are placed into a 2D lattice, where nearest-neighbor coupling is provided by the DDI, and the spin originates from the single valence electron. The rotational ground state can be coupled to an excited rotational state using microwave fields, and the interaction between molecules in such excited states is strongly spin-dependent in strength, direction, and range. This versatile coupling between spins allows for the simulation of a large variety of lattice spin models, some of which have topological order. In this way, research with polar molecules connects to the simulation of spin systems discussed in the previous section. Recently, simulations of spin-lattice models using pseudo-spins in bi-alkali ground-state molecules have also been proposed [Gor11b], but the control via both electric and magnetic fields is unique to molecules with an unpaired electron, which are often referred to as *open-shell molecules*.

Now, which specific alkali/alkaline-earth molecule would be suited for these experiments? The electric dipole moments of all ASr molecules have been calculated, A being an alkali element [Gué10]. The dipole moment is largest for A being heavy: 1.9 D for CsSr and 1.5 D for RbSr [Zuc10]. The ASr molecules are radicals from a chemistry point of view, and none of them is stable against decay of the form $2\,\mathrm{ASr} \rightarrow \mathrm{A}_2 + \mathrm{Sr}_2$. The well-established and comparably simple technique to create BECs of Rb makes RbSr the straightforward choice. Another advantage of Rb over Cs is the availability of two bosonic isotopes, which assures the existence of an isotopic Rb-Sr pair for each Sr isotope with non-diverging background scattering length [Zuc]. In addition, it is quite simple to switch the laser systems to K, which has three isotopes, one of them fermionic.

The route towards ground-state molecules might be simplified by the use of A-Sr magnetic Feshbach resonances. A suitable coupling mechanism has recently been identified [Zuc10], but such resonances might be challenging to access experimentally due to their minute width. As we will see later, molecules can also be created without the use of Feshbach resonances. Current experiments with the alkali/alkaline-earth pair Rb-Yb are working towards polar molecules [Nem09]. Similar experiments with the pair Li-Yb are motivated by the large mass imbalance and have succeeded to create double-degenerate mixtures [Har11, Han11], but the electric dipole moment of LiYb is almost zero, and the strongly dipolar regime cannot be accessed.

In conclusion, polar open-shell molecules constitute a very versatile platform, as they can be influenced by both electric and magnetic fields while at the same time allowing for interaction tuning through inter-molecular Feshbach resonances. The prospects of Rb-Sr mixtures are certainly not limited to the investigation of the spin models discussed above. Relating to proposals mentioned in the previous section, degenerate Rb in the superfluid bulk

[1] This is true for molecules in the singlet ground state. Molecules in the triplet ground state do have a magnetic moment, but their electric moment is reduced by a factor of about ten.

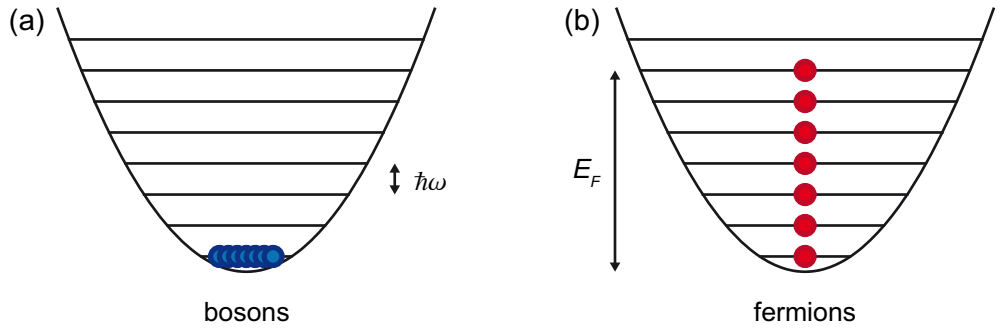

Figure 1.1: Bose and Fermi statistics. A quantum state, e.g. an oscillator state of a harmonic potential, can be occupied by any number of identical bosons (a), while for identical fermions, the occupation is limited to one (b).

phase could be used to remove entropy from a sample of Sr trapped in a species-selective lattice [Dal04, Die08]. Further applications of RbSr molecules include precision experiments [San67, Hud06] and the study of ultracold chemistry [Kre08].

1.3 Quantum degeneracy in atomic gases

All elementary and composite particles possess an extensive property called *spin*. This spin, which is the intrinsic angular momentum of the particle given in units of $\hbar$, can have either an integer or a half-integer value. Particles with integer spin are named *bosons*, and particles with half-integer spin are named *fermions*. This property is imperceptible in our everyday life, but it comes to life with a vengeance at temperatures approaching absolute zero, or, equivalently, at tremendously high densities.

The spin of a particle is related to its ensemble properties via the *spin-statistics theorem*, which rests on relativistic quantum mechanics. It demands that the wavefunctions of two particles be symmetric under the exchange of particles for the case of bosons, and anti-symmetric for the case of fermions. The implications for identical fermions are severe: The wavefunction $\Psi(\mathbf{r})$ describing two identical fermions with wavefunctions $\psi(\mathbf{r}_1)$ and $\psi(\mathbf{r}_2)$ reads $\Psi(\mathbf{r}) = (\psi(\mathbf{r}_1)\psi(\mathbf{r}_2) - \psi(\mathbf{r}_2)\psi(\mathbf{r}_1))/\sqrt{2}$ and vanishes for particles at the same position $\mathbf{r}$. Its non-existence is reflected in the *Pauli exclusion principle*: two identical fermions may never occupy the same quantum state.

The particles' spin also determines their scattering behavior: identical bosons can scatter only in the odd (s-, d-, g-, ...) partial waves, identical fermions only in the even (p-, f-, h-, ...) partial waves. Going to lower temperatures, the higher partial waves are gradually frozen out, and scattering occurs only in the lowest partial wave. This has again implications for gases of identical fermions. The centrifugal barrier of the interatomic potential, which needs to be overcome in a p-wave scattering event, has a height corresponding to a temperature in the range of a few $10\,\mu$K. Identical fermions below this temperature would need to tunnel through this p-wave barrier, and effectively do not scatter at all for $T \to 0$.

We consider a trapped gas of identical particles at a temperature $T = 0$. If the particles are bosonic, they will all occupy the lowest energy state, depicted in Fig. 1.1(a). In a

fermionic gas, however, the Pauli exclusion principle demands that every quantum state be occupied by at most one particle of a kind. The resulting distribution, shown in Fig. 1.1(b), is markedly different to the bosonic case: fermionic particles fill up all energy states up to the *Fermi energy* E_F. The regime, in which the behavior of an ideal gas is dominated by its spin nature rather than its temperature, is referred to as *quantum degenerate*. The deviation from thermal behavior is observed around a *critical temperature*

$$T_C \sim \frac{\hbar^2 n^{2/3}}{k_B m}, \tag{1.1}$$

where n is the density and m the mass of the particles. This temperature is very similar for bosonic and fermionic gases, but the implications of quantum degeneracy are very different.

There exists extensive literature on the theoretical description of degenerate quantum gases, to be found in review articles (e.g. [Ing99, Dal99] for bosonic and [Ing08, Gio08] for fermionic gases) and in a myriad of PhD theses that have appeared in the past 15 years (see e.g. [Sch02] for an excellent and coherent treatment of bosonic and fermionic gases). Here, we will only sketch the basic concepts and introduce a handful of quantities used throughout this thesis.

1.3.1 Bose-Einstein condensation

Bose-Einstein condensation (BEC) is the macroscopic occupation of a single-particle state at finite temperatures. The underlying formalism for photons was introduced by N. Bose in 1924 [Bos24], subsequently extended to massive particles by A. Einstein [Ein24, Ein25], and experimentally realized in 1995 [And95, Dav95].

BEC in a trapped gas

Let us consider a trapped Bose gas with energy states i. The average occupancy of such a state i with energy ϵ_i is

$$\bar{n}_i = \frac{1}{e^{\beta(\epsilon_i - \mu)} - 1}, \tag{1.2}$$

where $\beta = 1/k_B T$ is the inverse temperature and μ is the chemical potential. For a given temperature, the maximum occupation $n_{\max}$ of each state $i > 0$ is finite and given by the temperature T. Adding more than $N_{\max} = \sum_{i=1}^{\infty} n_{\max,i}$ particles to the system leads to a sudden macroscopic occupation of the $i = 0$ state. As the total atom number N increases, more and more particles *condense* into this state and into one single macroscopic wavefunction, called the *Bose-Einstein condensate*. The growth of the ground-state population N_0 is discontinuous as N is increased past $N_{\max}$, constituting a phase transition. Note that this situation of $k_B T \gg \epsilon_0$ is dramatically different to the case of $k_B T \ll \epsilon_0$, where the macroscopic occupation of the ground state is trivial.

For a non-interacting, homogeneous gas, the transition occurs at

$$\lambda_{\mathrm{dB}}^3 n = \zeta(3/2) = 2.612, \tag{1.3}$$

where $\lambda_{\mathrm{dB}} = h/\sqrt{2\pi m k_B T}$ is the thermal de Broglie wavelength and n is the density. The quantity $\lambda_{\mathrm{dB}}^3 n$ is called *phase-space density*. At a phase-space density of order unity, the de Broglie wavelength λ_{dB} is of the same size as the interparticle spacing n^{-3}, indicating an overlap of the single-particle wavefunctions. In a harmonic trap of mean trap frequency $\bar{\omega}$, the phase transition occurs at a critical temperature

$$T_C = 0.94 \frac{\hbar\bar{\omega}}{k_B} N^{1/3}. \tag{1.4}$$

The *condensate fraction* N_0/N is directly related to the critical temperature:

$$\frac{N_0}{N} = 1 - \left(\frac{T}{T_C}\right)^3. \tag{1.5}$$

The Gross-Pitaevskii equation

For a valid description of the BEC, we need to take into account the external trapping potential $V_{\mathrm{ext}}(\mathbf{r})$, as well as interactions. The Hamiltonian for an inhomogeneous, interacting BEC can be written as

$$\hat{H} = \int d\mathbf{r}\, \hat{\Psi}^\dagger(\mathbf{r}) \left(-\frac{\hbar^2\nabla^2}{2m} + V_{\mathrm{ext}}(\mathbf{r})\right) \hat{\Psi}(\mathbf{r}) + \frac{1}{2}\int d\mathbf{r} d\mathbf{r}'\, \hat{\Psi}^\dagger(\mathbf{r})\hat{\Psi}^\dagger(\mathbf{r}')V(\mathbf{r}-\mathbf{r}')\hat{\Psi}(\mathbf{r}')\hat{\Psi}(\mathbf{r}). \tag{1.6}$$

Here, $V(\mathbf{r}-\mathbf{r}')$ is the interparticle potential, which can be replaced by a pseudo-potential $V(\mathbf{r}) = g\delta(\mathbf{r})$ assuming only isotropic, short-range interactions. The coupling constant $g = 4\pi\hbar^2 a/m$ is set solely by the s-wave scattering length a and the atomic mass m. The emerging Schrödinger equation with the nonlinear mean-field term is called the *Gross-Pitaevskii equation* (GPE) of the *order parameter* $\psi(\mathbf{r}, t)$

$$i\hbar\frac{\partial}{\partial t}\psi(\mathbf{r},t) = \left(-\frac{\hbar^2\nabla^2}{2m} + V_{\mathrm{ext}}(\mathbf{r}) + g\,|\psi(\mathbf{r},t)|^2\right)\psi(\mathbf{r},t). \tag{1.7}$$

For a stationary gas in thermal equilibrium, the time dependence can be removed by a separation $\psi(\mathbf{r},t) = e^{-i\mu t/\hbar}\psi(\mathbf{r})$ to yield the time-independent GPE

$$\left(-\frac{\hbar^2\nabla^2}{2m} + V_{\mathrm{ext}}(\mathbf{r}) + g\,|\psi(\mathbf{r})|^2\right)\psi(\mathbf{r}) = \mu\,\psi(\mathbf{r}). \tag{1.8}$$

The Thomas-Fermi approximation

The terms on the left side of Eqn. 1.8 reflect the kinetic energy, the external potential, and the interaction energy, also called *mean-field energy*. In most BEC experiments, the kinetic energy is dominated by the mean-field energy and can be neglected. This is called the *Thomas-Fermi approximation*, which is valid for the case $Na/a_{ho} \gg 1$, where $a_{ho} = \sqrt{\hbar/m\bar{\omega}}$ is the *harmonic oscillator length* of the trapping potential. The trapping potential is often approximated as

$$V_{\mathrm{ext}}(\mathbf{r}) = \sum_{i=x,y,z} \frac{1}{2} m r_i^2 \omega_i^2 \tag{1.9}$$

in all three spatial directions, and $\bar{\omega} = (\omega_x \omega_y \omega_z)^{1/3}$ is the geometric mean of the three trap frequencies. Identifying $|\psi(\mathbf{r})|^2$ with the condensate density $n(\mathbf{r})$, Eqn. 1.8 reduces to

$$n(\mathbf{r}) = \max\left(\frac{\mu - V_{\text{ext}}(\mathbf{r})}{g}, 0\right). \tag{1.10}$$

The density distribution $n(\mathbf{r})$ thus takes the form of the inverted trapping potential (an inverted parabola), which extends to the *Thomas-Fermi radius*

$$R_{\text{TF},i} = \sqrt{\frac{2\mu}{m\omega_i^2}} \tag{1.11}$$

along the trap axis i. The size of the BEC is thus much larger than the harmonic oscillator ground state size a_{ho}. The central density can easily be read off as $n_0 = \mu/g$. The chemical potential, an important experimental parameter, is given by

$$\mu = \frac{\hbar\bar{\omega}}{2}\left(\frac{15Na}{a_{ho}}\right)^{2/5}. \tag{1.12}$$

It is important to recognize that the appearance of BEC is of purely statistical origin, but its behavior is determined by interactions. This is certainly true for the case of superfluid He, where *quantum depletion* limits the condensate fraction to a few percent. In atomic gases, the density needs to be ridiculously small to avoid inelastic collisions and decay into the metallic state[2], and quantum depletion is usually negligible. Still, interactions govern all relevant properties.

The *in-situ* density profile is hardly accessible, and most information about the condensate is drawn from absorption imaging after a time of free expansion, during which the momentum distribution of the BEC maps onto a real-space distribution. Upon release from the trapping potential, the mean-field energy gets converted into kinetic energy. In an anisotropic trap, the expansion is also anisotropic and depends on the initial confinement: The condensate expands fastest into the direction of strongest confinement, where the initial size is given by Eqn. 1.11. The resulting *inversion of the aspect ratio* during *time-of-flight* (TOF) is a prominent hallmark of BEC.

1.3.2 Degenerate Fermi gases

Analogous to Eqn. 1.2 for bosons, we can write down the mean occupation number of an energy state i for fermions as

$$\bar{n}_i = \frac{1}{e^{\beta(\epsilon_i - \mu)} + 1}, \tag{1.13}$$

known as Fermi-Dirac statistics. Clearly, the maximum occupation of any state is 1. For a homogeneous Fermi gas at $T = 0$, all energy states up to the *Fermi energy*

$$E_F = \hbar\bar{\omega}\,(6N)^{1/3} \tag{1.14}$$

[2]Typical densities are around $10^{14}\,\text{cm}^{-3}$. For comparison, the density of strontium in the bulk metal is about $2 \times 10^{22}\,\text{cm}^{-3}$, and the concentration in sea water is about $10^{17}\,\text{cm}^{-3}$.

are occupied; see again Fig. 1.1(b). Straightforward derivations of the Fermi energy are the *Fermi temperature* $T_F = E_F/k_B$ and the *Fermi momentum* k_F as $\hbar^2 k_F^2/2m = E_F$. The set of states with energy E_F and momentum k_F is called the *Fermi surface*, and the set of densely occupied states below is called the *Fermi sea*.

Temperature

There is another temperature in the system besides the Fermi temperature T_F: the "real" temperature T. The Fermi-Dirac distribution in Eqn. 1.13 is a step function for $T = 0$, but the discontinuity is smeared out for finite T: there are empty states below the Fermi surface, and occupied states above the Fermi surface. For $T > T_F$, the distribution approaches the classical Maxwell-Boltzmann distribution: the exponential term in the denominator of Eqn. 1.13 (and correspondingly Eqn. 1.2 for bosons) grows much larger than 1, and the distribution approaches the classical case of $\bar{n}_i = \exp(-\beta(\epsilon_i - \mu))$. The width of the step in the Fermi-Dirac distribution is approximately $E_F \times T/T_F$. Obviously, the degeneracy parameter T/T_F cannot be zero, and experiments typically reach $T/T_F = 0.05...0.2$.

There is no phase transition as we cool a gas into Fermi degeneracy, and the crossover is smooth. In the following, we will discuss three signatures of a *degenerate Fermi gas* (DFG), which shows clear deviations from the behavior of a thermal gas.

Pauli blocking

At degeneracies below $T/T_F \sim 0.5$, the occupation of states below E_F becomes dense. This has implications on the scattering rate of the atoms: From the Pauli exclusion principle, atoms can scatter only into final energy and momentum states that are not occupied. The chances of finding such scarce states is small for $T \to 0$, and the scattering rate is reduced. This suppression of scattering is called *Pauli blocking* and can be observed as a decrease in the thermalization rate. Evaporative cooling, which relies on thermalization, becomes increasingly inefficient in the degenerate regime[3].

A similar effect also appears for the scattering of photons. Atoms in excited states cannot decay into occupied ground states of the Fermi sea, and the decay of such atoms might be inhibited entirely if all energetically allowed final states are Pauli-blocked.

Spatial distribution

The Fermi pressure pushes atoms out of the center of the trap: the cloud is larger compared to a classical thermal distribution. The spatial extension of a Fermi gas into the direction i

[3]First off, evaporative cooling of fermions (relying on contact interactions) requires a mixture of at least two distinguishable atoms, as scattering of identical particles is suppressed by the p-wave barrier. Many experiments employ a two-component Fermi mixture, and suffer from Pauli blocking in both scattering partners. Using a mixture of one bosonic and the fermionic species might improve the situation. In our experiments with a ^{84}Sr-^{87}Sr mixture, we observe the formation of a large ^{84}Sr condensate fraction before reaching Fermi degeneracy. The BEC is superfluid to fermions with velocities below the speed of sound $c = \sqrt{gn/m}$, and the thermalization rate is drastically reduced. In addition, the Fermi pressure increases the size of the fermionic cloud and reduces the spatial overlap with the BEC. We find that a mixture of many (up to $N = 10$) spin states performs much better than a Bose-Fermi mixture.

is

$$R_{\mathrm{TF},i} = \sqrt{\frac{2E_F}{m\omega_i^2}}. \tag{1.15}$$

The spatial distribution depends on the degeneracy parameter T/T_F and can thus be used to measure T/T_F. The deviation from a Gaussian, however, is small and difficult to observe.

Momentum distribution

The spatial distribution of an ideal Fermi gas in a harmonic trap is preserved upon release from the trap. The cloud undergoes a re-scaling in the three directions i, which depends on the initial trap frequencies ω_i and the flight time. For sufficiently long times t_{TOF} ($\omega_i^2 t_{\mathrm{TOF}}^2 \gg 1$), the cloud becomes round, very much in contrast to the bosonic case. It is this rescaled distribution that we use to determine all relevant parameters of a Fermi gas.

The functional form of the distribution of a Fermi gas at finite temperature is derived in Ref. [DeM01a], and a reduced expression is given in Eqn. 5.1. We use these functions to perform two-dimensional *Fermi fits* to our absorption images.

Interactions

In Nature, Fermi systems can be found within the nuclei, in neutron stars, in white dwarfs, and the electron gas in metals. All of these regimes are strongly interacting, meaning that that the interaction energy scale exceeds all other relevant energy scales. For a homogeneous Fermi gas with s-wave scattering, this is fullfilled for $|k_F a| \gg 1$. Such strongly interacting (yet very dilute) systems can also be realized with ultracold atomic samples close to a Feshbach resonance [Tre11][4]. A Feshbach resonance can also be used to interconnect between strongly repulsive and strongly attractive gases, i.e. to study the famous BEC-BCS crossover (see e.g. [Gri08]). In Sr, the scattering length between distinguishable atoms of the fermionic isotope ^{87}Sr is small and cannot be tuned. Generally, the strongly interacting regime can also be reached by loading the atoms into a lattice, thereby making the interaction energy larger than the kinetic energy. This is relevant for the realization of lattice spin models, where the intersite interaction originates from super-exchange.

1.4 Thesis overview

This thesis does not aim to give a complete account of all details relevant to the experimental work with ultracold samples of strontium. This would hardly be possible, and more importantly, there exist already a number of excellent contributions. A first and very readable review article was published by the Florence group [Sor06], and contains all the information

[4] A molecular level can be tuned into resonance with the energy of two free atoms by changing the magnetic field, provided that the free atoms and the molecule have different magnetic moments. On resonance, the scattering length diverges, and it can assume any positive or negative value outside of the resonance. See e.g. Ref. [Chi10] for a review.

necessary for laser-cooling bosonic Sr isotopes. Cooling of the fermionic isotope was pioneered and beautifully described by the Tokyo group [Muk03]. Most of all, two theses from the JILA group [Boy07a, Lud08a] are highly recommended. These two masterpieces contain almost everything one needs to know about strontium, and we keep hardcopies of both of them in the lab and in every office.

This thesis *does* aim to give a complete picture of the current state-of-the-art of quantum degenerate samples of strontium. It aims to provide the reader with the knowledge required to generate degenerate samples of an alkaline-earth element, having in mind the delicate proposals outlined above. In addition, it might serve as a reference for my successors in the lab.

The remainder of this thesis is structured as follows: The first part of Chpt. 2 is devoted to the nuclear, electronic, and scattering properties, and discusses relevant implications for a quantum gas experiment. The second part contains a detailed description of the optical cooling process. Because of its importance and non-triviality, we review the dynamics of narrow-line cooling and discuss the phenomenon of momentum state crystals.

Chapter 3 describes the construction of the experimental apparatus. The vacuum chamber and the coil system to generate magnetic fields are described in brief. Emphasis is put on a description of the various near-resonant laser systems, as well as the dipole trap and the lattice. Technical details on the construction of stable cavities, spectroscopy cells, and the oven are deferred to the appendices.

Chapter 4 is the first one to present scientific results: the first BEC of Sr, created in September 2009. Experiments are performed with the ^{84}Sr isotope, which exhibits very favorable scattering properties.

Chapter 5 takes us onward to the fermionic ^{87}Sr isotope, which is the one of interest for the studies outlined above. We demonstrate a certain degree of control over the spin state composition, allowing us to prepare a spin-polarized degenerate Fermi gas. The fermions are sympathetically cooled with ^{84}Sr to form a double-degenerate Bose-Fermi mixture.

Chapter 6 shows a route to Bose-condense the isotope ^{86}Sr, which has a very large scattering length and requires an adaption of the evaporative cooling scheme.

Pursuing the ideas laid out in Sec. 1.1 requires precise control over the spin states. We devote the entire Chpt. 7 to both creation and detection of arbitrary spin compositions, and we take a first step to show that these states indeed have SU(N) character.

Over the years, our experimental capabilities have evolved dramatically, and we were able to improve key parameters of quantum gas experiments by orders of magnitude. Chapter 8 is a collection of many individual experiments reflecting the current status of our apparatus. Specifically, we present an ^{84}Sr BEC of 10^7 atoms, which is the largest BEC created in an optical trap to date, and a BEC of 10^5 atoms created in 2 seconds, which is the fastest cycle time ever reported. Further, we present Fermi degeneracy down to $T/T_F = 0.08$ in ^{87}Sr, along with a set of double-degenerate mixtures.

Some of the proposals described above utilize optical transitions originating from the metastable $^3P_{0,1,2}$ states. We present the novel spectroscopy scheme, allowing us to thoroughly investigate the $^3P_2 - 5s5d\,^3D_{1,2,3}$ transitions. This scheme, together with data on the $5s5d\,^3D$ hyperfine structure at MHz-precision, is presented in Chpt. 9.

Chapter 10 contains the implementation of yet another important ingredient to our ap-

paratus: a 3D optical lattice. We show the superfluid to Mott-insulator transition and other experiments performed in the lattice.

The Mott-insulator state with atoms on doubly occupied sites constitutes the starting point for the creation of fully state-controlled $^{84}Sr_2$ ground-state molecules. These are directly associated via STIRAP, thereby circumventing the need for magnetic Feshbach resonances. The experiment is presented in Chpt. 11, along with the relevant photoassociation spectroscopy data.

Chapter 12 does not strictly follow the lines of quantum simulation experiments, but re-visits a long-standing and hitherto elusive goal: the attainment of quantum degeneracy in atomic gases purely by laser cooling and thermalization, not relying on evaporation. We show how a properly prepared sample of ^{84}Sr atoms can undergo the BEC phase transition within a region of carefully designed optical potentials. This experiment immediately encourages novel approaches to create continuous sources of quantum matter.

In Chpt. 13, we conclude with an outlook on experiments planned for the near future, and projects envisioned for the more remote future. We close the loop by revisiting the proposals described in the beginning of the present chapter, and we discuss their feasibility in light of the experimental progress already made.

Chapter 2

Strontium: an alkaline-earth element

2.1 The discovery of strontium

We find ourselves in London, it is the year 1790. A. Crawford and his assistant W. Cruickshank are employed as physicians in St. Thomas' Hospital, just south of London bridge. Many diseases, such as cancer, are treated with mercurial salts at this time. Crawford and his co-workers are well aware of the serious side effects, and are attempting to substitute the mercury compounds with *muriated barytes* (barium chlorides, $BaCl_2$, where the mineral baryte is $BaSO_4$), while ceaselessly searching for ever better treatments. In a lead mine in Strontian, Argyllshire, Scotland, they discover a *new earth*, easily mistaken for the already-known *witherite* (barium carbonate, $BaCO_3$). They succeed to turn this *new earth* (strontium carbonate, $SrCO_3$) into a chloride ($SrCl_2$), which allows for extensive comparisons with the *muriated baryte*. They find striking differences in many properties, such as the specific weight, solubility in water, and crystalline structure. Crawford and co-workers conclude that this substance must contain an ingredient different from the one in the *muriated baryte* [Cra90].

At the same time, F.G. Sulzer describes the same mineral and names it *strontianite* in view of the location where it was found [Sul]:

> I have named this interesting fossil of my small collection, which seems to contain its own underlying earth, strontianite, and will sacrifice all that I have left of it for further studies. It is an [...] earth, some pieces of which have a clearly visible similarity with the witherite; but differ by its smaller specific weight, which amounts to 43 for the witherite, but less than 36 for the strontianite. Furthermore, ...

Sulzer and his co-workers examine the new mineral closely and find many differences to the *witherite*. In the following years, many chemists perform further studies with this *new earth*, most noticeably T.C. Hope in Edinburgh [Hop98], R. Kirwan in Dublin [Kir95], and M.H. Klaproth in Berlin [Kla93, Kla94]. All available knowledge of that time is gathered by Klaproth in his Chemisches Wörterbuch (Dictionary of chemistry, [Kla07]), in which he devotes a separate chapter to the *strontian earth*:

Figure 2.1: Chemists renowned for the discovery of strontium: William Cruickshank (source unknown), Thomas Charles Hope (courtesy of the Scottish National Portrait Gallery), Martin Heinrich Klaproth (Smithsonian Libraries), and Humphry Davy (*ibid.*, from left to right).

> Nature has not yet offered [strontian] earth in a pure state; the chemist therefore feels obliged to precipitate this earth from its natural compounds with carbonic acid und sulfuric acid. [...] The pure strontian earth[1] is a porous material of greyish-white color, caustic and alkaline taste. [...] It acts less severe onto the animal body than baryte earth, and it is not poisonous. It does not melt in front of the blow pipe, but it is permeated by light and surrounded by a white, glaring flame, hardly bearable to the eye.
>
> Baryte earth[2] and strontian earth approach each other in multiple properties. The main features, by which to tell the latter from the earlier, are the following: it is less caustic; has a lesser specific weight, phosphorizes in front of the blow pipe, stains the flame purple red; is infusible, requires a significantly larger amount of water to dissolve; it forms crystals of a different principal type, shows a more distant relationship towards acids, and does not exert poisonous properties on the animal body.
>
> One has initially deemed the strontianit (which contains a compound of this earth with carbonic acid, and was the first fossil in which this earth was found in exquisite quantities), to be barite carbonate. [...][3]

In his work, Klaproth describes a wealth of experiments carried out with different chemical compounds containing strontium, and how they compare to the corresponding compounds containing barium. It was not until 1808 that Sr became available as a pure metal.

[1] This is $SrCl_2$, not yet the pure metal.
[2] $BaCl_2$
[3] All translations by the author of this thesis.

isotope	natural abundance	statistics	nuclear spin
^{84}Sr	0.56%	bosonic	0
^{86}Sr	9.86%	bosonic	0
^{87}Sr	7.00%	fermionic	9/2
^{88}Sr	82.58%	bosonic	0

Table 2.1: Naturally ocurring isotopes of strontium, data taken from [NIS].

Sir H. Davy used electrolysis with mercury oxide to remove the Cl_2. He obtained strontium amalgam, from which the metal can be extracted by distillation, and he named it *strontium* [Dav08]. Appreciating the chemical similarity of Ca, Sr, and Ba and quantifying many of their properties contributed to the development of the periodic table some 70 years later.

2.2 Nuclear properties

There are four naturally occurring isotopes of Sr, three of them are bosonic and one is fermionic; see Tab. 2.1. The nuclear spin of all bosonic alkaline-earth elements is zero ($I = 0$), with a simple explanation: Given the two valence electrons and all inner shells filled with even numbers of electrons, the total electron number is even. The neutral overall charge requires the proton number to be even as well. The bosonic character of the atom then requires the total number of electrons, protons, and neutrons to be even, thus the neutron number needs to be even, too. In such even-even nuclei, the nucleons arrange in pairs of antiparallel spin, and the nuclear spin is zero. The nuclear spin of ^{87}Sr is $I = 9/2$, the highest of all stable alkaline-earth isotopes.

There are more than 20 unstable isotopes of Sr. The isotope most prominent to the general public is ^{90}Sr, which has a lifetime of 29 years and is produced in nuclear bombs and nuclear power plants. Both ^{89}Sr and ^{90}Sr are used in medical applications. The isotopic ratio ^{86}Sr/^{87}Sr can vary for different types of rock, and is also used for isotopic tracking. ^{87}Rb decays into ^{87}Sr, and the ratio of these two isotopes can be used to determine the age of rock on geologic timescales.

2.3 Electronic properties

Strontium is an alkaline-earth element and can be found in the second column of the periodic table. There is a class of elements with an electronic structure very similar to that of strontium. These elements are the other alkaline-earth species Be, Mg, Ca, Ba, and Ra, the members of the zinc-family Zn, Cd, Hg, and Cn, as well as Yb and No. These atoms are often referred to as “alkaline-earth like systems”, “group-II-atoms”, or “two-electron systems”. Neither of these terms seems convincing, and for simplicity, we will call all elements of this class “alkaline-earth atoms” throughout this thesis. In the following, we will show that these atoms are indeed very different from the alkalis.

	$^1S_0 - {}^1P_1$	$^1S_0 - {}^3P_1$	$^3P_1 - {}^3S_1$	$^3P_2 - 5s5d\,{}^3D_2$	$^3P_2 - 5s5d\,{}^3D_3$
^{84}Sr	−270.8	−351.49	≈ 200	−91.8	−91.6
^{86}Sr	−124.8	−163.81	≈ 100	−47.5	−46.6
^{87}Sr	−46.5	−62.15	54		
^{88}Sr	0	0	0	0	0

Table 2.2: Isotope shifts of the Sr isotopes, given in MHz. All values are referenced to the most abundant isotope ^{88}Sr. The hyperfine structure of the fermionic isotope ^{87}Sr is much larger than the isotope shift, which is stated here for an assumed $J = 0$ state. The relevant hyperfine structure can be found in Fig. 2.3.

2.3.1 Optical transitions

The ground-state electronic configuration of Sr reads [Kr]5s^2, featuring two valence electrons in the outer s-shell. The level structure of the excited states resembles that of the well-known helium atom[4]. The spins of the two valence electrons can be aligned anti-parallel (singlet states, $S = 0$) or parallel (triplet states, $S = 1$). We find broad transitions within the singlet and triplet systems, where almost all the transitions into low-lying states are in the visible range of the electromagnetic spectrum and nicely accessible with current laser technology.

The singlet and triplet states are connected by narrow intercombination lines. The linewidth of these transitions lies between the pHz and the MHz range, as we will discuss later. These transitions can be used for laser cooling, state preparation, and for the construction of frequency references in the optical domain. In addition, transitions originating from the metastable ^3P states into higher-lying singlet states can be used for quenching of the lifetime [Kra09, San11].

All alkaline-earth elements possess two different cooling transitions, originating from the $^1S_0$ ground state and addressing the $^1P_1$ and $^3P_1$ states. The lifetime of the $^1P_1$ state in Sr has been measured to be 5.22(3) ns [Nag05] and 5.263(4) ns [Yas06], which translates to a linewidth $\Gamma \approx 2\pi \times 30.5\,\mathrm{MHz}$ of the $^1S_0 - {}^1P_1$ transition[5]. The properties of the metastable $^3P_1$ state will be discussed later.

Isotope shifts — Most of the early Sr experiments were centered around the isotopes ^{87}Sr and ^{88}Sr, where the hyperfine structure of ^{87}Sr hides the isotope shift. Working now with all four isotopes of Sr requires consideration of the shifts of all relevant states. The shifts are on the order of 100 MHz, a frequency difference that can easily be bridged by acousto-optical modulators (AOMs). Table 2.2 states the isotope shifts of relevant transitions.

AC Stark shifts — Any radiation field couples to all atomic states and alters their energies. We employ these AC Stark shifts to locally and temporally change the energy of a

[4]The most prominent modification in Sr is the appearance of a $5s5p\,{}^3P$ manifold (the corresponding $1s1p\,{}^3P$ manifold does not exist in He), which lies below the $5s6s\,{}^3S_1$ state. The corresponding $1s2s\,{}^3S_1$ state is the lowest triplet state in He and used as the ground state in experiments with He*.

[5]Many values of the linewidth of this transition can be found in the literature. Although the value obtained by the Tokyo group is more precise ($\Gamma = 2\pi \times 30.24(2)\,\mathrm{MHz}$), we will stay with the earlier value of 30.49(17) MHz by the Rice group, which is also used by the JILA group. In our lab, we found 30.96(33) MHz from varying the detuning in absorbtion imaging.

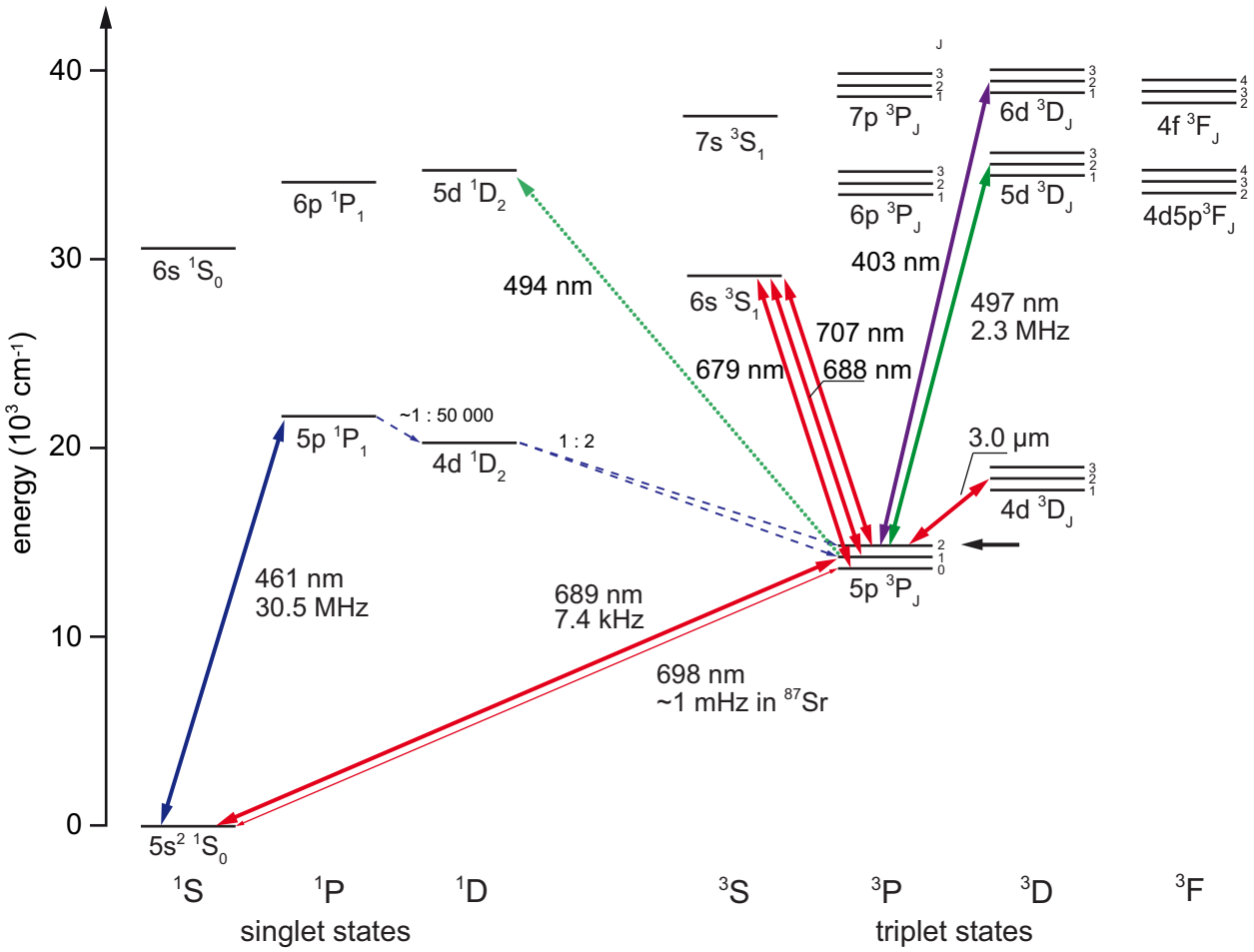

Figure 2.2: Selection of the level scheme of strontium. The position of the manifolds are drawn to scale, but the finestructure splittings are not. The MOT and repump transitions (solid arrows), decay paths from the $^1P_1$ state (dashed arrows) and branching ratios, a proposed quenching transition (dotted arrow), and the clock transition (thin arrow) are depicted. The $^3P_2$ reservoir state is indicated by a short arrow. The ionization threshold is at 45932.09 cm^{-1} (5.69485 eV). The position of the levels is taken from [NIS], additional information on lifetimes and branching ratios is available from [Pol05a].

specific state (see e.g. Chpt. 12), but differential AC Stark shifts are usually a nuisance and need to be avoided. The wavelength of a light field, for which the AC Stark shift of two states is equal, is called the *magic* wavelength. The wavelength, at which the AC Stark shift of two states is equal but of opposite sign, is called *anti-magic*. The two transitions, for which the light shifts play an important role, are the $^1S_0 - {}^3P_0$ clock transition and, to a much lesser degree, the $^1S_0 - {}^3P_1$ cooling transition. The magic wavelengths for these transitions are around 813 nm and 915 nm, respectively[6]. Further distinguished wavelengths are 627 nm, for which the $^3P_0$ polarizability is zero, and 689.2 nm, for which the $^1S_0$ polarizability vanishes. The reduction of light shifts induced by the dipole trap will be discussed on a few occasions throughout this thesis, but we refer the reader to Ref. [Boy07a] for a detailed treatment.

2.3.2 Metastable states

The decay of the metastable $^3P_{0,1,2}$ states into the $^1S_0$ ground state requires an electron spin-flip, which cannot be accomplished by emission of a single photon: these states should be stable! They may, however, acquire a finite lifetime through higher-order processes.

The $^3P_0$ state is *the* clock state in strontium. For the bosons with $I = 0$, spin-orbit interactions are absent, and the dominant decay path is the E1M1 two-photon decay. The rate of this decay is tiny, and the lifetime is calculated to be thousands of years. For the fermionic isotope, the nonzero magnetic dipole moment couples the $^3P_0$ state to other states of the same parity, among them the $^1P_1$ and $^3P_1$ states; this mechanism is called hyperfine coupling. These states can decay into the $^1S_0$ state by a simple electric dipole (E1) process. The lifetime of the $^3P_0$ state in this case is on the order of 100 s [Boy07c, San04].

The lifetime of the $^3P_1$ state is reduced by spin-orbit interaction, which mixes some $^1P_1$-state contribution into the $^3P_1$ state. This admixture allows for weak electric dipole (E1) decay, leading to a lifetime of 21.4 μs and a corresponding linewidth of $\Gamma = 2\pi \times 7.4$ kHz [Boy07a].

The $^3P_2$ state and its lifetime are relevant for our work as we use this state for shelving of atoms during the first cooling stage. This state can decay via different pathways. Two of these are parity-conserving one-photon decays of magnetic-dipole (M1) and electric-quadrupole (E2) type into the $^3P_1$ state and further into the ground state. For Sr, the dominant process is a magnetic octupole (M2) transition directly into the ground state, with a calculated lifetime of about 1000 s [Der01, San04]. The Tokyo group measured a lifetime of about 500 s, which was explained by radiative decay. Black-body radiation can excite atoms into the $5s4d\,{}^3D$ states, from where they decay into the $^3P_1$ state. Indeed, the lifetime was found to depend on the temperature of the environment [Yas04].

The finite lifetimes of the metastable states are beautifully explained and calculated for Mg, Ca, and Sr in [San04].

[6]The magic wavelength of the clock transition has been determined with MHz-precision. Another radiation field inducing a differential shift of the two clock states is the black-body radiation of the environment. Tremendous efforts are made to quantify and reduce the magnitude of this shift, e.g. by measuring the DC polarizability of the clock states ([She12] for Yb and [Mid12] for Sr), by interrogating the atoms in a well-defined or cryogenically cooled environment, or by choosing a comparably insensitive atomic species, such as Hg.

2.3.3 Nuclear and electron spin

Nuclear spin — The bosonic isotopes of Sr have zero nuclear spin, which has manifold implications. Obviously, there is only one spin state in the $^1S_0$ and $^3P_0$ states, $m_J = 0$. Certain laser-cooling techniques, such as sub-Doppler cooling and VSCPT, require more than one m_F state and are not possible in bosonic strontium. The nuclear magnetic moment is zero, precluding the appearance of hyperfine structure. The lack of hyperfine structure simplifies laser cooling compared to the alkalis, as no repumping from a "wrong" lower hyperfine state is required. On the other hand, certain techniques such as the dark spot magneto-optical trap (MOT) require a hyperfine structure and are not possible in alkaline-earth systems. The fermionic isotope ^{87}Sr carries a nuclear spin of $I = 9/2$, giving rise to ten magnetic substates in the $^1S_0$ and $^3P_0$ states.

Electronic spin — The electron spin and the associated electronic magnetic dipole moment of the singlet $^1S_0$ state are zero ($J = 0$) due to the antiparallel alignment of the two valence-electron spins. This fact brings about at least three immediate consequences: the absence of hyperfine structure even for the case of $I \neq 0$, the absence of magnetic Feshbach resonances [Chi10][7] and a tremendously reduced sensitivity to B-fields. The only magnetic moment of the atom arises from the nuclear spin, which is smaller by a factor of about 1000, or, more precisely, about the proton-to-electron mass ratio[8]. The performance of conventional magnetic Stern-Gerlach separation, which relies on a force $F_z = \mu_{\mathrm{atom}}\, \partial B/\partial z$, is substantially reduced and would require ridiculously large magnetic field gradients. The absence of an electron spin makes this state comparably insensitive to B-fields, which is advantageous for many applications in precision measurements.

The absence of an electron magnetic moment also leads to a much reduced Zeeman-splitting of the m_F states in the fermionic $^1S_0$ state: the g_F factor is again smaller by a factor $\sim 10^3$. For the narrow-line MOT, the g_F factors of the ground state and excited $^3P_1$ state are therefore very different, leading to an exotic operation of the MOT, which will be described in Sec. 2.7.

All of these characteristics also apply to the $^3P_0$ state, which has zero electron spin as well ($J = 0$). This is a remarkable property: On the $^1S_0 - {}^3P_0$ clock transition, the nuclear and electron spin are almost completely decoupled. This allows us to store a piece of quantum information in the nuclear spin ($m_F = -9/2 \ldots + 9/2$) of an atom, and to optically transfer the atom between the $^1S_0$ and $^3P_0$ states without disturbance of the qubit. The $^1S_0$ and $^3P_0$ states can be addressed individually by light fields, facilitating transport, state preparation, and state read-out [Dal08].

Hyperfine structure — For the fermionic isotope, we finally do obtain hyperfine structure for the states with $J \neq 0$. The splittings between adjacent F-states are between a few 10 MHz and 1 GHz, easily accessible by acousto-optical modulators. The ordering of the F-states can be perturbed or even inverted, depending on the hyperfine parameters A and

[7] Feshbach resonances might exist in the fermionic ^{87}Sr isotope, but would be incredibly weak [Jul].

[8] Recall that the Bohr magneton is $\mu_B = e\hbar/2m_p$, and the nuclear magneton is $\mu_B = e\hbar/2m_e$. The g_F factors of the $^1S_0$ and $^3P_0$ clock states, as well as their difference, are on the order of 100 Hz/G [Boy07c].

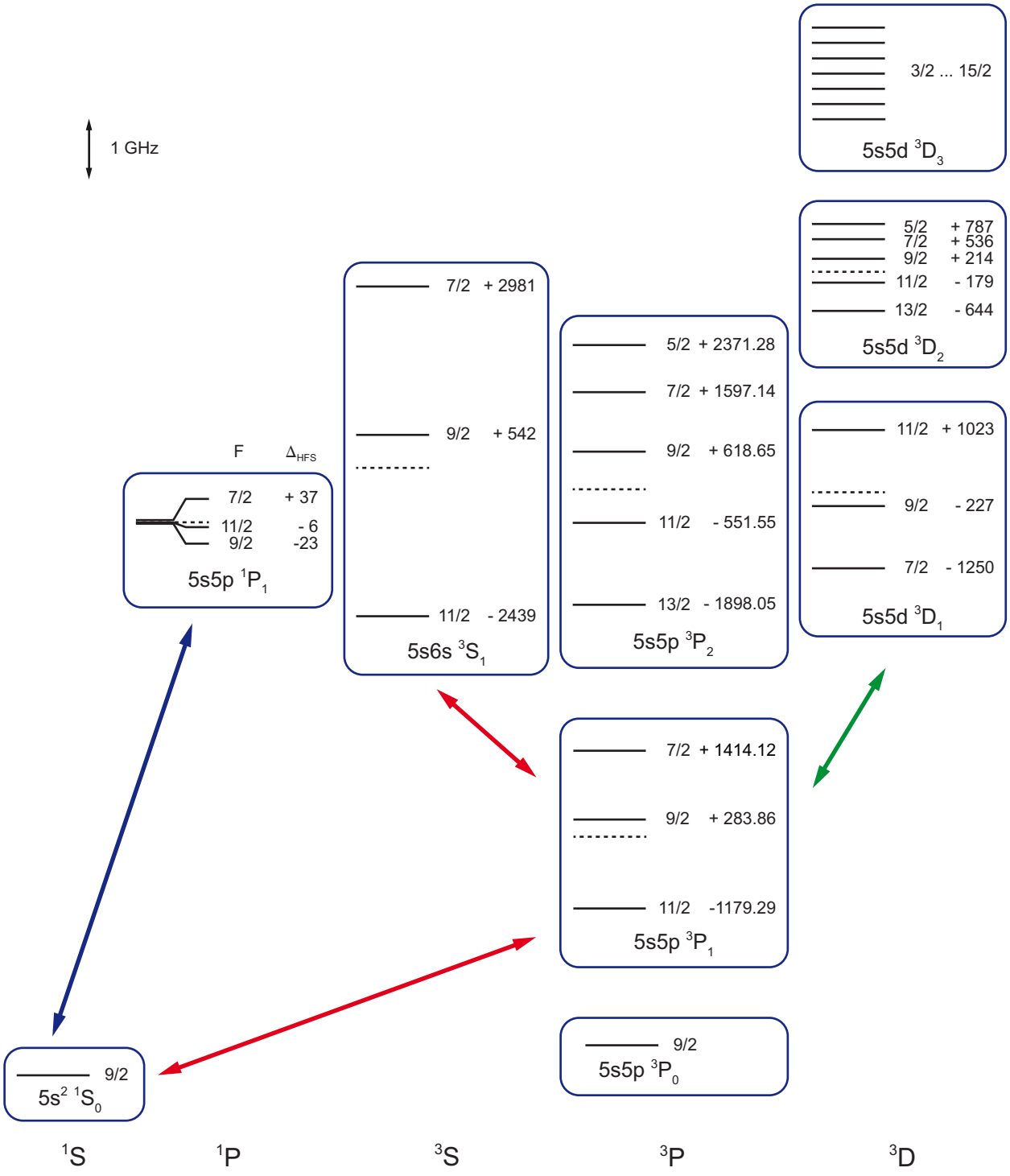

Figure 2.3: Hyperfine structure for relevant states of ^{87}Sr. The splittings are given in MHz and calculated with respect to an assumed $I = 0$ state, indicated by a dashed line. The calculation is based on the A and Q interaction constants taken from [Boy07a] and determined in the measurements presented in Chpt. 9.

	$^1S_0 - {}^1P_1$ (MHz)	$^1S_0 - {}^3P_1$ (MHz)	g_F	$g_F\mu_B$ (kHz/G$\times m_F$)
$F = 7/2$	-9.7	1352.0	$-1/3$	-467
$F = 9/2$	-68.9	221.7	2/33	85
$F = 11/2$	-51.6	-1241.4	3/11	382

Table 2.3: A choice of experimentally relevant hyperfine parameters of ^{87}Sr, given in MHz. The $^1S_0 - {}^1P_1$ and $^1S_0 - {}^3P_1$ transition frequencies in the first two columns are referenced to the ^{88}Sr isotope, which gives the strongest spectroscopy signal and is often used for locking purposes. The Zeeman-splittings $\Delta E = m_F g_F \mu_B B$ of the three $^3P_1$ hyperfine states need to be calculated quite frequently, the coefficients are given in the last column. Here, $\mu_B = 1.400\,\mathrm{MHz/G}$ is the Bohr magneton.

Q. The splitting in the $^1P_1$ state is smaller than the linewidth of the transition, leading to a decreased performance of the MOT. The hyperfine structure of the $^3P_1$ state, however, can be resolved very well on the intercombination line and has been measured to great accuracy together with the structure of the $^3S_1$ state [Cou05, QV05]. A measurement of the $5s5d\,^3D_{1,2}$ structure will be presented in Chpt. 9.

The hyperfine structure of the $^3P_2$ state in the alkaline-earth systems is unique as it reveals information about the structure of the nucleus. Measuring the hyperfine splittings with a precision of 1 kHz allows one to determine the nuclear octupole moment to within 10% [Bel08]. The current best values have an uncertainty of a few kHz [Hei77].

The hyperfine splittings of all states relevant for this thesis are given in Fig. 2.3. In the experiment, the important quantity is usually the detuning from the respective ^{88}Sr transition, and we state relevant numbers in Tab. 2.3 for easy reference. All $^3P_1 - {}^3S_1$ hyperfine transitions are listed in Ref. [QV05], and the ones of the $^3P_1 - 5s5p\,^3D_{1,2}$ transitions can be found in Chpt. 9. A full account of all relevant parameters and appropriate references can be found in [Boy07a].

2.4 Scattering properties

The scattering properties of an atomic species are of utmost importance for quantum gas experiments: they govern e.g. the performance of evaporative cooling, the stability of a degenerate gas, and the magnitude of mean-field shifts. Many phenomena, such as the BEC-BCS crossover or the Efimov scenario, are intimately connected to interactions. For low temperatures, the scattering behavior can be captured in one single parameter: the s-wave scattering length a.

$a(B)$ vs $a(m)$ — For alkali atoms with a sizeable magnetic moment in the ground state, the scattering length a can be tuned by an external B-field ($a(B)$) to assume any value $-\infty < a < \infty$ in the vicinity of a Feshbach resonance [Chi10]. This is not possible with the alkaline-earth systems due to $J = 0$ in the ground state, and a is fixed by the binding energy of the last bound vibrational state of the ground-state molecular potential of the two

	^{84}Sr	^{86}Sr	^{87}Sr	^{88}Sr
^{84}Sr	124	32	−56	1800
^{86}Sr	32	830	164	98
^{87}Sr	−56	164	97	55
^{88}Sr	1800	98	55	−1

Table 2.4: Scattering lengths between the strontium isotopes, given in units of a_0. The values are averages of the values given in [Mar08] and [Ste08], and the uncertainty is a few a_0 except for the two very large values, where the uncertainty is larger.

scattering atoms (or the first state above threshold)[9].

The shape and depth of the ground-state potential and thus the binding energy of the vibrational states depends on the mass of the two atoms involved. This implies that the position of the last bound vibrational state with respect to the free-atom threshold depends on the isotope! Two very pleasant features congregate in the alkaline-earth systems: (i) For atoms heavier than Ca [Dam11], the last vibrational level moves away from threshold (downwards) by less than half a vibrational level spacing per mass increase by one atomic mass unit ($1u \approx m_{\text{neutron}}$). The scattering length of a "string" of isotopes therefore follows a somewhat simple and highly predictable pattern, as we will see later. (ii) The heavy alkaline-earth elements possess many isotopes, which can be understood from a nuclear physics' point of view: the even number of protons leads to a stable nucleus, even for a variety of neutron numbers. Both Rb and Cs possess only one stable isotope[10], while Sr and Ba, with only one additional proton, feature four and seven stable isotopes, respectively. These two features allow for an (admittedly very coarse) *mass-tuning* of the scattering length, which becomes finer for elements with higher masses, as illustrated for Sr and Yb in Figs. 2.4 and 2.5. For all elements heavier than Ca, it is certain that there exists at least one bosonic isotope with positive scattering length.

Strontium isotopes — Early work on Sr focused on the most abundant ^{88}Sr isotope. It was realized quite soon that the scattering length a_{88} would be small, which is great for precision measurements, but fatal for evaporative cooling [Ido00, Pol05b, Yas06]. An attempt to sympathetically cool ^{88}Sr with ^{86}Sr was hindered by the large value of a_{86} [Fer06a]; see Tab. 2.4.

The scattering length of ^{84}Sr was calculated for us in the summer of 2008 by R. Ciuryło, using photoassociation (PA) data from the Rice group [Mic05]. He obtained a value of $a_{84} = 124\,a_0$ with a small error, where a_0 is the Bohr radius [Ciu]. This calculation greatly influenced our approach to reach BEC in strontium[11]. Two separate publications appeared

[9] It should be noted that magnetic Feshbach resonances do exist between atoms in the $^1S_0$ and $^3P_2$ states.

[10] The isotope ^{87}Rb occurs naturally, but is strictly speaking not stable with a half-life of 50 billion years.

[11] A spectroscopic determination of a_{86} and a_{88} existed already in the summer of 2005 [Mic05], while a more accurate value of a_{88} alone had been published earlier that year by the Tokyo group [Yas06]. The obtained values agree well with later measurements, but were not precise enough to obtain an accurate prediction of a_{84}. In hindsight, it is amusing to speculate to which degree a_{84} could have been calculated already at that time, and if the outcome would have had an impact on the research pursued in our community.

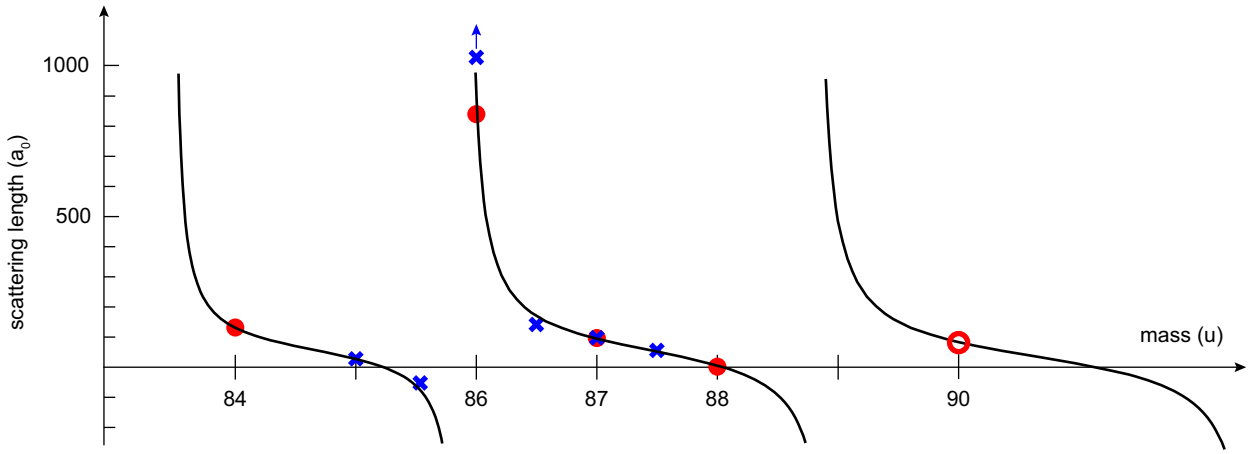

Figure 2.4: Mass tuning of the scattering length. The homonuclear scattering lengths of the four stable Sr isotopes (red dots) are approximated by a tangent function. The heteronuclear scattering lengths (blue crosses placed at the averaged masses) match this fit as well. From this simple plot, the scattering length of ^{90}Sr (red circle) can be estimated to be around $100\,a_0$. Mass scaling works best for heavy elements.

a few weeks later, confirming this result. The group of E. Tiemann used Fourier transform spectroscopy together with earlier photoassociation (PA) measurements [Mic05, Yas06] to calculate the ground-state potential and scattering lengths. The Rice group performed two-photon PA spectroscopy to directly measure the binding energy of the last bound state in ^{88}Sr, and inferred the scattering lengths of the other isotopes by mass scaling [Mar08]. The three values of a_{84} were obtained using somewhat different methods and are in remarkable agreement of 1%, which is well within the uncertainty of the individual determinations. The high accuracy of simple mass scaling had been shown already for the case of Yb [Kit08] one year earlier.

Optical Feshbach resonances — A continuous tuning of the scattering length a would be highly desirable for many experiments, for example to facilitate evaporation, to enter the strongly interacting regime, or to minimize mean-field shifts. Not only magnetic fields, but also light fields close to a PA resonance can influence the scattering length [Fed96a]. These *optical* Feshbach resonances (OFRs) have been studied in Rb [The04] and observed to be accompanied by strong losses. There has been considerable hope that the losses would be orders of magnitude smaller if a PA feature associated to a narrow transition was used. Extensive work by the JILA group on the $^1S_0 - {}^3P_1$ transition in ^{88}Sr observed a clear alteration of the elastic scattering rate, but losses were substantially larger than initially expected [Bla11b]. Related work by the Rice group [Mar09b] and in Yb [Yam10] showed that the scattering length can be changed for time scales on the order of 10^{-3} s. Many applications, such as evaporative cooling and clock interrogation, however, require timescales on the order of seconds, and it seems unlikely that OFRs will be helpful. The resonance strength of an

OFR is expected to be orders of magnitude larger for isotopes with a bound state close to threshold, e.g. ^{172}Yb, ^{86}Sr, or ^{40}Ca. Such experiments have not yet been performed.

SU(N) character — The scattering lengths between different m_F states in the alkalis, e.g. Rb, are similar, but slightly different. This dependence of scattering behavior on the spin state is also reflected in the possibility of spin-changing collisions, in which the total angular momentum $M_F = m_{F,i} + m_{F,j}$ is conserved, but the two colliding atoms i and j might change their internal state. In the alkaline-earth elements, the $^1S_0$ and $^3P_0$ states possess no electronic magnetic moment, such that the nuclear moment cannot couple to the electronic structure [Boy07c]. The spin state is encoded in the nucleus, well isolated from the environment, and we expect identical scattering lengths for every pair of two different m_F states, as well as the absence of spin-changing collisions. This higher degree of "similarity" between the m_F states is referred to as SU(N) symmetry and forms the basis of many proposals for quantum simulation [Gor10]; see Chpt. 1.1.

Inelastic scattering of bosons in the $^3P_2$ state — The $^3P_2$ state seems like a picture-perfect world for magneto-optical trapping and evaporation. This state gets already populated during the broad pre-cooling MOT, and further cooling can proceed on the broad $^3P_2 - 5s5d\,^3D_3$ transition at 497 nm, followed by narrow-line cooling on the $^3P_2 - 5s4d\,^3D_3$ transition at 2.92 μm. This transition has a linewidth of about 50 kHz, and the magnetic substructure of the $^3P_2$ state even allows for sub-Doppler cooling. The large wavelength implies a very low recoil temperature of 110 nK. This transition is also very closed: There is no other state below the $5s5d\,^3D_3$ state that could open up an additional decay channel with a reasonable decay rate. The fermionic isotope ^{87}Sr exhibits hyperfine structure in the two states involved, but the hyperfine splitting is on the order of 10^4 linewidths, such that excitation of the "wrong" state is negligible. Evaporation could proceed in either an optical or a magnetic trap, and imaging of atoms in the $^3P_2$ state could be performed on a variety of transitions.

This marvelous setting is spoiled by the presence of inelastic two-body collisions. Upon a collision, an atom can change its Zeeman substate m_J, its fine-structure quantum number J, or go directly into the ground state. The energy released in any of these processes greatly exceeds the trap depth, leading to trap loss. Such rapid loss has been observed in Ca [Han06], Yb [Yam08], and Sr [Tra09] (inelastic decay rate coefficient $\beta_{in} \approx 1 \times 10^{-10}\,\mathrm{cm}^3/\mathrm{s}$), leaving little hope that evaporative cooling in the $^3P_2$ state will be successful.

Inelastic scattering of bosons in the $^3P_0$ state — A similar experiment was performed in the $^3P_0$ state of ^{88}Sr [Tra09, Lis09], where the only energy-releasing mechanism is a direct decay into the ground state. The ratio of the elastic and inelastic collision rates was found to be of order unity, which precludes evaporative cooling. The loss rate coefficient was determined to be about $\beta_{in} \approx 2 \times 10^{-11}\,\mathrm{cm}^3/\mathrm{s}$ [Tra09]. The PTB group also measured the inelastic loss rate for two atoms in the $^1S_0 + {}^3P_0$ combination to be a factor of 10 smaller than in the $^3P_0 + {}^3P_0$ combination [Lis09].

Inelastic scattering of fermions in the $^3P_0$ state — Many of the proposals outlined

in Chpt. 1 require the presence of two or more distinguishable fermions on the same lattice site. The atoms would be in the $^1S_0$ or $^3P_0$ state, which naturally raises the question of stability. The JILA group has approached this subject by measuring the loss of atoms at μK-temperatures in a 1D optical lattice [Bis11]. The loss rate coefficient of a mixture prepared in a single $^3P_0$ spin state was found to be high ($K_{ee} \approx 10^{-11}\,\mathrm{cm}^3/\mathrm{s}$, which is comparable to the bosons) and temperature-dependent. The rate coefficient is only slightly larger for a sample prepared in an equal mixture of two different $^3P_0$ spin states. The rate coefficient for collisions between $^1S_0 + {}^3P_0$ atoms was too small to be measured, which agrees again with the bosonic case.

The system envisioned for quantum simulation purposes would harbor atoms on very small lattice sites at extremely low temperatures, with all atoms occupying a well-defined band of the lattice. This scenario is qualitatively different from the one studied by the JILA group, and further investigation of this important subject is currently under way.

2.5 Other two-electron systems

Strontium is certainly not the only suitable element to pursue the ideas laid out in Chpt. 1. Although we have placed our bets on Sr already years ago, we should spend some time to compare Sr to other two-electron systems. We will not consider the best-known two-electron system, helium, as its transitions from the singlet ground state into the excited states are in the XUV range, which is not accessible with current laser technology.

Ytterbium

Ytterbium, a lanthanide element with two valence electrons, turns out to be quite similar to strontium. Ytterbium has five bosonic and two fermionic isotopes, all of which (except for the ^{172}Yb isotope, which has a large and negative scattering length) have been brought to degeneracy by the Tokyo group. The first one was ^{174}Yb already in 2003 [Tak03], the last one was ^{168}Yb in 2011 [Sug11]. Work on fermionic Yb is also performed by the Seattle group [Han11]. In the summer of 2012, BEC in Yb was achieved in the Florence, Hamburg, and Munich groups.

The scattering lengths of the isotopes cover the complete range from positive to vanishing and negative values; see Tab. 2.5. Two-photon PA spectra have been taken for a number of isotope combinations, and all homo- and heteronuclear scattering lengths have been determined and compared to theory [Kit08]. This *mass tuning* is shown in Fig. 2.5. There are two bosonic and two fermionic isotopes with positive homonuclear scattering length and reasonable natural abundance, which are well-suited for quantum gas experiments. It is a lucky coincidence that the most abundant isotope, ^{174}Yb, has a scattering length very well suited for evaporative cooling, and BECs of 150 000 atoms have been achieved[12]. The largest atom numbers of the other isotopes are around 10 000, but these numbers do not seem to be fundamental limits. The selection of isotopes allows for the generation of Bose-Bose [Sug11], Bose-Fermi [Fuk09b], and Fermi-Fermi [Tai10] mixtures. A comparison to Sr-Sr mixtures

[12]Note that this number is still a factor of almost 100 smaller than the largest Sr BEC atom number.

isotope	abundance	statistics	I	scatt. length	BEC/DFG	atom number
^{168}Yb	0.12%	boson	0	$251\,a_0$	[Sug11]	10 000
^{170}Yb	2.98%	boson	0	$64\,a_0$	[Fuk07a]	7 000
^{171}Yb	14.08%	fermion	1/2	$-3\,a_0$	[Tai10]	8 000
^{172}Yb	21.69%	boson	0	$-598\,a_0$		
^{173}Yb	16.10%	fermion	5/2	$199\,a_0$	[Fuk07b]	10 000
^{174}Yb	32.02%	boson	0	$105\,a_0$	[Tak03] ([Yam10])	150 000
^{176}Yb	13.00%	boson	0	$-24\,a_0$	[Fuk09b]	< 250

Table 2.5: All stable isotopes of Yb with their respective natural abundance [Lae06], spin statistic nature, nuclear spin, homonuclear scattering length [Kit08], reference to the first (largest) reported BEC or degenerate Fermi gas, and the largest atom number reported so far.

will be given in Chpt. 8. The ^{172}Yb isotope with its large and negative scattering length is a very unique candidate to study OFRs: due to the small energy difference between the free-atom threshold and the nearest bound state, the resonance strength is expected to be a factor of 10^5 stronger than of ^{88}Sr [Jul].

The availability of two different fermionic isotopes might be an advantage over Sr, but we are not aware of any experiments which would require different isotopes[13]. Much more important is the fact that ^{87}Sr offers ten nuclear states, compared to two and six for the ^{171}Yb and ^{173}Yb isotopes. This is fundamentally important for the study of SU(N) magnetism, where the ordering of spins is expected to depend on the number of spin states N.

The electronic structure of Yb is similar to Sr at first glance (Fig. 2.6), but there are some subtle differences. The blue $^1S_0 - {}^1P_1$ transition can be addressed by light from a diode laser, which is an advantage over strontium. The $^1D_2$ state, which happens to lie below the $^1P_1$ state in Sr and opens the celebrated decay path from the pre-cooling MOT into the metastable states, lies above the $^1P_1$ state in ytterbium. The only leak of atoms from the blue transition leads into the triplet $^3D_{1,2}$ states, and from here into the $^3P_{0,2}$ states. This branching ratio, however, is two orders of magnitude smaller than in Sr. In addition, the lifetime of the $^3P_2$ state in Yb is only 14 s, compared to 500 s in strontium. Almost all present experiments with Yb use the $^1S_0 - {}^1P_1$ transition only for Zeeman-slowing, but not for the MOT. We believe, however, that a "blue" MOT and subsequent storage of atoms in the metastable $^3P_2$ state could increase the atom number available for further cooling. As a first step in this direction, it was recently shown that the atom number of a MOT operated on the $^1S_0 - {}^1P_1$ transition can be increased by about 30% when continuously repumping the $^3P_{0,2}$ states [Par]. The filling of the reservoir could possibly be accelerated by actively pumping atoms from the $^1P_1$ into the $^3S_1$ state. The vapor pressure of Yb is significantly higher than that of Sr, which should allow for fast loading of the relatively short-lived reservoir.

The $^1S_0 - {}^3P_1$ transition at 556 nm has a linewidth of 182 kHz, roughly 25-times broader than in Sr and 500-times broader than in calcium. Consequently, the Doppler tempera-

[13]The Zeeman shift of the $^3P_1$ states is large enough to selectively address single spin states by optical means already at low magnetic fields.

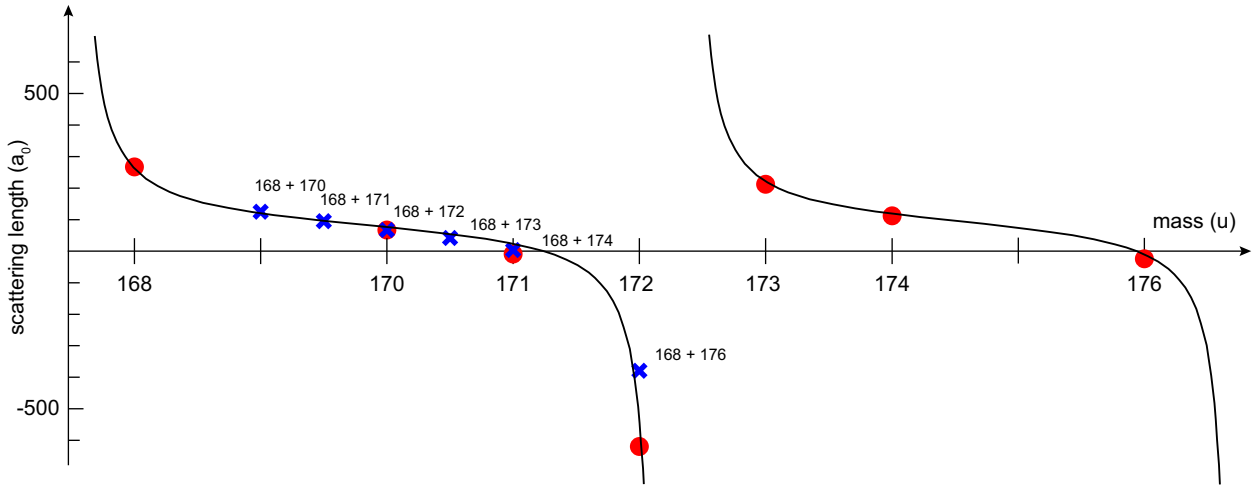

Figure 2.5: Mass tuning of the scattering length in Yb. The homonuclear scattering lengths of the seven stable isotopes (red dots) are fit by a tangent function. The heteronuclear scattering lengths of the ^{168}Yb isotope (blue crosses) are drawn as well. Values are taken from [Kit08].

ture of this MOT is 25-times higher than in Sr, which is a tremendous disadvantage for subsequent evaporative cooling and finally leads to comparatively low BEC atom numbers. From a technical point of view, the light at 556 nm is typically generated by a dye laser or a frequency-doubled diode laser, where in Sr a simple laser diode can be used. There are still some advantages of a broader intercombination line: The ratio of linewidth and hyperfine splitting of the $^3P_1$ states in the fermions is just right to perform optical Stern-Gerlach (OSG) separation with a single-frequency OSG beam. While the state-selective imaging of m_F states in the fermions requires larger magnetic fields than in Sr, the signal-to-noise should be much better, since the photon recoil limit is much smaller than the Doppler limit. Although absorption imaging on the 556 nm transition could be state-selective and would offer good spatial resolution, it has not been implemented in present experiments.

The large mass of Yb might be appealing, for example for the creation of molecules with a large mass imbalance, such as LiYb. It turns out, however, that the electric dipole moment of LiYb in the rovibronic ground state is extremely small, about 0.05 D.

Taking all these considerations into account, we believe that Sr is the better choice. Nonetheless, many new Yb machines are currently being constructed.

Calcium

The work on Ca has been similar to the one on strontium: ^{40}Ca was and still is used in optical lattice clocks (e.g. at NIST and PTB), and there have been early attempts to reach quantum degeneracy both in the ground and metastable states, most noticeably in the group of A. Hemmerich in Hamburg [Grü02, Han03]. BEC of ^{40}Ca in the ground state was hindered by the large scattering length of about $440\,a_0$ for a long time, and finally achieved by the PTB group [Kra09] a few months before BEC in Sr, and later in Hamburg [Hal12]. The

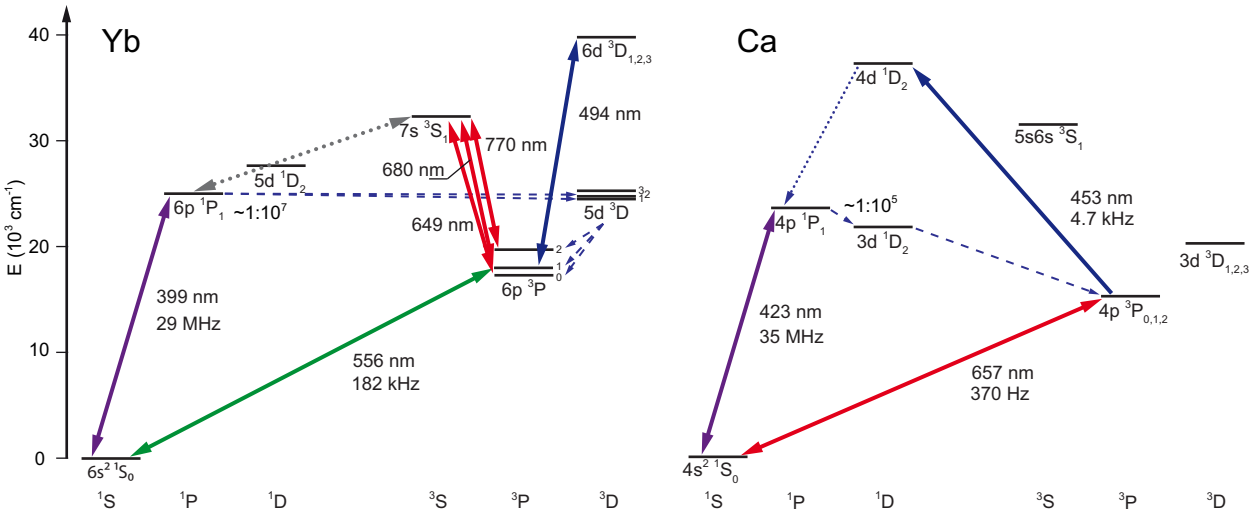

Figure 2.6: Left: Reduced level scheme of Yb with the decay paths from the $^1P_1$ state (dashed arrows), possible repump lines (red and blue arrows) and a proposed way to accelerate outcoupling of atoms from the blue MOT cycle (dotted arrow). Right: Corresponding level scheme of Ca with decay paths from the $^1P_1$ state (dashed arrows), the quench laser (blue) and decay from the $4d\,^1D_2$ state (dotted arrow).

pure BEC of the PTB experiment contained 10 000 atoms, and the route to BEC did not prove to be particularly robust; the Hamburg group reported a BEC of 3000 atoms. The scattering lengths of the other even isotopes of Ca have been calculated in Ref. [Dam11]. It was found that the periodicity of the position of the last bound state coincides exactly with two mass units of the reduced mass, meaning that all even isotopes of Ca have roughly the same large and positive homonuclear scattering length. In other words, the other isotopes will not be suited better for evaporative cooling. Evaporation of atoms in the metastable $^3P_2$ state towards condensation seems impossible due to large inelastic cross sections [Han06].

The second most abundant isotope, bosonic ^{44}Ca, has an abundance of 2.1% and has not been investigated in experiments so far. The only stable fermionic isotope ^{43}Ca comes at 0.14% abundance, it has nuclear spin $I = 7/2$ and a scattering length of about $65\,a_0$ [Dam11]. Enriched sources of Ca are available only in the carbonate form and would need to be reduced to the metal; see Appendix B for details.

The broad $^1S_0 - {}^1P_1$ transition is used for Zeeman-slowing and the first MOT stage. Just as in Sr, the $^1D_2$ level lies below the $^1P_1$ level and provides a leak for atoms from the MOT cycle with a branching ratio of 1 : 100 000 [Bev89][14]. After pre-cooling, atoms are transferred into a narrow-line MOT on the intercombination line. This transition has a width of only 370 Hz, which results in a scattering rate too small for stable operation of a MOT. The upper state is therefore quenched using the $^3P_1 - {}^1D_2$ transition at 453 nm, which has a linewidth of about 5 kHz and requires frequency-broadening of the laser. This way, the scattering rate can be increased by a factor of 15 [Bin01] and results in 10^8 atoms at $15\,\mu$K at the end

[14]Repumping of atoms from the metastable reservoir was not necessary for the PTB experiment [Kra09].

of the second MOT stage [Kra09]. This quenching method might also be applicable to Sr, here the relevant transition would be $^3P_1 - 5s6p\,^1P_1$. If not quenched, however, the 370 Hz intercombination line might be used as a powerful diagnosis tool for tomography of ultracold samples: The linewidth is smaller than typical light shifts induced by the dipole trap, mean field shifts, and interaction shifts on a lattice site.

Magnesium

Working with the lighter alkaline-earth elements becomes increasingly difficult as all transitions shift into the UV, and the linewidths of most relevant transitions become very narrow. Experimental work on magnesium is driven by the desire to build an optical clock on the ultranarrow $^1S_0 - {}^3P_2$ clock transition of 70 μHz. The small wavelength of all relevant transitions makes Mg optical clocks rather insensitive to blackbody radiation.

Laser cooling of ^{24}Mg was pioneered by the Hanover group, including the first MOT [Sen94] and quenching of the $^3P_1$ state for operation of the narrow-line MOT [Reh07]. An optical lattice clock is currently implemented by the Hanover group [Fri11]; further research is performed by the Copenhagen group [Jen11]. It is interesting to note that the $^{1,3}D$ states lie above the $^{1,3}P$ states in Mg. They shift downwards as the atomic number increases, falling between the ^1P and ^3P states in Ca and Sr and ultimately drop below both of these states in barium.

Apart from the bosonic ^{24}Mg isotope, there are the fermionic ^{25}Mg ($I = 5/2$) and the bosonic ^{26}Mg isotopes, each with natural abundances of about 10%. Little is known about the scattering properties of these species. One might conclude that Mg is very appealing for the optical clock community thanks to its very narrow transitions and the insensitivity to blackbody radiation, but possibly too involved for the quantum gas community.

Barium and radium

Laser cooling and trapping of the heavy alkaline-earth elements is motivated by the study of fundamental symmetries with well-controlled, cold and dense samples of Ra atoms. Radium is uniquely sensitive to fundamental symmetry violation, such as permanent electric dipole moments (EDMs). The observation of an EDM would be a sign of CPT violation, the current best atomic EDM measurements being performed with ^{199}Hg [Rom01]. Various calculations predict that the nuclear octupole deformation of Ra should allow for a sensitivity increase by two or three orders of magnitude. In addition, atomic parity-violation (APV) effects are enhanced by orders of magnitude due to the near-degeneracy of the parity-odd $7s7p\,^3P_1$ and parity-even $7s6d\,^3D_2$ levels; see [Gue07] and references therein. The absence of stable Ra isotopes has precluded such measurements so far. Barium, which has a similar level structure to Ra, can be used as a model system for laser cooling of these heavy elements.

Operation of a ^{138}Ba MOT was reported in 2009 [De09] and further described in Ref. [De08]. The strong $^1S_0 - {}^1P_1$ transition is used for the slowing and trapping. This transition is not closed, as $^1P_1$ atoms can decay into either the singlet $^1D_2$ state (lifetime 0.25 s) or into the triplet $^3D_{1,2}$ states (lifetimes on the order of minutes) with a combined branching ratio of 1 : 300. Repumping atoms from all of these three states back into the $^1P_1$ state allows for the operation of stable MOTs with 10^6 atoms and a lifetime of many seconds. Laser cooling

on the intercombination line is difficult due to a large branching ratio from the $^3P_1$ into lower-lying $6s5d\,^3D$ states.

The energy levels and transition linewidths shift further as we go to the next heavy element, radium. Just as in Ba, the strong $^1S_0 - {}^1P_1$ transition is not cycling anymore due to a 0.3% branching ratio from the $^1P_1$ into the $^1D_2$ state. Instead, the $^1S_0 - {}^3P_1$ transition with a linewidth of 380 kHz is used for the MOT. Also this transition is only quasi-cycling, as atoms in the $^3P_1$ state can decay into a $^3D_1$ state and further into the $^3P_0$ clock state. Repumping from this state is done passively through blackbody radiation at room temperature back into the $^3D_2$ state, from where repumping via the $^1P_1$ state returns atoms into the MOT cycle. Magneto-optical trapping of the fermionic ^{225}Ra ($I = 1/2$, $t_{1/2} = 14.9$ days) and the bosonic ^{226}Ra ($t_{1/2} = 1600$ years) has been reported [Gue07], with MOT atom numbers of 20 and 700, respectively.

Mercury

Mercury with its nuclear charge of $Z = 80$ is one of the heaviest elements with stable isotopes. Laser-cooling has been pioneered by the Tokyo group and is aimed at two different applications: The clock transition of Hg is deep in the UV at 265.5 nm and a factor of ten less sensitive to blackbody radiation than strontium. Second, the large nuclear charge is well-suited for the study of fundamental symmetries: the parity-violating amplitudes and atomic CP-violating permanent EDMs scale as Z^3, and CP-violating polarizabilities even scale as Z^5 [Hac08].

There are six Hg isotopes with natural abundances exceeding 6%, two fermionic ($I = 1/2$ and $I = 3/2$) and four bosonic ones. The $^1S_0 - {}^1P_1$ transition lies at 185 nm, and even the intercombination line at 254 nm requires frequency quadrupling of an IR diode laser. A MOT operated on this transition does not require repump lasers, and up to 10^6 atoms could be loaded into the MOT from a vapor cell and cooled to the Doppler temperature of 50 μK [Hac08]. The MOT was demonstrated for all six abundant isotopes $^{198-204}$Hg, making ^{204}Hg the heaviest laser-cooled stable atom so far. Related work is performed in Darmstadt [Vil11] and at SYRTE [Yi11].

Cadmium

The element Cd is somewhat similar to Hg and Yb, but substantially lighter. There did exist a MOT of Cd [Bri07], containing a few thousand atoms. In this experiment, the atoms were captured directly from the background vapor. The linewidth of the $^1S_0 - {}^3P_1$ transition (70 kHz) is likely to be too narrow for a first cooling stage, and the broad $^1S_0 - {}^1P_1$ transition at 229 nm was used in this experiment. A photon at this wavelength carries enough energy to ionize an atom in the $^1P_1$ state, leading to ionization loss and limiting the MOT atom number.

The strategy of Zeeman-slowing on the broad transition combined with trapping and cooling on the narrow transition has been very successful in Yb [Tak03] and Er [Fri12]. This strategy should also be applicable to Cd, yielding excellent starting conditions for evaporative cooling.

element	A	B/F	I	λ_S (nm)	Γ_S (MHz)	λ_T (nm)	Γ_T (kHz)	$\Delta^{^1P_1}_{^1D_2}$ (cm^{-1})
Be	9	0/1	3/2	235		455		−14 317
Mg	24	2/1	5/2	285	79	457	0.036	−11 352
Ca	40	1/0	-	423	35	658	0.37	1 803
Sr	88	3/1	9/2	461	32	689	7.6	1 549
Ba	138	3/2	3/2, 3/2	554	19	791	48	6 665
Ra	226	2/1	3/2	483	29	714	380	3 634
Cd	114	6/2	1/2, 1/2	229	91	325	70	−15 527
Hg	202	4/2	1/2, 3/2	185	30	254	1270	−17 226
Yb	174	4/2	1/2, 5/2	399	29	558	182	−2 609

Table 2.6: Comparison of all alkaline-earth elements and the elements Cd, Yb, and Hg, listing the mass number A of the most abundant or stable isotope, the number of bosonic (B) and fermionic (F) isotopes with natural abundances $> 0.5\%$ and lifetime > 2 weeks, the nuclear spin I of the fermionic isotope(s), the wavelengths λ and linewidths Γ of both the $^1S_0 - {}^1P_1$ transition (S) and the $^1S_0 - {}^3P_1$ intercombination line (T), and the energy difference Δ between the $^1P_1$ and nearest $^1D_2$ state. Data taken from [NIS].

2.6 Experiments with thermal gases of strontium

Many groups around the world perform experiments with thermal gases of strontium. Most noticeable, Sr is used in optical lattice clocks [Der11], originally proposed and first realized by the Tokyo group [Tak05]. Such clocks are currently operated at many laboratories, including JILA (Boulder, USA), SYRTE (Paris, France), LENS (Florence, Italy), PTB (Braunschweig, Germany), and various institutes in Tokyo (Japan). Further clocks are currently set up, e.g. at NPL (UK), at NIMC (China), and in Moscow (Russia). Strontium lattice clocks around the world achieve the best agreed-upon frequency [Bla08], making them a candidate for a possible re-definition of the SI second. Having lacked behind the best ion clocks in terms of stability in the past [Lud08b], Sr lattice clocks have very recently reached the same record 1×10^{-17} fractional stability as Al^+ ion clocks [Cho10, Nic12].

Some of the groups mentioned above are employing optical clocks as force sensors, for example to measure the gravitational field [Pol11]. Applications in geodesy would require portable clocks, which are currently being developed and could also provide a platform for satellite missions.

A very different type of precision measurement can be performed with Sr_2 ground-state molecules: The binding energies of the various vibrational states of the ground-state potential depend differently on the electron-to-proton mass ratio $\mu = m_e/m_p$. A repeated and sufficiently precise measurement of the binding energies of different states might reveal temporal drifts of μ and, with a lesser sensitivity, of the fine structure constant α; see Chpt. 11. This research is pursued at the University of Columbia (NYC, USA) [Rei12].

The two valence electrons provide an advantageous handle to Rydberg gases: while one electron is excited into the Rydberg state, the other one can be used for cooling, trapping, or imaging. This research line is followed by the Durham group [Mil10]. Closely related is

the study of ultracold plasmas, where one of the two valence electrons is completely ionized [Kil07b]; such studies are performed by the Rice group [Sim04, Kil07a].

2.7 Optical cooling procedure

We employ a sequence of three cooling stages to bring Sr atoms into the regime of degeneracy. The first stage is a MOT operated on a broad transition, ideally suited to capture atoms and cool them to mK temperatures. The second stage is a MOT operated on a narrow transition, capable of cooling the atoms to thousand-times lower temperatures at million-times higher densities. Such a sample is loaded into an optical dipole trap. The third stage, evaporative cooling, leads into quantum degeneracy. While the details of the last cooling stage depend on the respective isotope and the objective of the experiment, the first two cooling stages are rather similar for all experiments and will be described in this section.

2.7.1 The blue MOT

A stream of Sr atoms at $\sim 600\,^{\circ}\mathrm{C}$ is emitted from an oven (see Appendix C) and directed into the UHV chamber (see Chpt. 3.1). By design, the atomic beam has a divergence of order 10 mrad, which is consistent with observations. Over time, the divergence increased significantly due to redistribution of material in our oven.

This divergence is given by the geometry of the oven, and can be reduced by a 2D optical molasses, also known as *transverse cooling*. We use light blue-detuned by $\Gamma/2 \approx 15\,\mathrm{MHz}$ from the ${}^1S_0 - {}^1P_1$ transition at 461 nm. This light is split into two beams, propagating orthogonal to each other and to the atomic beam, intersecting with the atoms about 100 mm downstream from the oven. The interaction region is about 50 mm long. The beams are retro-reflected, and we tried different schemes of round and elliptical beams of different sizes, and multi-pass configurations. We ended up with simple retro-reflected elliptical beams with aspect ratio 1 : 5 (diameter about 30 mm in the longitudinal and 6 mm in the transverse direction) with close to 10 mW in each axis.

Transverse cooling increased the number of atoms in the ^{84}Sr MOT by about a factor of three for the early case of a well-collimated atomic beam, and by a much larger factor for the oven with increased divergence. Note that the transverse cooling beams can also be used to fine-tune the direction of the atomic beam towards the MOT region in an isotope-selective way[15].

The broad 30-MHz transition allows for fast Zeeman-slowing and offers a high capture velocity of the MOT. We use a spin-flip Zeeman-slower of 800 mm length. The Zeeman slower was originally designed for alkali atoms, and implemented into our machine with the long-term vision of a combined alkali/alkaline-earth experiment in mind. Typical Sr Zeeman slowers are much shorter and likely to perform better. The Zeeman-slower beam contains about 35 mW of power, it is slightly focussed onto the aperture of the oven and has a waist of about 8 mm at the position of the MOT.

[15] As an extreme case, the atomic beam leaving the oven would be directed away from the MOT region to minimize vacuum degradation, and only the selected isotope would be deflected into the MOT region.

Atoms in the MOT region are illuminated by three retro-reflected MOT beams, one vertical of about 4 mm waist and two horizontal of 5 mm waist. They have intensities of $I_{\mathrm{vert}} = 0.1\, I_{\mathrm{sat}}$ and $I_{\mathrm{hor}} = 0.25\, I_{\mathrm{sat}}$, corresponding to about 1 mW in the vertical and 4 mW in the horizontal beams. The detuning is $-1.0\,\Gamma \approx 32$ MHz, and the gradient of the quadrupole field is 55 G/cm in the vertical direction. The Doppler temperature of this "blue" MOT is $T_D = 720\,\mu$K, much higher than the recoil temperature $T_r = 690$ nK. Sub-Doppler cooling is hindered by the absence of a magnetic substructure ($I = 0$ for the bosonic isotopes), and repumping in the classic sense is not required due the lack of hyperfine structure ($J = 0$).

As we will see later, atoms from the upper MOT level can decay via the $^1D_2$ level into the metastable $^3P_2$ level, which possesses a magnetic moment, and atoms in weak-field-seeking m_F states of this level can be trapped in a magnetic field. We do not optimize the MOT for fluorescence or atom number, but for the loading rate of the *metastable reservoir*, which we define as the container formed by the magnetic trap for $^3P_2$ atoms. The loading rate depends on various experimental parameters, among them the temperature (i.e. the flux) of the oven, the amount of light available at 461 nm (i.e. the slowing and capture efficiency), the natural abundance of the respective isotope, and the temperature of the blue MOT. This last parameter is somewhat surprising, and we will explain it briefly.

Our glass cell has an inner height of 22 mm, such that atoms can take excursions of only 11 mm from the quadrupole center. With a vertical B-field gradient of 55 G/cm, the cut-off B-field is about $B_{\mathrm{max}} = 60$ G. A comparison of the Zeeman-energy $E = g_J m_J \mu_B B$ and the thermal energy $E = \frac{3}{2} k_B T$ gives a maximum temperature of 4.0 mK for $m_J = 1$, up to which atoms are trapped within the glass cell, higher energetic atoms will stick to the walls[16]. We indeed observe fluorescence within the entire volume of the glass cell when illuminating the $^3P_2$ atoms in the reservoir with light on the quasi-cycling $^3P_2 - {}^3D_3$ transition. Apart from this observation, we do not have a suitable imaging system to measure the temperature of the blue MOT.

The $^1P_1$ hyperfine structure of the fermionic isotope cannot be resolved on the blue transition, leading to undesired excitation of the $F' = 7/2$ and $F' = 9/2$ states. We do not have the means to measure the atom number of the blue MOT directly, but by comparison of the fluorescence of the ^{86}Sr and ^{87}Sr MOTs, we estimate that the fermionic MOT performs a factor of about two worse than its bosonic counterpart. Sub-Doppler cooling is possible due to the magnetic substructure and has indeed been observed by the JILA group [Xu03]. Given that the g_F factors of the fermionic $^3P_2$ states are substantially smaller than in the bosonic case, it is very fortunate that colder temperatures can be achieved.

We usually operate the blue MOT until a few 10^7 to 10^8 atoms are accumulated in the reservoir. This takes between 50 ms and 10 s, depending on the abundance of the isotope.

[16] Atoms in higher m_F states will of course also be trapped at higher energies. Note that the g_F factors for the hyperfine states for the fermionic isotope are different and substantially smaller than for the bosonic one.

2.7.2 Repumping

General considerations

The electronic structures of Ca, Sr, Ba, and Ra share a common feature: a $ns(n-1)d\,^1D_2$ state appears below the $nsnp\,^1P_1$ state. Here, n is the principal quantum number of the valence electrons, ranging from 4 to 7. The nonzero branching ratio between the $^1P_1$ and the $^1D_2$ states opens a decay channel from blue MOT cycle. This branching ratio is roughly $1:50\,000$ for Sr, similar for Ca and much larger for Ba and Ra: roughly $1:300$ [17]. The atoms decay further into the $^3P_{1,2}$ metastable triplet states with a branching ratio of $2:1$. Atoms in the $^3P_1$ state have a lifetime of only $21\,\mu$s before they decay back into the $^1S_0$ state. On the other hand, the $^3P_2$ state has a lifetime of 500 s [Yas04]. Atoms in this state have a magnetic moment, and, provided they are in a low-field seeking m_F state, can be trapped in the quadrupole field of the MOT. These atoms can be returned to the ground state either during or after [Kat01] the blue MOT through optical pumping into short-lived metastable states. The decay mechanism from the MOT can be both a blessing or a curse. For the work presented in this thesis, it turned out to be a very fortunate blessing, and we will describe the necessary repumping in all detail.

The decay from the upper state reduces the lifetime of the Sr blue MOT to a few 10 ms. In order to increase both lifetime and atom number, early experiments as well as present clock experiments aim to continuously pump atoms from the $^3P_2$ into the $^3P_1$ state, from where they decay quickly into the ground state[18]. A large number of repumping trajectories can be used; see Fig. 2.2:

- $5s6s\,^3S_1$ — Use of this state actually requires two repump lasers for optimum performance: Atoms from the $^3S_1$ state can also decay into the $^3P_0$ clock state, which has a long limetime and needs to be repumped as well. The two transitions are at convenient diode laser wavelengths of 707 and 679 nm. They are employed by the Tokyo, JILA, Rice, and SYRTE groups.

- $5s4d\,^3D_2$ — There is an infinite ladder of $^3D_2$ states which can be used for repumping[19]. Atoms can decay back down into the $^3P_2$ state to be repumped again, or eventually decay into the desired $^3P_1$ state. The lowest $^3D_2$ state is addressed by a laser at $3.0\,\mu$m. Such lasers are typically optical parametric oscillators (OPOs), which are more involved than diode lasers. This state is used by the Rice group.

- $5s5d\,^3D_2$ — The next $^3D_2$ state is reached by a laser at 497 nm. Such a frequency-doubled diode laser is used in Florence, Tokyo, and in our group. The branching ratio from the $^3D_2$ into the $^3P_{1,2}$ states is $2:1$, such that three photons need to be

[17] As in Yb, there is an additional decay channel into the $ns(n-1)d\,^3D_{1,2}$ states, which is orders of magnitude smaller and will be neglected here.

[18] One might also try to repump atoms already from the $^1D_2$ into the upper $5s6p\,^1P_1$ state. This transition at 717 nm is inconvenient for current diode laser technology, and the branching ratio from the $5s6p\,^1P_1$ state into the desired $5s6d\,^1S_0$ state is unfavorable. In addition, the absorption of two repump photons would ionize the atom.

[19] It is worth mentioning that the $^3D_1$ states could be used as well, however at reduced repump efficiency as a substantial fraction decays into the dark, long-lived, and untrapped $^3P_0$ state.

absorbed on average to return an atom to the ground state. There is a small leak from the $5s5d\,^3D_2$ into the $5s6p\,^3P_{1,2}$ states, which can guide atoms into the dark $5s5p\,^3P_0$ state. This loss, however, is small and reduces the repump efficiency by at most a few percent.

- $5s6d\,^3D_2$ — The next $^3D_2$ state comes at 403.5 nm, which is a very convenient as powerful and inexpensive laser diodes developed for the Blu-ray technology exist in this range. This transition has not been used so far. More and more additional decay channels open up as one advances towards higher $^3D_2$ states. While the branching ratios have not been investigated, we estimate the reduction in repump efficiency to be small.

Fermions

Repumping of the bosonic isotopes is straightforward even in isotopic mixtures, since the isotope shifts are at most 100 MHz. In the case of ^{87}Sr, efficient repumping is complicated by the hyperfine structure of the involved states. We find that all five hyperfine states $F = 5/2$ through $F = 13/2$ of the $^3P_2$ level are populated during the blue MOT, however at different relative amounts. Three different parameters determine the distribution of atoms in the five hyperfine states. At first, the blue MOT operates on the $F = 9/2 \rightarrow F' = 11/2$ transition. The hyperfine splittings of the $^1P_1$ state are only on the order of the transition linewidth, such that also the $F' = 7/2$ and $F' = 9/2$ states become populated and contribute to the decay. The second and most important class of parameters are the branching ratios of all three $^1P_1$ states into the five $^1D_2$ and further into the five $^3P_2$ states. And third, not all $^3P_2$ hyperfine states are trapped equally well in the quadrupole field. The fraction of the velocity distribution of atoms leaving the blue MOT that can be trapped depends not only on the temperature of the atoms and the strength of the magnetic field, but also on the g_F factor of each state and the m_F state of the individual atoms. The g_F factors differ by up to a factor of six (see Ref. [Boy07a]) and are particularly small for the $F = 7/2$ and $F = 9/2$ states. The maximum $|m_F|$ increases with F, such that we expect atoms in the $F = 13/2$ state to have the highest probability to remain trapped.

This is what we find in the experiment qualitatively: The majority of atoms populate the $F = 13/2$ and $F = 11/2$ states, with some additional atoms in the $F = 5/2$ state. We find that additional repumping of the $F = 7/2$ and $F = 9/2$ states does not increase the total number of repumped atoms by more than a few percent. The exact population of each state is not straightforward to determine, since atoms cycle a few times on the $^3P_2 - {}^3D_2$ transition before eventually decaying into the $^3P_1$ state, and they might not fall into their initial hyperfine state. Spectroscopic data on this repumping transition can be found in Chpt. 9. In the typical experimental cycle, we perform repumping only on the $F = 11/2 \rightarrow F' = 13/2$ and $F = 13/2 \rightarrow F' = 13/2$ transitions.

Further investigation

We would like to estimate the fidelity of our repumping scheme, but we have no direct means of quantification. Instead, we investigate the lifetime of the blue MOT with and

without continuous repumping. The MOT lifetime is strongly density-dependent, therefore measurements are taken at low atom number. Measurements are taken with both the ^{86}Sr and ^{87}Sr isotopes[20]. Without repumping, the MOT lifetime is 30(5) ms for both isotopes, which is consistent with a $^1P_1$ lifetime of 5 ns, a decay probability of 1 : 150 000 into the $^3P_2$ level, and an effective MOT light intensity of $0.1\,I_{\mathrm{sat}}$. In presence of the repumping light, the lifetime increases to 950(50) ms for the bosonic and 120(10) ms for the fermionic isotope, where we repump only the $F = 11/2$ and $F = 13/2$ states.

The increase by a factor of 30 in the bosonic case shows that the fidelity of repumping is very high: Atoms are repumped from the $^3P_2$ state at least 30 times on average before they are ultimately lost. This factor of 30 will be recovered in a different measurement; see Chpt. 9. Besides standard loss mechanisms of a MOT, we suggest decay into the dark $^3P_0$ as the dominant loss channel[21].

In the case of the fermions, the lifetime is increased by only a factor of four. In a crude simplification, we deduce that only 80% of the atoms that have leaked out of the MOT cycle go into the $^3P_2$ $F = 11/2$ and $F = 13/2$ states, the other 20% are distributed over the other states. In addition, we know that the fermionic MOT performs worse than the bosonic MOT: If, despite the fact that the measured bare MOT lifetimes are the same within the errorbars, standard loss from the MOT is higher in the fermionic case, then the branching ratio into the non-repumped hyperfine states would be even smaller. Repumping also the $F = 5/2$ state would require two additional frequencies about 3 GHz away from the present ones. We believe that this effort would not be worth the gain.

In a next step, we will discuss a way to accelerate the loading of the metastable reservoir, particularly for the fermions. On timescales on the order of the MOT lifetime, the loading rate could be increased by a factor of about 3 if atoms that have decayed into the $^3P_1$ state were added to the $^3P_2$ state. This would also be helpful if the size of the MOT is already saturated (as possible in the case of a large ^{88}Sr MOT) or if loss mechanisms other than the decay into metastable states play a role (as possibly in the ^{87}Sr MOT). Experiments striving for fast cycle times (such as optical clocks) or suffering from poor vacuum could also benefit from fast reservoir loading. Optical pumping from the $^3P_1$ into the $^3P_2$ state while avoiding the $^3P_0$ state can be performed with a combination of the $^3P_1 - {}^3S_1$ and $^3P_0 - {}^3S_1$ transitions at 688 and 679 nm, or with a single laser addressing a $^3D_2$ state at either 2692, 487.4, or 397.0 nm.

At the time of writing this thesis, we have only the laser at 688 nm operational to perform a preliminary measurement on depopulation of the $^3P_1$ state, very similar to work done at SYRTE [Cou05, QV05]. We illuminate the blue MOT with light resonant on the $^3P_1 - {}^3S_1$ transition to pump atoms into the $^3P_{0,2}$ states. For all bosonic isotopes, the blue MOT atom number is drastically reduced by 78(5)%. In the case of the fermionic isotope, we expect a drop in atom number at seven frequencies, corresponding to the hyperfine transitions allowed by selection rules. We confirm the resonance positions found by the SYRTE group and measure the reduction of the MOT atom number on each resonance. Considering only

[20] The ^{84}Sr and ^{88}Sr isotopes show results very similar to ^{86}Sr. The ^{84}Sr MOT delivers poor signal-to-noise due to is small size, whereas the ^{88}Sr MOT shows signs of saturation.

[21] We learned from the JILA group that using the $^3S_1$ state for repumping both the $^3P_0$ and $^3P_2$ states increases the lifetime of the MOT to about 8 s, which is the same value as their vacuum lifetime [Mar].

$\Delta F = \pm 1$ transitions, which tend to be stronger than $\Delta F = 0$ transitions, we find a reduction of 35(5)% upon depletion of the $F = 7/2$ state, and correspondingly 50(5)% for the $F = 9/2$ and 60(5)% for the $F = 11/2$ state. We conclude that the decay into the three $^3P_1$ hyperfine states is rather uniform, and that optimized pumping into the $^3P_2$ reservoir state would involve all of these states.

Experimental parameters

The lifetime of metastable atoms in the reservoir in our experiment is about 30 s. This value is largely independent on the number of atoms in the reservoir (i.e. the density)[22]. The lifetime is somewhat shorter than that of ground-state atoms in the dipole trap. One might speculate that the black-body radiation of the oven shortens the lifetime of the $^3P_2$ state considerably, an observation made already in measurements with vapor cells [Xu03]. The lifetime is certainly long enough to allow for sequential loading of different isotopes when working with mixtures.

The repumping flash lasts typically 50 ms and contains roughly 100 μW of light in a beam collimated to a diameter of 10 mm, corresponding to roughly 0.05 I_{sat}. The light contains the correct frequency for each isotope involved, but repumps only the $F = 11/2$ and $F = 13/2$ states in ^{87}Sr [23]. The repumping conditions are very relaxed, as only very few photons need to be scattered. We did not measure the repump efficiency in dependence on the parameters involved, but we can state that a reduction of the repump duration to 5 ms, an intensity decrease by one order of magnitude, or a frequency detuning of 50 MHz (20 linewidths) do not reduce the performance significantly.

2.7.3 The red MOT

The presence of narrow intercombination lines in Sr offer the intriguing opportunity to add a second cooling stage after the blue MOT in order to reduce the temperature and increase the (phase space) density of the ensemble further. The second cooling stage is often referred to as *narrow-line MOT* and frequently named "red" MOT, owing to the color of the transition wavelength at 689 nm.

In general, a first limit of the attainable temperature in a MOT is set by the Doppler limit of $T_D = \hbar\Gamma/(2k_B)$, where in this case the linewidth is $\Gamma = 2\pi \times 7.4$ kHz. The Doppler temperature is $T_D = 179$ nK, a factor of 4300 smaller than for the blue transition. This impressive number demonstrates the power of narrow-line cooling. For linewidths on the order of kHz, the Doppler temperature becomes comparable to a second figure of merit of a MOT transition: the recoil temperature $T_r = \hbar^2 k^2/(k_B m)$, where $k = 2\pi/\lambda$ is the wave vector of the light field and λ the wavelength. We find $T_r = 460$ nK on the narrow transition, and the minimal attainable temperature is $T_r/2$. Thus, Doppler and recoil limit almost coincide for the red transition in strontium.

[22] The cloud of atoms in the reservoir is very dilute: even at full loading, 10^8 atoms are dispersed over $\sim 35\,\mathrm{cm}^3$, equivalent to a partial pressure of 3×10^{-11} mbar. Two- and even more so three-body collisions should be rare.

[23] As a coincidence, the $F = 11/2 \rightarrow F' = 13/2$ and $F = 9/2 \rightarrow F' = 7/2$ transitions overlap, such that some atoms in the $F = 9/2$ state are repumped as well.

Narrow-line cooling of Sr has been established by the Tokyo group [Kat99] and later studied extensively by the JILA group [Lof04b, Lof04a]. We will limit ourselves to an intuitive description of the cooling process and report our experimental parameters, but refer to the literature for an in-depth investigation.

Bosons

The atoms are repumped from the reservoir at temperatures set by the Doppler temperature of the blue MOT, roughly 1 mK. A single frequency would not provide sufficient capture efficiency, and we frequency-broaden the MOT light to match the frequency spectrum to the velocity distribution of the atoms. We use an AOM to scan the frequency of the MOT light with a rate of about 20 kHz, thereby creating a comb of lines extending from roughly -200 kHz to -5 MHz detuning[24]. We have about 2.5 mW of laser power available on each MOT axis, collimated to a waist of about 3 mm. The saturation intensity $I_{\mathrm{sat}} = \pi hc/3\lambda\tau$ on this transition is $I_{\mathrm{sat}} = 3\,\mu\mathrm{W/cm}^2$, yielding a maximum intensity of $2000\,I_{\mathrm{sat}}$ for our experimental setup. Here, $\tau = 21\,\mu$s is the lifetime of the $^3P_1$ state. Considering a scan range of 5 MHz comprising 250 comb lines at a spacing of 20 kHz, the intensity per comb line is about $10\,I_{\mathrm{sat}}$. We apply this broad-band red MOT already during the repumping process. The quadrupole field gradient along the vertical direction is quickly ramped to $\partial B/\partial z = 1.15$ G/cm. This capture phase lasts 50 ms and is rather robust: the lifetime of this MOT exceeds 1 s.

It is helpful to visualize the geometric region in which atoms interact with the MOT light: in the case of narrow-line cooling, the detuning Δ is much larger than the natural linewidth, $\Delta \gg \Gamma$. The light is only resonant with the atomic transition in regions where the B-field induced Zeeman shift $\Delta\nu = m_J g_J \mu_B B$ balances the detuning. Here, $\mu_B = 1.4$ MHz/G is the Bohr magneton, and the Landé g-factor is $g_J = 1.5$ for the $^3S_1$ state. This region is the surface of an ellipsoid, where the vertical radius ζ of this ellipsoid is given by $\zeta = \Delta/(m_J g_J \mu_B\, \partial B/\partial z)$. Typical sizes are about 4 mm for a gradient of 1 G/cm and a detuning of 1 MHz, but only 100 μm for a detuning of $3\,\Gamma \approx 20$ kHz. The thickness of such a shell is on the order of 10 μm for a small saturation parameter $s = I/I_{\mathrm{sat}}$. As we apply a frequency comb that stretches from near-zero to -5 MHz, atoms can get into resonance with the light on 250 narrow, but overlapping shells, filling the entire volume of the ellipsoid[25]. For each shell, $\Delta \gg \Gamma_s \approx \Gamma$. The maximum acceleration due to photon scattering is $\Gamma \cdot \hbar k/2m$. For the case of Sr, this value is 16-times larger than gravity, thus gravity starts to play a role.

In a second phase, we narrow the scan range down to 2 MHz, where the comb line closest to resonance is 100 kHz red-detuned to the transition. During this phase of 200 ms, the total light intensity is reduced to about $100\,I_{\mathrm{sat}}$ (corresponding to about I_{sat} per comb line), and the magnetic field gradient remains unchanged. Afterwards, we jump to single-frequency operation with a detuning of -800 kHz. The parameters of this phase are rather insensitive,

[24] The scan rate can be varied between 5 and 35 kHz without a decease in capture efficiency. Similarly, the lower boundary of the scan range can be varied between -3 and -10 MHz, depending on the available laser power. The highest frequency comb line must not be blue-detuned to the atomic transition.

[25] The optimization of our MOT is likely to be influenced by the small height of our glass cell, which the atoms fill entirely. Experiments with large steel chambers might operate at slightly different parameters.

e.g. a reduction of the scan range to 4 MHz within 100 ms will produce a similar result. The variation of intensity and detuning, as well as the evolution of atom number and temperature, are depicted in Fig. 12.6.

In the third stage, which we call the single-frequency MOT, we shift the frequency very close to resonance while reducing the intensity dramatically to $0.5\,I_{\mathrm{sat}}$ [26]. This stage lasts 200 ms and is concluded by a 50 ms wait at the final parameters. It is important to understand that the MOT is driven through very different regimes during this ramp: We begin in the condition $|\Delta| \gg \Gamma_{\mathrm{sat}} \gg \Gamma$, where Γ is the natural and $\Gamma_{\mathrm{sat}} = \Gamma\sqrt{1+s}$ the intensity-broadened linewidth. Atoms are in resonance with the light on a single shell, whose thickness is enlarged by the factor $\sqrt{1+s}$ compared to the low-intensity case. The large intensity ensures that the scattering rate is high enough to keep the atoms in the MOT, and lifetimes are typically 400 ms. In this regime, the behavior of the atoms can be described semiclassically [Lof04b], and the expected temperature is $T = \hbar\Gamma_{\mathrm{sat}}/2k_B$ [27]. Note that this temperature is independent of the detuning, and set only by the light intensity. In a simplified picture, the decrease of the detuning provides compression, and the decease in intensity provides cooling.

At the end of this stage, the detuning becomes comparable to the linewidth, and s approaches unity: $|\Delta| \sim \Gamma_{\mathrm{sat}} \sim \Gamma$. The behavior of the atoms is determined by single photon recoils, and the system requires a full quantum treatment [Cas89]. The temperature limit approaches $T_r/2$. There is, however, a compromise between atom number and temperature. A temperature of $T_r/2$ is reached only for very low intensity, accompanied by a very low scattering rate[28]. Atoms live only on a very thin shell (the bottom of the ellipsoid) and interact predominantly with the upward propagating beam; see Fig. 2.7(a). At low intensity, an atom is at risk to fall through this shell without absorption of a photon, and be lost. This limits the lifetime at this stage to a few 10 ms.

In a final stage, the atoms are loaded into the dipole trap at 1064 nm. At this wavelength, AC Stark shifts reduce the energy of both the $^1S_0$ and $^3P_1$ states, but are stronger for the $^1S_0$ state (see [Kat99] and [Boy07a] for calculations), therefore atoms in the center of the trap see the MOT light further red-detuned. To cool atoms into and inside the dipole trap, we sweep the laser frequency about 40 kHz into the blue while reducing its intensity to zero over a ramp time of 50 ms. This stage is crucial for efficient loading of the dipole trap, and we are able to transfer 50% of the atoms from the single-frequency MOT into the dipole trap. The attainable temperature is limited by heating due to the re-absorption of photons, and we typically achieve temperatures around 800 nK with about 10^7 atoms for ^{84}Sr, corresponding to a phase-space density of about 0.1. The temperature in the dipole trap strongly depends on the density and the scattering behavior of the atoms, and can be as low as 400 nK for the non-interacting isotope ^{88}Sr or equivalently ^{84}Sr at very low densities. A full account of limitations to the maximally attainable phase-space density, including a discussion and references, is given in Chpt. 12.

Note that the light is still far detuned from the bare atomic transition, and that the atoms occupy the shell of an ellipsoid with a size of a few 100 μm, not its volume. The

[26] Unlike all other groups, we do not increase the magnetic field gradient here.

[27] This simplified equation lacks a numerical factor of about 2, see [Lud08a].

[28] In other species with an even smaller linewidth, such as Ca and Mg, this scattering rate needs to be increased by quenching of the $^3P_1$ state.

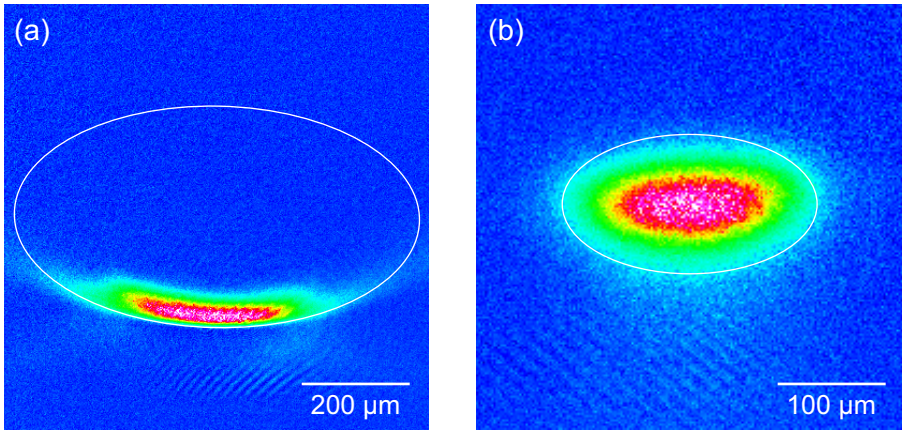

Figure 2.7: Narrow-line MOTs of (a) the bosonic ^{88}Sr and (b) the fermionic ^{87}Sr isotopes, shown by *in-situ* images in the horizontal direction. In case (a), we operate at $\Delta = -50\,\mathrm{kHz}$, $I = I_{\mathrm{sat}}$ and $\partial B/\partial z = 1.15\,\mathrm{G/cm}$. The atoms occupy the shell of an ellipsoid with vertical radius $\zeta = \Delta/(g_J \mu_B \partial B/\partial z)$, which is $210\,\mu\mathrm{m}$ in this case. The white ellipse is a guide to the eye. In the fermionic case (b), we operate at $\Delta_{\mathrm{trap}} \sim \Delta_{\mathrm{stir}} \sim \Gamma$ and $I_{\mathrm{trap}} \sim I_{\mathrm{stir}} \sim I_{\mathrm{sat}}$, and the atoms occupy the volume of an ellipsoid with only minuscule sagging. The aspect ratio of the white ellipse is identical to the value of the anisotropy $\frac{\partial B}{\partial z}/\frac{\partial B}{\partial r}$ of the quadrupole field given in Chpt. 3.2. The difference in shape is a direct consequence of the MOT dynamics; see the text for details. The atom number is $1.3(1) \times 10^6$ in both cases, and the temperature is about 700 nK. Note the different length scales.

vertical position of the horizontal dipole trap beam determines the spatial reference point, and an additional homogeneous offset B-field is used to shift the atoms into this position. The overlap of the dipole trap with the resonance position of the atoms is sensitive to about $100\,\mu\mathrm{m}$ in the horizontal plane[29] and, more importantly, $10\,\mu\mathrm{m}$ in the vertical direction, which requires a high stability of both the B-field (around $200\,\mu\mathrm{G}$ for our current setup) and the laser frequency (below 500 Hz). The curvature of the quadrupole field sets the density of the cloud, which is a rather sensitive parameter as well. Generally, the details of the shape and loading procedure of the dipole trap highly depend on the atomic scattering properties, which are different for all isotopes. Details are given in Chpts. 2.7.4 and 3.5.4.

Fermions

The bosonic isotopes, for which we have discussed the red MOT dynamics in the previous section, have nuclear spin $I = 0$ and therefore only one magnetic substate in the $^1S_0$ ground state. The fact that the magnetic moment $g_J \mu_B$ is zero due to the singlet configuration of

[29] The position of the MOT also depends on the light forces of the six MOT beams, where the vertically downward propagating one can safely be omitted. As a result of insufficient balancing of the retro-reflected MOT beams, the MOT position changes as the intensity is reduced. While doing so, the offset B-field needs to be constantly adapted in order to keep the MOT overlapped with the position of the dipole trap. We call this the high art of *magnetic tracking*.

the two valence electrons ($J = 0$) did not become apparent. This however changes as we consider the fermionic ^{87}Sr isotope with $I = 9/2$ and its ten magnetic states. The magnetic moment is now given by the nuclear moment, which is still orders of magnitude smaller than an electronic magnetic moment. To understand the implications of the unusual condition of $J = 0$ and $I \neq 0$ in the ground state, let us look at a conventional alkali MOT first. For simplicity, we will only consider the behavior along one dimension x.

An atom gets into resonance with the σ^+-polarized cooling light (and experiences a restoring force) at a position where the condition

$$h\Delta = ((m \pm 1)g_e - mg_g)\mu_B B(x) \tag{2.1}$$

is fulfilled. Here, m is the ground-state magnetic quantum number of the atom, and g_g and g_e are the Landé factors of the ground- and excited states. The $\pm$ sign denotes interaction with σ^+ and σ^+-polarized light from the two counterpropagating MOT beams; see Fig. 2.8(a). The B-field is usually proportional to the position along one axis, $B = \alpha x$, and Δ is the detuning from resonance, with $\Delta < 0$ for red detuning. As long as the right side of Eqn. 2.1 is positive for all m, there will be a restoring force for any spatial position. This leads to the conditions

$$\begin{aligned} \frac{F}{F+1} < \frac{g_e}{g_g} < \frac{F}{F-1} \qquad & \text{for } F \to F+1 \text{ transitions} \\ \frac{F-1}{F} < \frac{g_e}{g_g} < \frac{F}{F-1} \qquad & \text{for } F \to F \text{ transitions} \end{aligned} \tag{2.2}$$

for stable MOT operation, which are readily fulfilled for alkali MOTs[30]. This situation is depicted in Fig. 2.8(a): The Zeeman shifts of the ground and excited states are similar enough such that circularly polarized light is nearly resonant with all possible $m_F \to (m_F \pm 1)$ transitions, especially considering the large linewidth of a few MHz. The textbook MOT diagram in Fig. 2.8(b) with red detuning of a few linewidths reveals that the resonance condition for the different $m_F \to (m_F \pm 1)$ transitions is only slightly position-dependent and leads to a restoring force over the entire range.

This situation is very different for the alkaline-earth elements, where $g_e/g_g \gg 1$. The $^1S_0$ substates are almost degenerate, and a light field at a given magnetic field can be resonant, blue-detuned, or red-detuned depending on the lower m_F state; see Fig. 2.8(c). Considering the varying B-field of a MOT, the resonance position is different for all $m_F \to (m_F \pm 1)$ transitions; see Fig. 2.8(d). Even more importantly, some transitions expel the atom from the center of the trap. This is shown in the simplified diagram in Fig. 2.8(e). We consider a ground-state atom in the $m_F = 9/2$ state. The beam with σ^+-polarized light can drive a transition to the $m_{F'} = 11/2$ state, which would push the atom towards the trap center, while the σ^--polarized beam can drive a transition to the $m_{F'} = 7/2$ state, which would push the atom *away* from the center. The probability of these processes is given by the Clebsch-Gordan coefficients (Fig. 2.8(f)), which grow with $|m_F|$ for the $m_F \to (m_F \pm 1)$ transitions with $\sigma^\pm$-polarized light. In the most extreme case, which is the one shown in

[30]For the $F = 2 \to F' = 3$ MOT transition in Rb, $g_J(5^2S_{1/2}) \approx 2$ and $g_J(5^2P_{3/2}) \approx 4/3$, resulting in $2/3 < 2/3 < 2$ for the above condition.

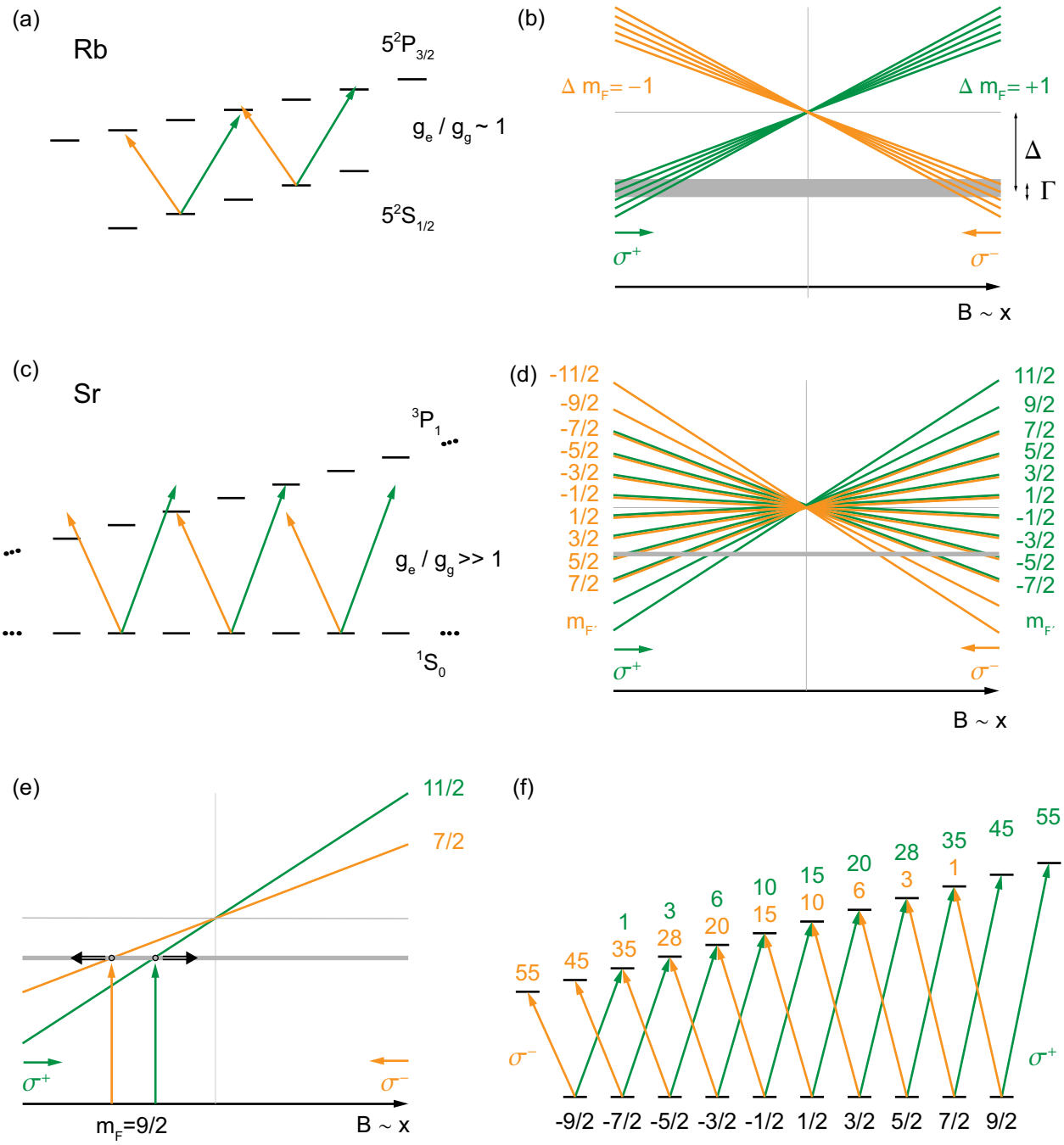

Figure 2.8: Principle of the fermionic red MOT. For the paradigmatic $F = 2 \rightarrow F' = 3$ Rb MOT (a and b), the spatial position of the resonance (grey bar) is almost independent of the specific m_F state. This is very different for ^{87}Sr (c and d), where a given frequency can be both blue- and red-detuned for different m_F transitions. Atoms in an unfortunate state can be pushed away from the trap center (e), and effective trapping is achieved by averaging over the polarization-dependent Clebsch-Gordan coefficients (f); see the text for details.

Fig. 2.8(e), the ratio of the restoring vs the expulsive force is 55 : 1. As with all MOTs, stable trapping is achieved by an averaged restoring force over many absorption processes. In this case, stable trapping is guaranteed by the favorable transition probability difference for $\sigma^{\pm}$-polarized light.

The restoring force is maximized for atoms in the $m_F = 9/2$ state on the left-hand side of the diagram. However, if this atom happens to be on the right-hand side of the diagram, i.e. at positive B-field, it cannot get into resonance with either of the two light fields anywhere in this hemisphere, and is lost from the trap[31]. A fast randomization of m_F states would be desirable to avoid the loss of such atoms from the trap. Narrow-line MOTs do not provide efficient randomization, as already a few photon recoils move the atom out of the resonance region set by the small linewidth. A second MOT beam driving the $F = 9/2 \rightarrow F' = 9/2$ transition is used to thoroughly *stir* the m_F states of the atoms. This "stirring" light is superimposed with the "trapping" light of the $F = 9/2 \rightarrow F' = 11/2$ transition and red-detuned such that the regions of resonance overlap. The Zeeman shift of the $F' = 9/2$ state is about five times smaller than that of $F' = 11/2$ state, thus broadening the resonance region by the same factor.

Note that the resonance position of each of the $m_F \rightarrow (m_F \pm 1)$ transitions is different, such that the two MOT beams are resonant with the m_F states on different shells. These shells merge for a small detuning Δ or a large saturation parameter s. The atoms occupy the *volume* of an ellipsoid, unlike in the bosonic case, where atoms are found only on the lower *surface* of the ellipsoid; see Fig. 2.7.

The first experimental realization of the fermionic red MOT of Sr has been achieved by the Tokyo group and beautifully described in [Muk03]. Following the MOT cooling, atoms have been loaded into a 1D lattice, optically pumped into one spin state, and further cooled close to the recoil limit, corresponding to $T/T_F = 2$. In the following, we will briefly describe our experimental parameters, which are slightly different to those of the Tokyo and JILA [Boy07a, Lud08a] experiments.

Just as in the bosonic case, we use the maximum available power on both the trapping and stirring beam to capture the atoms emerging from the metastable reservoir. Conditions for the broad MOT are identical to the bosonic case described above. As we move the single-frequency MOT towards resonance and reduce the intensity, we find that larger intensities are needed compared to the bosons. Final conditions of the red MOT are a gradient field of 1.15 G/cm, trapping and stirring beam intensity of a few I_{sat}, and detunings of a few linewidths. We add a short wait time of 50 ms to ensure equilibration and attain typical temperatures of 800 nK with 10^7 atoms.

Loading of both bosons and fermions into an optical dipole trap is slightly complicated by the fact that bosons and fermions do not reside in the same position: The shell of bosonic atoms is located up to 500 μm below the cloud of fermionic atoms. We first load the fermions into the dipole trap by ramping both trapping and stirring beams towards the blue, while reducing both of their intensities to 0.6 I_{sat} over 100 ms. During this entire time, the detuning

[31] Remember that the detuning is much larger than the linewidth. Note also that the situation described here is the same for $m_F = -9/2$-state atoms at negative B-fields and applies also to all other states on the "wrong" side.

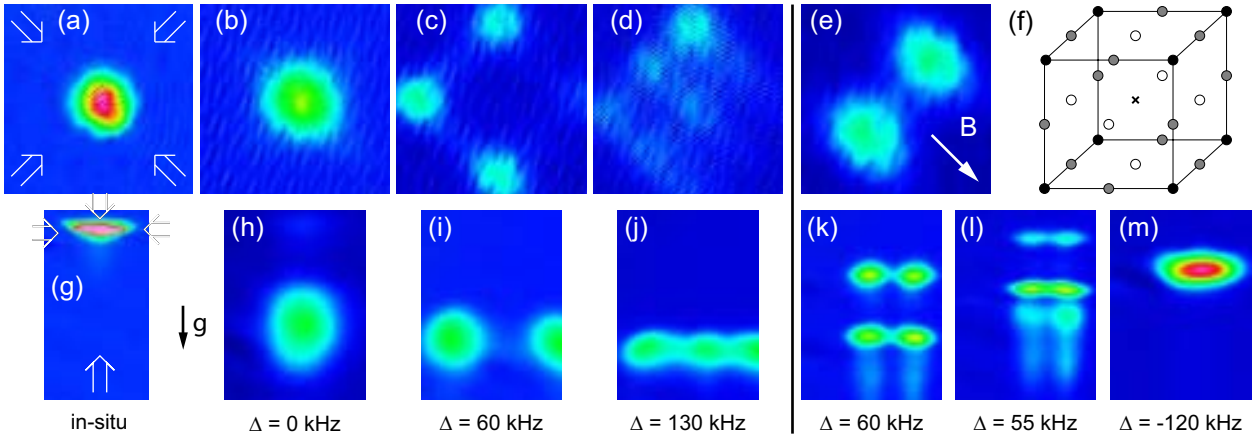

Figure 2.9: Formation of momentum state crystals at blue detunings. The top (bottom) row shows absorption images in the vertical (horizontal) direction. Images (a) and (g) show *in-situ* images of the atomic cloud, the white arrows indicate the direction of the molasses beams. Images (b) - (d) and (h) - (j) are taken with different detunings of the laser pulse. A B-field along one axis was applied in (e), and (k) and (l) show the appearance of two and three lattice points in the vertical direction. Panel (f) illustrates the geometry of a unit cell, and (m) shows the scenario of levitation at red detuning. Imaging is performed along the crystal axes, the height of each absorption image is 4 mm.

of the bosons is large, such that the two clouds do not overlap. The beams for the fermions are switched off, and the center of the quadrupole field is lifted upwards to superimpose the bosonic atoms with the dipole trap. We find that the loading efficiency of the two isotopes is reduced by around 10% compared to the individual case.

Momentum state crystals

While investigating the dynamics of the red MOT, we accidentally *re-discovered* the phenomenon of momentum state crystals at blue detuning. Later, we *discovered* the extensive work by the JILA group on this topic, and *recovered* their findings. While working with 25-times colder samples, we extend their description to the case of non-vanishing magnetic field and connect to the phenomenon of levitation for red detuning.

Let us start out with the experimental observation: We use a standard red MOT to prepare $> 10^7$ atoms of bosonic Sr at a temperature of 500 nK. The MOT light and the quadrupole field are switched off. A 4-ms wait time, in which the atoms drop due to gravity, ensures that the quadrupole field has decayed to less than 300 mG/cm, while the offset field is set to zero with an uncertainty of 10 mG. We then flash all three retro-reflected MOT beams (which form a molasses in this case) onto the atoms (pulse duration 12 ms, intensity $I = 5(1)I_{\mathrm{sat}}$) and take absorption images in the horizontal and vertical directions immediately after. Interesting density distributions occur in dependence of the detuning of the molasses beams. We will focus on the dynamics in the horizontal plane first, since the behavior in the vertical direction is perturbed by gravity, changing the atom's velocity.

While the cloud of atoms remains undisturbed by the molasses beams at near-zero detuning (see Fig. 2.9(b)), we observe the appearance of remarkably well-defined clouds of atoms in a symmetric pattern as we go to blue detunings of about 50 kHz; see Fig. 2.9(c). At first sight, this is very reminiscent of superradiance [Ino99, Koz99], especially since the atoms follow strictly the directions of the molasses beams[32]. However, as explained in [Lof04b] and [Lof04a] by a semiclassical model and numerical calculations, the separation into well-defined momentum states can be understood in terms of detuning-dependent absorption of photons, and does not involve coherent or collective behavior. We will give only a qualitative sketch here and refer to the literature for a quantitative description.

The atoms in the red MOT are already cooled to the Doppler limit and can hardly be decelerated further. However, they can certainly be *accelerated* by blue-detuned light. Subjected to the six molasses beams, the atoms will be preferentially accelerated, since this process provides positive feedback, whereas deceleration does not: Once an atom has been accelerated by a blue-detuned beam (which is initially about ten linewidths and about 20 recoil frequencies detuned from resonance), it comes closer to resonance with this beam, and is more likely to be accelerated further. For a sufficiently long pulse, the acceleration continues up to a final velocity $v_f = (\Delta + \Gamma\sqrt{1+s}/2)/k$, where $\Delta = \omega_L - \omega_A$ is the detuning, $\Gamma = 2\pi \times 7.4\,\mathrm{kHz}$ is the linewidth, $s = I/I_{\mathrm{sat}}$ denotes the saturation parameter, and k is the wave vector of the light field [Lof04a]. The atoms are not accelerated beyond v_f, as they fall out of resonance with the molasses beams at this velocity. The final velocity is independent of the initial velocity and position, atomic mass, offset B-field, and interaction between the atoms[33]. Indeed, it depends only on the detuning Δ and the additional term representing the intensity-broadened linewidth. Both terms are about equal in our case, while the latter term was dominating in the JILA experiments[34]. It is remarkable that the final velocity spread of each cloud can be smaller than the initial one. The separation of the clouds could be increased further by increasing Δ, s, the length of the pulse t, or the subsequent time-of-flight t_{TOF}. In our case, we are limited by the field of view of the imaging system.

We observe the appearance of four "momentum states" in the horizontal plane, corresponding to the directions of the four molasses beams. Each atom's selection of the final momentum state is of a stochastic nature in the early phase of the acceleration pulse: Whichever beam excites an atom first is likely to excite the atom another time and accelerate it into its direction. This probability of photon absorption along one axis certainly depends on the relative intensities of the two counterpropagating beams, especially for small s. The distribution of atoms into the two momentum states after acceleration is thus a very sensitive probe of the intensity imbalance of a pair of counterpropagating beams, as small differences are amplified. This is visible in our experimental data: In many images of Fig. 2.10, there is an imbalance of atom number along one of the two directions. One of our horizontal MOT

[32]Remember that superradiance does not require a degenerate sample. The coherence time needs to be larger than the superradiant decay time, which is the time between successive Rayleigh scattering events.

[33]We observed momentum state crystals with all bosonic isotopes, having near-zero, moderate, and large s-wave scattering lengths.

[34]In the case of small Δ and large s, one can think of the Δ providing the seed and the s ensuring the amplification.

axes is also used for imaging purposes and contains lenses and polarization optics. These attenuate the retro-reflected beam, leading to a reduced intensity of the reflected beam. This is not the case for the other horizontal MOT axis, proven by the roughly equal atom numbers along the corresponding direction.

As we increase the detuning further, it becomes more and more likely for atoms to *not* absorb a photon and therefore *not* undergo the positive feedback to end up in an excited momentum state. This is shown in Fig. 2.9(d). Atoms that have undergone acceleration into both horizontal axes are found at any of the four corners of the square. Atoms that have "locked" to only one of the beams are located on the sides of the square, while entirely untouched atoms occupy the center of the square. The population of the center increases as we increase the detuning, and finally converges into the unperturbed case of large detuning.

When generalized to three dimensions, the atoms are located at the corners of a simple cubic unit cell, hence the name "momentum state crystal". The dimensionality of the crystal can be reduced either by the omission of pairs of beams, or by the application of a strong enough B-field along one direction. The latter case is shown in Fig. 2.9(e).

Along the vertical direction, the situation becomes more complex due to the influence of gravity. Atoms falling downward with gravity naturally get into resonance with the downward propagating beam at some point. Thus, there is an underlying bias which will always favor the downward-propagating over the upward-propagating beam, making the momentum states pointing downwards more populated than the ones pointing upwards. This is seen in typical sideview images such as Figs. 2.9(h)-(j), in which only the lower momentum states are populated. It is, however, possible to find configurations in which two (Fig. 2.9(k)) or three (Fig. 2.9(l)) momentum states are occupied.

We will now make a connection to the case of large red detuning. In this case, the atoms are cold enough such that they never get into resonance with the laser beams, except for the one pointing upwards: The atoms fall downward with gravity until they come into resonance with that beam, which transfers upwards pointing momentum kicks to the atoms that cancel the force of gravity. The atoms are levitated in a very well-defined cloud without heating, see Fig. 2.9(m). One observes that the location of the atoms after a certain pulse length moves downward as one goes to larger detuning.

In summary, we have discovered a sequence of clearly distinguishable scenarios: going from blue to red detuning, we observe the formation of an immature crystal turning into a fully stretched crystal followed by the unperturbed case on resonance, the levitation at red detunings, and the unperturbed case for even larger red detuning.

Let us now consider the case of nonzero offset B-field. The $^3P_1$ state splits into three m_J magnetic sublevels with Zeeman shifts of $\Delta\nu = m_J g_J \mu_B B$, with $g_J = 1.5$ and $\mu_B = 1.4\,\mathrm{MHz/G}$. We apply a B-field in the vertical direction and set its strength such that the induced Zeeman splitting exceeds the typical range over which the formation of momentum state crystals and levitation are observed. The atoms can interact with the light fields in the vicinity of each of the three resonance positions. This can be seen in Fig. 2.10: Going from blue to red detuning, the sequence of scenarios described above repeats itself around each of the three m_J-state resonance positions. Note that perfect levitation occurs only

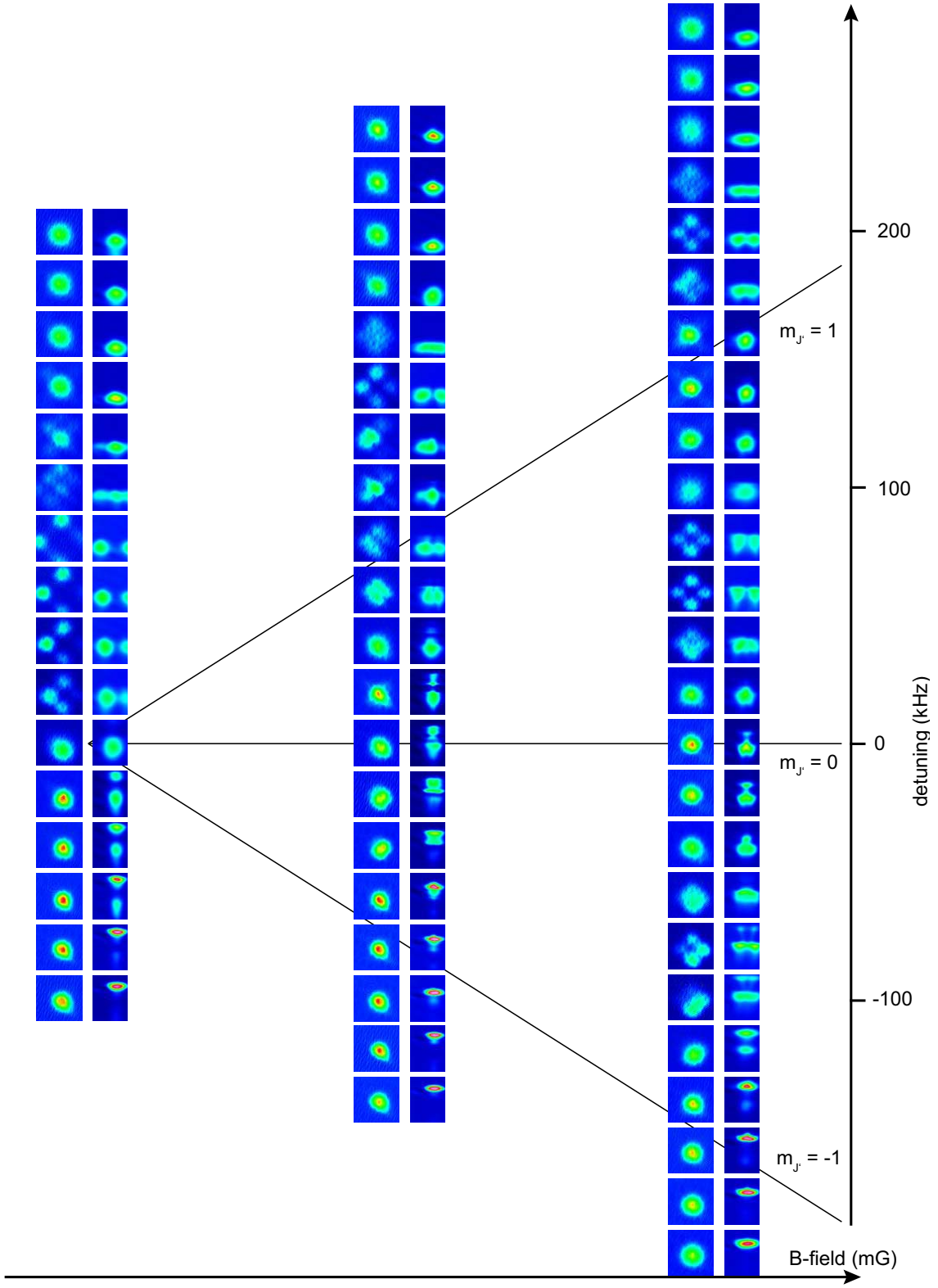

Figure 2.10: Three sequences of absorption images taken in the vertical (left columns) and horizontal (right columns) directions. The sequences are taken in presence of a vertical magnetic fields with a value of around 0, 40, and 80 mG. The detuning of the molasses beams changes by 20 kHz between consecutive image pairs.

for frequencies that are red detuned to all three transitions. Not surprisingly, the situation becomes very unclear when the Zeeman splitting is of the same value or smaller than the preferred detuning for crystal formation or levitation. In these cases, different processes compete and lead to a mixture of momentum states that lack the beauty of symmetry.

The momentum state crystals are not unique to bosons, but appear for fermions as well. This is remarkable, given the complexity of the red MOT. Both the trapping and stirring beams need to be employed, and given a suitable choice of parameters, the momentum distributions are exactly identical to the ones of the bosons presented in Figs. 2.9 and 2.10.

2.7.4 Loading of the dipole trap

We will now elaborate on the transfer of atoms into the optical dipole trap. Our knowledge about this delicate process evolved over time, and different trap shapes were used for the work presented in the following chapters. Here, we will present the most recent status, which was used for the measurements in Chpts. 8, 11, and 12. The details of the evaporation itself depend strongly on the isotope or isotopic mixture used and will not be presented here. The actual setup of the dipole trap is described in Chpt. 3.5.4.

The shapes of the bosonic and fermionic red MOTs are very different; see Fig. 2.7. In the bosonic case, the atoms occupy the surface of an ellipsoid, where the resonance condition $\Delta = \delta m_J g_J \mu_B B$ is fulfilled. The force of gravity is comparable to the restoring light force, and atoms accumulate on the lower part of the shell [Kat99, Lof04b]. The size of the shell, and thus the density of the cloud, is set by the detuning Δ and the B-field gradient, which is $\partial B/\partial z = 1.15\,\mathrm{G/cm}$ in our case. We typically operate at a detuning of $150\,\mathrm{kHz} \approx 20\,\Gamma$, such that the atoms are located about $600\,\mu$m below the quadrupole center, forming a disc of about $500\,\mu$m diameter.

The fermionic red MOT operates very differently due to the multitude of Zeeman states and the large difference between ground- and excited-state g_F factors. The atoms occupy the entire volume of an ellipsoid, where the circumference is again set by the detuning and B-field gradient. We operate the MOT very close to resonance to achieve densities similar to the bosonic case. The positions of the bosonic and fermionic red MOTs are thus very different, which has implications for dipole trap loading.

We will now describe the loading of atoms into a crossed dipole trap, consisting of a horizontal and a near-vertical beam. The main contribution to the trapping potential stems from the horizontal trapping beam. This beam supports the atoms against gravity, sets the trap depth, and thus determines the evaporation trajectory. It is derived from a multimode 5-W Yb-doped fiber laser operating at 1065 nm. The light intensity is set by means of an AOM but not actively stabilized. A polarization-maintaining single-mode optical fiber behind the AOM is used for mode-cleaning. The transfer of atoms from the red MOT into the dipole trap can be optimized by proper mode-matching. Since the red MOT is pancake-shaped, we send the horizontal dipole trap beam through a cylindrical telescope to make it elliptic in shape. The beam is then focused onto the position of the atoms. In its focus, it has a vertical waist of 17μm and a horizontal waist of $240\,\mu$m, thus an aspect ratio of about 14. With the typical power of 2.0 W used for loading of the dipole trap, this corresponds to trapping

frequencies of $\omega_{\mathrm{vert}} = 740\,\mathrm{Hz}$ in the vertical, $\omega_{\mathrm{trans}} = 50\,\mathrm{Hz}$ in the transverse (horizontal), and $\omega_{\mathrm{ax}} = 7\,\mathrm{Hz}$ in the axial (horizontal) directions and a trap depth of $k_B \times 13\,\mu\mathrm{K}$. These beam parameters are unchanged for all experiments presented in this work, and we will stay with this naming convention of trap frequencies even if further trapping beams are added. The elliptic horizontal beam provides sufficient confinement against gravity, but only little confinement in the horizontal plane, leading to a relatively low average trap frequency of $\overline{\omega} = 65\,\mathrm{Hz}$ at the beginning of evaporation.

During evaporation, atoms will leave the trap predominantly vertically downwards, aided by gravity. The evaporation efficiency benefits from a high vertical trap frequency: once a high-energy atom is produced in a collision, it can escape the trap before colliding with another atom. The vertical trap frequency should thus be large compared to the scattering rate: this requirement suggests a pancake-shaped trap. It is fortunate that both the loading of the dipole trap and the evaporation efficiency are optimized with the same trap shape.

The low average trap frequency $\overline{\omega}$ is very well suited for atoms with negative or large and positive scattering lengths or samples of high atom number, as we will see later. In some cases, however, an increase in confinement and density is desired. For this purpose, we add a vertically propagating beam to provide confinement in the horizontal plane, but not against gravity. This beam is derived from another 5-W laser source identical to the one used for the horizontal beam. To cover a broad range of beam sizes, we use two independent vertical beams, tilted to each other by less than 30 mrad, and overlapped on the position of the atoms. These beams are focused onto the atoms by a common spherical lens, but are collimated to different waists on this last lens, such that the waists of their foci are different, typically by a factor of five. These trapping beams are sent through optical fibers, and the choice of the outcoupler allows for a simple and reliable adjustment of the beam size in discrete steps. The size of each beam on the atoms can be set between $20\,\mu$m and about $300\,\mu$m, with typical waists of $55\,\mu$m. The focusing lens is mounted on a translation stage, and the vertical position of the focus can be adjusted with an uncertainty of about $100\,\mu$m. Moving this lens allows for fine-tuning of the beam size at the position of the atoms. Due to optical restrictions, the two beams are not exactly vertical but propagate at an angle of 22° with respect to gravity. The trap frequencies are measured by excitation and observation of sloshing modes along the three principal axes. The precision of these measurements is usually about 10^{-3}. The precision in the calculation of the dipole trap waists is restricted to a few percent by incomplete knowledge of the exact laser beam powers.

The dipole trap is turned on from the beginning of the red MOT, and atoms are continuously loaded into the dipole trap once spatial overlap is achieved and the temperature drops below the trap depth. We reach a transfer efficiency of about 50% while maintaining the temperature of the MOT. Once the atoms are loaded into the dipole trap, the MOT light is kept on for another 100 ms at an intensity of about $0.5\,I_{\mathrm{sat}}$. During this time, the atoms are pushed into the center of the dipole trap by the horizontal MOT beams, thereby increasing the density. For the bosonic case, the quadrupole center is placed about $600\,\mu$m above the horizontal dipole trap beam. The detuning of the cooling light from the Zeeman-shifted and light-shifted σ^+-resonance position is about $-3\,\Gamma$. In the fermionic case, the quadrupole center is overlapped with the dipole trap. Working with a mixture of bosonic and fermionic

isotopes requires a sequential loading scheme, in which we load the Fermions first and then shift the quadrupole center upwards to load the Bosons.

As for the red MOT, we find that the attainable temperature depends on the density and interaction between the atoms. In the following, we will address two important details: the light shifts induced by the dipole trap, and the stability of the experiment required for optimized transfer.

A systematic effect influencing in-trap cooling is the differential light shift between the two states involved, and a careful consideration is indispensable. During the cooling, atoms interact predominantly with the upward propagating, circularly polarized MOT beam. Different polarizabilities of the ground and excited state lead to a position-dependent detuning across the sample, which needs to be minimized for optimal performance. The so-called magic wavelength, at which the light shifts of the two states are equal, would be at 915 nm [Boy07a] for a dipole trap with π-polarization. At a wavelength of 1065 nm and for typical intensities used in our experiment, differential light shifts can reach 100 kHz. These shifts can be reduced, however, by choice of the correct polarization. The B-field at the position of the atoms is oriented vertically, and we set the linear polarization of the horizontal beam to be vertical as well. The vertical beams are set to the opposite circular polarization of the upward propagating MOT beam. Using narrow-line absorption imaging (see Chpt. 7), the shifted resonance position can be measured with an uncertainty of about 1 kHz. By optimizing the polarization of the dipole trap beams, the differential light shift of the trapping beam can be reduced to below 20 kHz for all settings used in our experiments. In a typical trap used for evaporative cooling, the atoms explore about one tenth of the trap depth. Using this value, we arrive at light shift of 2 kHz across the sample, which is comparable to the linewidth of our laser.

The transfer of atoms from the red MOT into the dipole trap requires a good spatial overlap in the vertical direction. Any displacement will reduce the fraction of transferred atoms and increase the temperature of the sample. The quadrupole field of the MOT amounts to 1.15 G/cm in the vertical direction, and a shift of 1 mG in the offset B-field displaces the atom cloud already by 9 μm. Similarly, a shift of the cooling laser frequency by 1 kHz displaces the cloud by 4 μm. Comparing these values to the vertical waist of the horizontal trapping beam (17 μm) gives an estimate on the required stability of the B-field and the absolute laser frequency.

In our experiment, we measure the dependence of the temperature of the sample in the dipole trap on the detuning of the cooling light to be 25 nK/kHz over a range of 20 kHz. Knowing this dependence, we can relate the shot-to-shot variation of the temperature to a variation of the detuning of the cooling light at the position of the atoms. We measure an rms noise in temperature of about 10 nK for a series of a few dozen experimental runs, which translates to a stability of the absolute laser frequency of better than 400 Hz over the course of about an hour. The same variation can be caused by a B-field fluctuation of 200 μG [35] or a rotation of the polarization of any dipole trap beam by a few degrees. Our shot-to-shot

[35] A similar value for the B-field stability will be derived from a different measurement in Chpt. 3.

reproducibility of the atom number is about 1%.

Another important parameter is the lifetime and heating rate of atoms confined in the dipole trap. We measure the lifetime of a dilute sample of atoms after evaporation in a slightly re-compressed trap to be 2 minutes, much longer than typical evaporation timescales. The heating rate is too small to be quantified and estimated to be below 1 nK/s.

We have shown that the use of one horizontal and one vertical beam gives independent control over the trap depth (horizontal beam) and the density of the sample (vertical beam). This is an ideal setting when working with different isotopes of Sr, which have very different scattering lengths; see Tab. 2.4. Tuning of the scattering behavior is hampered through the absence of magnetic Feshbach resonances, while optical Feshbach resonances were shown to be accompanied by strong losses [Bla11b]. This leaves the density as the only adjustable parameter to improve evaporation efficiency. The scattering rate scales as $\sim a^2 n$ with the density n and the scattering length a, and a too-low density does not provide fast enough evaporation to overcome heating and loss due to technical reasons. On the other hand, 3-body losses scale as $\sim a^4 n^2$, which sets an upper limit to the density. From these two relations, it becomes immediately clear that the optimum density for evaporation depends on the scattering behavior.

While we limit our discussions to cigar- and pancake-shaped dipole traps in this thesis, these are certainly not the only viable trapping geometry for the ^{84}Sr isotope. By increase of the horizontal confinement, one can match the horizontal and vertical trap frequencies, thus creating a nearly perfectly spherical trap: $\omega_{\mathrm{vert}} \approx \omega_{\mathrm{ax}} \approx \omega_{\mathrm{trans}}$. If we increase the horizontal confinement even further, such that the horizontal trap frequencies dominate, $\omega_{\mathrm{ax}}, \omega_{\mathrm{trans}} \gg \omega_{\mathrm{vert}}$, the BEC is cigar-shaped with the long axis aligned with gravity, and expands into a horizontal disc during time-of-flight. Using only the horizontal beam with the cylindrical telescope entirely removed, the trap can have an aspect ratio $\omega_{\mathrm{trans}}/\omega_{\mathrm{ax}}$ as high as 50 and contain a few 10^5 atoms.

Chapter 3

Experimental setup

The machine constructed within the framework of this thesis and described in this chapter has been designed for quantum gas experiments from the very beginning. This approach is in contrast to most other Sr machines around the world, which are aimed for the operation of optical clocks.

The machine has been designed along the following guidelines:

- The vacuum in the UHV chamber should allow for long lifetimes of the atomic ensembles, keeping the collision rate with background atoms well below $0.1\,\mathrm{s}^{-1}$.
- A multi-species oven should allow for the operation with samples of different isotopic composition or elements at temperatures of up to 800 °C.
- The machine, in particular the Zeeman-slower, should have the potential to operate for all alkali species and strontium.
- It should be possible to generate B-fields of a few 1000 G and gradient fields of a few 100 G/cm.
- Good optical access should allow for all necessary MOT and imaging beams, dipole traps, and lattices, while offering a resolution $< 2\,\mu$m in two orthogonal directions.

Great care was taken to construct the machine as stable as possible. Many sources of noise, heat, dust, or vibration, such as power supplies, certain lasers, water cooling, and air conditioning, have been moved to the basement floor below the lab. The temperature in the lab is stabilized to within 0.1 °C. The lab contains two large optical tables: One of them supports the vacuum chamber and a few laser systems, while most of the lasers are located on the second table.

A very similar machine, dedicated to the study of strongly interacting Fermi-Fermi mixtures, has been constructed in Innsbruck from 2005 on, and we could greatly benefit from the developments made for that machine [Wil09]. In the following, we will describe some of the systems in detail: the design of the vacuum vessel, the coils to generate magnetic fields, and the laser systems.

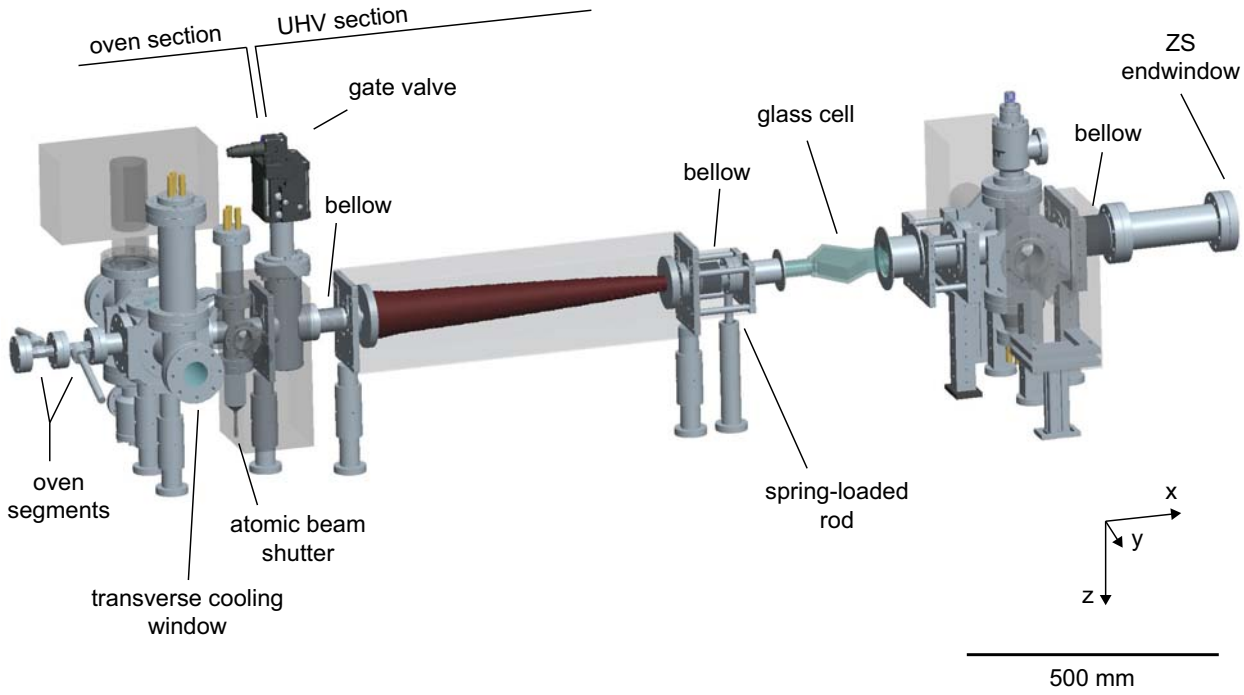

Figure 3.1: Assembly of the vacuum chamber. The entire vessel and part of the support structure are shown, while most of the magnetic coils and protective housings are removed. A gate valve separates the oven section from the UHV section to allow for a rapid exchange of the oven. The two segments of the oven used in this work are clearly visible.

3.1 Vacuum system

The layout of the vacuum system follows very closely that of the FeLiKx machine [Wil09]. An overview is given in Fig. 3.1. The vessel is divided into two sections, separated by a gate valve: The oven section contains the actual oven and differential pumping stages to provide a high pressure gradient, and the UHV chamber contains the glass cell, in which the experiments take place. This concept allows for a fast exchange of individual reservoirs or even the entire oven without breaking the precious vacuum of the UHV section.

Oven section — We use the multi-species oven developed for the FeLiKx machine. This oven is a linear stack of multiple ovens, and produces a collimated beam of atoms that travel down the main axis of the vacuum chamber, see [Wil09] and the Appendix C for details. It is attached to a CF 63 cube which contains windows for transversal cooling on the top and bottom, and branches to a T and a cross on either side. These contain windows for transversal cooling also in the horizontal axis, one 55 l/s ion pump, one Ti-sub pump, and a valve for initial pumping[1]. The Sr emanating from the oven and deposited on the walls of the

[1]We use CF 40 all-metal angle valve models 54032 and 57132 from VAT throughout, where the model 54032 is certainly sufficient. The gate valve is model 48132. Ion pumps are from Varian Inc. (now with Agilent), and Ti-sub pumps are from VG Scienta.

vacuum chamber acts as a supreme getter material and carries a large share in establishing a good vacuum already in the oven section. Counter-intuitively, the vacuum quality in the oven section improves when the oven is turned to higher temperatures.

The atomic beam passes through a first differential pumping stage of 108 mm length and 5 mm inner diameter and enters into the second chamber made by a six-way CF 40 cross with one 40 l/s ion pump and one Ti-sub pump. A valve allows for initial pumping, and a wobble stick is attached to a servo motor to make a motorized atomic beam shutter. A gate valve allows for a separation of the oven section from the UHV section, which is important for filling or exchanging of the oven. The gate valve is followed by a second differential pumping tube (137 mm length, 6 mm diameter), which helps to establish another factor of up to 100 in pressure difference. This entire oven section is mounted on a number of adjustable posts and connected to the UHV chamber by a bellow, and can thus be moved and rotated in all six degrees of freedom. In this way, the oven flux can be directed precisely into the MOT region.

UHV section — The UHV section begins with the Zeeman-slower, which is about 800 mm long with an inner diameter of 14 mm and acts as yet another differential pumping stage. A welded bellow connects to the glass cell, whose front end is placed on a spring-loaded rod to make it free of any mechanical stress. The back part is rigidly fixed to a six-way CF 63 cross. Details on the design of the glass cell can be found in Ref. [Wil09], the mounting procedure is described in Ref. [Flo]. Two 55 l/s ion pumps, one Ti-sub pump and one valve are attached to this cross in the transverse directions. The atomic beam impinges on a CF 63 sapphire window through which the ZS beam is sent into the chamber. Precaution has been taken to avoid deposition of a reflective layer of Sr on this window. First, sapphire is used instead of standard glass as its surface is less sensitive to etching of aggressive materials. Second, the window is placed inside a double-walled box and heated to 150 °C to increase the chances of atoms to detach from the surface again[2]. Third, the window is mounted on a CF 63 straight nipple, which is attached to the six-way cross by a bellow, allowing the window to be moved in case part of the window becomes coated. And fourth, the atomic beam shutter is opened only during the blue MOT phase, which reduces the accumulated flux substantially.

To assess the vacuum quality, we routinely measure the lifetime of atoms in the metastable $^3P_2$ state held in a magnetic trap. The lifetime is around 30 s, with variations below 20% over years. This lifetime dropped to 20 s approximately one year after initial bake-out, and flashing the Ti-sub pumps immediately re-established the 30-s lifetime. Note that this measurement procedure is suitable only for relatively short vacuum lifetimes, as the lifetime of the $^3P_2$ state itself is only about 30 s in our experimental environment, likely limited by black-body radiation. Once cold clouds in a dipole trap became available, we measured their lifetime, and found it to be about 2 minutes. This lifetime is also limited by off-resonant absorption of photons and possibly 3-body loss, such that the vacuum lifetime might be even longer.

[2] A failure of the heating went unnoticed for a few days or weeks, during which a reflective coating of about 1 inch diameter formed already. Such coatings cannot be removed at reasonable temperatures of up to around 250°C.

3.2 Magnetic field coils

Many quantum gas experiments require precise control of the magnetic field, often combined with the desire to reach comparably high fields or field gradients. Let us make a rough estimate on the target precision and magnitude of the field needed for the experiments laid out in Chpt. 1.

- **Precision** The magnetic substates of the $^3P_1$ state in the bosonic isotopes experience a Zeeman shift of $2.1\,\mathrm{MHz/G}\times m_F$. A field change of 2 mG shifts a $^1S_0 \rightarrow {}^3P_1$ transition with $\Delta m_J = \pm 1$ already by more than half a linewidth. We therefore need a precision and stability well below 1 mG at low fields.

- **Offset field** One might envision optical pumping and state-resolved imaging of ^{87}Sr isotope on the blue transition. Splitting adjacent m_F sublevels of the $^1P_1$ state by more than ten linewidths would require fields of a few kG, depending on the hyperfine state. Another appealing goal is the exploration of RbSr Feshbach resonances. Their positions have been calculated to appear rather evenly spread over fields of up to a few kG, and to grow in width when going to larger fields [Zuc10]. Such fields of a few kG are technically feasible.

- **Gradient fields** Performing magnetic Stern-Gerlach separation of fermions in the $^1S_0$ state requires very strong gradient fields, as the force acts only on the *nuclear* magnetic moment, which is about three orders of magnitude weaker than an electronic magnetic moment. Experiments with alkali atoms typically employ gradient fields of a few 10 G/cm, which would translate to insane gradients of a few T/cm required for strontium. Large gradient fields are also required for some quantum computation schemes, in which single-site addressing is achieved by splitting neighboring lattice sites by a few linewidths. A few 100 G/cm would be both sufficient [Dal08] and technically feasible.

In conclusion, we aim for a maximal magnitude of about 5000 G (such coils can also be used to create gradient fields of more than 1000 G/cm) and a precision of below 1 mG at low fields. The magnetic field strength in the center between two coils depends on the geometry of the coils as

$$B(z=0) = I\mu_B \frac{r^2}{(r^2+h^2)^{3/2}}, \tag{3.1}$$

where I is the current in the coils, r is the radius of the coils, and $2h$ is their distance. It becomes immediately clear that the size of and, more importantly, the distance between the coils should be as small as possible. The coil design should also be as compact as possible to not restrict optical access. We are very fortunate that such a coil system had already been developed for the FeLiKx experiment (see [Wil09] for detailed documentation) and proved to reach a stability of 2 mG at a field of a few 100 G, corresponding to roughly 10^{-5} fractional instability. Our coil system is an almost identical copy of that one, but presently operated with weaker power supplies and reduced pressure on the water cooling system.

coil	N	$I_{\max}^{\text{design}}$ [A]	$\frac{B}{I}$ $\left[\frac{\text{G}}{\text{A}}\right]$	$\frac{\partial B}{\partial zI}$, $\frac{\partial B}{\partial rI}$ $\left[\frac{\text{G}}{\text{cm A}}\right]$	$B_{\max}^{\circ}$ [G]	$(\frac{\partial B}{\partial z})_{\max}^{\circ}$ $\left[\frac{\text{G}}{\text{cm}}\right]$
Feshbach	30	1200	3.28	0.52 0.28	~ 600	~ 100
Curvature	10	600	1.51	0.64 0.35	~ 400	~ 200
Fast	6	200	1.06		~ 20	
Anti-Curvature	5	20	~ 0.8		~ 20	
Offset X	40	16	0.281		4.5	
Offset Y	40	16	3.17		50	
Earth Comp X	10	16	0.081		1.3	
Earth Comp Y	10	16	0.038		0.6	
Earth Comp Z	10	16	0.159		2.5	
FeLiKx Comp X	3	0.25	0.021		~ 0.005	
FeLiKx Comp Y	1	0.25	0.079		~ 0.02	
FeLiKx Comp Z	1	0.25	~ 0.2		~ 0.05	
3rd ZS	14	200	~ 0.03		~ 130	
ZS Comp	8	200	~ 0.1		~ 130	

Table 3.1: Magnetic field coils: the number of windings N per coil, design value of the maximum current $I_{\max}^{\text{design}}$, calculated or measured field per current $\frac{B}{I}$ in Helmholtz-configuration, field gradient per current in the vertical and horizontal directions $\frac{\partial B}{\partial zI}$ and $\frac{\partial B}{\partial rI}$ in anti-Helmholtz configuration, and the maximum field $B_{\max}^{\circ}$ and field gradient $(\frac{\partial B}{\partial z})_{\max}^{\circ}$ of the currently used configuration. Values are given for each pair of coils, except for the two ZS coils, which are not in Helmholtz-configuration and driven independently.

The heart of the coil system is composed of two pairs of coils in approximately Helmholtz-configuration[3]: The "Feshbach coils" and the "Curvature coils" are meant to generate large and homogeneous B-fields[4]. When used in anti-Helmholtz configuration, these two coils generate the quadrupole field of a MOT. A copper wire with a $4 \times 4\,\text{mm}^2$ square cross section and $2 \times 2\,\text{mm}^2$ square bore is used for these coils, and water-cooled from the inside with a pressure of 8 bar. These coils are placed into two glass-fiber reinforced PVC boxes and fastened with epoxy. These boxes also contain two smaller coils with a small number of windings to allow for fast switching: the "Fast coils", which are made of a $2 \times 2\,\text{mm}^2$ square copper wire with $1 \times 1\,\text{mm}^2$ square bore for water cooling, and the "Anti-Curvature coils", which are made of flat copper wires with $1 \times 5\,\text{mm}^2$ cross section. Sets of RF coils are glued onto the outside of the boxes, very close to the glass cell.

All coils mentioned so far lie in the horizontal xy-plane, generating fields in the vertical z-direction. To create offset fields in the horizontal directions, we wind coils onto rectangular frames around the glass cell. These are made of lacquered $1\,\text{mm}^2$ copper wire and receive

[3]A pair of circular coils with $2h = r$ generates a very homogeneous B-field at its symmetry point, where all spatial derivatives up to $\frac{\partial^4 B}{\partial z^4}$ vanish; such a design is called Helmholtz-configuration. Two coils with counterpropagating currents, placed at $2h = \sqrt{3}$, create a very uniform gradient field in the center, the second and third derivative being zero. This is called anti-Helmholtz configuration. In this thesis, we will use the terms "(anti-) Helmholtz configuration" for any coil geometry generating offset (quadrupole) fields.

[4]The Curvature coils are explicitly designed to create a field curvature $\partial B/\partial r = 0.2\,\text{G}/(\text{cm}^2\,\text{A})$ in Helmholtz configuration, which is important for the evaporation of certain species, such as lithium.

no cooling. Fields of more than 10 G can be achieved in any direction, which is helpful e.g. for the optical Stern-Gerlach (OSG) experiment. All of the coils mentioned so far are equipped with IGBTs (Feshbach and Curvature coils) or relays to disconnect them entirely from the power supplies. The direction of all fields can be changed with relays. In addition, the Feshbach and Curvature coils can to be toggled between Helmholtz and anti-Helmholtz configuration with sets of relays[5].

We have not yet considered external perturbations to the magnetic field. These come in two flavors: static and dynamic ones. Static fields stem from the (on small scales) homogeneous earth magnetic field and the inhomogeneous B-field created by our ion pumps, both of which are on the order of a few 100 mG and add up to a field of about 500 mG. They are canceled by large compensation coils made of 2.25 mm^2 lacquered wire, forming a cube of about 1 m^3 size surrounding the experimental chamber. We null only the B-field at the position of the atoms, not its gradient.

The time-varying B-fields are harder to control. The experimental cycle is synchronized to the 50 Hz line, which does not remove any line noise, but increases the reproducibility of the experiments. We identify two major sources of disturbance: The FeLiKx machine, which is located about 5 m away, and two elevators close to the laboratory, which are about 5 and 7 m away. Both create fluctuating fields of a few mG in the horizontal plane. These small field fluctuations are negligible during all but one stage in the experiment: the loading of the dipole trap from the red MOT. The MOT is operated at a field gradient of 0.6 G/cm in the horizontal direction. A field change of 3 mG in the horizontal direction displaces the red MOT by 50 μm, where the radius of the cloud is typically a few 100 μm. Any change in MOT position leads to a significantly reduced number of atoms loaded into the dipole trap due to a mismatch in position, nicely seen in Fig. 3.2.

There are a number of possible solutions: passive μ-metal shielding of the experimental chamber, measurement of the B-field at different locations and active feed-back onto the experiment, active feed-forward, and synchronization. We follow the feed-forward strategy.

A typical experimental cycle of the FeLiKx experiment involves MOT-loading with a quadrupole field and subsequent evaporation at a field of around 1000 G. These two settings generate very different stray fields in our lab. We use three analog outputs of the FeLiKx machine to drive coils around the Sr experiment, compensating these stray fields. The coils are added to the frames of the existing x and y offset coils. The conversion of currents sent through the coils at the FeLiKx machine and the adequate compensation at the Sr machine has to be determined for all relevant coils in all relevant configurations. In this way, we were able to reduce the influence of the FeLiKx machine to about the noise level induced by other sources.

[5]We use TDK Lambda power supplies models ZUP 6-132, GEN 6-200, and GEN 8-300 to generate currents in excess of 100 A. Simple power supplies from EA (models EA-PS 3016-20 B and 3016-10 B) have initially been used for smaller currents of up to 20 A, but proved to be too unstable. They have been replaced by TDK Lambda models ZUP 20-10 and ZUP 10-20. All power supplies are current-controlled via optocoupled analog inputs of the computer control system. All currents are monitored using LEM current transducers from Danfysik, models IT60-S, IT150-S, and IT400-S of the Ultrastab series. Small PCB models from LEM of the type HX xx-P/SP2 have proven to be insufficient even for small currents.

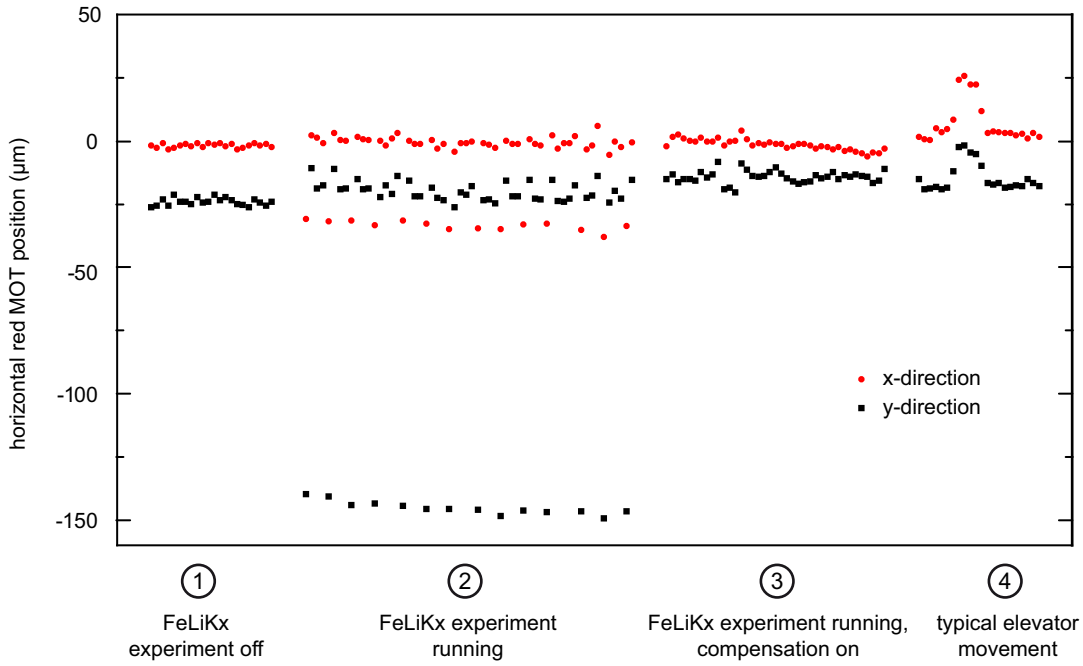

Figure 3.2: The position of the red MOT is a sensitive probe of the B-field and its stability. We record the MOT position in a series of experimental runs, under the influence of stray fields from the FeLiKx machine (data sets 2 and 3) and a near-by elevator (set 4). Periodic B-field changes of the FeLiKx machine and movements of the elevator are clearly visible. A position shift of 10 μm, which is about our residual noise (set 3), corresponds to a B-field variation of 600 μG. The noise can approach 100 μG on a quiet Sunday night (set 1). The cycle time of the experiment is about 15 s.

We measure the position of each elevator with commercial distance meters placed below the elevators. These devices generate an output voltage proportional to the distance, making the implementation of a feed-forward system straightforward. This approach is currently pursued.

Apart from these coils arranged around the glass cell, there are a total of four coils used for the Zeeman-slower (ZS). We employ a spin-flip slower originally designed for alkali atoms. The first section has a length of 600 mm and carries a total of 1300 windings made from $1 \times 5\,\mathrm{mm}^2$ copper wire. The vacuum tube is double-walled with cooling water flowing in the void, such that the ZS is water-cooled from the inside. The ZS is set into a sealed box and flushed with air for additional cooling. The second (increasing-field) section has a length of 45 mm and is made of the same $1 \times 5\,\mathrm{mm}^2$ copper wire. It is capped with a short yet strong coil of 12 windings of $4 \times 4\,\mathrm{mm}^2$ square water-cooled wire that provides the steep cut-off of the field: the 3$^{\mathrm{rd}}$ ZS coil. The field at the position of the MOT is compensated by the ZS Compensation coil, which is similar to the 3$^{\mathrm{rd}}$ ZS coil. Details of the design and related calculations can again be found in Ref. [Wil09].

3.3 Control system

The machine is steered by a control system developed by Florian Schreck, Todd Meyrath, and Gerhard Hendl. A C-based program equipped with a graphical user interface generates the experimental sequence, which is sent from the computer onto a bus system via a National Instruments NI6533 card. The communication is entirely digital; the clock cycle is 2 MHz, and each piece of data contains 16 bits. Each bus can address 256 devices, where we have currently three buses installed. Each bus connects to various devices, such as analog and digital outputs, analog inputs, and direct digital synthezisers (DDS) for the generation of RF signals to drive AOMs. The DDS are home-built based on the AD9852 chip by Analog Devices and generate any frequency between DC and 135 MHz with 12-bit dynamic range in amplitude. A complete documentation of this control system, which is successfully used in many labs around the world, can be found in Ref. [Con].

3.4 Optical access

The experiments take place in a sophisticated glass cell. The cell is made of Spectrosil® 2000, has a wall thickness of 5 mm, and is not coated[6]. The inner height is 22 mm, chosen to guarantee good imaging resolution while at the same time keeping the distance between the Helmholtz coils small. The design of the shape in the horizontal plane is guided by two demands: two orthogonal axes should cross the windows at or near right angles and intersect in the center, while two of the four windows should be oriented such as to allow for a beam to pass through them at Brewster's angle for operation of a high-power optical dipole trap. The resulting shape can be seen in Fig. 3.1 and is described in Ref. [Wil09].

The geometry of such a glass cell naturally suggests a system of three mutually orthogonal axes to be used for the MOT- and imaging beams. We use 1-inch optics, and the clear aperture of these beams is 22 mm. The MOT beams at 461 nm and 689 nm (as well as the future 780-nm beams for Rb) are overlapped with dichroic mirrors and sent through the same achromatic $\lambda/4$ waveplate[7], the MOT is retro-reflected. The MOT- and imaging beams are multiplexed using polarization optics. We use $f = 70$ mm Gradium® lenses and $f = 140$ mm standard achromats to image the atoms onto the CCD cameras[8].

It is convenient to introduce a coordinate system, which will also be used throughout this thesis. The positive x-axis coincides with the direction of the atoms travelling along the Zeeman-slower, and the positive z-axis is given by gravity. The y-axis therefore lies in the horizontal plane, coinciding with the horizontal dipole trap.

The axis originally planned for an optical resonator is now used for the horizontal dipole trap. The vertical dipole trap axis is inclined by roughly 20° to gravity and enters the

[6] Our glass cell is from Hellma Analytics (Müllheim, Germany).

[7] We use dichroic mirrors from Laser Optik Garbsen and achromatic waveplates from Thorlabs.

[8] We use two Andor Luca R EMCCD cameras, which are cost-effective and very compact in size. The Gradium® lenses are obtained from AMS Technologies, and the achromats are from CVI Melles Griot. Dichroic mirrors are used to combine blue and red imaging light. A motorized stage allows for the movement of the second vertical imaging lens to correct for chromatic aberrations between blue and red imaging. All beams are fiber-coupled, and it is crucial to position blue and red MOT beams independently.

chamber from below. The three lattice beams form an (almost) mutually orthogonal system. One beam is almost co-aligned with a horizontal MOT-beam and orthogonal to the horizontal imaging axis, the other two lattice beams enter the chamber from the top. The positions of all dipole trap and lattice beams on the atoms are imaged onto small TV cameras, and light is sent onto photodiodes for monitoring. In total, 24 different beams enter into the glass cell, nine of them are retro-reflected, and 15 of them are monitored on TV cameras.

3.5 Laser systems

3.5.1 The blue laser system

We use a frequency-doubled diode laser system to drive the ${}^1S_0 - {}^1P_1$ transition at 461 nm. The system was originally built by LEOS, but modified in many ways as it proved to be much too unstable. We use a Toptica DLpro master laser at 922 nm with a non-antireflection (AR) coated diode that emits 50 mW at a typical current of 130 mA. This light is used to seed a tapered amplifier (TA), which emits 1.1 W, measured behind the isolator. The IR light is sent through an lithium triborate (LBO) crystal for frequency doubling[9]. The doubling efficiency is greatly enhanced by a bow-tie cavity, which is locked in a Hänsch-Couillaud scheme. The doubling cavity is built of discrete elements and therefore mechanically unstable and unpleasant to align.

The LBO crystal suffers from a slow loss in doubling efficiency in regions of high light intensity. We never characterized this ageing process, but the $1/e$ decay is about one month. Moving the crystal by a few 10 μm restores the original doubling efficiency. The crystal is heated to 50 ° to avoid deposition of dust on its surfaces. Some information on the ageing of crystals can be found in Ref. [Bla11a].

When carefully optimized, the laser power of the blue light can be close to 500 mW. After degradation of the system, a half-day effort can usually yield a power of 420 mW, which is a typical good value for operation. The output power drops by about 20% per week due to the ageing of the crystal, making it necessary to move the crystal about every other week. The master laser itself is unbelievably stable and runs continuously for more than three years, without ever changing its mode. The TA chip ran for about five years continuously without drop in output power, and the LBO crystal has been used for fours years. The laser is placed into a box of multi-layer wood, cushioned with a layer of dense vinyl and an acoustic foam for thermal and acoustic insulation[10]. Some of the light from the IR laser goes to a Fabry-Pérot interferometer (FPI) and towards a high-finesse cavity, which can in the future be used for linewidth reduction of the laser[11].

[9] The LBO crystal is from Raicol Crystals Ltd. Very recently, blue laser diodes with up to 50 mW output at 461 nm became available, and TA chips are being developed to appear on the market in a few years.

[10] We use SheetBlok material from Auralex Acoustics for dampening of low frequencies, and standard acoustic foam from Schaumstoffe Wegerich (Würzburg, Germany) to dampen higher frequencies.

[11] The laser does not need to be very stable, since the atomic linewidth is 30 MHz, but any frequency jitter on ms-time scales might result in a change in interference pattern in the absorption- and reference images, which leads to interference fringes in the processed image. Therefore, we set up a high-finesse cavity to lock the laser.

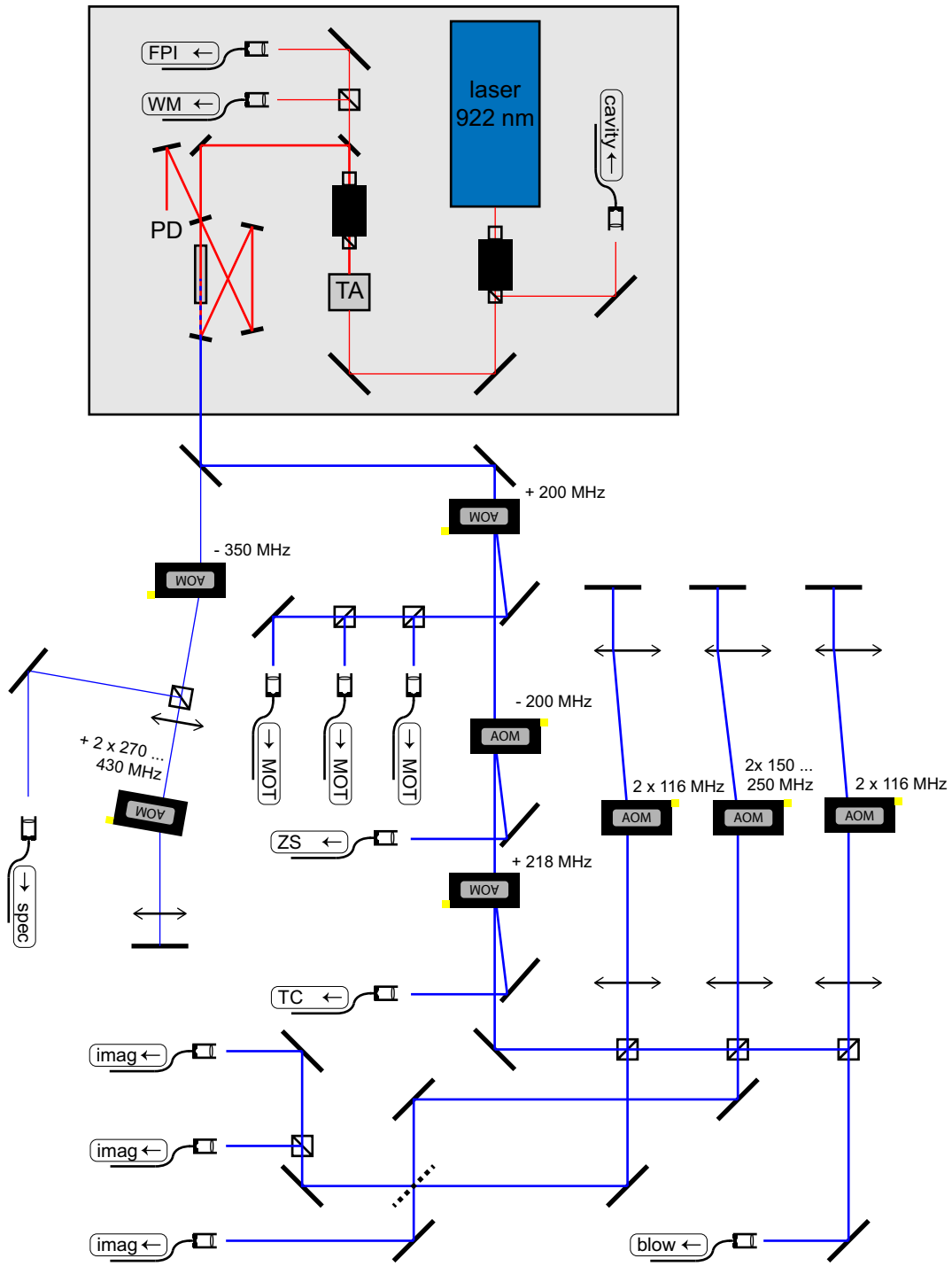

Figure 3.3: Setup of the blue laser system. The SHG laser itself is placed in a housing for thermal and acoustic insulation (top grey-shaded area). The light is split into various paths, frequency-shifted, and coupled into fibers. In this drawing, all waveplates, shutters, irises, and other passive elements have been omitted for clarity. Abbreviations: Fabry-Pérot interferometer (FPI); wavemeter (WM); photodiode (PD).

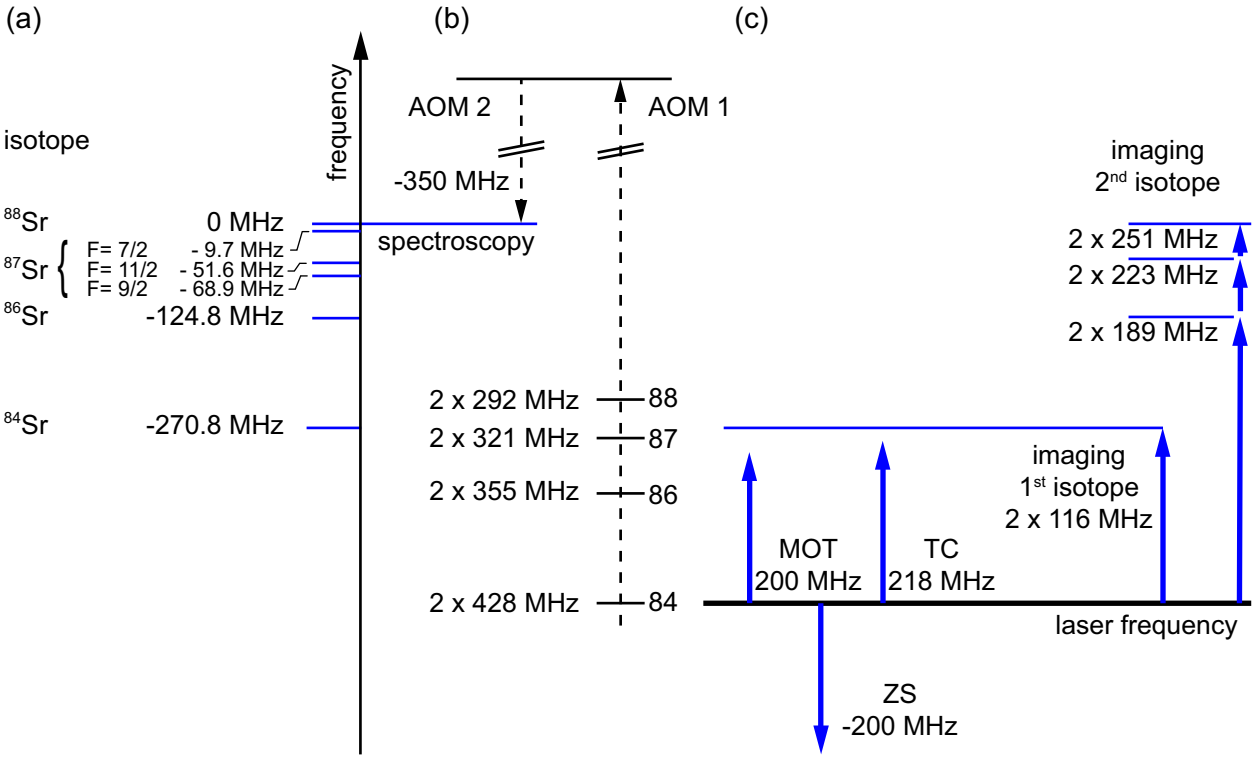

Figure 3.4: Frequency scheme of the blue laser system used to address all stable isotopes. (a) The isotope and hyperfine shifts of the ${}^1S_0 - {}^1P_1$ transition, referenced to the ^{88}Sr line. (b) The laser is always locked to the ^{88}Sr spectroscopy signal, but the frequency offset between laser and spectroscopy can be tuned with AOMs 1 and 2 to shift the laser frequency around. (c) The frequencies used for the MOT, ZS, TC, and imaging lights, shown here for the case of ^{84}Sr. When working with mixtures of isotopes, the time delay between the imaging flashes for the two isotopes is too short to adjust the frequency of the master laser accordingly, and we use a second AOM for this purpose (far right arrow).

Spectroscopy lock — There are a number of different options to stabilize the frequency of the 461-nm laser. The Florence group uses conventional spectroscopy cells, which need only little adaptations to work at about 350 °C. The PTB group locks the laser to a stable reference cavity, the group at JILA uses hollow cathode lamps. Locking to a transfer cavitiy or to a wavemeter (both schemes used by the Tokyo groups) are also viable. We decided to employ a spectroscopy cell.

About 6 mW of the blue light are sent into the spectroscopy path. The frequency of the light is shifted down by 350 MHz [12] and then passes through another 350 MHz AOM

[12] We use Crystal Technology acousto-optical modulators (AOMs) throughout, obtained from the German distributor EQ Photonics. More specifically, we use models 3080-120 and -121, 3110-120, 3200-120, -121, and -125, as well as 3350-199 and -192 for the near-resonant lasers. They provide diffraction efficiencies of up to 90% with less than 1 W RF power, and have a bandwidth of 25% of their nominal frequency. Especially the newly developed models at 350 MHz have been indispensable. The RF is generated by our DDS (DC−135 MHz at -10 dBm), doubled or quadrupled if required, and amplified by our home-built amplifier.

in double-pass configuration to end up in a fiber; see Fig. 3.4. This double-pass 350-MHz AOM can be driven with frequencies between 270 and 430 MHz, which conveniently spans the isotope shift of 270 MHz between ^{84}Sr and ^{88}Sr. When addressing different isotopes, we shift the frequency offset between the laser and the spectroscopy, which is always set to the most abundant isotope ^{88}Sr. The telescope around this AOM, the position of the AOM in the exact focus of the telescope, and the fiber coupling need to be adjusted carefully to provide sufficient coupling efficiency into the fiber over the entire frequency range. The RF output power of the DDS is adjusted such that the optical power behind the fiber is independent of the AOM frequency. This adjustment compensates for the frequency-dependent output levels of the DDS, gain curves of the RF frequency doublers and the RF amplifier, misalignment of the Bragg angle, diffraction efficiency of the AOM, and fiber coupling efficiency. We use typically 100 μW behind the fiber, with less than 1% intensity modulation across the 270 MHz scan range. Much more power would be available, leaving room for degradation of the system before maintenance needs to be performed. The spectroscopy lock itself follows the standard Pound-Drever-Hall scheme[13], with both pump and probe light impinging onto a photodiode[14]. The error signal is fed into the Toptica PID, which controls grating and current of the laser head via the backplane of the laser rack, and has a fast output onto the bias-T. The laser can be scanned across the four isotopes by sweeping the frequency of the spectroscopy double-pass AOM in 100 ms without falling out of lock.

Light for the experiment — The remainder of the blue light is used for MOT, Zeeman-slower (ZS), transversal cooling (TC), and imaging. The mode quality of the light is rather poor and worsens when propagating along the beam path. Additionally, the beam is rather small as it exits the doubling stage. We tried different setups to maximize the amount of usable light from the laser, and stopped optimizing with a very compact setup that does not use any telescopes around the AOMs. The light passes through three 200 MHz AOMs in series, at distances of about 10 cm, where one AOM uses the non-diffracted zeroth order of the preceding AOM. The first AOM diffracts light at +200 MHz for the MOT beams, this light is split into three paths and coupled into three fibers[15]. The second AOM splits off light at -200 MHz for the ZS, which is also sent into a fiber. Finally, the third AOM picks off light at +218 MHz for the TC. The zeroth order of this AOM is split into three paths: Two imaging paths and a so-called blow beam, which is used to resonantly remove atoms from the scene without sending light onto the CCD cameras; a 110 MHz double-pass AOM

[13]For all our lasers, we use home-built electro-optical modulators (EOMs) for modulation of sidebands. Their $LiNbO_3$ crystals have a length of 30 mm and AR-coated facets with $3 \times 3\,\mathrm{mm}^2$ surface, and are housed in a copper block. A self-built resonator tank with resonance frequency of about 13 MHz amplifies the voltage of the RF across the crystal.

[14]The spectroscopy cell is a heat pipe operated at 340 °C, and the windows are water-cooled. The cell is filled with about 10 g of Sr and about 10^{-3} mbar of Ar as buffer gas, and has been running continuously for about four years without loss in vapor pressure or coating of the windows. The pump and probe beams are focused at their intersection to obtain a high intensity. The error signal amounts to about 1 V without much optimization, with the noise level being a few percent. The quality of the locking scheme is illustrated by our ability to lock also to the ^{86}Sr absorption feature, which is a factor of ten smaller than the ^{88}Sr feature.

[15]We use Schäfter + Kirchhoff fiber couplers (models 60FC) and angle-cut single-mode polarization-maintaining fibers (models PMC) throughout. The fiber couplers are placed into mirror mounts with home-built adapters.

experiment	spec. AOM 1 (MOT)	spec. AOM 1 (imag.)	imag. 1 AOM	imag. 2 AOM
84 + 86	428 MHz + 355 MHz	428 MHz	116 MHz	189 MHz
84 + 87	428 MHz + 321 MHz	428 MHz	116 MHz	223 MHz
84 + 88	428 MHz + 292 MHz	412 MHz	100 MHz	235 MHz
86 + 87	355 MHz + 321 MHz	365 MHz	126 MHz	160 MHz
86 + 88	355 MHz + 292 MHz	355 MHz	116 MHz	178 MHz
87 + 88	321 MHz + 292 MHz	336 MHz	134 MHz	152 MHz

Table 3.2: Blue spectroscopy and imaging AOM frequencies for experiments involving two isotopes. The spectroscopy AOM 1 sets the locking point of the laser during the MOT (second column) and imaging (third column) phase. The frequencies of the imaging 1 AOM (nominal frequency 110 MHz) and imaging 2 AOM (200 MHz) are given in the last two columns. All AOMs are used in double-pass configuration.

sends the light into a fiber.

The two imaging paths use AOMs of different nominal frequencies and allow for simultaneous imaging of two different isotopes[16]. These double-pass AOMs actually use telescopes. The beams are overlapped on a non-polarizing beamsplitter and sent into two fibers for horizontal and vertical imaging. Some light out of the horizontal imaging can be picked off and sent into a third fiber for a future wide-field imaging system.

All fibers are equipped with mechanical shutters[17]. Additional shutters are set in front of each imaging AOM, and a global shutter directly behind the laser blocks all blue light, but the spectroscopy beam. All of these shutters are closed after the blue MOT stage[18]. The entire laser system is shown in Fig. 3.3.

We frequently work with mixtures of different isotopes. The sequential loading of different isotopes into the metastable reservoir is achieved by adjustment of the locking point of the laser, using the double-pass AOM in front of the spectroscopy. The blue transition is not entirely isotope-selective, and we usually image only one isotope per experimental run. It might, however, be desired to image any combination of two isotopes within a few ms during the same run. This is not possible by sweeping the laser frequency because of the limited bandwidth of the doubling cavity. Instead, we set the locking point of the laser to a suitable position and employ the two different AOMs mentioned above (nominal frequencies of 110 and 200 MHz with a RF bandwidth of about ±25%) to address the two isotopes; see Tab. 3.2.

[16] For future optimization, it would be convenient to use a 350 MHz in double-pass to address all isotopes, analogous to the spectroscopy AOMs

[17] The shutters are made of small metal sheets, moved into the beam path by small servo motors, which can be obtained from any electronic distributor, e.g. Conrad Electronic. This design is comparably slow (~ 100 ms), but very cheap and simple, with a lifetime of about 10^6 cycles.

[18] For all of our near-resonant laser systems, we use New Focus model 9801 mirror mounts throughout, available from Newport. We use home-built adapters to mount optical elements other than mirrors (beamsplitter cubes, AOMs, EOMs, fiber couplers,...), or we modify the mounting plate accordingly. The remaining optomechanics are entirely from Thorlabs. Mirrors are from Thorlabs and Laser Components, simple singlet lenses from Thorlabs and CASIX, and polarization optics are from CVI Melles Griot and Qioptiq (formerly Linos).

3.5.2 The green laser system

During the blue MOT phase, we collect atoms in the metastable $^3P_2$ reservoir state. These atoms need to be returned to the $^1S_0$ ground state, which is done by optical pumping into the $5s5d\,^3D_2$ state, from where atoms relax into the $^3P_1$ state and further into the ground state. The transition has a width of a few MHz. Isotope shifts are relatively small, but hyperfine splittings are of a few GHz; see Chpt. 9 for spectroscopic data.

Generation of multiple frequencies — We use a Toptica SHG system to generate the 497-nm light. An IR diode at 994 nm generates about 300 mW of power and is monitored on a FPI and a wavemeter. The light is coupled into a SHGpro doubling cavity, which generates up to 40 mW of green light if optimized. This light is coupled into a fiber for mode-cleaning and ease of operation; see Fig. 3.5. The fiber guides the light to a system dubbed the *green rainbow*, where a comb of frequencies (hence the term "rainbow") is generated to address all necessary transitions. A set of five AOMs with nominal frequencies of 200 or 350 MHz, all of them in double-pass configuration, can be used in parallel or in series, or in a combination of the two. This versatile setup allows for very different applications with only minor changes to the system. The 350 MHz AOMs have reasonable diffraction efficiency up to 80 MHz away from the center frequency, thus five of these AOMs in series offer a massive tuning range of 1280 MHz, which is very useful for spectroscopic measurements. On the other hand, two or three AOMs in parallel, with all paths combined behind the AOMs and sent into the same fiber, can be used for different isotopes or hyperfine transitions in the fermionic isotope. Out of a total of 13 hyperfine transitions, we address only the $^3P_2 - {}^3D_2$, $F = 11/2 \rightarrow F' = 13/2$ and $F = 13/2 \rightarrow F' = 13/2$ transitions (see Chpt. 9), which are separated by 1350 MHz. Adding a bosonic isotope is particularly simple for the combination ^{84}Sr + ^{87}Sr, as the $F = 11/2 \rightarrow F' = 13/2$ transition in ^{87}Sr is only a few MHz away from the transition in ^{84}Sr.

Long-term stability — A few 100 μW of power on each transition are needed to securely repump all atoms, much less than we have available. Especially during the first experiments on ^{84}Sr, when we had orders of magnitude more light available than needed, we had the IR master diode running freely and tweaked the current maybe twice a day to get the laser back onto resonance. As the experiment grew in complexity and less power became available on each transition, we decided to lock the IR master laser to a stable reference cavity. This application does not demand a narrow linewidth, but some decent long-term stability. We use the cavity design described in Appendix A. We use mirrors designed for 1030 nm, which give a modest finesse at 994 nm, with one mirror mounted onto piezos in a standard way. The laser is set to resonance with the atomic transition by observation of its influence on the blue MOT. With the laser on resonance with the atomic transition, the cavity is tuned to resonance with the laser by either applying a voltage to the piezos, or, more elegantly, by using the 350 MHz double-pass AOM between laser and cavity. The laser stays locked to the cavity for more than a week. The IR diode is not AR-coated, and the mode-hop free plateaus are relatively small: whenever a mode-hop approaches the resonance position, the laser will inevitably fall out of lock. The drift of the cavity amounts to a few 10 MHz per day,

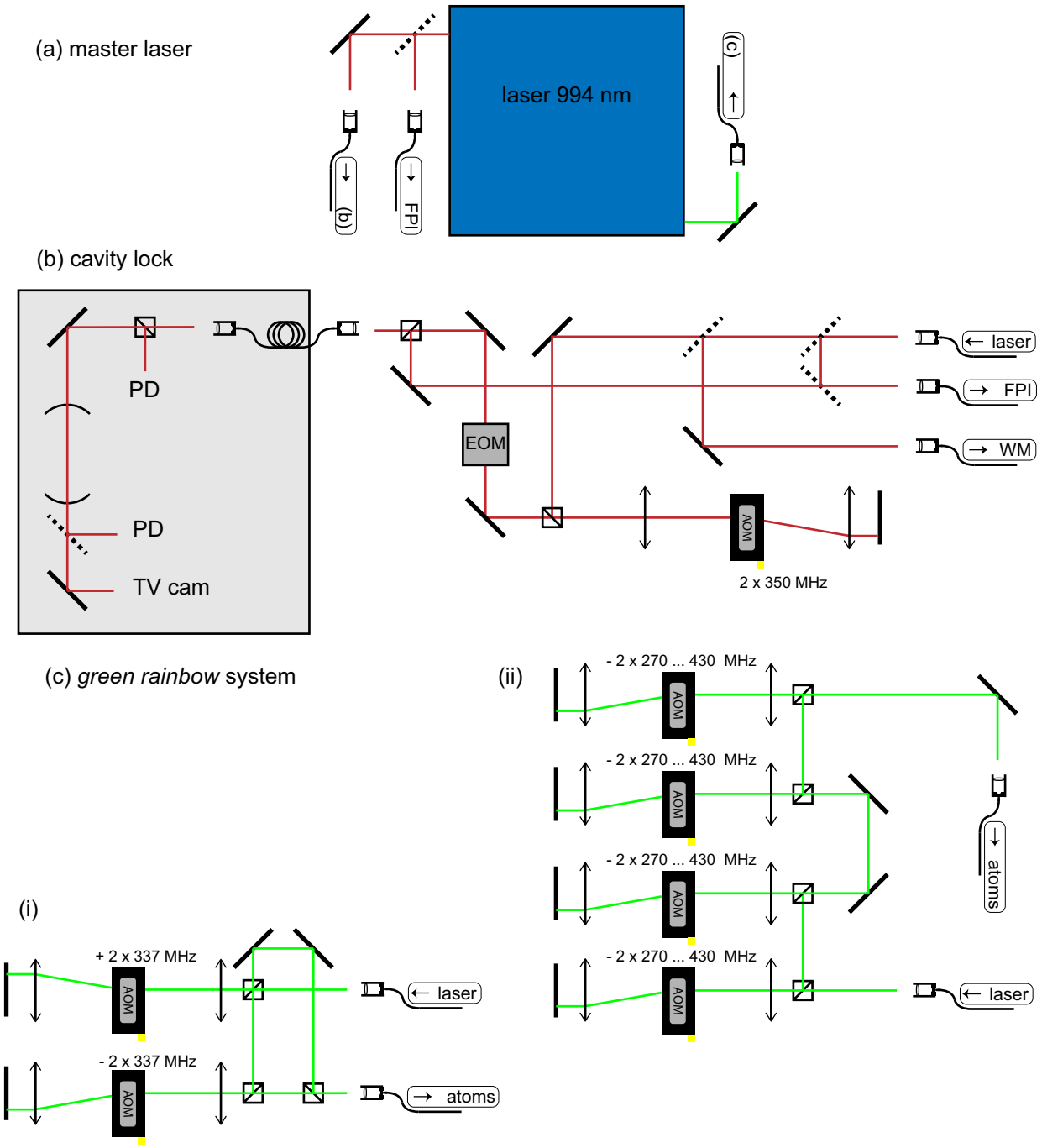

Figure 3.5: The green laser system at 497 nm. (a) The frequency-doubled laser system with IR and VIS outputs. (b) The IR light is locked to a high-finesse cavity. An AOM allows to shift the laser frequency onto a cavity transmission line. (c) The green light is sent through many AOMs either in parallel ((i), e.g. in experiments involving only fermions) or in series ((ii), as used in the spectroscopy measurements described in Chpt. 9), or combinations of the two (e.g. in mixture experiments, not shown here). All waveplates, shutters, and other optical elements are omitted entirely.

which is tolerable and likely caused by piezo creep and residual temperature fluctuations.

3.5.3 The red laser system

The red laser system at 689 nm is currently the most sophisticated laser system in our lab. The ${}^1S_0 - {}^3P_1$ intercombination transition has a natural width of 7.4 kHz, so the laser needs to have a linewidth and long-term stability smaller than this value. As another requirement, we need to address the transition in all isotopes and hyperfine states, where isotope shifts and hyperfine splittings are up to a few GHz; see Fig. 2.3. In the following, we will show how these requirements are met.

Linewidth reduction — The master laser is a Toptica DLpro with an intrinsic linewidth of about 1 MHz and is locked to a *high-finesse cavity* to reduce its linewidth to a few kHz[19]. The laser light passes through a fiber for mode-cleaning and then through an EOM for modulation of sidebands, before entering into another short fiber. Some care has to be taken to avoid amplitude modulation: we use waveplates to set the polarization correctly, use a small beam diameter to avoid clipping, and aim to reduce reflections from the fiber coupling. A photodiode behind the fiber is used to monitor the amplitude modulation, which is certainly below 10^{-3}.

About 100 μW of light are coupled into a cavity with a finesse of about 15 000, formed by two curved mirrors with rcc = 250 mm and 99.98% reflectivity around a 100 mm Zerodur spacer. One of the two mirrors is glued onto a stack of two piezos. The cavity was originally placed into vacuum, which likely degraded over the years of operation as no vacuum pumps are attached. There is some thermal insulation, but no active temperature stabilization. The cavity design is further described in Appendix A. The cavity resonance is shifted into the vicinity of the atomic resonance by driving one of the piezos with a HV amplifier. This HV amplifier is static and has a time constant of minutes. The laser is then locked to the cavity in a standard Pound-Drever-Hall scheme. We use the Toptica FALC for this purpose. The obtained linewidth, as estimated from the noise of the locking signal, is about 2 kHz. We take care to double-shield all BNC cables and keep their lengths as short as possible. The Toptica laser rack is placed about 20 cm away from the laser head to provide fast feedback. The laser and cavity are housed in a 14 mm multi-layered wooden box, with a dual-layer thermal and acoustic shielding. The laser typically stays locked for a few days. The design can certainly be improved in many ways. Using a higher modulation frequency of 50 MHz on the EOM will increase the locking bandwidth by a factor of three. Adding an ion pump to the steel chamber would establish a good vacuum and might reduce acoustic noise on the cavity. Such a cavity with an upgraded design exists already and is sometimes used to analyze the performance of the first cavity.

Long-term stability — Having now successfully reduced the linewidth of the laser, the next step is to keep the laser frequency on the atomic resonance. We cannot hope that our cavity will keep its resonance frequency stable within a few kHz over long time scales.

[19] We find it important to use an AR-coated diode, which we obtain from Sacher Lasertechnik (Marburg, Germany). Two optical isolators in series are used for increased protection from unwanted backreflections.

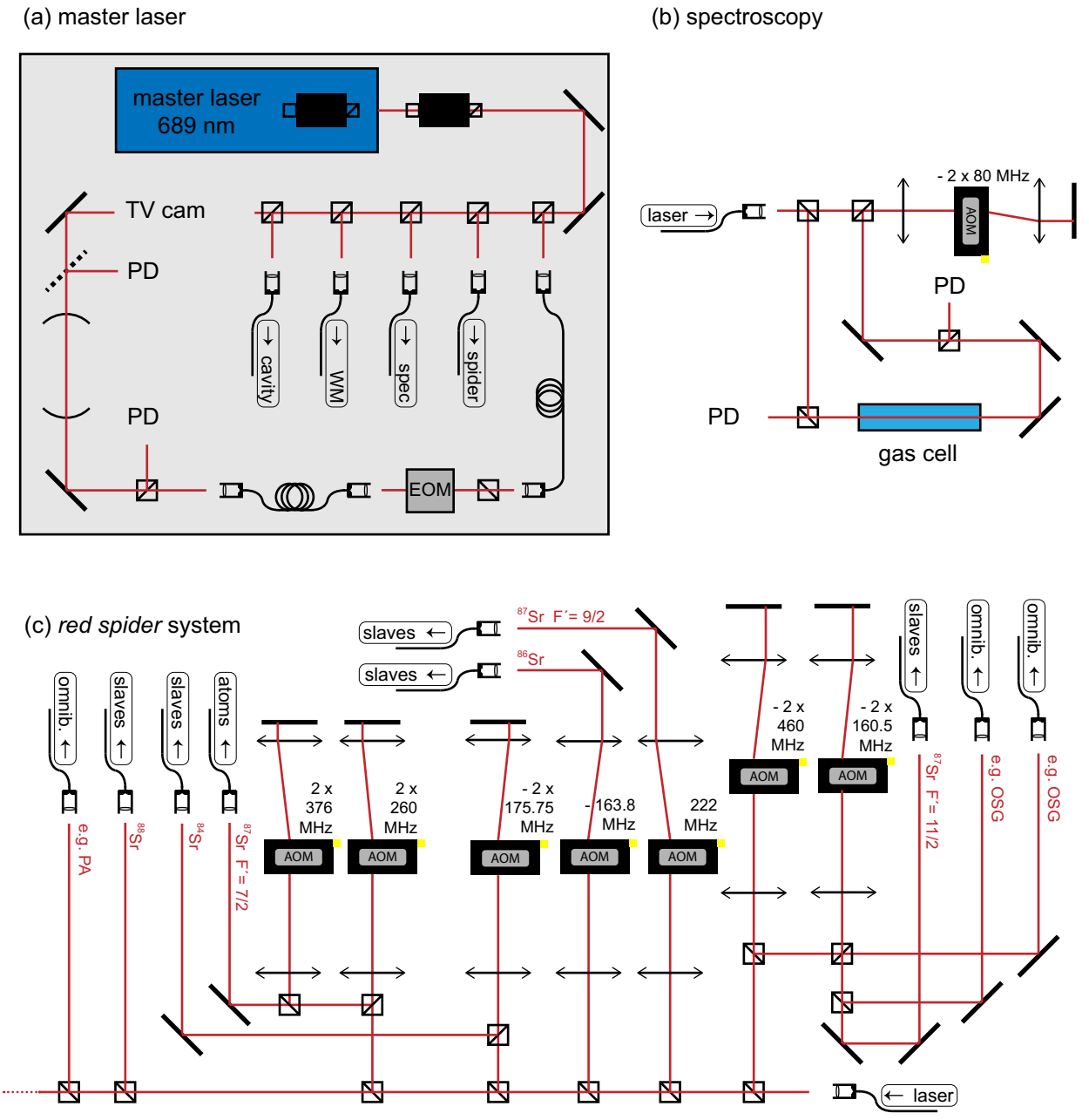

Figure 3.6: (this page and next) The red laser system at 689 nm. Light of the master laser is sent to a high-finesse cavity for linewidth reduction (a), to a spectroscopy cell for locking (b), and to a system called the *red spider* (c), in which AOMs are used to shift the light to all frequencies used in the experiment (certain outputs have been omitted for simplification). The individual outputs are amplified by a number of slave lasers, used for the red MOT (d) and for other purposes (e). Again, all waveplates, shutters, irises, and other passive elements have been omitted for clarity.

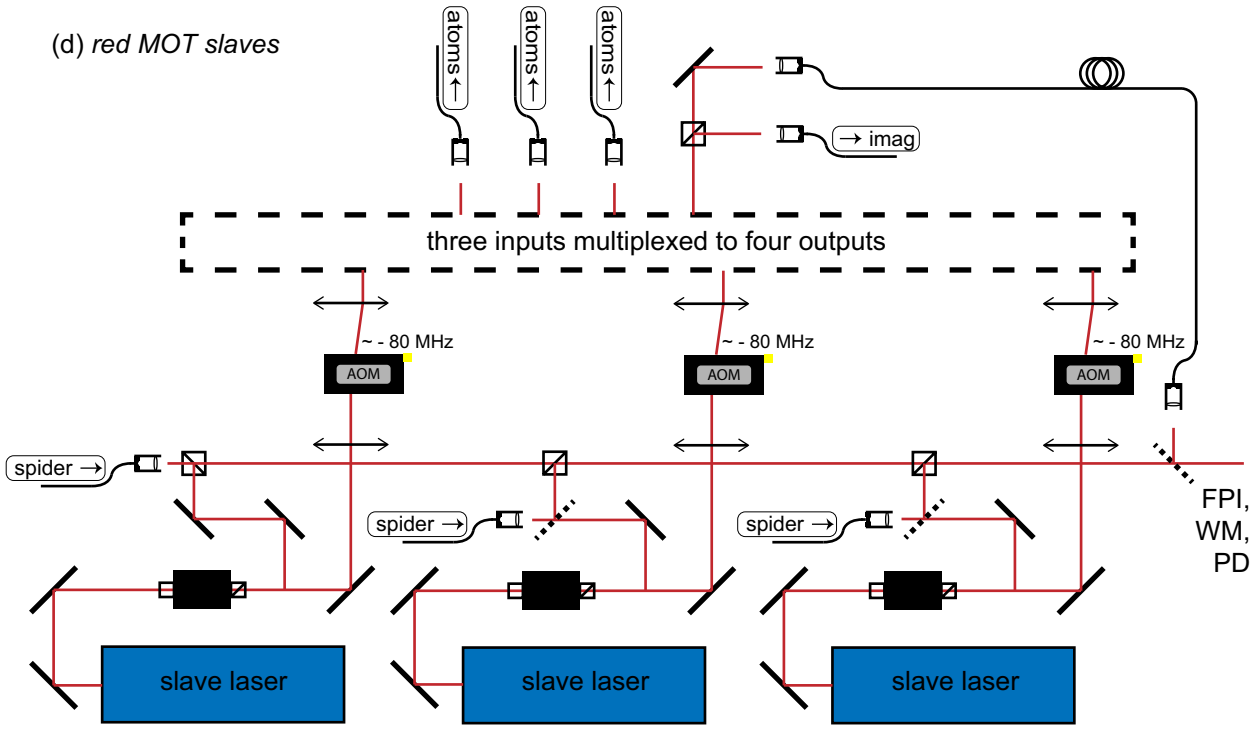
(d) red MOT slaves
atoms
atoms
atoms
→ imag
three inputs multiplexed to four outputs
~ - 80 MHz
AOM
~ - 80 MHz
AOM
~ - 80 MHz
AOM
spider →
spider →
spider →
FPI,
WM,
PD
slave laser
slave laser
slave laser

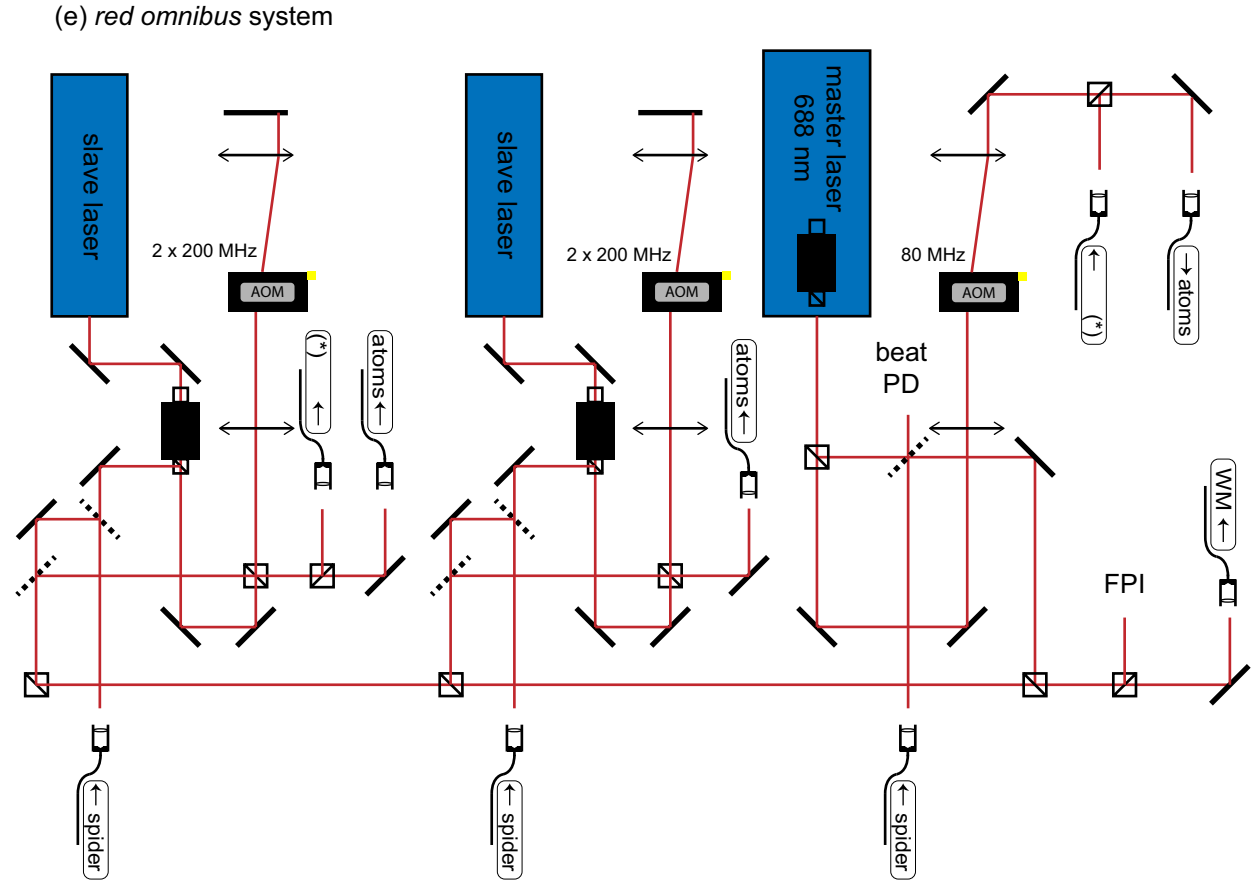
(e) red omnibus system
slave laser
2 x 200 MHz
AOM
(*)
atoms
slave laser
2 x 200 MHz
AOM
atoms
master laser
688 nm
80 MHz
AOM
(*)
atoms
beat
PD
WM
FPI
spider
spider
spider

This would have required a much better design of the cavity[20]. Other approaches would be a lock to a stabilized frequency comb, a transfer lock to a cavity referenced to another narrow optical transition, or a feedback from the red MOT itself[21]. We decided to construct a *narrow-line spectroscopy cell* as direct frequency reference.

The design of the spectroscopy cell is described in Appendix B. Light from the master laser is sent through a fiber and split into two paths. One path goes through an 80 MHz AOM in double-pass configuration and then passes through the spectroscopy cell. About half of the power of this probe beam is split off before the spectroscopy cell and sent onto a quiet photodiode, and the entire power emerging behind the spectroscopy cell is sent onto a photodiode as well. This referencing approach allows us to cancel intensity fluctuations in the probe light. The second beam counterpropagates the first one through the spectroscopy cell, with an extinction of about 70% on resonance. The Doppler-broadened profile has a width of about 2 GHz (FWHM), and the narrow Doppler-free peak is clearly visible. Note that we are probing a velocity class of atoms shifted by 80 MHz from the natural transition. We lock to the ^{88}Sr peak, as it is roughly ten times stronger than any other feature. We use a relatively strong loudspeaker magnet to generate an inhomogeneous B-field that pushes the transitions into the $m_{J'} = \pm 1$ states away and smears them out, thereby allowing us to probe only the $\Delta m_F = 0$ transition.

The 80 MHz RF signal of the AOM is frequency-modulated to obtain sidebands at $\pm$ 10 kHz. The two photodiode signals are delivered to a Stanford Research lock-in amplifier (model SR830 DSP), whose output goes to a very slow PID. This PID controls the length of the second piezo of the cavity with a time constant of a few 10 s. Again, great care is taken to double-shield all cables and to avoid ground loops. We do not observe any drifting of the spectroscopy lock on any timescale.

Generation of frequencies — The isotope shift of the $^1S_0 - {}^3P_1$ transition is about 75 MHz per mass unit for the four stable isotopes. The hyperfine splitting separates the $F' = 7/2$ and $F' = 11/2$ states in ^{87}Sr by 2.5 GHz. In total, six atomic transitions need to be addressed: one in each of the three bosonic isotopes, and three hyperfine transitions in ^{87}Sr. There are a couple of different approaches to this problem: Many experiments use beat locks to reference grating-stabilized lasers to the master laser. This technique offers very high flexibility, but adds complexity to the system and might require some monitoring of the locking quality. Another option is the use of fiber-based EOMs, which can certainly generate sidebands in the range of many GHz, but might also generate a multitude of sidebands. We chose the approach to shift the frequency of the master laser by AOMs. This is done by a system dubbed the *red spider* (the name originates from the fact that a total of eight (and presently even more) black optical fibers lead to this bread board, just as eight legs of a spider). A number of AOMs, many of them in double-pass and some of them in series, shift the frequency and send the light into fibers, which is then used to seed slave

[20] Such cavities are now commercially available for a fairly low price from Stable Lasers, Inc., with drifts of less than 100 kHz/day.

[21] The position of the single-frequency red MOT is very sensitive to the frequency of the light. The usual measurement cycles could be interleaved with such a measurement every few minutes to compensate for slow drifts.

lasers; see Fig. 3.6. Not only the frequencies required for the red MOT, but also for the $F = 9/2 \rightarrow F' = 7/2$ optical pumping light, the OSG, and the PA spectroscopy/STIRAP are generated here.

Amplification — The light power emerging from the red spider is about 100 μW per output frequency. To begin, let us roughly estimate the typical power needed for the red MOT: The saturation intensity of the red transition is 3 μW/cm^2, and the MOT beams are typically 2 cm in diameter, giving rougly 10 μW for all three MOT beams. For the broadband red MOT, we need to span a frequency comb with a spacing of a few linewidths (say, 20 kHz) over a few MHz (say, 5 MHz), giving 250 comb lines. With each comb line containing 10 μW, the total power amounts to a few mW. We thus need to amplify the power of the "red spider" output by a factor of at least 100. There are many commercial laser diodes available at this wavelength, emitting 30 mW of power with a tuning range of a few nm [22]. Three fibers connect the red spider system with the *red MOT laser* system. Each fiber seeds a Toptica DL100 slave laser via the "wrong" output of the isolator. All three seeding beams are overlapped and sent to a FPI. The beams of the three slave lasers pass through individual 80 MHz AOMs and shutters and are combined using non-polarizing 50:50 beam splitters[23]. Multiplexing three beampaths will always result in four output paths. Three of them are used for the three MOT axes, and are coupled into fibers for mode-cleaning, stability issues, and ease of maintanance[24]. The fourth output port is split into two paths: one is used for imaging on the red transition, the other one is sent to the same FPI as the seeding lasers. This makes it very convenient to monitor the seeding quality of the slaves[25]. The 80 MHz AOMs are used during the red MOT phase to generate the sidebands and shift the frequency. Although it is only a single-pass configuration, we find that the coupling efficiency into the fibers is good enough over a range of 10 MHz. Each output port is equipped with a shutter in order to address the three MOT paths and the imaging light individually. The whole system is placed on the vacuum table and cased into an insulated 5 mm-aluminum housing. The red MOT system works very stable and does not need any surveillance over weeks. Each slave laser addresses one isotope, or one hyperfine transition in ^{87}Sr: the system can work with a combination of the fermionic isotope together with any bosonic one, or all three bosonic isotopes. Changing between isotope combinations is just a matter of exchanging fibers in the red spider system, and is usually done within a minute.

During an upgrade of the experiment in late 2010, we found it convenient to add additional lasers operating on the $^1S_0 - {}^3P_1$ transition. They would be used for the generation of light for the OSG experiment, imaging on the red transition, two-color PA spectroscopy and

[22] We use laser diodes from Toptica, as well as Opnext diodes HL6738MG, which can be obtained from Thorlabs. For beam shaping, we use cylindrical lenses throughout. We consider them much superior to anamorphic prism pairs, by which up to 30% of the power are sacrificed. The lenses are placed with a tilt to the optical axis to avoid backreflections into the laser.

[23] We use custom-made beamsplitters from Laser Components, as VIS broadband beamsplitters are far away from equal powers in the two outputs.

[24] A note to the careful reader: we can modify the multiplexing of the three slave lasers such that each slave laser serves a different MOT axis. This feature is used in the experiments of Chpt. 12.

[25] There exist additional beam paths behind each slave that lead towards the FPI and wavemeter via a flip mirror. These paths are used when changing the laser diodes.

STIRAP, construction of dipole traps, as spares of the existing MOT slaves, and possibly for other experiments, such as optical Feshbach resonances. Many of these applications require more power than available from the red master laser, and are at frequencies different from the red MOT transitions. In addition, the $^3P_1 - {}^3S_1$ transition at 688 nm is only 1.5 nm away and could be used for repumping and the construction of state-selective dipole traps. As the afore mentioned applications would not be used at the same time, we constructed a very flexible laser system that can be used for any purpose. It is dubbed *red omnibus*, derived from Latin *omnibus* "for all". It consists of two Toptica DL100 slave lasers and one Toptica DLpro master laser[26]. Similar to the red MOT laser system, the two slave lasers are injection-locked via the optical isolator, and all seeding laser beams and output laser beams are overlapped on a FPI and a wavemeter port. The light of the master laser is overlapped with light from the red spider system on a GHz photodiode for a versatile beat lock. The lights of these three lasers pass through double-pass AOMs, shutters, and are sent into fibers. On top of this basic configuration, we often split the light of a slave laser into two fibers, or combine the light of any two of these lasers into one fiber, or exchange the double-pass AOMs against models with different nominal frequency. These changes can be done quickly, making this system a very helpful tool. The optics for the two OSG beams, the STIRAP beams, and the transparency beam (mentioned in Chpt. 12) are permanently installed around the glass cell.

3.5.4 The optical dipole trap

After cooling and compression of atoms in the red MOT, they are loaded into the optical dipole trap. We employ a crossed-beam optical dipole trap in the infrared. The type of laser used as source, as well as the geometry of the dipole trap, underwent some evolution during the past years, which we will sketch here.

Our very first setup mimicked the one of the FeLiKx-machine: two horizontal beams of similar waist, intersecting at an angle of about 30°, and derived from a broadband 100 W IPG fiber laser at 1070 nm. This setup was never used: during the Group-II-meeting in September 2009, we learned that other groups had unsuccessfully tried to evaporate ^{84}Sr, however the reasons for the observed heating and loss were not known. In other elements, such as lithium, it is well known that an atom can absorb a photon of one laser beam and emit it into the mode of the other laser beam, thus driving Raman-transitions into lower vibrational levels via excited molecular states. This leads to considerable heating and loss, which can be avoided by careful alignment of polarizations and completely eliminated by the use of a laser with narrow linewidth. Also, we learned that the PTB-group used a combination of one horizontal and one vertical beam when condensing Ca for the first time; the same geometry had been used before in Yb-experiments in the Kyoto group. We therefore changed our setup for one horizontal and one vertical beam, and used an ELS disc laser as source.

The ELS laser was borrowed from another lab, and soon after the first BEC measurements, we changed back to the IPG laser. We could generate BECs of comparable size, and

[26] Very recently, TA systems at 689 nm became available, delivering 400 mW of output power. These systems might simplify our current setup substantially.

therefore concluded that coupling to molecular levels due to the broad laser linewidth of about 3 nm is negligible in strontium. As our understanding of the machine improved with time, we did find multiple sources of heating and loss of atoms from the dipole trap. One of them was the IPG laser itself: Experimentally, we found that we could create large BECs with decent lifetimes right after switch-on of the IPG laser, but as we kept the machine cycling, the BEC atom number decreased by 40% during the next 30 minutes of operation, and the lifetime decreased to below 5 s. We speculate that the linewidth of the laser, or its intensity noise, increase dramatically as the laser heats up. This behavior was not observed during the early years of operation, and it seems that the high-power versions of the IPG lasers degrade over the years, becoming unusable after around five years.

We replaced the 100-W IPG laser by two 5-W models[27], which deliver more power than needed. One laser is used for the horizontal, the other for the vertical dipole trap beam, thereby intrinsically inhibiting any stimulated processes. These lasers operate to our fullest satisfaction. In the meantime, we also evaluated fiber amplifiers from Nufern[28], but gave up on these systems after sequentially testing three different units, all of which broke after a few days of operation. For future purposes, such as a deep dipole trap for Rb and an IR lattice, we acquired a new 100-W IPG fiber laser and a 42-W Mephisto from Innolight.

Another concern is the mechanical stability of the system. We strive to keep optical beam paths short, but the major improvement came about when we fiber-coupled all dipole trap beams[29]. Before, we observed a sloshing motion of the atoms in the trap, causing them to appear at varying positions after long TOF. This variation is now reduced to below the effective camera pixel size.

The geometric shape of the dipole trap also underwent some evolution. The guiding principle is the following: a typical trap used for evaporation is characterized by three parameters: the trap depth, the vertical trap frequency, and the average horizontal trap frequency. The vertical trap frequency is usually restricted to a small range due to the influence of gravity and the limited available laser power. To optimize the evaporation, we seek to have independent control over the trap depth and the geometric mean of the trap frequencies $\bar{\omega}$. We employ a horizontal beam that sets the trap depth and vertical trap frequency, and evaporation trajectory, and a vertical beam that sets the axial confinement

[27] IPG YLD-5-LP, operating at 1065 nm with a specified linewidth of 0.5 nm.

[28] These devices are capable of amplifying mW-powers of light with kHz-linewidth to up to 15 W, while maintaining the narrow linewidth; e.g. our model NUA-1063-PD-0015-C0.

[29] The light exits an IPG laser head, passes through a Crystal Technology 3080-194 AOM, and is coupled into a short fiber. We employ high power fibers from OZ optics (model PMJ-A3AHPC-A3AHPC-1064-6/125-3AS-1.2-1, distributed by AMS Technologies), which we tested to easily transmit more than 10 W. The polarization within these fibers turns a bit as they heat up, and we use standard PM fibers from Schäfter + Kirchhoff for powers below 2 W. The beam paths before and behind the fibers are below 50 cm. We use lenses made of Suprasil® 3001. Compared to quartz glass, this type of glass contains roughly 1000-times less OH-centers, which are known to absorb light in the IR, leading to heating and thermal lensing. The absorption at 1064 nm is typically 2.5×10^{-7}/cm. The coating of these lenses is from LaserOptik Garbsen (Germany). We use high-power mirrors from Laser Components. We use the Ultima A100 mirror mounts from Newport, but replace the screws by Mitutoyo micrometer screws of model 148-205, which are very compact and feature 6.5 mm travel with 2 μm resolution. We use sophisticated and home-built air- and water-cooled beam dumps. The entire system is contained in a 5 mm aluminum housing, and constantly flushed with filtered air to avoid the deposition of dust particles.

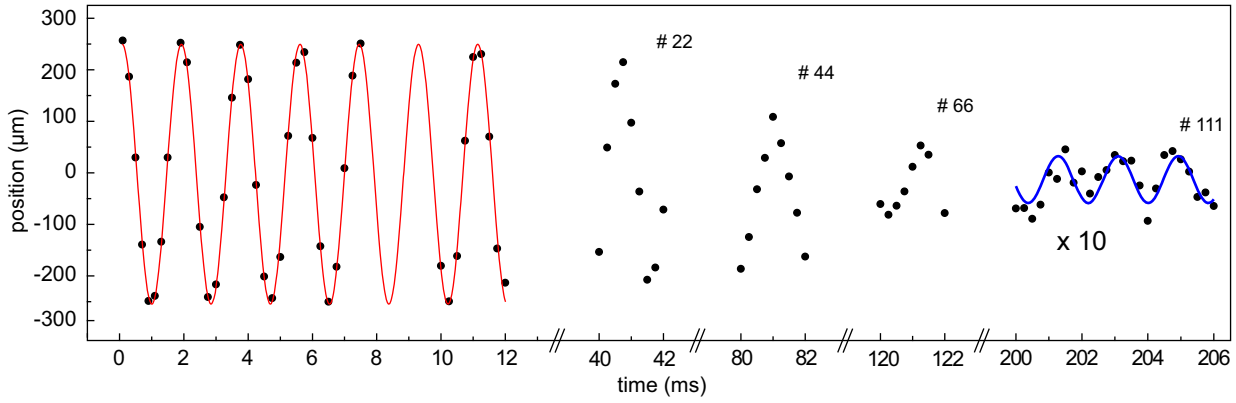

Figure 3.7: Measurement of trap frequencies by observation of the center-of-mass motion in TOF. More than one hundred oscillations can be recorded. There is a slight increase in frequency for very long hold times, but already the first six periods are sufficient to obtain a precision in the 10^{-4} range (red line). Here, we measure a frequency of 542.7(5) Hz in the vertical direction. The blue line is a fit to only the last three oscillations.

and thus influences the density, but does not contribute to evaporation; see Chpt. 8 for details. The two beams are focused onto the position of the atoms by $f = 150\,\mathrm{mm}$ and $f = 250\,\mathrm{mm}$ lenses, respectively. These lenses can be moved by translation stages. Changing the output collimator lenses behind the fibers allows us to adjust the waist in discrete steps.

Great improvement came about when we inserted a telescope of cylindrical lenses to shape the horizontal beam elliptically. The aspect ratio can be as extreme as 1 : 20, where one of the cylindrical lenses is placed on a translation stage to smoothly vary the ellipticity. Such a trap is pancake-shaped, which has at least three main advantages: First, the mode-matching with the final red MOT, which is also pancake-shaped, is optimized. Second, this shape allows for a high trap frequency in the vertical direction, while keeping the average trap frequency $\bar{\omega}$ low. Evaporation proceeds mainly downward, aided by gravity, and evaporation efficiency is improved when the trap frequency is at least comparable compared to the elastic scattering rate. And third, having one dimension of tight confinement makes it convenient to distinguish the BEC from the thermal fraction in TOF.

The four isotopes of Sr have very different scattering lengths a. The evaporation efficiency is set by the interplay between events of elastic scattering (which scale as $a^2 n$) and inelastic ones ($\sim a^4 n^2$). The only tuning parameter is the density n, which depends directly on $\bar{\omega}$. As we are working with a multitude of different isotopes and mixtures, we need to be able to change $\bar{\omega}$ substantially. This is realized by the implementation of three different vertical beams, having very different waists. Two of them enter into the glass cell from below, separated by an angle of about 1°, at an angle of 22° to gravity. They share a common lens for focusing onto the atoms. One of the two is usually called the *vertical beam* and has a typical waist of 100...300 μm. The other one is called the *dimple beam* and has a waist of 20...100 μm, depending on the choice of the output collimator lens. The third vertical beam enters through the top of the glass cell, at an angle of 15° towards gravity. Its waist can be as small as 5 μm. This port is used for the *transparency beam* mentioned in Chpt. 12.

The trap frequencies are measured by excitation of sloshing modes along the three principal axes of the dipole trap. For the two horizontal axes, we make use of the two vertical beams: Gently displacing the atoms with one of the beams allows us to measure the trap frequency of the other beam. The vertical frequency is measured by exploiting the gravitational sagging: the horizontal beam power is adiabatically lowered and then suddenly increased, setting the atoms into motion. Similar schemes are employed for the lattice, OSG, STIRAP, and other beams. We routinely achieve a precision in the 10^{-3} range with records in the 10^{-4} range; see Fig. 3.7. The subsequent calculation of the beam waists is limited by the uncertainty in the measurement of the power in the beams, which we generally estimate to be 2%, and uncertainty in the beam shape.

3.5.5 The lattice

The strong dipole transition at 461 nm allows us to use a Verdi at 532 nm to generate a red-detuned lattice. Compared to lattices in the near IR, which are commonly used with alkali atoms, the lattice spacing in a Verdi lattice is reduced to half, which significantly reduces all timescales associated with tunneling. We use a Verdi V18 from Coherent, which provides single-mode operation at a linewidth below 1 MHz.

The setup of a lattice with a cubic unit cell requires a system of three pairwise orthogonal lattice beams. The implementation of such beams demands its own share of optical access, which poses a problem to most experiments. Our MOT and imaging beams are reflected off dichroic mirrors in the vicinity of the glass cell. These dichroic mirrors are transmittive at 532 nm and could be used as access ports for a lattice. There are, however, two fundamental differences between MOT and lattice beams: polarization[30] and focus size[31]. These two properties make it very challenging to combine MOT and lattice beams, and we decided to set up an independent lattice system.

The Verdi light is split into three paths for the three lattice beams, sent through individual AOMs and shutters and is delivered to the experiment via fibers. One of the beams is horizontal and orthogonal to the horizontal imaging axis. The two other beams are sent onto the atoms through the top and bottom surfaces of the glass cell, at angles of 37.5° to the vertical axis. They are orthogonal to the horizontal lattice beam, but enclose an angle of only 75° with each other. Due to the construction of the coil system, the desired angle of 90° cannot be achieved. In this way, two lattice axes are not completely decoupled.

Great care was taken to design a mechanically stable optical setup. The lattice beams exit from S+K fibers and collimators and are focused by CVI $f = 400$ mm achromats. With this two-lens approach, a change in the beam waist at the position of the atoms, which is 100 μm with the present setup, can only be achieved in discrete steps by exchange of the

[30] The lattice beams require a linear polarization, whereas the MOT beams are circularly polarized. One would like to place the MOT quarter-waveplate behind the dichroic mirror, since dielectric coatings tend to scramble non-trivial polarizations. This is not compatible with the lattice beams.

[31] Some of the MOT beams are multiplexed with the imaging beams, and lenses used for imaging need to be placed close to the atoms to achieve a large numerical aperture. The resolution of our imaging system is of a few μm, but the lattice beams should have waists of order 100 μm. These two requirements cannot be met with a single lens. Motorized flip-mirrors, as used in some experiments, could solve this problem if silver-coated mirrors were used.

collimator lens. The polarizations of all beams are mutually orthogonal, and cubes are used for polarization cleaning. On the opposite side of the glass cell, the beam is re-collimated again and retro-reflected. The leakage through this mirror is monitored on a TV camera for alignment purposes. The back reflection is easily aligned by re-coupling into the fiber. The light passes through the fiber and the AOM, where the first order is sent onto a photodiode. This signal is very convenient for optimization of the lattice.

Chapter 4

Publication: Bose-Einstein condensation of strontium†

Phys. Rev. Lett **103**, 200401 (2009)

Simon Stellmer,[1,2] Meng Khoon Tey,[1] Bo Huang,[1,2] Rudolf Grimm,[1,2] and Florian Schreck,[1]

[1] *Institut für Quantenoptik und Quanteninformation, Österreichische Akademie der Wissenschaften, 6020 Innsbruck, Austria*
[2] *Institut für Experimentalphysik, Universität Innsbruck, 6020 Innsbruck, Austria*

We report on the attainment of Bose-Einstein condensation with ultracold strontium atoms. We use the ^{84}Sr isotope, which has a low natural abundance but offers excellent scattering properties for evaporative cooling. Accumulation in a metastable state using a magnetic-trap, narrow-line cooling, and straightforward evaporative cooling in an optical trap lead to pure condensates containing 1.5×10^5 atoms. This puts ^{84}Sr in a prime position for future experiments on quantum-degenerate gases involving atomic two-electron systems.

Ultracold gases of strontium atoms have been attracting great attention for various reasons. A major driving force for the development of cooling and trapping techniques since the early 1990s [Kur90] has been the realization of ultraprecise optical clocks [Ido03, Boy07b, Lem09b]. Many other intriguing applications related to metrology [Sor06], novel schemes for quantum computation [Dal08, Gor09], and quantum simulators of unique many-body phenomena [Her09, Gor10] rely on the special properties of this species. Moreover, there is considerable interest in ultracold Sr_2 molecules [Ciu04, Koc08] and their possible applications for testing the time variation of fundamental constants [Kot09]. Ultracold plasmas

†The author largely contributed to the construction of the experiment, namely the vacuum chamber, the laser systems, and the coils. The setup of the coil system and all the electronics was greatly supported by Gerhard Hendl, and B. H. contributed to the construction of the high-finesse cavity. The author created the first strontium BEC in a concerted effort together with M.K. T. and F. S. He operated the experiment, acquired the data, and contributed to the writing of the manuscript. All stages of the experiment, including the writing of the manuscript, were supported by R. G.

[Kil07b] represent another fascinating application of strontium atoms. Many of the possible experiments could greatly benefit from the availability of quantum-degenerate samples.

The two valence electrons of strontium and the resulting singlet and triplet states are at the heart of many of these applications. The two-electron nature also has very important consequences for cooling and trapping strategies towards degeneracy. Because of its singlet character the electronic ground state does not carry a magnetic moment. Therefore optical dipole traps [Gri00] are the only option to implement evaporative cooling. Moreover, magnetic Feshbach resonances, frequently applied to tune the scattering properties of other atomic systems [Chi10], are absent. Research on Bose-Einstein condensation (BEC) and degenerate Fermi gases involving atomic two-electron systems was pioneered by the Kyoto group, using various isotopes of Yb [Tak03, Fuk07b, Fuk07a, Fuk09b]. Very recently, a BEC of ^{40}Ca was produced at the Physikalisch-Technische Bundesanstalt in Braunschweig [Kra09].

Experiments towards quantum degeneracy in strontium have so far been focused on the three relatively abundant isotopes ^{86}Sr (9.9%), ^{87}Sr (7.0%), and ^{88}Sr (82.6%), the first and the last one being bosons. The necessary phase-space density for BEC or Fermi degeneracy could not be achieved in spite of considerable efforts [Kat01, Fer06a]. For the two bosonic isotopes the scattering properties turned out to be unfavorable for evaporative cooling [Fer06a]. The scattering length of ^{88}Sr is close to zero, so that elastic collisions are almost absent. In contrast, the scattering length of ^{86}Sr is very large, leading to detrimental three-body recombination losses. As a possible way out of this dilemma, the application of optical Feshbach resonances [Chi10] to tune the scattering length is currently under investigation [Mar09b, Ye].

In this Letter, we report on the attainment of BEC in ^{84}Sr. This isotope has a natural abundance of only 0.56% and, apparently for this reason, has received little attention so far. We show that the low abundance does not represent a serious disadvantage for BEC experiments, as it can be overcome by an efficient loading scheme. Because of the favorable scattering length of $+123\,a_0$ (Bohr radius $a_0 \approx 53\,\mathrm{pm}$) [Ciu, Ste08, Mar08] there is no need of Feshbach tuning, and we can easily produce BECs containing 1.5×10^5 atoms.

Our experimental procedure can be divided into three main stages. In the first stage, the atoms are accumulated in a magnetic trap, using a continuous loading scheme based on optical pumping into a metastable state. In the second stage, the atoms are first pumped back into the electronic ground state, laser cooled using a narrow intercombination line, and loaded into an optical dipole trap (ODT). In the third stage, evaporative cooling is performed by lowering the depth of the ODT and, thanks to the excellent starting conditions and collision properties, BEC is attained in a straightforward way.

The accumulation stage takes advantage of magnetically trapped atoms in the metastable triplet state $^3P_2$; see Fig. 4.1. Remarkably, such atoms are automatically produced [Kat01, Lof02, Xu03, Nag03, Fer06a, Tra09, Mic09] when a standard magneto-optical trap (MOT) is operated on the strong $^1S_0 - {}^1P_1$ transition at a wavelength of 461 nm [1]. A weak leak

[1] Loading of the blue MOT follows standard laser cooling and trapping procedures. Atoms emitted from an effusive beam source are transversely laser cooled to increase the loading flux of the low-abundant isotope. They are the Zeeman slowed to be captured by the MOT. Our MOT laser beams have a waist of 9 mm, a peak intensity of $5\,\mathrm{mW/cm^2}$, and a detuning of $-33\,\mathrm{MHz}$. The quadrupole magnetic field has a gradient of 61 G/cm along its symmetry axis. The temperature in the MOT is Doppler-limited to a few mK.

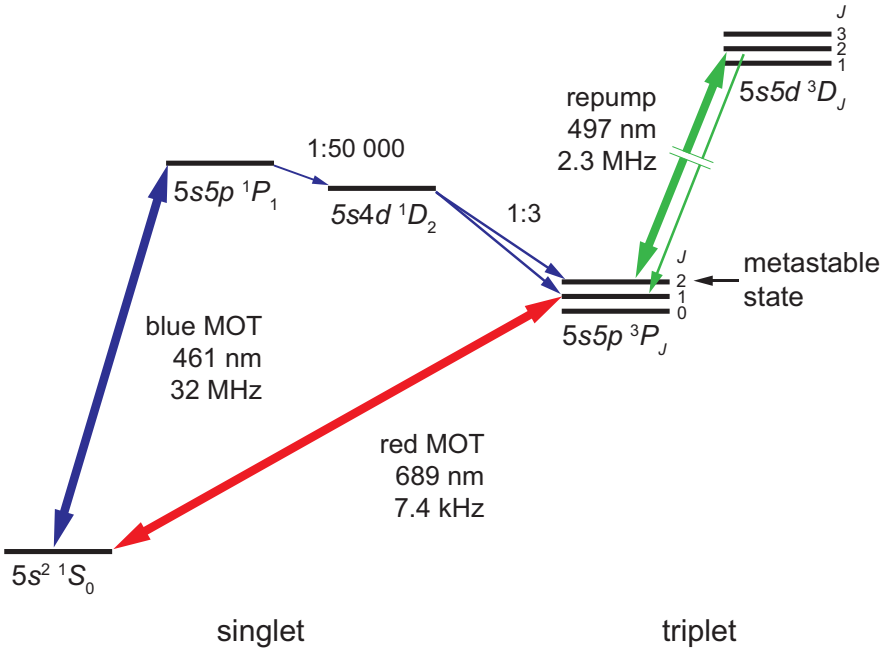

Figure 4.1: Schematic illustration of the energy levels and transitions used for cooling and trapping of Sr atoms. The blue MOT is operated on the strong $^1S_0$-$^1P_1$ transition. The loading of the magnetic trap proceeds via the weak leak of the excited state (branching ratio 1:50 000) into the $^1D_2$ state, which itself decays with a 1:3 probability into the metastable $^3P_2$ state. Here the atoms can be magnetically trapped and accumulated for a long time. The transition $^3P_2$-$^3D_2$ allows us to depopulate the metastable state by transferring the atoms into the $^3P_1$ state. The latter represents the excited state of the $^1S_0$-$^3P_1$ intercombination line, used for narrow-line cooling in the red MOT.

of the excited state out of the cooling cycle of this "blue MOT" continuously populates the metastable state and the atoms are trapped in the magnetic quadrupole field of the MOT. This continuous magnetic-trap loading mechanism is our essential tool to prepare a sufficiently large number of ^{84}Sr atoms despite the low natural abundance of this isotope. With a steady-state number of about 3×10^5 atoms in the blue MOT, we can reach an estimated number of roughly 10^8 atoms in the magnetic trap after typically 10 s of loading. This enormous gain is facilitated by the long lifetime of about 35 s for the magnetically trapped atoms under our ultrahigh vacuum conditions, which is about 3 orders of magnitude larger than the leak time constant of the blue MOT. Note that the same scheme has been applied to increase the number of ^{84}Sr atoms for spectroscopic measurements [Mic09]. Also note that a very similar loading scheme was crucial for the attainment of BEC in Cr [Gri05].

In the narrow-line cooling stage, a MOT is operated on the $^1S_0 - ^3P_1$ intercombination line (wavelength 689 nm, linewidth 7.4 kHz) using a scheme pioneered by Katori *et al.* [Kat99], which has become an almost standard tool for the preparation of ultracold Sr. Loading of this "red MOT" [2] is accomplished by pumping the atoms out of the metastable reservoir using a

[2]The 689-nm laser system is a master-slave combination. The master laser is stabilized on a 100 kHz linewidth cavity by optical feedback, resulting in a linewidth of $\sim$ 2 kHz. The laser frequency is locked to the

flash of laser light resonant with the $^3P_2 - {}^3D_2$ transition at 497 nm [Sor06]; see Fig. 4.1. In the initial transfer phase, the magnetic field gradient is reduced from 61 G/cm as used for the magnetic trap to 3.6 G/cm within about 0.1 ms. To increase the capture velocity of the red MOT we frequency modulate the light, producing sidebands that cover a detuning range between −250 kHz and −6.5 MHz with a spacing of 35 kHz; here each of the MOT beams has a waist of 5 mm and a peak intensity of 10 mW/cm^2. In a compression phase, the red MOT is then slowly converted to single-frequency operation with a detuning of about −800 kHz by ramping down the frequency modulation within 300 ms. At the same time the intensity of the MOT beams is reduced to 90 μW/cm^2 and the magnetic field gradient is increased to 10.4 G/cm. At this point, we obtain 2.5×10^7 atoms at a temperature of 2.5 μK in an oblate cloud with diameters of 1.6 mm horizontally and 0.4 mm vertically.

To prepare the evaporative cooling stage, the atoms are transferred into a crossed-beam ODT, which is derived from a 16-W laser source operating at 1030 nm in a single longitudinal mode. Our trapping geometry follows the basic concept successfully applied in experiments on Yb and Ca BEC [Tak03, Fuk07a, Fuk09b, Kra09]. The trap consists of a horizontal and a vertical[3] beam with waists of 32 μm and 80 μm, respectively. Initially the horizontal beam has a power of 3 W, which corresponds to a potential depth of 110 μK and oscillation frequencies of 1 kHz radially and a few Hz axially. The vertical beam has 6.6 W, which corresponds to a potential depth of 37 μK and a radial trap frequency of 250 Hz. Axially, the vertical beam does not provide any confinement against gravity. In the crossing region the resulting potential represents a nearly cylindrical trap[4]. In addition the horizontal beam provides an outer trapping region of much larger volume, which is of advantage for the trap loading.

The dipole trap is switched on at the beginning of the red MOT compression phase. After switching off the red MOT, we observe 2.5 $\times 10^6$ atoms in the ODT with about 10^6 of them residing in the crossed region. At this point we measure a temperature of $\sim 10\,\mu$K, which corresponds to roughly one tenth of the potential depth and thus points to plain evaporation in the transfer phase. We then apply forced evaporative cooling by exponentially reducing the power of both beams with a $1/e$ time constant of ~ 3 s [5]. The evaporation process starts under excellent conditions, with a peak number density of 1.2×10^{14} cm^{-3}, a peak phase-space density of $\sim 2 \times 10^{-2}$, and an elastic collision rate of about 3500 s^{-1}. During the evaporation process the density stays roughly constant and the elastic collision rate decreases to $\sim$700 s^{-1} before condensation. The evaporation efficiency is very large as we gain at least 3 orders of magnitude in phase-space density for a loss of atoms by a factor of 10.

The phase transition from a thermal cloud to BEC becomes evident in the appearance of a textbooklike bimodal distribution, as clearly visible in time-of-flight absorption images and the corresponding linear density profiles shown in Fig. 4.2. At higher temperatures the

[88]Sr intercombination line and frequency shifted by 351.4 MHz to the red to account for the isotope shift. A 30-mW slave laser diode is injection locked to the master to obtain sufficient light for the MOT. The red light is superimposed with the blue MOT beam using dichroic mirrors.

[3]For reasons of optical access the beam is not exactly vertical, but inclined by 20°.

[4]To avoid perturbations by interference effects the beams are orthogonally polarized and have a frequency difference of 160 MHz.

[5]The evaporation process turns out to be very robust, and common or individual variations of the ramping time constants for both beams are not found to have strong effects on the evaporation efficiency.

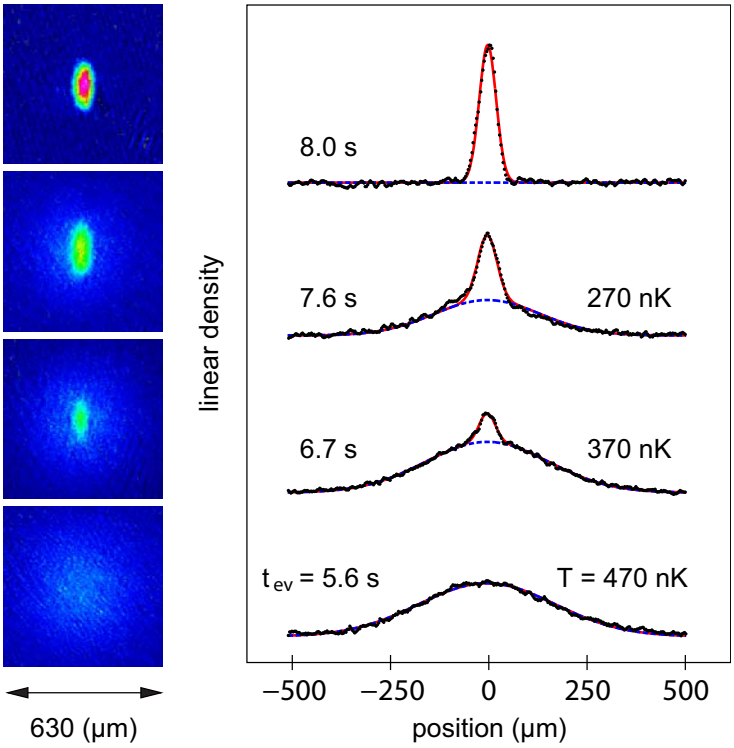

Figure 4.2: Absorption images and integrated density profiles showing the BEC phase transition for different times t_{ev} of the evaporative cooling ramp. The images are along the vertical direction 25 ms after release from the trap. The solid line represents a fit with a bimodal distribution, while the dashed line shows the Gaussian-shaped thermal part, from which the given temperature values are derived.

distribution is thermal, exhibiting a Gaussian shape. Cooling below the critical temperature T_c leads to the appearance of an additional, narrower and denser, elliptically shaped component, representing the BEC. The phase transition occurs after 6.3 s of forced evaporation, when the power of the horizontal beam is 190 mW and the one of the vertical beam is 410 mW. At this point, with the effect of gravitational sag taken into account, the trap depth is 2.8μK. The oscillation frequencies are 59 Hz in the horizontal axial direction, 260 Hz in the horizontal radial direction, and 245 Hz in the vertical direction.

For the critical temperature we obtain $T_c = 420$ nK by analyzing profiles as displayed in Fig. 4.2. This agrees within 20%, i.e. well within the experimental uncertainties, with a calculation of T_c based on the number of 3.8×10^5 atoms and the trap frequencies at the transition point. Further evaporation leads to an increase of the condensate fraction and we obtain a nearly pure BEC without discernable thermal fraction after a total ramp time of 8 s. The pure BEC that we can routinely produce in this way contains 1.5×10^5 atoms and its lifetime exceeds 10 s.

The expansion of the pure condensate after release from the trap clearly shows another hallmark of BEC. Figure 4.3 demonstrates the well-known inversion of the aspect ratio [And95, Ing99], which results from the hydrodynamic behavior of a BEC and the fact that

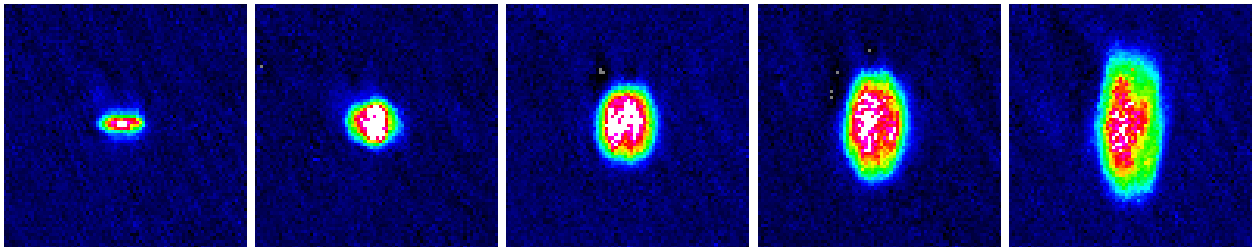

Figure 4.3: Inversion of the aspect ratio during the expansion of a pure BEC. The images (field of view 250 μm × 250 mum) are taken along the vertical direction. The first image is an *in-situ* image recorded at the time of release. The further images are taken 5 ms, 10 ms, 15 ms, and 20 ms after release.

the mean field energy is released predominantly in the more tightly confined directions. Our images show that the cloud changes from an initial prolate shape with an aspect ratio of at least 2.6 (limited by the resolution of the *in-situ* images) to an oblate shape with aspect ratio 0.5 after 20 ms of free expansion. From the observed expansion we determine a chemical potential of $\mu/k_B \approx 150$ nK for the conditions of Fig. 4.3, where the trap was somewhat recompressed to the setting at which the phase transition occurs in the evaporation ramp. Within the experimental uncertainties, this agrees with the calculated value of $\mu/k_B \approx 180$ nK.

It is interesting to compare our number of 1.5×10^5 atoms in the pure BEC with other BECs achieved in two-electron systems. For ^{174}Yb up to 6×10^4 atoms were reported [Fuk09b], and for ^{40}Ca the number is 2×10^4 [Kra09]. It is amazing that our BEC clearly exceeds these values with little efforts to optimize the number after our first sighting of BEC (26 September 2009). We anticipate that there is much more room for improvement, in particular, in the transfer from the red MOT into the ODT. We interpret the amazing performance of ^{84}Sr as the result of a lucky combination of favorable scattering properties with excellent conditions for narrow-line cooling, and we believe that this makes ^{84}Sr a prime candidate for future experiments on BEC with two-electron systems.

We finally discuss a few intriguing applications which seem to be realistic on a rather short time scale. The ^{84}Sr BEC may serve as an efficient cooling agent to bring other isotopes into degeneracy. A BEC of ^{88}Sr would be a noninteracting one [Chi10], as the intraisotope scattering length is extremely small [Fer06a, Mar08]. This would constitute a unique source of low-momentum, noninteracting, and magnetically insensitive atoms, ideal for precision measurements [Sor06]. The fermionic isotope ^{87}Sr offers a nuclear spin decoupled from the electronic degrees of freedom, which is very favorable for quantum computation [Dal08, Gor09] and the essential key to a new class of many-body physics with ultracold atoms [Her09, Gor10]. The realization of a Mott insulator state appears to be a straightforward task [Fuk09a]. Another fascinating application would be the creation of ultracold dimers made of an alkali-metal atom and a two-electron atom [Nem09]. Since all-optical evaporative cooling strategies for ^{87}Rb and ^{84}Sr proceed under very similar conditions [Bar01, Cen03, Kin05], the creation of SrRb molecules seems to be a realistic option. Such molecules would be qualitatively different from the bi-alkali-metal atoms currently applied in heteronuclear

molecule experiments [Kre09] as they offer a magnetic rovibrational ground state [Nem09].

We thank Andreas Trenkwalder and Christoph Kohstall for technical assistance with the dipole trap laser. We furthermore thank Andrew Daley, Peter Zoller, and Hanns-Christoph Nägerl for stimulating discussions on the prospects of strontium for future experiments. We also acknowledge fruitful discussions with Jun Ye, Thomas Killian, and Yoshiro Takahashi.

Chapter 5

Publication: Double-degenerate Bose-Fermi mixture of strontium†

Phys. Rev. A **82**, 011608(R) (2010)

Meng Khoon Tey,[1] Simon Stellmer,[1,2] Rudolf Grimm,[1,2] and Florian Schreck,[1]

[1]*Institut für Quantenoptik und Quanteninformation, Österreichische Akademie der Wissenschaften, 6020 Innsbruck, Austria*
[2]*Institut für Experimentalphysik, Universität Innsbruck, 6020 Innsbruck, Austria*

We report on the attainment of a spin-polarized Fermi sea of ^{87}Sr in thermal contact with a Bose-Einstein condensate (BEC) of ^{84}Sr. Interisotope collisions thermalize the fermions with the bosons during evaporative cooling. A degeneracy of $T/T_F = 0.30(5)$ is reached with 2×10^4 ^{87}Sr atoms together with an almost pure ^{84}Sr BEC of 10^5 atoms.

Ground-breaking experiments with ultracold Fermi gases [Ing08, Gio08] have opened possibilities to study fascinating phenomena, as the BEC-BCS crossover, with a high degree of control. Most experiments have been performed with the two alkali fermions ^{40}K and ^{6}Li. Fermions with two valence electrons, like ^{43}Ca, ^{87}Sr, ^{171}Yb, and ^{173}Yb, have a much richer internal state structure, which is at the heart of recent proposals for quantum computation and simulation [Gor10, Caz09, FF10, Her09, Ger10, Dal08, Gor09]. Unlike bosonic isotopes of these elements, the fermions have a nuclear spin, which decouples from the electronic state in the $^1S_0$ ground state. This gives rise to a SU(N) spin symmetry, where N is the number of nuclear spin states, which is 10 for ^{87}Sr. This symmetry can lead to new quantum phases in optical lattices [Gor10, Caz09, FF10, Her09], like the chiral spin liquid. Non-abelian gauge potentials can be realized by engineering state dependent lattices [Ger10]. In addition, the nuclear spin can be used to robustly store quantum information, which can be manipulated using the electronic structure [Dal08, Gor09]. Double-degenerate Bose-Fermi

†The author expanded the capabilities of the experiment to the cooling of the fermionic isotope and isotopic mixtures. He invented the levitation scheme, developed the m_F-state detection scheme together with F. S., acquired the data together with M.K. T., and contributed to the writing of the manuscript.

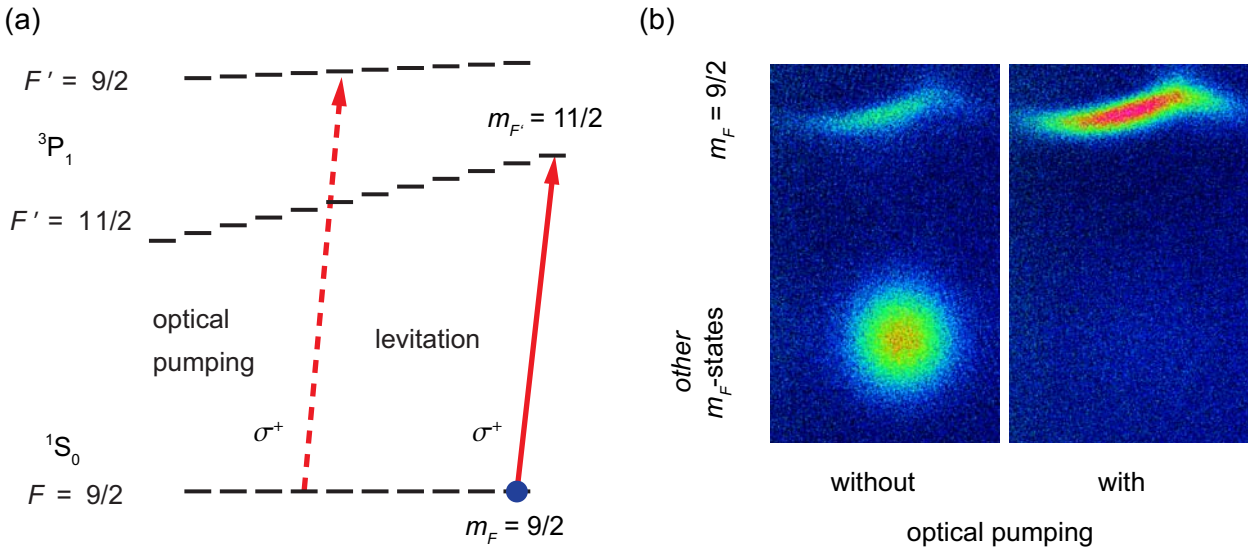

Figure 5.1: Optical pumping and state detection of ^{87}Sr. a) Internal states and transitions of ^{87}Sr used for optical pumping and detection of spin polarization. The optical pumping beam (dashed arrow) is scanned in frequency to address all m_F states. Internal state detection is performed by levitating only the $m_F = 9/2$-state atoms against gravity using a σ^+-polarized laser beam on a cycling transition (solid arrow). b) Levitated $m_F = 9/2$-state atoms and atoms in all other m_F states, 15 ms after switching off the dipole trap.

mixtures extend the possibilities even further, allowing to study phase-separation and the effects of mediated interactions.

Evaporative cooling of ultracold atoms to quantum degeneracy relies on elastic collisions to thermalize the sample. Identical fermions do not collide at low temperatures, therefore mixtures of spins [DeM99, Gra02, Fuk07b, DeS10, Tai10], isotopes [Tru01, Sch01, McN06], or elements [Roa02, Had02, Sil05] are used for evaporation. ^{87}Sr has a large nuclear spin of $I = 9/2$, which leads to a tenfold degenerate ground state. Recently, ^{87}Sr in a mixture of these states was cooled to quantum degeneracy [DeS10]. In this rapid communication, we report on the attainment of a spin-polarized quantum degenerate Fermi gas of ^{87}Sr together with a BEC of ^{84}Sr. Interisotope collisions are used to thermalize the fermions with the bosons. The system provides a clean starting point for the exploration of alkaline-earth Bose-Fermi mixtures.

Our scheme to generate a BEC of ^{84}Sr is described in Ref. [Ste09]. We have extended this scheme to the preparation of Bose-Fermi mixtures. In the following, we briefly summarize the basic preparation steps, while technical details will be presented elsewhere. We take advantage of atoms in the metastable $5s5p\,^3P_2$ state that can be trapped in the quadrupole magnetic field of the magneto-optical trap (MOT). These atoms are automatically produced when operating a "blue MOT" on the $5s^2\,^1S_0 - 5s5p\,^1P_1$ transition at a wavelength of 461 nm. The 461-nm laser system is initially tuned to the ^{84}Sr line and metastable-state bosons are accumulated in the magnetic trap. After 5 s, the laser frequency is shifted by 210 MHz to the ^{87}Sr line and metastable-state fermions are added to the magnetic trap for another 6 s

[Pol05b].

Further cooling and density increase of the mixture is achieved by operating "red MOTs" for each isotope simultaneously on the 7.4 kHz linewidth $^1S_0 - {}^3P_1$ intercombination lines at 689 nm. Since ^{87}Sr has a nuclear spin, its $^3P_1$ state is split into three hyperfine states with $F' = 11/2$, 9/2, and 7/2. The ^{87}Sr MOT uses the transitions to the $F' = 9/2$ and $F' = 11/2$ states simultaneously [Muk03]. To increase the capture velocity of the red MOTs, we frequency modulate the light, producing sidebands, which cover a detuning range from a few ten kHz to a few MHz to the red of the transition. To load the red MOTs, the metastable-state atoms in the magnetic trap are optically pumped to the $^1S_0$ ground state using the $5s5p\,{}^3P_2 - 5s5d\,{}^3D_2$ transition at 497 nm. The nuclear spin of ^{87}Sr leads to a splitting of the $^3P_2$ and $^3D_2$ states into five hyperfine states each. We use two of the 13 transitions between these states for repumping [Ste]. After loading, the MOT is compressed by reducing the MOT beam intensity and ramping off the frequency modulation, resulting in a colder and denser sample. After compression, the ^{84}Sr and ^{87}Sr MOTs are spatially separated as a consequence of different red MOT dynamics [Ste, Kat99, Muk03]. The MOTs each contain $\sim 10^7$ atoms at a temperature of $\sim 2\,\mu$K.

For evaporative cooling, the atoms are transferred into a crossed-beam optical dipole trap (ODT) based on a broadband ytterbium fiber laser operating at 1075 nm. The trapping geometry consists of a horizontal and a nearly vertical beam with waists of 80 μm. During the red MOT compression phase, the horizontal and vertical beams are ramped to a power of 4.2 W and 1.6 W, respectively, corresponding to an average trap oscillation frequency of 170 Hz and a trap depth of 13 μK.

Loading of the dipole trap is achieved in two sequential stages to overcome the spatial separation of the MOTs, first ^{87}Sr then ^{84}Sr. For each stage, the center of the respective MOT is overlapped with the cross of the ODT by shifting the center of the quadrupole field. For optimum loading, we adjust the intensities and detuning of the MOT beams before switching off the MOT beams. After loading both isotopes, the ODT power is suddenly increased to 6 W in the horizontal and 2 W in the vertical beam, resulting in a trap depth of 22 μK and an average trap frequency of 200 Hz.

In order to obtain a spin-polarized sample of ^{87}Sr, we perform optical pumping on the $^1S_0(F = 9/2) - {}^3P_1(F' = 9/2)$ transition with a σ^+-polarized laser beam[1] parallel to a homogeneous guiding field of 3 G; see Fig. 5.1(a). The $m_F = 9/2$ state is a dark state of this transition. The frequency of the optical pumping light is scanned over the transitions of the different m_F states, which are spread over 2 MHz. After 30 ms of optical pumping, the temperature of the mixture has increased to 3.4 μK.

To perform state detection, we selectively levitate only the $m_F = 9/2$-state atoms to separate them from atoms in all other states after switching off the ODT. An upward propagating σ^+-polarized laser beam near the $^1S_0(F = m_F = 9/2) - {}^3P_1(F' = m_{F'} = 11/2)$ cycling transition is used to levitate the atoms. The intensity and detuning of this beam are adjusted to optimize the levitation. At the magnetic field of 3 G, the splitting between adjacent $m_{F'}$ states is ~ 1.1 MHz, which is about 10 times the power-broadened linewidth.

[1]The laser beams used for optical pumping and state detection are identical to the red MOT beams oriented vertically upwards and have an intensity of 10 μW/cm^2 and 150 μW/cm^2, respectively. The other five MOT beams are blocked by shutters.

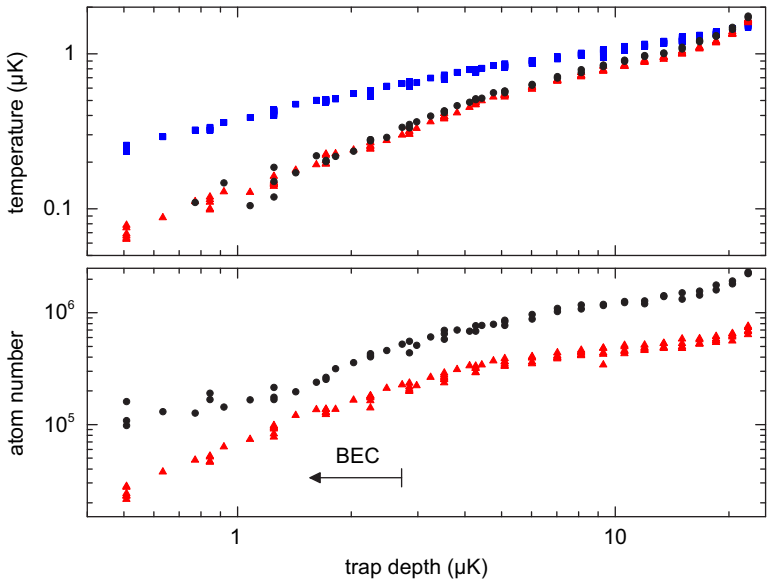

Figure 5.2: Temperature and atom number in dependence of the trap depth during evaporative cooling. The upper panel shows the temperature of ^{84}Sr (black circles) and the temperature (red triangles) and Fermi temperature (blue squares) of ^{87}Sr. The lower panel shows the atom number of ^{84}Sr (black circles) and ^{87}Sr (red triangles). A BEC forms below a trap depth of 2.8 μK (arrow).

Atoms in the $m_F \neq 9/2$ states are therefore not levitated. Figure 5.1 (b) shows the atoms in the $m_F = 9/2$ state separated from the other atoms after time of flight, with and without optical pumping. From these images we conclude that more than 95% of the atoms are in the same spin state.

After 500 ms plain evaporation, the mixture thermalizes at 1.7 μK with 2.2×10^6 ^{84}Sr atoms at a phase-space density of 0.3 and 7×10^5 ^{87}Sr atoms at $T/T_F = 1.2$, already close to quantum degeneracy. At this point, the elastic collision rate of bosons with fermions is $\sim 170\,\mathrm{s}^{-1}$. The collision rate between bosons of $\sim 1600\,\mathrm{s}^{-1}$ is much higher because of the larger scattering length ($a_{84,84} = 123\,a_0$ versus $a_{84,87} = -56\,a_0$ [Ste08, Mar08]) and because of the factor of two resulting from Bose enhancement. These conditions are well suited for evaporative cooling to quantum degeneracy. To force evaporation, we reduce the power of both dipole trap beams with 1/e time constants of 5.7 s for the horizontal and 9.0 s for the vertical beam, starting directly after optical pumping. To characterize the performance of evaporative cooling and ultimately detect quantum degeneracy, we stop forced evaporation after a varying time between 0 and 8 s, wait 500 ms to ensure thermalization of the sample, and take absorption images after a time of flight t_{TOF} of 10 ms [2]. This expansion time is sufficiently large for the observed density distribution to correspond to the *in-situ* momentum distribution, even for the lowest trap frequencies of 85 Hz examined. We determine the atom number and temperature using Bose-Einstein or Fermi-Dirac distribution fits. The results

[2]The absorption images are taken using a cycling transition. Images of ^{84}Sr and ^{87}Sr are taken in consecutive runs of the experiment.

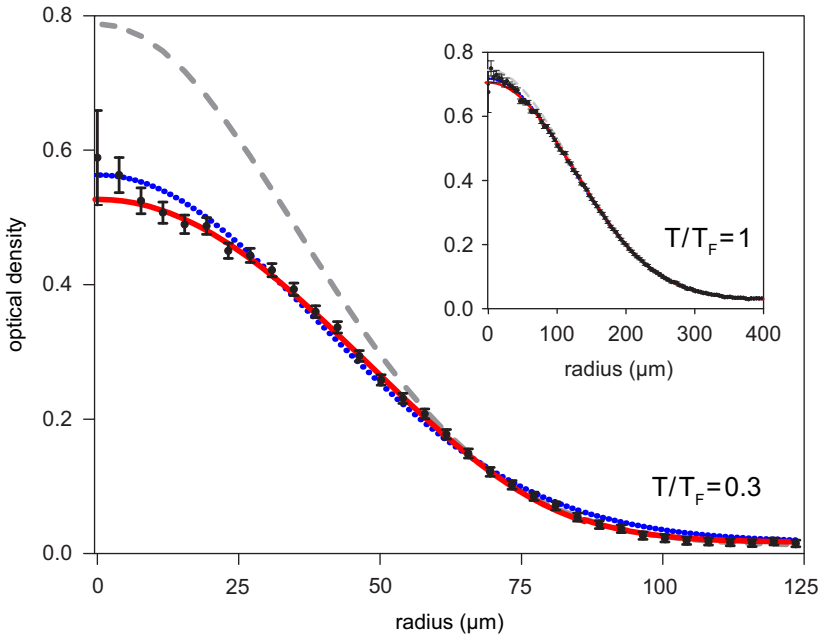

Figure 5.3: Azimuthally averaged density distributions of a degenerate Fermi gas at $T/T_F = 0.3$ and a thermal fermionic cloud at $T/T_F = 1$ (inset) after 10 ms of free expansion. Fermi-Dirac distributions (solid red lines) fit both measurements well. The quantum degenerate sample deviates in shape from a Gaussian (dotted blue line). The difference between the degenerate and thermal samples becomes even more evident when fitting a Gaussian to only the outer wings, outside the disk with radius $\sqrt{2}w$ (dashed line), where w is the 1/e width of a Gaussian fit to the full distribution. For $T/T_F = 1$ (inset), the difference between the three fits is barely visible.

show that both bosons and fermions are evaporated and are well thermalized with each other (Fig. 5.2). To demonstrate the importance of interisotope collisions for the cooling of spin-polarized ^{87}Sr, we perform the same evaporative cooling sequence in absence of ^{84}Sr. The fermions are lost faster than in presence of bosons and do not reach as low temperatures. In addition, the momentum distributions are in this case inconsistent with Fermi-Dirac distributions, which is expected since the sample cannot thermalize. During the evaporation of both isotopes, the BEC phase transition is detected after 6 s by the appearance of a bimodal distribution [Ste09, Mar09a]. At that moment 5×10^5 bosons remain at a temperature of 300 nK.

Fermionic degeneracy manifests itself in subtle changes of the momentum distribution. Pauli blocking limits the occupation of low momentum states to one fermion per state, leading to a flatter and wider momentum distribution than expected classically. This change in shape is evident in the azimuthally averaged time-of-flight density distributions shown in Fig. 5.3. The inset shows a thermal cloud at the beginning of evaporation and the main figure a colder sample after 7.6 s of evaporation. The momentum distribution after evaporation is very well described by a Fermi-Dirac distribution, but not by Gaussian fits.

To quantify the degeneracy, we determine the ratio of the temperature T and the Fermi

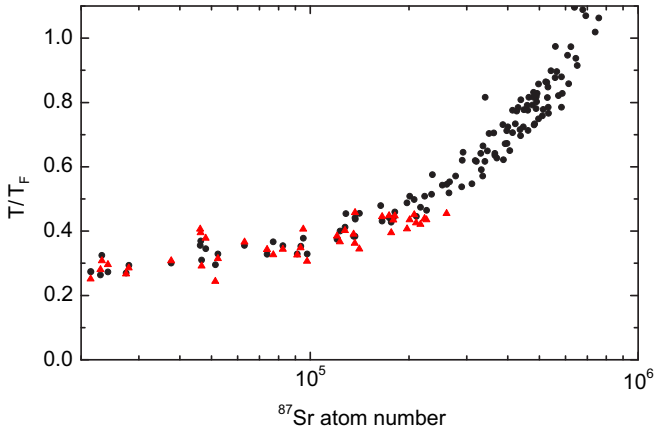

Figure 5.4: T/T_F in dependence of the ^{87}Sr atom number during evaporative cooling. T/T_F is determined from Fermi fits to absorption images. Two independent fit parameters are used to calculate T/T_F, the width of the fitted function (filled circles) and the fugacity (triangles). The statistical error visible in the scatter of the data is larger than systematic uncertainties.

temperature T_F from fits to absorption images. For a harmonic potential and a time-of-flight larger than the trap oscillation periods, the spatially once integrated Fermi-Dirac density distribution can be closely approximated by [DeM01a]

$$n(\rho) = A\,\mathrm{Li}_2\left(-\zeta e^{-\frac{\rho^2}{2\sigma^2}}\right), \tag{5.1}$$

where Li_n is the n^{th}-order polylogarithm, ρ the radial displacement from the center of the atom cloud, σ the width of the cloud, and ζ the fugacity. A, ζ and σ are fit parameters. We use two independent methods to determine T/T_F. The first one rests upon the size of the cloud σ, which is related to the temperature by $T = m\sigma^2/k_B t_{\mathrm{TOF}}^2$. T_F is calculated from the atom number N and the average trap frequency $\overline{f}$ using $T_F = (6N)^{1/3}\hbar 2\pi\overline{f}/k_B$. The second method is based on the examination of the shape of the distribution, characterized by the fugacity ζ. T/T_F is directly related to the fugacity through the relation $T/T_F = [-6\mathrm{Li}_3(-\zeta)]^{-1/3}$. The second method is only applied for fugacities greater than 2, corresponding to $T/T_F \leq 0.46$. Using numerical simulations, we verified that mean field effects between the BEC and the degenerate Fermi gas, as well as the increased anharmonicities of the trapping potential in the vertical direction due to gravitational sagging, do not influence the determination of T/T_F under our conditions. Figure 5.4 shows T/T_F in dependence of the ^{87}Sr atom number using the same data set as for Fig. 5.2. Both methods to determine T/T_F agree well. With 10^5 ^{87}Sr atoms left we obtain $T/T_F = 0.35(5)$ with $T = 160(15)\,\mathrm{nK}$ and $T_F = 450(20)\,\mathrm{nK}$. The lowest degeneracy, $T/T_F = 0.30(5)$, is reached with 2×10^4 fermions at $T = 65(5)\,\mathrm{nK}$. The efficiency of evaporation is reduced in the quantum degenerate regime because of Pauli blocking [DeM01b] and the superfluidity of the BEC [Tim98, Chi00]. This reduction, together with heating and loss, limits the obtainable fermionic degeneracy.

For the deepest evaporation examined, the potential depth corresponds only to two times the Fermi energy. The shallow potential can lead to increased evaporation of fermions in

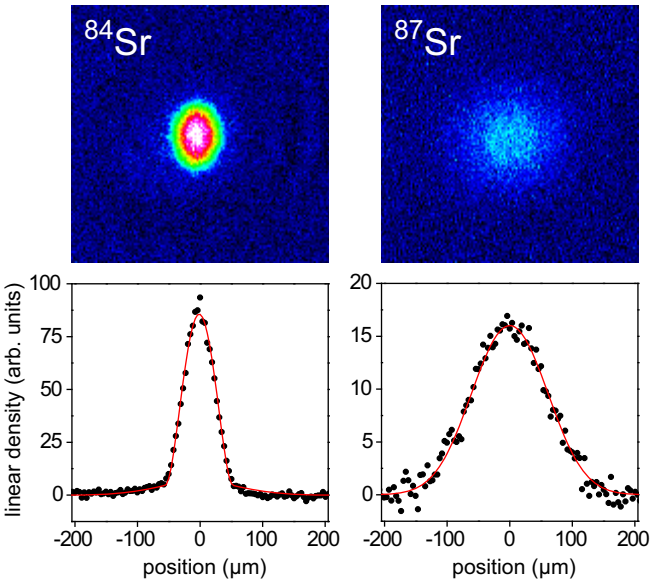

Figure 5.5: Time-of-flight absorption images of a nearly pure ^{84}Sr BEC and a ^{87}Sr Fermi gas at $T/T_F = 0.45$ after 15 ms of expansion.

the $m_F = 9/2$ state compared to bosons and fermions in other spin states. This preferential evaporation can reduce the polarization of the fermionic sample. We verified that more than 90% of the fermions occupy the $m_F = 9/2$ state even at the end of evaporation.

Our degenerate Fermi sea is accompanied by a BEC containing 10^5 atoms. Figure 5.5 shows time-of-flight absorption images of a BEC and a Fermi gas with $T/T_F = 0.45$, taken 15 ms after release from a cigar-shaped trap with trap frequency ratio of 1.5. The BEC expansion is mean-field driven and leads to an inverted aspect ratio. By contrast, the ^{87}Sr image shows the isotropic momentum distribution of the fermions.

In conclusion, we have created a double-degenerate Bose-Fermi mixture with the fermions prepared in a single spin state. In the future, we plan to implement optical pumping and state detection methods for the controlled preparation of fermions in multiple internal states. Loading the mixture into an optical lattice and further cooling of the sample are the next steps towards the exploration of the $SU(10)$ symmetric Hubbard model, and quantum computation and simulation with strontium.

We thank Andrew Daley and Sebastian Diehl for stimulating discussions on the prospects of strontium Bose-Fermi mixtures for future experiments.

Chapter 6

Publication: Bose-Einstein condensation of ^{86}Sr†

Phys. Rev. A **82**, 041602 (2010)

Simon Stellmer,[1,2] Meng Khoon Tey,[1] Rudolf Grimm,[1,2] and Florian Schreck,[1]

[1] *Institut für Quantenoptik und Quanteninformation, Österreichische Akademie der Wissenschaften, 6020 Innsbruck, Austria*
[2] *Institut für Experimentalphysik, Universität Innsbruck, 6020 Innsbruck, Austria*

We report on the attainment of Bose-Einstein condensation of ^{86}Sr. This isotope has a scattering length of about $+800\,a_0$ and thus suffers from fast three-body losses. To avoid detrimental atom loss, evaporative cooling is performed at low densities around $3 \times 10^{12}\,\mathrm{cm}^{-3}$ in a large volume optical dipole trap. We obtain almost pure condensates of 5×10^3 atoms.

Quantum degenerate gases of atoms with two valence electrons are an exciting field of research. The electronic structure of these atoms is the basis for applications like ultraprecise optical clocks [Ido03, Lud08b, Lem09b, Ste04, Lem09a, Hon05, Koh09]. Quantum degenerate samples open new possibilities such as the study of unique quantum many-body phenomena [Her09, Caz09, Gor10, Ger10] and novel schemes of quantum computation [Dal08, Gor09, Rei09, Sto08]. They are also an ideal starting point for the creation of molecules of two-electron atoms [Ciu04, Koc08] and molecules of two-electron atoms with alkali atoms [Zuc10, Gué10], which have applications in precision measurement [Kot09] or quantum simulations with spin-dependent anisotropic long range interactions [Mic06]. The first two-electron atom cooled to quantum degeneracy was ytterbium [Tak03, Fuk07a, Fuk09b], followed by calcium [Kra09] and strontium last year. Quantum degenerate samples of bosonic ^{84}Sr and ^{88}Sr [Ste09, Mar09a, Mic10], as well as of fermionic ^{87}Sr [DeS10, Tey10] have been created, but Bose-Einstein condensation (BEC) of ^{86}Sr has so far been elusive [Fer06a].

†The author developed the novel dipole trap design, improved the experimental setup, acquired the data, and contributed to the writing of the manuscript.

The success of evaporative cooling with the goal to reach quantum degeneracy depends largely on the ratio of elastic to inelastic collisions of the atomic species used [Ket96]. The four isotopes of strontium differ significantly in this respect. Despite its low natural abundance of 0.56%, ^{84}Sr was the first to be Bose condensed as it offers ideal scattering properties [Ste09, Mar09a]. ^{88}Sr, which has a scattering length close to zero, and spin-polarized fermionic ^{87}Sr barely collide at ultralow temperatures. They could only be cooled to quantum degeneracy using mixtures with other isotopes or spin states [Mic10, DeS10, Tey10]. ^{86}Sr poses the opposite challenge: its large scattering length of $+800\,a_0$ [Ste10a] leads to a large three-body loss rate constant [Fer06a]. Previously reported conditions of ^{86}Sr in a dipole trap led to an elastic to inelastic collision ratio that was insufficient for evaporative cooling [Fer06a]. Magnetic tuning of the scattering properties, as was an essential ingredient to circumvent similar difficulties on the way to BEC of cesium [Web03], is not available in alkaline-earth elements. Another approach to increase the ratio of elastic two-body collisions and inelastic three-body collisions is to lower the density. This approach was important for BEC of ^{40}Ca, which is also an isotope with large scattering length [Kra09], as well as for BEC of cesium.

In this Rapid Communication, we show that it is indeed possible to create ^{86}Sr BECs by performing evaporation at comparatively low densities around $3 \times 10^{12}\,\mathrm{cm}^{-3}$. To obtain sizeable atom numbers at these low densities, we implement a large volume optical dipole trap.

Our experimental procedure initially follows the one used for Bose condensation of ^{84}Sr [Ste09]. Zeeman-slowed atoms are captured and cooled by a "blue" magneto-optical trap (MOT) operating on the $5s^2\,{}^1S_0 - 5s5p\,{}^1P_1$ transition at a wavelength of 461 nm. A weak leak of the excited state of the cooling cycle continuously populates the $5s5p\,{}^3P_2$ metastable state. Weak-field seeking atoms in this state can be trapped in a magnetic trap formed by the quadrupole magnetic field used for the MOT. Metastable state atoms are accumulated in the magnetic trap for 1 s. Further cooling and density increase is achieved by operating a "red MOT" on the 7.4 kHz linewidth ${}^1S_0 - {}^3P_1$ intercombination line at 689 nm. To increase the capture velocity of the red MOT, we frequency modulate the light, producing sidebands, which cover a detuning range from a few ten kHz to a few MHz to the red of the transition. To load the red MOT, the metastable-state atoms in the magnetic trap are optically pumped to the ${}^1S_0$ ground state using the $5s5p\,{}^3P_2 - 5s5d\,{}^3D_2$ transition at 497 nm. After loading, the MOT is compressed by reducing the MOT beam intensity and ramping off the frequency modulation, resulting in a colder and denser sample. At this point the MOT contains 2×10^7 atoms at a temperature of $1\,\mu$K.

The following evaporative cooling stage significantly differs from our previous experiments on ^{84}Sr. The atoms are transferred into a crossed-beam optical dipole trap, which is much larger than the one used before. The trapping geometry consists of a horizontal and a nearly vertical beam, derived from a broadband ytterbium fiber laser operating at 1075 nm. The horizontal beam has an elliptic beam shape with a horizontal waist of $300\,\mu$m and a vertical waist of $33\,\mu$m. The vertical beam is circular with a waist of $290\,\mu$m and is used to provide additional confinement along the weak direction of the horizontal beam towards the end of evaporation. Initially, only the horizontal dipole trap beam is used and set to a power of 2 W. The resulting trap is oblate with horizontal trap oscillation frequencies of 3 Hz and

30 Hz, a vertical trap oscillation frequency of 260 Hz, and a potential depth of 3.7 μK, taking into account gravitational sagging. This oblate trap geometry combines the requirement of strong enough confinement against gravity in the vertical direction with the requirement of a large trap volume.

For optimum loading of the dipole trap, we adjust the intensity and detuning of the red MOT beams before switching them off. After 1 s of plain evaporation, 2.5×10^6 atoms at a temperature of 500 nK remain in the trap. The peak density is $3 \times 10^{12}\,\mathrm{cm}^{-3}$ and the peak phase-space density is 0.05. Even at the temperature of 500 nK, unitary limitation leads to a reduction of the thermally averaged elastic scattering cross section by a factor of two compared to the zero temperature value. The elastic collision rate is $380\,\mathrm{s}^{-1}$.

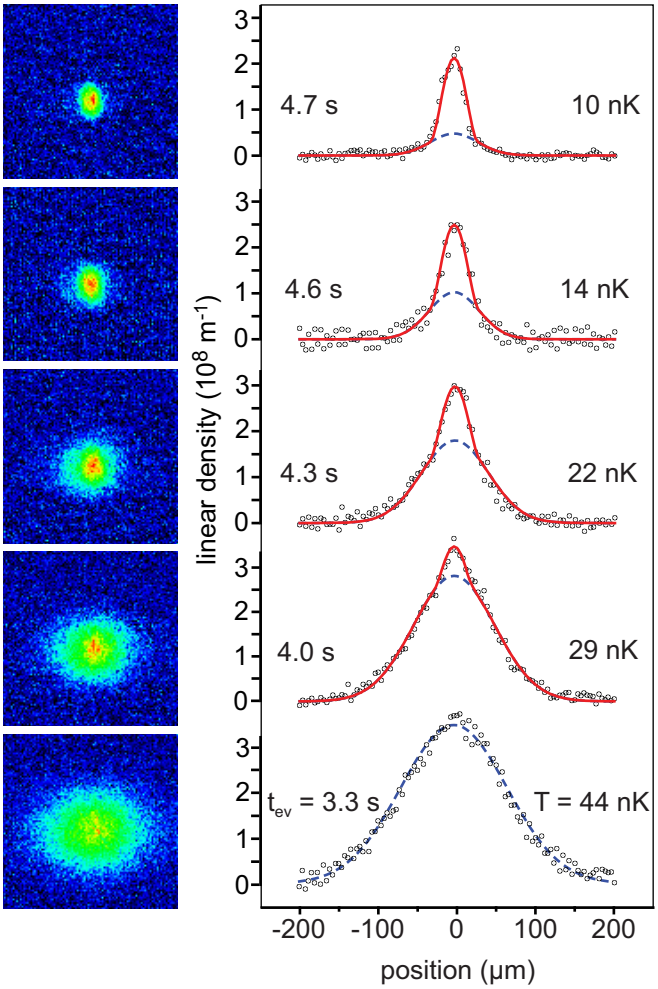

Figure 6.1: Absorption images and integrated density profiles showing the BEC phase transition for different times t_{ev} of the evaporative cooling ramp. The images are taken in the horizontal direction at 45° to the horizontal trap axes, 25 ms after release from the trap. The field of view is 400 μm by 400 μm. The solid line represents a fit with a bimodal distribution, while the dashed line shows the Gaussian-shaped thermal part, from which the given temperatures are derived.

After the plain evaporation stage, forced evaporation is performed over 4.8 s. The power of the horizontal dipole trap beam is reduced nearly exponentially to 740 mW, with a longer time constant during the last 1.5 s. During the first 2.3 s of forced evaporation, the vertical dipole trap beam is increased to a power of 0.5 W, at which it stays for the rest of the evaporation sequence. The vertical beam increases the confinement along the weak direction to 5 Hz and does not provide any confinement along the vertical direction. The potential depth of the vertical beam in the radial directions is 200 nK. During evaporation atoms escape the trap mainly downwards by leaving the trap over the potential barrier formed by the horizontal beam and gravity. It is beneficial for evaporation that the vertical trap oscillation frequency remains higher than the elastic collision rate, so that high energy atoms produced by collisions can quickly move out of the trap. During evaporation the peak density slightly drops to $10^{12}\,\mathrm{cm}^{-3}$ and the elastic collision rate drops to $70\,\mathrm{s}^{-1}$ before condensation. At this point the temperature is ~ 30 nK and the thermally averaged scattering cross section is very close to the zero-temperature value.

The phase transition from a thermal cloud to a BEC becomes evident in the appearance of a bimodal distribution, as clearly visible in time-of-flight absorption images and in the corresponding linear density profiles shown in Fig. 6.1. At higher temperature the distribution is thermal, exhibiting a Gaussian shape. Cooling below the critical temperature T_c leads to the appearance of an additional, narrower and denser, elliptically shaped component: the BEC. The phase transition occurs after 4 s of evaporative cooling, when the power of the horizontal beam is 820 mW. At this point, the horizontal trap oscillation frequencies are 5 Hz and 18 Hz, the vertical trap oscillation frequency is $f_{\mathrm{vert}} = 115$ Hz and the trap depth is about 110 nK, taking into account gravitational sagging. Note that despite the large scattering length, we are not in the collisionally hydrodynamic regime since the elastic scattering rate is only one tenth of $2\pi f_{\mathrm{vert}}$ [Kag97].

In order to analyze the phase-transition precisely, we fit bimodal distributions to the time-of-flight absorption images. The bimodal distributions consist of a Gaussian for the thermal part of the cloud and an inverted paraboloid integrated along one direction for the BEC. We extract the amount of condensed atoms N_0, the total amount of atoms N and the temperature T of the sample from the fits[1]. The condensate fraction N_0/N as a function of temperature, scaled by the transition temperature of a non-interacting gas in the thermodynamic limit T_c^0, is shown in Fig. 6.2. From this data we extract a critical temperature of $T_c/T_c^0 = 0.9(1)$, where the error is dominated by uncertainties in T_c^0 resulting from the uncertainty in the atom number of about 25%. The phase-transition occurs at a temperature of 30(2) nK with $3.7 \pm 1 \times 10^4$ atoms. The theoretically expected critical temperature T_c is reduced by 14% compared to T_c^0 by interaction effects. Finite-size effects add a minor reduction of 1%. These effects give a theoretically expected transition temperature of $T_c = 0.85\,T_c^0$ [Gio96], which is within the uncertainty of our data.

After 4.8 s of evaporation, a nearly pure BEC of 5×10^3 atoms is produced in a trap with

[1]To determine if a BEC is present, we also fit single Gaussian distributions to the images. If the fit residue of such a fit is comparable to that of a bimodal fit, we consider the distribution as purely thermal and extract temperature and atom number from the single Gaussian fit, otherwise from the bimodal fit. The temperature is determined from the size of the Gaussian component in the vertical direction, in which the cloud has expanded far enough beyond its initial size to show the momentum distribution.

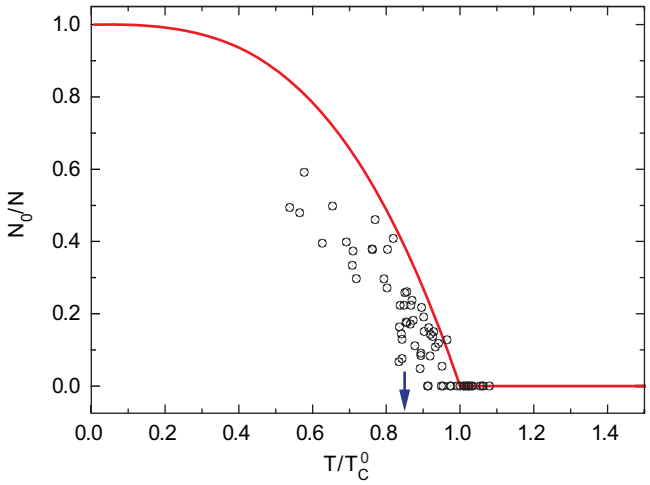

Figure 6.2: The condensate fraction N_0/N as a function of the temperature scaled by the critical temperature of an ideal gas in the thermodynamic limit T_c^0. The line shows the behavior expected for an ideal gas. The arrow indicates the expected transition temperature $T_c = 0.85\,T_c^0$ when interactions and minor contributions from finite size effects are taken into account.

oscillation frequencies of 5 Hz and 16 Hz in the horizontal plane and 70 Hz in the vertical direction. The peak-density of the BEC is $3 \times 10^{12}\,\mathrm{cm}^{-3}$ and the chemical potential is 7 nK. The BEC has an oblate shape with calculated *in-situ* Thomas-Fermi radii of 40 μm and 12 μm in the horizontal plane and 3 μm in the vertical direction. After release from the trap, the BEC undergoes a mean-field driven expansion, with the strongest expansion in the vertical direction, resulting in an inversion of ellipticity as shown on the absorption images in Fig. 6.3.

We extract an upper bound for the three-body loss rate constant from the lifetime measurement of a nearly pure BEC. The initial atom loss rate per atom from the BEC is $N_0^{-1} dN_0/dt = 3(1)\,\mathrm{s}^{-1}$. This value is determined from the initial slope of an exponential fit to 500 ms of decay data. Assuming only three-body loss, the loss of atoms is described by $dN_0/dt = -(1/6)K_3 \int n_0^3 dV$, where n_0 is the density distribution of the BEC and the factor 1/6 takes into account the difference of three-body correlations of a thermal gas and a BEC. The resulting upper bound for the three-body loss rate constant is $K_3 = 6(3) \times 10^{-24}\,\mathrm{cm}^6/\mathrm{s}$. This value is about six times higher than the value measured by Ferrari *et al.* [Fer06a]. Moreover it is an order of magnitude higher than the maximally expected loss rate constant, which is $K_3 = 210\hbar a^4/m = 5 \times 10^{-25}\,\mathrm{cm}^6/\mathrm{s}$, assuming that three atoms are lost during each three-body loss event [Fed96b, Bed00]. Here a is the scattering length and m is the mass of ^{86}Sr. Several explanations are possible for the unusually large measured value. More than three atoms might be lost per three-body loss event resulting from secondary collisions, possibly augmented by an enhanced atom-dimer scattering cross section [Zac09, Pol09]. Evaporation of atoms heated by technical noise of the dipole trap is an example for an explanation other than three-body loss. Our present data is insufficient to distinguish these different loss scenarios and further studies are needed to resolve this issue.

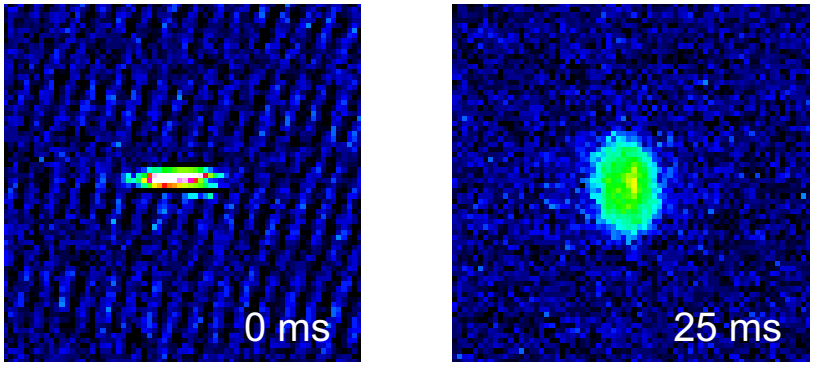

Figure 6.3: Inversion of aspect ratio during the expansion of a pure BEC. The images (fields of view 300 μm $\times$ 300 μm) are taken along the horizontal direction and show the BEC in the trap (left) and after 25 ms free expansion (right).

In conclusion, we have produced a Bose-Einstein condensate of ^{86}Sr containing 5×10^3 atoms. With this achievement all stable isotopes of strontium have been cooled to quantum degeneracy. The large scattering length of ^{86}Sr leads to a very large three-body loss rate coefficient, which poses a challenge for evaporative cooling. We have shown that performing evaporation at low density in a large volume trap is a possible way to overcome this problem. The BEC of ^{86}Sr enriches the possibilities opened up by strontium quantum gases. The large scattering length of ^{86}Sr originates from a weakly bound state in the molecular potential. This state will influence the properties of optical Feshbach resonances [Ciu05, Eno08]. The BEC of ^{86}Sr increases the options for quantum degenerate mixtures of different Sr isotopes or of mixtures of Sr with other elements. This wider choice can be important, for example in the search for magnetic Feshbach resonance in Sr-alkali mixtures suitable for molecule creation [Zuc10].

We thank P. S. Julienne for fruitful discussions. We gratefully acknowledge support by the Austrian Ministry of Science and Research (BMWF) and the Austrian Science Fund (FWF) in the form of a START grant under project number Y507-N20. We also gratefully acknowledge support by the European Commission under project number 250072 iSENSE.

Chapter 7

Publication: Detection and manipulation of nuclear spin states in fermionic strontium[†]

Phys. Rev. A **84**, 043611 (2011)

Simon Stellmer,[1,2] Rudolf Grimm,[1,2] and Florian Schreck,[1]

[1] *Institut für Quantenoptik und Quanteninformation, Österreichische Akademie der Wissenschaften, 6020 Innsbruck, Austria*
[2] *Institut für Experimentalphysik, Universität Innsbruck, 6020 Innsbruck, Austria*

Fermionic ^{87}Sr has a nuclear spin of $I = 9/2$, higher than any other element with similar electronic structure. This large nuclear spin has many applications in quantum simulation and computation, for which preparation and detection of the spin state are requirements. For an ultracold ^{87}Sr cloud, we show two complementary methods to characterize the spin-state mixture: optical Stern-Gerlach state separation and state-selective absorption imaging. We use these methods to optimize the preparation of a variety of spin-state mixtures by optical pumping and to measure an upper bound of the ^{87}Sr spin relaxation rate.

7.1 Introduction

Fermions with two valence electrons, like ^{43}Ca, ^{87}Sr, ^{171}Yb, and ^{173}Yb, have a rich internal state structure, which is at the heart of recent proposals for quantum simulation and computation [Caz09, Gor10, Wu03, Wu06, FF10, Her09, Xu10, Hun11, Ger10, Coo11b, Bér11, Gór11a, Dal08, Gor09]. Unlike bosonic isotopes of these elements, the fermions

[†]The author performed the necessary upgrade of the machine, mainly involving additional laser systems and B-field coils. He invented the bi-chromatic OSG and introduced the enhancement by an applied B-field, and he and F. S. explored the narrow-line imaging. He acquired the data and contributed to the writing of the manuscript. The numerical simulations were performed by F. S.

have a nuclear spin, which decouples from the electronic degrees of freedom in the $^1S_0$ ground state and the $^3P_0$ metastable state. This gives rise to a SU(N) spin symmetry, where N is the number of nuclear spin states, which can be as high as 10 for ^{87}Sr [Caz09, Gor10]. Rich quantum phases have been predicted to exist in such Fermi systems [Wu03, Wu06, Caz09, FF10, Her09, Gor10, Xu10, Hun11]. The nuclear spin is also essential for the implementation of artificial non-abelian gauge fields [Ger10, Bér11, Gór11a]. Furthermore it can be used to robustly store quantum information, which can be manipulated using the electronic structure [Dal08, Gor09]. After the recent attainment of quantum degeneracy in ^{171,173}Yb [Fuk07b, Tai10] and ^{87}Sr [DeS10, Tey10], these ideas are coming closer to realization.

Essential tools for quantum simulation and computation with these degenerate gases are the detection and manipulation of the spin-state mixture. Several alkaline-earth spin-state detection schemes were already demonstrated. The number of atoms in the highest m_F state was determined by selectively cooling [Muk03] or levitating [Tey10] atoms in this state. The number of atoms in an arbitrary m_F state was determined using state-selective shelving of atoms in a metastable state, which requires a "clock"-transition laser [Boy07c]. Recording the full m_F-state distribution with this method is possible, but needs one experimental run per state. Determination of the m_F-state distribution in only two experimental runs was recently shown for quantum-degenerate Yb gases, using optical Stern-Gerlach (OSG) separation [Tai10].

In this Article, we first show two nuclear spin-state detection schemes for ^{87}Sr that have advantages over the previously used schemes. In Sec. 7.2, we present an adaptation and extension of the OSG separation scheme of [Tai10], which in our implementation is able to resolve all ten nuclear spin-states of Sr in a single experimental run. In Sec. 7.3, we describe state-selective absorption imaging using the intercombination line of Sr. Unlike OSG separation, this method gives spatial information about the spin-state distribution and is also applicable to samples before evaporative cooling. In Sec. 7.4, we demonstrate the preparation of a desired spin-state mixture by optical pumping, using spin-state detection to optimize the optical pumping procedure. In Sec. 7.5, we determine an upper limit of the ^{87}Sr spin-relaxation rate, using our spin-state preparation and detection methods.

7.2 Optical Stern-Gerlach separation

Here, we describe the operation principle of optical Stern-Gerlach (OSG) separation (Sec. 7.2) and our experimental implementation (Sec. 7.2). In Sec. 7.2, we describe a simulation of the OSG process. In Sec. 7.2 we determine the number of atoms in each spin state.

Operation principle

The Stern-Gerlach technique separates atoms in different internal states by applying a state-dependent force and letting the atomic density distribution evolve under this force [Ger22]. The implementation of this technique for alkali atoms is simple. Their single valence electron provides them with a m_F-state dependent magnetic moment that, for easily achievable

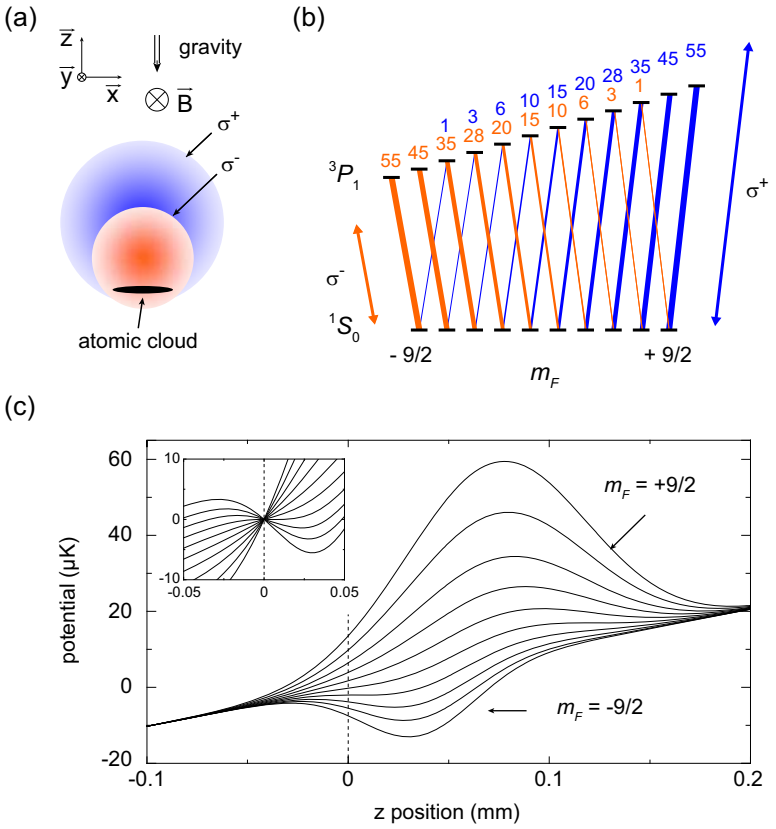

Figure 7.1: Principle of OSG separation. (a) σ^+- and σ^--polarized laser beams propagating in the y-direction create dipole forces on an atomic cloud that is located on the slopes of the Gaussian beams. (b) The laser beams are tuned close to the $^1S_0(F = 9/2) - {}^3P_1(F' = 11/2)$ intercombination line, creating attractive (σ^- beam) or repulsive (σ^+ beam) dipole potentials. Each m_F state experiences a different potential because of the varying line strength of the respective transition. (c) The potentials resulting from dipole potentials and the gravitational potential. The dashed line marks the initial position of the atoms. The inset shows the relevant region of the potentials, offset shifted to coincide at the position of the atoms, which clearly shows the different gradient on each m_F state.

magnetic field gradients, results in m_F-state dependent forces sufficient for state separation [SK98a]. By contrast, atoms with two valence electrons possess only a weak, nuclear magnetic moment in the electronic ground state, which would require the application of impractically steep magnetic field gradients. An alternative is OSG separation, where a state dependent dipole force is used. OSG separation was first shown for a beam of metastable helium [Sle92], where orthogonal dressed states of the atoms were separated by a resonant laser field gradient. The case of interest here, OSG m_F-state separation, was recently realized for a quantum degenerate gas of Yb, by using m_F-state dependent dipole forces [Tai10].

We first explain the basic operation principle of Sr OSG separation before discussing our experimental implementation. The experimental situation is shown in Fig. 7.1(a). An ultracold cloud of ^{87}Sr atoms in a mixture of m_F states is released from an optical dipole

trap. The m_F-state dependent force is the dipole force of two laser beams propagating in the plane of the pancake-shaped cloud, one polarized σ^+, the other σ^-. The diameter of these OSG laser beams is on the order of the diameter of the cloud in the x-direction. The beams are displaced vertically by about half a beam radius to produce a force in the z-direction on the atoms. To create a m_F-state dependent force, the OSG beams are tuned close to the ${}^1S_0(F = 9/2) - {}^3P_1(F' = 11/2)$ intercombination line (wavelength 689 nm, linewidth 7.4 kHz), so that this line gives the dominant contribution to the dipole force. A guiding magnetic field is applied in the direction of the laser beams such that the beams couple only to σ^+ or σ^- transitions, respectively. The line strength of these transitions varies greatly with the m_F state [Met99], see Fig. 7.1(b), resulting in different forces on the states. For ^{173}Yb, this variation, together with a beneficial summation of dipole forces from transitions to different ${}^3P_1$ hyperfine states, was sufficient to separate four of the six m_F states using just one OSG beam [Tai10]. The remaining two m_F states could be analyzed by repeating the experiment with opposite circular polarization of the OSG beam.

Strontium, which has nearly twice as many nuclear spin states, requires an improved OSG technique to separate the states. The improvement consists of applying two OSG beams with opposite circular polarization at the same time. The σ^+-polarized beam produces dipole forces mainly on the positive m_F states, the σ^- beam mainly on the negative m_F states. By positioning the beams in the appropriate way (see below), the forces point in opposite directions and all m_F states can be separated in a single experimental run. A second improvement is to enhance the difference in the dipole forces on neighboring m_F states by tuning already strong transitions closer to the OSG beam frequency using a magnetic field, which splits the excited state $m_{F'}$ states in energy. For our settings, the difference in forces on neighboring high $|m_F|$ states is enhanced by up to 25%, which helps to separate those states. This enhancement scheme requires the σ^+-polarized OSG beam to be tuned to the blue of the resonance, whereas the σ^- beam has to be tuned to the red of the resonance; see Fig. 7.1(b). Both beams are centered above the atomic cloud so that the repulsive blue detuned beam produces a force pointing downwards, whereas the attractive red detuned beam produces a force pointing upwards.

Experimental demonstration

We demonstrate OSG separation of a cloud of 4.5×10^4 ^{87}Sr atoms in a mixture of m_F states. To prepare the cloud, Zeeman slowed ^{87}Sr atoms are laser cooled in two stages, first in a "blue" magneto-optical trap (MOT) on the broad-linewidth ${}^1S_0 - {}^1P_1$ transition, then in a "red" MOT on the narrow-linewidth ${}^1S_0 - {}^3P_1$ transition [DeS10, Tey10]. Next, the atoms are transferred to a pancake-shaped optical dipole trap with strong confinement in the vertical direction. The sample is evaporatively cooled over seven seconds. At the end of evaporation the trap oscillation frequencies are $f_x = 19$ Hz, $f_y = 11$ Hz, and $f_z = 85$ Hz, where the coordinate system is defined in Fig. 7.1(a). The collision rate at this stage is only $1\,\mathrm{s}^{-1}$, which is insufficient for complete thermalization. Since atoms are evaporated mainly downwards, along the z-direction, the sample is not in cross-dimensional thermal equilibrium, having a temperature of 25 nK in the z-direction and twice that value in the xy-plane. The sample is non-degenerate and the $1/e$-widths of the Gaussian density distribution

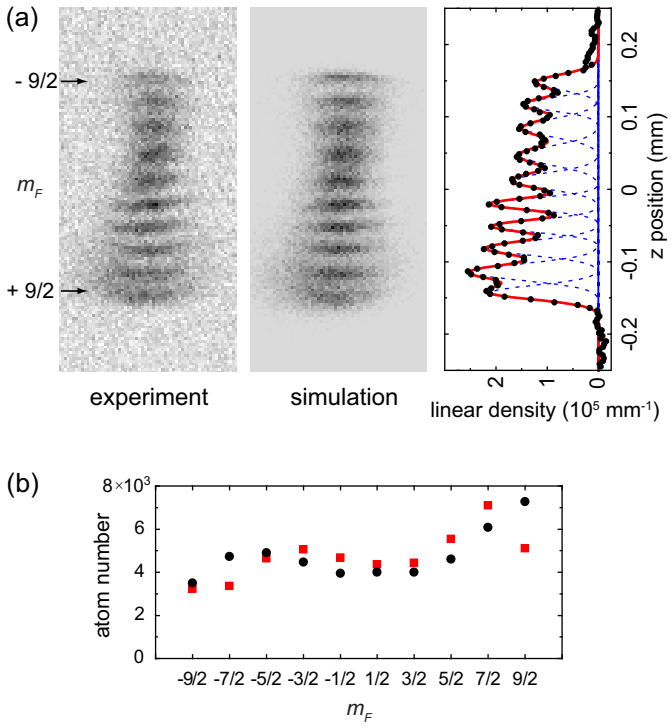

Figure 7.2: OSG separation of the ten ^{87}Sr nuclear spin states. (a) Atomic density distribution after OSG separation integrated over the $((\hat{\mathbf{x}} + \hat{\mathbf{y}})$-direction obtained in experiment and simulation. On the right, the density distribution of the experiment integrated along the x- and y-directions is shown together with a fit consisting of ten Gaussian distributions. (b) Atom number distribution determined from the area of the Gaussian distributions (red squares) and the fit of the simulation to the experiment (black circles).

are $w_x = 55\,\mu$m, $w_y = 85\,\mu$m, and $w_z = 7\,\mu$m.

The OSG beams propagate along the y-direction. The power of the σ^+ (σ^-) beam is 4 mW (0.5 mW), the waist is $\sim 80\,\mu$m ($\sim 60\,\mu$m), and the beam center is displaced $\sim 70\,\mu$m ($\sim 40\,\mu$m) above the cloud. Both beams create dipole forces of similar magnitude since the reduced power of the σ^- beam compared to the σ^+ beam is partially compensated by its decreased waist. At zero magnetic field, the $\sigma^\pm$ beam is detuned ± 100 MHz from resonance. To increase the difference in dipole potential on neighboring m_F states, a magnetic field of 16 G is applied parallel to the OSG beams, which splits neighboring $^3P_1(F' = 11/2)$ $m_{F'}$ states by 6.1 MHz. With this field applied, the $\sigma^\pm$ beam has a detuning of ± 66.4 MHz to the $^1S_0(F = 9/2, m_F = \pm 9/2) - {}^3P_1(F' = 11/2, m_F = \pm 11/2)$ transition and a detuning of ± 121.4 MHz to the $^1S_0(F = 9/2, m_F = \mp 9/2) - {}^3P_1(F' = 11/2, m_F = \mp 7/2)$ transition, see Fig. 7.1(b).

OSG separation is started by simultaneously releasing the atoms from the dipole trap and switching on the OSG beams. The atoms are accelerated for 1.6 ms by the OSG beams. Then the beams are switched off to avoid oscillations of atoms in the dipole trap formed by the red detuned OSG beam. The atoms freely expand for another 2.3 ms before an absorption image on the $^1S_0 - {}^1P_1$ transition is taken. The result is shown in Fig. 7.2(a). All ten m_F

states are clearly distinguishable from each other.

To obtain a good separation of the m_F states and an even spacing between them, OSG beam waists, the timing of the OSG separation sequence, the applied magnetic field, and the beam positions were optimized. We found that for all other parameters fixed, the position of the OSG beams is critical and has to be aligned to better than 10 μm.

To quantify the separation of the states, we fit ten Gaussian distributions to the density distribution integrated along the x- and y-directions, see Fig. 7.2(a). We obtain a separation of adjacent states between 28 and 38 μm, similar to the $1/e$-widths of the distributions, which are between 24 and 36 μm. The $1/e$-width expected from initial size and temperature after 3.9 ms total expansion time is 19 μm in the z-direction, slightly narrower than the width of the narrowest distributions observed. From the Gaussian fits we also obtain an estimation of the atom number in each state, see Sec. 7.2.

OSG separation works only well for very cold samples. If the temperature is too high, the sample expands too fast and the individual m_F-state distributions cannot be distinguished. For a density minimum to exist between two neighboring m_F-state distributions of Gaussian shape, the $1/e$-widths have to be smaller than $\sqrt{2}$ times the distance between the maxima of the distributions. For our smallest separation of 24 μm, this condition corresponds to samples with a temperature below 100 nK, which can only be obtained by evaporative cooling.

Simulation

We perform a simulation of classical trajectories of atoms to better understand the OSG separation process. The simulation takes into account the dipole potentials of the OSG beams, discrete spontaneous scattering events of OSG beam photons, and gravity. The phase-space distribution of simulated atoms is initialized using the experimentally measured trap frequencies and temperatures. The calculated density distributions are fit to the experimental result using the OSG beam waists and positions and the atom number of each state as fit parameters. The detunings and intensities of the OSG beams and the value of the magnetic field are fixed to the values used in the experiment[1]. The parameters of the σ^+ (σ^-) beam resulting in the best fit are a waist of 90 μm (56 μm) and a displacement of the beam center relative to the atomic cloud's center by 74 μm (35 μm) in the z-direction and by 0 μm (7 μm) in the x-direction. With these parameters, the simulation matches the experimental result well, see Fig. 7.2(a).

We now analyze the OSG separation process in detail using the simulation. The OSG beam potential gradients on atoms in different m_F states are nearly evenly distributed between 47 m/s^2 downwards for the $+9/2$ state and 32 m/s^2 upwards for the $-9/2$ state (see inset of Fig. 7.1(c)), resulting in the nearly evenly spaced m_F-state distribution after OSG separation. About 25% of the atoms spontaneously scatter photons from the OSG beams, which leads to a widening of the individual m_F-state distributions in the z-direction by at most 20%, which only insignificantly reduces our ability to distinguish the m_F states.

Also the $^3P_1$ $F' = 7/2$ and $F' = 9/2$ hyperfine levels contribute noticeably to the dipole forces created by the OSG beams on the low $|m_F|$ states, which at first glance might be

[1] Assuming OSG beam intensities different by $\pm 20\%$ from the measured values did not change the outcome of the simulation significantly after fitting OSG beam waists and positions again.

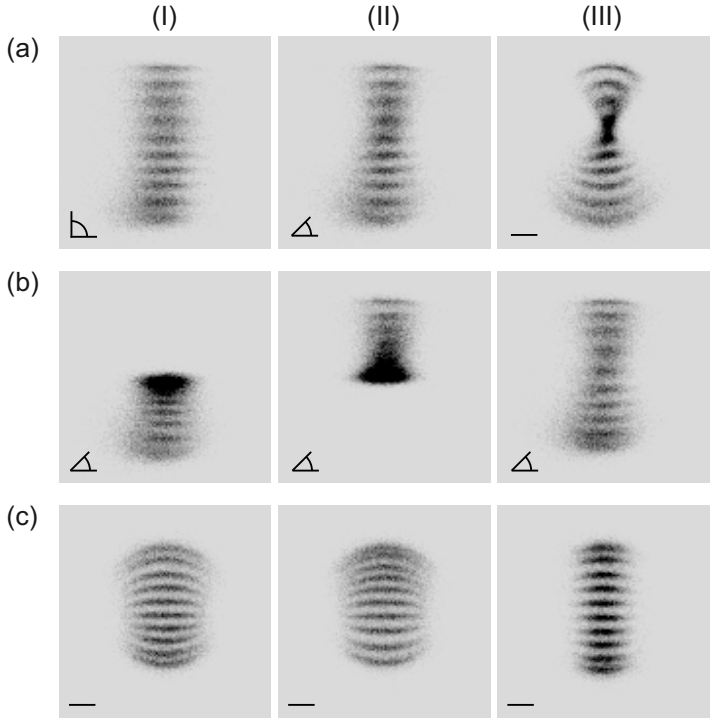

Figure 7.3: Simulated density distributions of atoms after OSG separation. Shown are distributions integrated along x (aI), along the $(\hat{\mathbf{x}}+\hat{\mathbf{y}})$-direction (aII,b), and along y (aIII,c). The angle symbols indicate the angle between the direction of integration and the direction of the OSG beams, the y-direction. (a) The density distribution obtained from a simulation with parameters fitted to the outcome of the experiment, integrated along different directions. The experimental situation corresponds to (aII). (b) Influence of the two OSG beams and the magnetic field on OSG separation. (bI) As (aII), but no σ^- beam. (bII) As (aII), but no σ^+ beam. (bIII) As (aII), but no magnetic field and reduced OSG beam detuning. (c) Alternative scheme of OSG separation using two blue detuned OSG beams and variations of that scheme, see main text.

surprising since the detuning of the OSG beams from those states is more than an order of magnitude larger than the detuning from the $F' = 11/2$ state. The reason is that the dipole forces from the σ^+ and σ^- OSG beams considering only the $F' = 11/2$ hyperfine level nearly compensate each other for low $|m_F|$ states, whereas the dipole forces from both beams considering the other hyperfine levels point into the same direction and in addition are strongest for low $|m_F|$ states. The positions of the low $|m_F|$ states after a simulated OSG separation with and without considering the influence of the $F' = 7/2$ and $F' = 9/2$ levels changes by up to $13\,\mu$m. By contrast, the positions of the $m_F = \pm 9/2$ states are changed by less than $2\,\mu$m. It is not possible to obtain a good fit of the simulation to the experiment if the influence of the ${}^3P_1$ $F' = 7/2$ and $F' = 9/2$ hyperfine levels is neglected.

The shape of the density distribution is analyzed in row (a) of Fig. 7.3. The density distribution is shown as it would appear using absorption imaging along the x- (aI), the $(\hat{\mathbf{x}} + \hat{\mathbf{y}})$- (aII), or the y-direction (aIII). Case (aII) is the one realized in the experiment.

Strong distortions of the spatial distribution of each m_F state compared to a free expansion are visible. They are induced by the finite size of the OSG beams. The blue detuned beam expels high m_F-state atoms onto cylindrical surfaces, whereas the red detuned beam attracts low m_F-state atoms and acts like a focussing lens.

The role of each OSG beam and the magnetic field are demonstrated in row (b) of Fig. 7.3. Shown are the results of simulations with only the blue (bI) or the red (bII) detuned OSG beam present. With only one OSG beam, at best four m_F states can be well separated, illustrating the need of two beams for Sr OSG separation. In simulation (bIII) the magnetic field was set to zero, which removes the energy splitting of the ${}^3P_1(F' = 11/2)$ manifold. To achieve the same acceleration on the $m_F = \pm 9/2$ states as with magnetic field, the detuning of the $\sigma^{\pm}$ OSG beam was set to $\pm 66.4\,\mathrm{MHz}$ from the center of the $F' = 11/2$ manifold. Without magnetic field, the spatial splitting between neighboring high $|m_F|$ states is slightly reduced. To separate these states further than done in the experiment, a larger magnetic field could be used.

The simulation also suggests an alternative OSG separation scheme, which is demonstrated in row (c) of Fig. 7.3, but which we did not check experimentally. Instead of one blue and one red detuned OSG beam, the scheme uses two blue detuned OSG beams of opposite circular polarization. As before, the σ^+ beam is placed above the cloud, acts mainly on the high m_F-state atoms and pushes them downwards. The σ^- beam uses now the same detuning, power, and waist as the σ^+ beam, but is placed below the initial center of the atomic cloud. The location of the two beams in the z-direction is symmetric with respect to the initial position of the atomic cloud. The σ^- beam acts mainly on the negative m_F-state atoms and pushes them upwards. Since this beam is now blue detuned, it does not act similar to a lens as the red detuned σ^- beam used in the experiment and leads to less distortion of the cloud. Three cases of this alternative scheme are shown in row (c), always assuming an even atom number distribution over the m_F states. Case (cI) uses σ^+-beam parameters equivalent to the ones used for the simulations of row (a) and σ^--beam parameters deduced from those as described above. In addition the magnetic field is set to zero. This situation leads to a nearly symmetric separation of positive and negative m_F states, where the symmetry is only slightly broken by gravity. Compared to the situation realized in the experiment, atoms in low m_F states are better separated.

One slight drawback of this scheme is that the application of a magnetic field as used in the experiment will only increase separation of positive m_F states. The separation of negative m_F states will even be decreased. This effect is demonstrated in case (cII), where a magnetic field similar to the one used in the experiment is assumed and the detunings of the OSG beams changed such that the initial accelerations of the $m_F = \pm 9/2$ states are the same as in case (cI). The reason for the decreased separation of negative m_F states is a reduction of the difference in the dipole forces of the σ^- beam on neighboring m_F states. This reduction comes from the Zeeman splitting of the ${}^3P_1$ $F' = 11/2$ level, which will tune transitions with strong line strength farther away from the σ^--beam wavelength than transitions with weak linestrength.

The distortions of the density distribution after OSG separation can be reduced if more power is available for the OSG beams. Then the waist of the OSG beams can be made wider in the x-direction keeping the same potential in the z-direction. This leads to a reduction

of unwanted potential gradients along x, which are the source of the distortions well visible e.g. in (aIII) or (cI). The reduction is demonstrated in case (cIII), where the power and waist in the x-direction of the OSG beams has been doubled compared to case (cI).

Determination of the atom number distribution

To obtain the number of atoms in each m_F state, we use two approaches. The first one determines the atom numbers from ten Gaussian fits to the density distribution integrated along the x- and y-directions, see Fig. 7.2(a). The second approach uses the fit of the simulation to the data described above, which takes the distortions of the distribution better into account, but relies on our ability to accurately model the OSG separation process. A systematic effect should be considered in both approaches: the m_F-state dependence of the average photon number absorbed by an atom during absorption imaging. This dependence has its origin in the m_F-state dependent line strength of the absorption imaging transition. Under our imaging conditions (probe beam of circularly polarized light on the ${}^1S_0 - {}^1P_1$ transition with an intensity of $0.5\,\mathrm{mW/cm^2}$, an angle of 45° to the quantization axis given by the magnetic field, and $40\,\mu$s exposure time), on average about 40 photons are scattered per atom, making optical pumping during absorption imaging important. We simulate this optical pumping process to obtain an estimate of the number of photons scattered by an atom in dependence of its initial m_F state. We find that the optical pumping process depends strongly on the detuning of the absorption imaging beam to the closely spaced hyperfine states of the ${}^1P_1$ excited state, which are mixed at the 16 G magnetic field applied. Because of this dependence, not only the absolute number of photons scattered per atom depends on the detuning, but also the ratio of the number of photons scattered for different initial states. For atoms starting in the $m_F = +9/2$ or the $m_F = -9/2$ state the ratio is highest, about 1.2(2), where the error comes from the uncertainty of the laser detuning used in the experiment. Further experimental study of this effect is needed to determine the relative atom numbers better. Simply assuming equal and maximal absorption by atoms in each m_F state, the atom number distributions resulting from the two approaches are shown in Fig. 7.2(b). The atom numbers of both approaches agree to better than 20% for all but two m_F states. The agreement is less good for the $m_F = +9/2$ state, which has the most distorted distribution, and the $m_F = -7/2$ state, for which the Gaussian fit underestimates the width.

7.3 Spin-state dependent absorption imaging

We also demonstrate a complementary method of m_F-state detection: m_F-state dependent absorption imaging. This method is often used for alkali atoms employing a broad linewidth transition [Mat98]. For Sr, m_F-state resolved imaging on the broad ${}^1S_0 - {}^1P_1$ transition is not possible since the magnetic field splitting of the exited state $m_{F'}$ states is smaller than the linewidth of the transition [Boy07c]. But m_F-state dependent imaging can be realized using the narrow ${}^1S_0(F = 9/2) - {}^3P_1(F' = 11/2)$ intercombination line. To achieve state selectivity, we apply a magnetic field of 0.5 G, which splits neighboring $m_{F'}$ states by 200 kHz, which is 27 times more than the linewidth of the imaging transition. The advantages of this method

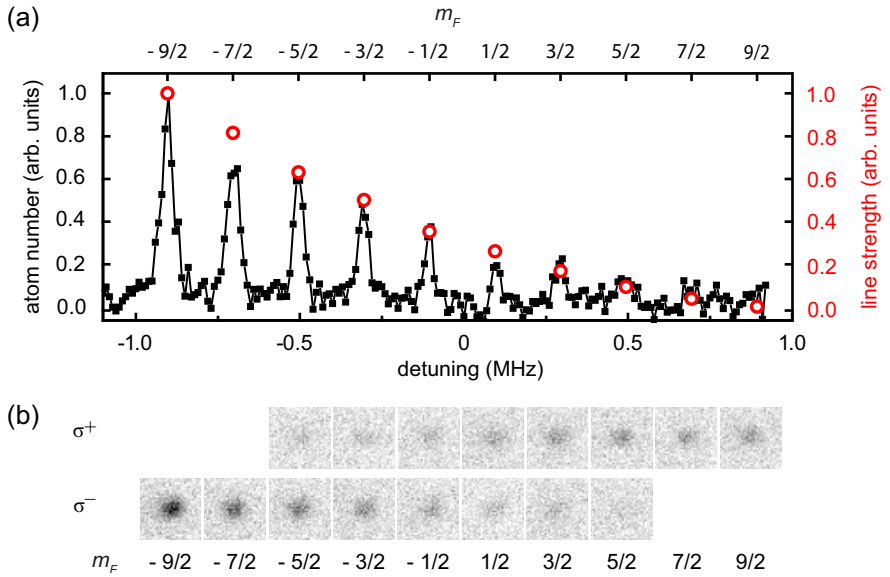

Figure 7.4: m_F-state resolved absorption imaging on the ${}^1S_0(F = 9/2) - {}^3P_1(F' = 11/2)$ intercombination line. (a) Spectrum of a ^{87}Sr sample with nearly homogeneous m_F-state distribution. The spectrum was obtained using σ^--polarized light and shifting transitions corresponding to different m_F states in frequency by applying a magnetic field of 0.5 G. The circles give the line strengths of the transitions. (b) Absorption images taken on the maxima of absorption of each m_F state using σ^+ or σ^- polarized light.

compared to OSG separation is its applicability to samples that have not been evaporatively cooled, spatially resolved imaging, and a near perfect suppression of signal from undesired m_F states. A disadvantage of this method is that it delivers a reduced signal compared to imaging on the ${}^1S_0 - {}^1P_1$ transition, as done after OSG separation. The reduction comes from the narrower linewidth, optical pumping to dark states during imaging, and weak line strengths for some m_F states.

To demonstrate absorption imaging on the intercombination line, we use a sample of 10^6 atoms at a temperature of 0.5 μK in a trap with oscillation frequencies of $f_x = 45$ Hz, $f_y = 40$ Hz, and $f_z = 220$ Hz, obtained after 1.4 s of evaporation. Figure 7.4 shows a spectroscopy scan and absorption images taken on the maxima of the absorption signal of this sample. The absorption is strongly m_F-state dependent and to obtain the best signal, the polarization of the absorption imaging light has to be adapted to the m_F state of interest: $\sigma^+(\sigma^-)$ for high (low) m_F states and π for low $|m_F|$ states. For our absorption imaging conditions (an intensity of 15 μW/cm^2, which is 5 times the saturation intensity, and an exposure time of 40 μs), even atoms in m_F states corresponding to the strongest transition will on average scatter less than one photon. Therefore, for a sample with homogeneous m_F-state distribution, the maximum absorption is expected to be nearly proportional to the m_F-state dependent line strength of the transition, which we confirm using a simulation of the absorption imaging process[2]. This proportionality is observed in the experimental

[2]The simulation determines the average number of photons scattered by an atom in a certain m_F state for a distribution of atoms corresponding to the one used in our experiment. It takes into account the

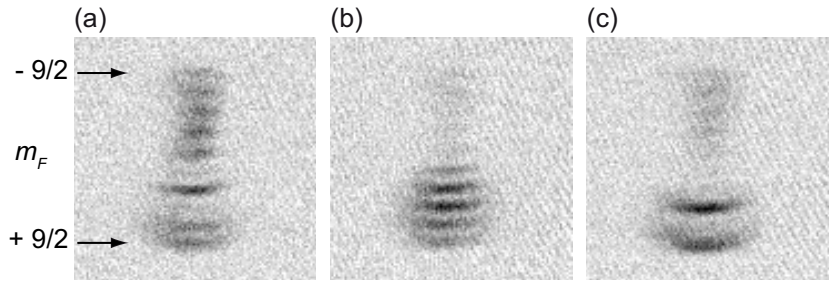

Figure 7.5: Examples of state mixtures prepared by optical pumping and analyzed using OSG separation. (a) The $m_F = 1/2$ and $5/2$ states were pumped to the $3/2$ state using σ^+ and σ^- light, respectively. (b) The negative m_F states were pumped to the positive m_F states. (c) A two-state mixture obtained by pumping the lower m_F states to the $m_F = 5/2$ and $7/2$ states and subsequently pumping the $m_F = 7/2$ state to the $m_F = 9/2$ state.

data, indicating that the sample used has a nearly homogeneous m_F-state distribution. The Lorentzian linewidth of the absorption lines is $\sim 40\,\mathrm{kHz}$. Power and interaction-time broadening result in a linewidth of 30 kHz. In addition Doppler broadening and collisional broadening are expected to contribute to the linewidth [Ido05].

7.4 Preparation of spin-state mixtures

For applications of ^{87}Sr to quantum simulation and computation, the m_F-state mixture needs to be controlled. We produce a variety of different mixtures by optical pumping, making use of OSG separation to quickly optimize the optical pumping scheme and quantify the result. Optical pumping is performed on the $^1S_0(F = 9/2) - {}^3P_1(F' = 9/2)$ intercombination line, before evaporative cooling. A field of 3 G splits neighboring excited state $m_{F'}$ states by 255 kHz. This splitting is well beyond the linewidth of the transition of 7.4 kHz, allowing transfer of atoms from specific m_F states to neighboring states using $\sigma^{\pm}$- or π-polarized light, the choice depending on the desired state mixture. Sequences of pulses on different m_F states can create a wide variety of state mixtures, of which three examples are shown in Fig. 7.5. Optical pumping on the $^1S_0(F = 9/2) - {}^3P_1(F' = 7/2)$ and $^1S_0(F = 9/2) - {}^3P_1(F' = 11/2)$ transitions yields similar results.

7.5 Determination of an upper bound of the spin-relaxation rate

A low nuclear spin-relaxation rate is an essential requirement to use ^{87}Sr for quantum simulation and computation [Caz09, Gor10]. The rate is expected to be small since the nuclear

Zeeman splitting of the excited state, the Doppler shift, acceleration of atoms by photon absorption and emission, and optical pumping. The result of the simulation is that the number of photons absorbed by an atom initially in a certain m_F state is to within 10% proportional to the line strength of the transition corresponding to this m_F state.

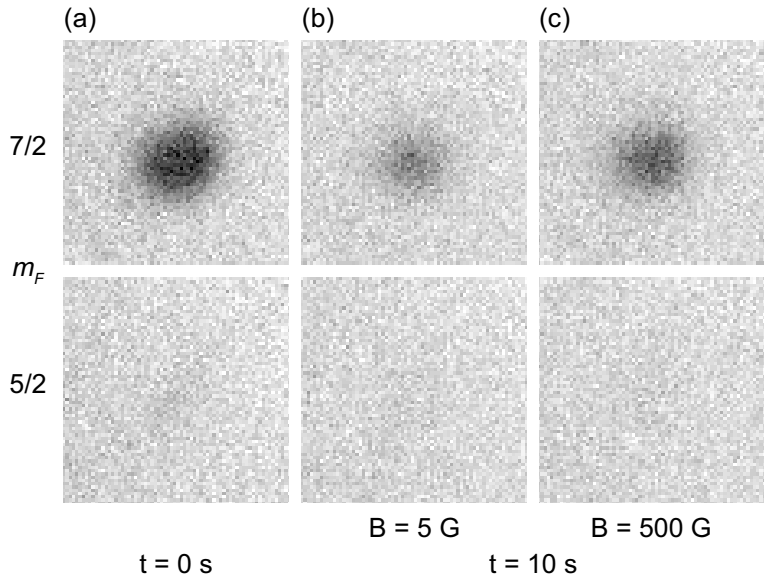

Figure 7.6: Absence of spin relaxation in ^{87}Sr. Shown are absorption images of the $m_F = 5/2$ and 7/2 state averaged over 25 runs of the experiment. Atoms were initially removed from the $m_F = 5/2$ state by optical pumping, whereas all other m_F states remained populated (a). After 10 s hold at a magnetic field of 5 G (b) or 500 G (c) no $m_F = 5/2$ atoms are detectable, showing the low rate of spin relaxation.

spin does not couple to the electronic degrees of freedom in the ground state. Here, we use our nuclear spin state preparation and detection techniques to determine an upper bound for this spin relaxation rate. We start with a sample of 1.5×10^6 atoms with near uniform m_F-state distribution and a temperature of $T = 1.5\,\mu$K, confined in a trap with oscillation frequencies $f_x = 68$ Hz, $f_y = 67$ Hz, and $f_z = 360$ Hz, obtained after transferring the atoms from the magneto-optical trap to the dipole trap and adiabatic compression of the trap. We optically pump all atoms from the $m_F = 5/2$ state to neighboring states and look out for the reappearance of atoms in this state by spin relaxation during 10 s of hold. The atom number in the $m_F = 5/2$ state and, as a reference, the $m_F = 7/2$ state are determined from absorption images. During 10 s of hold at a magnetic field of either 5 G or 500 G the number of $m_F = 5/2$ atoms remains below our detection threshold of about 10^4 atoms, indicating a low spin-relaxation rate, see Fig. 7.6. From this observation, we can obtain an upper bound for the spin-relaxation rate. To obtain a conservative bound, we assume that the dominant process leading to the creation of $m_F = 5/2$-state atoms are collisions of $m_F = 7/2$- with $m_F = 3/2$-state atoms, forming two $m_F = 5/2$-state atoms. Since the second order Zeeman effect is negligible no energy is released in such a collision and the resulting $m_F = 5/2$-state atoms will remain trapped. The number of atoms created in the $m_F = 5/2$ state by spin relaxation after a hold time t is $N_{5/2} = 2N_{\mathrm{state}} g_{\mathrm{sr}} \overline{n} t$, where $N_{\mathrm{state}} = 1.5 \times 10^5$ is the atom number in each populated state, g_{sr} the spin-relaxation rate constant, $\overline{n} = 7.5 \times 10^{11}\,\mathrm{cm}^{-3}$ the mean density and the factor 2 takes into account that two atoms are produced in the $m_F = 5/2$ state per collision. From our measurement we know that $N_{5/2} < 10^4$, from which we obtain an upper bound of $5 \times 10^{-15}\,\mathrm{cm}^3\mathrm{s}^{-1}$ for the spin-relaxation rate constant. This

bound for the rate constant corresponds for our sample to a spin relaxation rate which is 2000 times smaller than the elastic scattering rate. The rate constant could be even orders of magnitude smaller than the already low upper bound we obtained [Jul].

7.6 Conclusion

In conclusion, we have demonstrated two complementary methods to characterize the spin-state mixture of an ultracold cloud of ^{87}Sr. Optical Stern-Gerlach separation can characterize the spin-state mixture of an evaporatively cooled sample in a single experimental run and is very useful for fast optimization of optical pumping, which we have demonstrated by three examples. State selective absorption imaging can deliver spatially resolved information about the spin state, also for samples at μK temperatures. Using these methods, we have determined an upper bound for the ^{87}Sr spin relaxation rate and have found it to be low, as expected. These methods will be necessary tools for the implementation of quantum simulations and quantum computation making use of the ^{87}Sr nuclear spin.

We gratefully acknowledge support from the Austrian Ministry of Science and Research (BMWF) and the Austrian Science Fund (FWF) through a START grant under project number Y507-N20 as well as support from the European Commission under project number 250072 iSENSE.

Chapter 8

Improved production of degenerate quantum gases of strontium

We report on improved experiments to generate Bose-Einstein condensates (BECs) and degenerate Fermi gases of strontium. The main improvement results from the use of a different dipole trap laser and a new geometry of the trap; see Chpt. 2.7.4. Together with a reduced linewidth of the 689-nm laser and an increased flux from the oven, we are able to create a BEC of the ^{84}Sr isotope exceeding 10^7 atoms, which is a 50-fold improvement over the experiments reported in Chpt. 4 and [Mar09a]. We improve the current atom number of the ^{86}Sr BEC by a factor of five compared to the work presented in Chpt. 6, and refine the generation of the attractively interacting ^{88}Sr BEC. We present a scheme to generate ^{84}Sr BECs with a cycle time of 2 s, which is the fastest production rate of BECs ever achieved. We create deeply-degenerate Fermi gases with T/T_F as low as 0.1, where the number of spin states can be set to any value between 1 and 10. Furthermore, we report on a total of five different double-degenerate Bose-Bose and Bose-Fermi mixtures. These studies bridge the gap between proof-of-principle experiments performed in the past three years, and applications of these degenerate samples that are anticipated in the near future.

8.1 Introduction

All of the bosonic Sr isotopes have already been brought to degeneracy [Ste09, Mar09a, Mic10, Ste10b], and degenerate Fermi gases have been reported as well [DeS10, Tey10]. These experiments demonstrate the feasibility of degeneracy in Sr, which was sought-after for so long. Many applications, however, require some or all out of a number of key parameters to be fulfilled: a sufficiently high atom number, a robust strategy to create the degenerate sample, a fast cycle time, and a sufficiently long lifetime. For the fermionic isotope, a high degree of degeneracy and full control over the spin states are desired as well. Not all of these properties were fulfilled in the experiments to date.

In this chapter, we describe a scheme to create degenerate samples that satisfies all of the above criteria and improves many key properties substantially. These experiments are performed with one universal experimental setup that can be used for all isotopes, as well as mixtures among them, with only little modifications.

	^{84}Sr	^{86}Sr	^{87}Sr	^{88}Sr	abundance (%)
^{84}Sr	**124**	**32**	**-56**	1800	0.56
^{86}Sr	**32**	**830**	**164**	**98**	9.86
^{87}Sr	**-56**	**164**	**97**	**55**	7.00
^{88}Sr	1800	**98**	**55**	**-1**	82.58

Table 8.1: Scattering lengths a between the strontium isotopes, given in units of a_0. The values are averages of the values given in [Mar08] and [Ste08], and the uncertainty is a few a_0 except for the two very large values ($a > 500\,a_0$), where the uncertainty is much larger. All mixtures of isotopes, of which double-degenerate samples are presented in this chapter, are marked in bold. The natural abundance is given in the last column.

8.2 Fifty-fold increase in ^{84}Sr BEC atom number

The first Sr isotope cooled to quantum degeneracy was ^{84}Sr [Ste09, Mar09a]. To overcome its low natural abundance, we operate the blue MOT for 40 s to accumulate atoms the metastable reservoir. This time is slightly longer than the lifetime of the gas in the reservoir, and further loading does not increase the atom number. The atoms are returned into the ground state, compressed and cooled by the red MOT, and transferred into the dipole trap. For this experiment, we use only the horizontal dipole trap beam, which provides initial trapping frequencies in the vertical, transverse, and axial direction of 800, 57, and 8 Hz, respectively. About 4×10^7 atoms are loaded into the dipole trap at a temperature of 1.5 μK. The power of the dipole trap is reduced exponentially from 2.36 W to 426 mW within 10 s, resulting in trap frequencies of 250, 18, and 3 Hz. At the end of evaporation, we obtain an almost pure BEC of $1.1(1) \times 10^7$ atoms, see Fig. 12.1.

We investigate the phase transition by careful analysis of absorption images. These images are taken after a free expansion of 30 ms, and the imaging light is detuned by $1.5\,\Gamma \approx 48$ MHz from the $^1S_0 - {}^1P_1$ transition to reduce the optical density. We perform a full 2D fit to the absorption image. During the early stage of evaporation, the momentum distribution of the atom cloud can be described by a single Gaussian, indicating a well thermalized sample; see Fig. 12.1(c). The phase transition occurs after about 6 s of evaporation, and we employ a bimodal fit to our data, describing the BEC and the thermal fraction of atoms. The temperature of the sample is extracted from the Gaussian part of the fit.

The size of this BEC is a factor of almost 100 larger than in our previously reported work [Ste09], and is to the best of our knowledge the largest BEC ever created in an optical trap. A comparison with other two-electron systems allows us to identify the beneficial properties of Sr that yield such large BECs.

$^1S_0 - {}^3P_1$ linewidth — The ytterbium isotope ^{174}Yb has a scattering length similar to ^{84}Sr, and BECs of 1.5×10^5 atoms have been reported [Yam10]. The narrow cooling transition in Yb is about 25-times broader than in Sr, resulting in a correspondingly higher Doppler temperature and less favorable starting conditions for evaporative cooling. A cooling transition of a few kHz seems ideal for the second cooling stage.

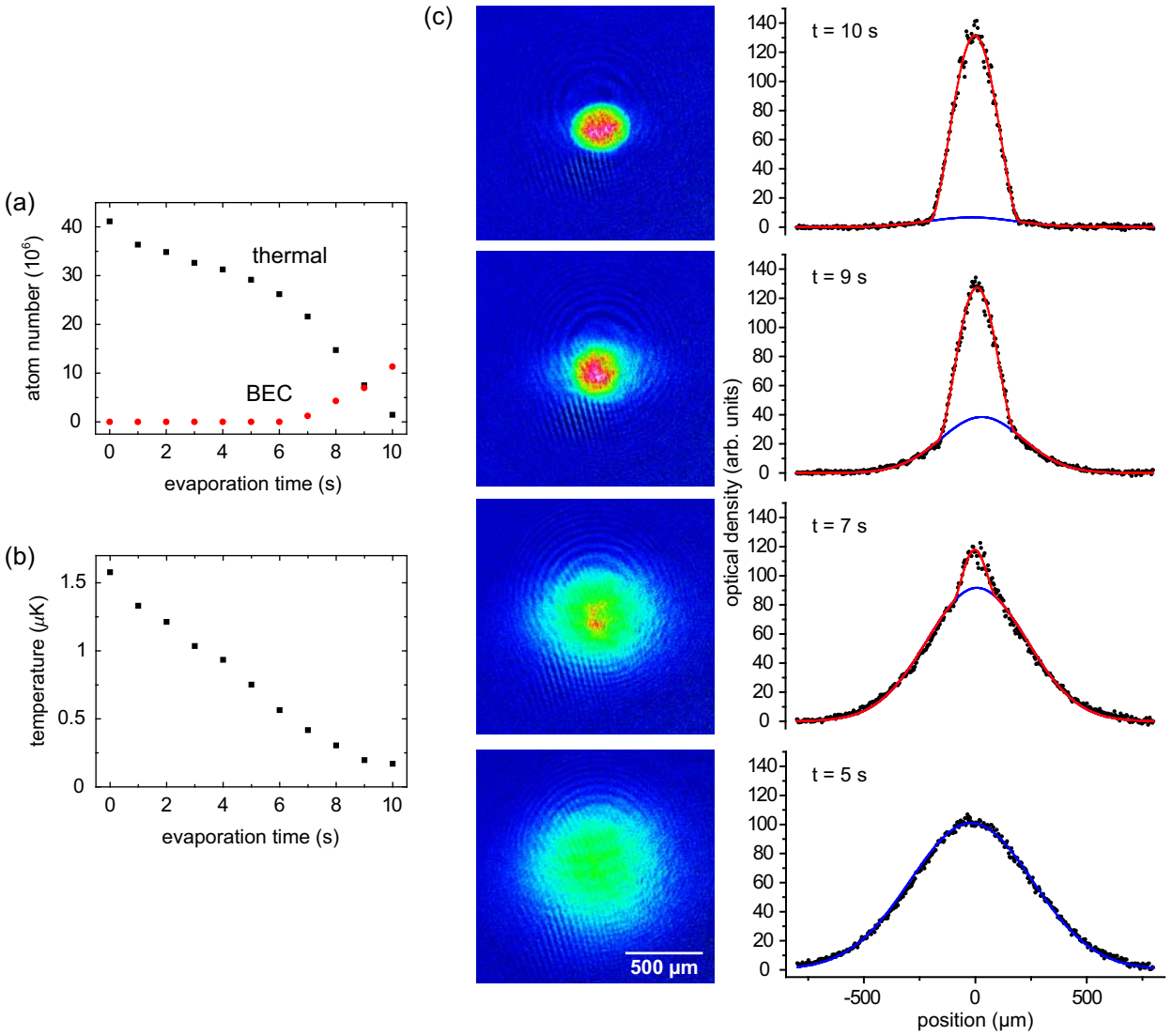

Figure 8.1: Generation of BECs exceeding 10^7 atoms. Panel (a) shows the evolution of the atom number in the thermal (black squares) and condensate fraction (red circles) during evaporation. The temperature of the thermal fraction is shown in (b). Panel (c) shows a series of absorption images (left) and integrated density profiles (right) for different times along the evaporative cooling ramp. The black circles are data points, which are fitted with a bimodal distribution (red line), capturing the thermal fraction (blue line) and the BEC.

Loading rate of blue MOT and accumulation in the $^3P_2$ state — The isotope ^{168}Yb has a similarly low natural abundance as ^{84}Sr and a comparable scattering length, and BECs of 10 000 atoms have been reached [Sug11]. In this experiment, the very small loading rate of the MOT seemed to be the limiting factor. Collection of atoms on the broad $^1S_0 - {}^1P_1$ transition in Sr allows us to capture many atoms, while the low-lying $^1D_2$ state opens the path towards accumulation in the metastable reservoir.

Scattering property — The calcium isotope ^{40}Ca combines both a high natural abundance and a narrow intercombination line, but BEC sizes reached so far amount to 20 000 atoms [Kra09] or 3000 atoms [Hal12], depending on the cooling strategy. The scattering length of ^{40}Ca is large and comparable to the case of ^{86}Sr, which leads to strong three-body decay and therefore demands for a low atom number density.

We find no fundamental limit to the attainable atom number of the ^{84}Sr BEC. The lifetime of this BEC is about 15 s, indicating that 3-body losses are manageable. To further increase the BEC atom number, an oven with a much higher flux is currently installed in our experiment and is expected to increase the number of atoms loaded into the reservoir. The red MOT could be operated at a larger detuning to increase the size of the ellipsoid (see Fig. 2.7) to reduce the density of atoms in the MOT. With more power available for the dipole trap, the volume can be increased, such that the same density can be preserved even at higher atom number. Atom numbers approaching 10^8 seem within reach.

8.3 Generation of BEC with a cycle time of 2 seconds

In the previous section, we have reported on experiments optimized for a large number of atoms in the BEC. We can also optimize our experimental sequence for a short cycle time. Many experiments, for example precision measurements such as optical clocks, require high repetition rates or a favorable ratio of probe time vs cycle time. Experiments taking place in an environment of poor vacuum quality could also benefit from fast cycle times. So far, cycle times for optically trapped degenerate quantum gases are in the range of a few 10 s. Using magnetic trapping near the surface of a microchip [Far10, Hor06], narrow cooling transitions [Kra09], or vigorous trap deformation [Kin05], cycle times can be as low as 3 s .

Making use of the very high phase space density achieved already in the red MOT, as well as the excellent scattering properties of ^{84}Sr, we are able to reduce the cycle time to 2 s; see Fig. 12.2(a). At the beginning of the cycle, we operate the blue MOT for 800 ms to load the metastable reservoir. A short flash of repump light returns the metastable atoms into the ground state, where they are trapped, compressed, and cooled to about 1.2 μK by the red MOT. Close to 4×10^6 atoms are loaded into a dipole trap which is formed by the horizontal sheet and a vertical beam of 25 μm waist. Forced evaporation reduces the trap depth over 550 ms with a time constant of about 250 ms; see Fig. 12.2(b).

Absorption images taken after 22 ms TOF and analyzed as described above. In this experiment, however, we find that a single Gaussian is not sufficient to describe the thermal fraction. After about 100 ms of evaporation, the distribution begins to deviate from a Gaussian (see Fig. 12.2(d (i)), indicating that part of the atoms reach a lower temperature than the rest of the sample. These are the atoms located in the crossing region of the horizontal and vertical beams, where the density is higher and evaporation is more efficient. After further evaporation, two samples with different temperatures are clearly visible, and we use a double Gaussian to fit our data (case ii). The phase transition occurs after about 270 ms of evaporation, and we employ a trimodal fit to our data, describing the BEC, the thermal fraction of atoms in the crossing region, and the thermal atoms in the horizontal beam (cases

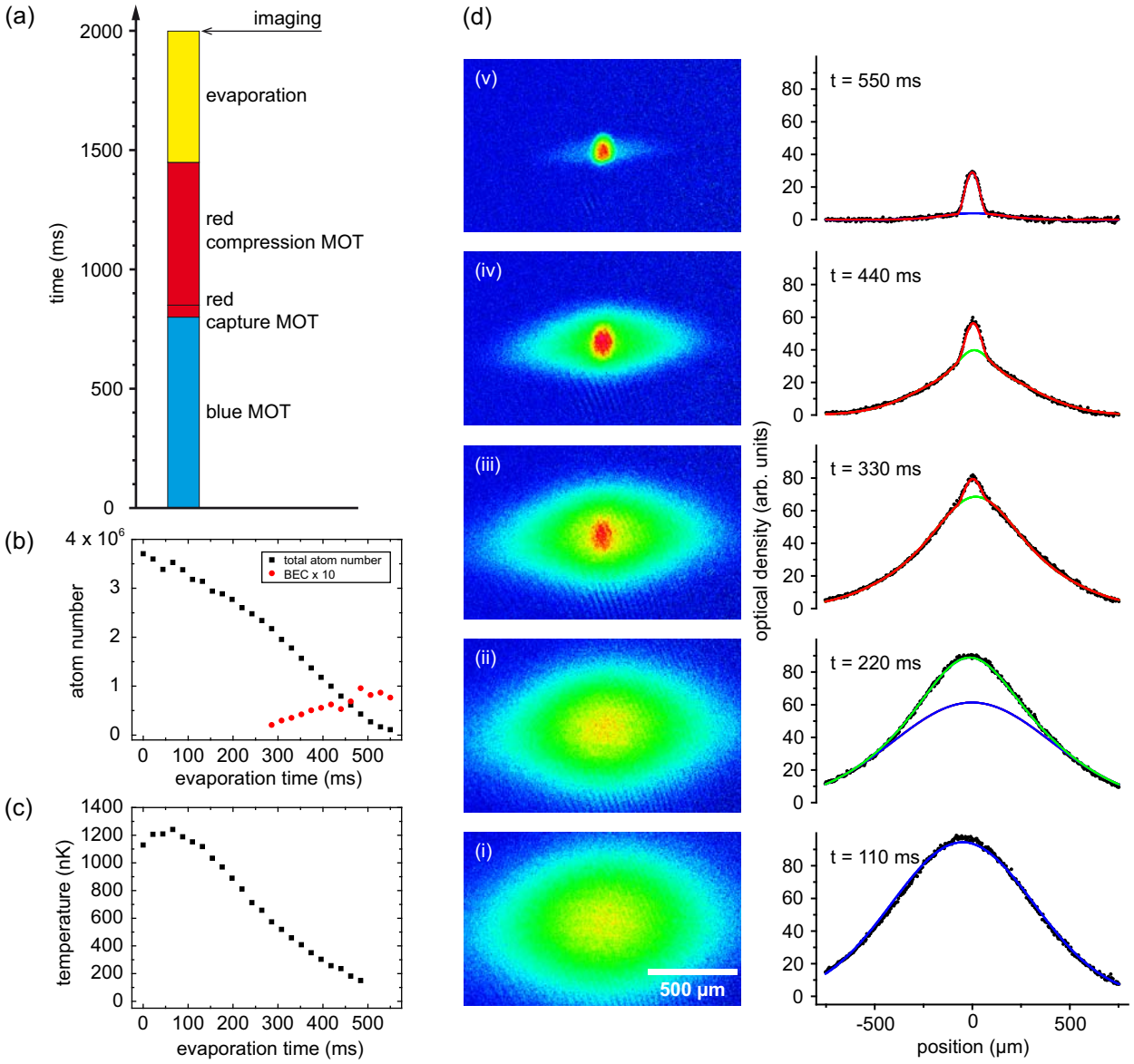

Figure 8.2: Generation of BEC with a short cycle time. Panel (a) shows a sketch of the experimental sequence. The development of atom number (b) and temperature of the dimple region (c) during the evaporation trajectory are shown. Absorption images taken after 22 ms TOF and integrated density profiles show the appearance of an an almost pure BEC of 100 000 atoms at the end of evaporation (d). Blue lines indicate Gaussians, green lines double-Gaussians, and red lines bi- and trimodal distributions, see the text for details.

iii and iv). After about 480 ms of evaporation, the thermal fraction within the crossing region cannot be discerned, indicating an essentially pure BEC in this region. Further evaporation does not increase to BEC atom number, but efficiently removes atoms located outside the crossing region. For the last stage of evaporation, we employ a bimodal fit to the data, capturing the BEC and the thermal atoms outside the crossing region (case v). About 10^5

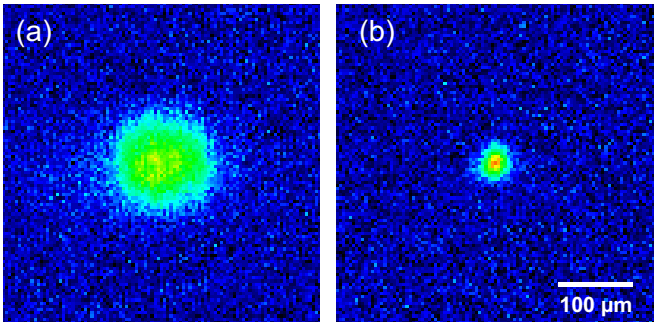

Figure 8.3: Essentially pure BECs of (a) ^{86}Sr and (b) ^{88}Sr. The free expansion time is 25 ms for both images, and the geometric and color scales are identical. The BEC of ^{86}Sr contains 25 000 atoms and expands to much larger size compared to the almost non-interacting BEC of ^{88}Sr, which contains 5 000 atoms.

atoms reside in the BEC at the end of evaporation. The read-out of the charged-coupled device (CCD) chip used for imaging can be performed during the consecutive experimental cycle and is therefore not included in the 2-s period.

The cycle time could be improved substantially if the reservoir loading time (800 ms in this experiment) was reduced, e.g. by increasing the oven flux. It seems that cycle times approaching 1 s are within reach. Fast preparation times are greatly acknowledged in quantum gas experiments as they allow for a high data acquisition rate, and mandatory for precision measurements, where the performance depends directly on the ratio of probe time vs cycle time.

8.4 Five-fold increase in ^{86}Sr BEC atom number

Some isotopes of alkaline-earth atoms feature large positive scattering lengths, such as ^{40}Ca, ^{42}Ca, ^{44}Ca [Dam11], and ^{86}Sr. While scattering between atoms provides thermalization during evaporation, there is a downside of a very large scattering length a: Inelastic three-body losses scale as $\sim a^4$, and can reduce the evaporation efficiency drastically. Magnetic Feshbach resonances, a widely used means to tune the scattering length in ultracold samples, are absent in the alkaline-earth species, and a different strategy to reach degeneracy despite the large scattering length is needed.

In a previous experiment [Ste10b], we have shown degeneracy of ^{86}Sr, which has a scattering length of about $830\,a_0$ [Mar08]. Here, the crucial innovation was a drastic reduction of the atom density in the dipole trap of large volume. Two-body collisions, vital for thermalization, scale proportional with the density n, while detrimental three-body collisions scale as $\sim n^2$. At small enough densities, evaporation can be efficient even for large scattering lengths. In this experiment, we worked in an oblate trap with trapping frequencies of 70 (16, 5) Hz in the vertical (horizontal) directions. The horizontal beam was strongly elliptic in the horizontal plane, and we found that a rather large trapping frequency in the vertical direction is helpful for evaporation in the direction of gravity.

Improving this experiment, we are now going to an even more elliptic horizontal beam

(aspect ratio 1:14), while keeping the horizontal confinement the same. The higher vertical trap frequency allows for a faster evaporation time, moves the phase transition to an earlier stage with more atoms at a higher temperature, and ultimately supports larger BECs. Instead of 4.8 s, evaporation now proceeds within 800 ms. The onset of BEC is observed at a temperature of about 70 nK with 350 000 atoms present. At the end of evaporation, trap frequencies are 157, 20.2, and 4.6 Hz, and we reach almost pure BECs of 25 000 atoms; see Fig. 12.3(a). A vertical dipole trap beam was added during the last part of evaporation to increase the axial trapping frequency slightly.

8.5 Reliable generation of an attractive ^{88}Sr BEC

The isotope ^{88}Sr is by far the most abundant one, and early research on cold gases of Sr focused on this isotope. The s-wave scattering length a of ^{88}Sr turned out to be very close to zero, which makes it an excellent choice for precision measurements [Tak05, Fer06b]. Optical clocks, for example, suffer from density-dependent mean-field shifts, which scale as $\sim a$. Similarly, elastic collisions lead to a dephasing of Bloch oscillations. No other atomic species that has been laser-cooled so far combines the properties of high natural abundance, non-magnetic ground state, and very small interaction.

It is this small (and slightly negative) scattering length that hampered evaporative cooling of ^{88}Sr towards degeneracy for a long time [Ido00, Pol05b]. Sympathetic cooling with the second-most abundant isotope, ^{86}Sr, could not reach quantum degeneracy because of the large 3-body recombination rate of ^{86}Sr [Fer06a].

Efficient evaporation to quantum degeneracy was first achieved by the Rice group [Mic10] using the fermionic isotope ^{87}Sr as cooling agent. An ultracold gas of ^{88}Sr is slightly attractive for $T \to 0$, and indeed Mickelson and co-workers observed a limited number of atoms in the BEC, in good agreement with a simple mean-field model [Rup95].

Here, we verify the results of the Rice group and highlight a few differences of our own experimental work. We start with an isotopic mixture in a crossed-beam dipole trap, containing 4.5×10^6 atoms of ^{88}Sr at 560 nK and 1.9×10^6 atoms of ^{87}Sr at 1.0 μK. The sample thermalizes within the first second of forced evaporative cooling, and remains thermalized for the remainder of the 4-s ramp. The BEC of ^{88}Sr appears after 2.1 s, with 2.7×10^6 atoms present at a temperature of 320 nK. Further evaporation does not increase the BEC atom number beyond a few 1 000 atoms, but the thermal fraction can be removed to obtain very pure BECs at the end of evaporation; see Fig. 12.3(b).

A homogeneous BEC with negative scattering length is unstable for all atom numbers, but a trapped BEC can be stabilized (through the zero-point kinetic energy of the trap) up to a maximum atom number of $N_0 = 0.575\, a_{\rm ho}/a$. Here, $a_{\rm ho} = \sqrt{\hbar/(m\bar{\omega})}$ is the harmonic oscillator length, and the prefactor is only slightly dependent on the trapping geometry. The maximum atom number thus depends only weakly on the mean trap frequency $\bar{\omega}$, and one cannot expect substantial improvements from a change in trapping geometry. As the BEC atom number increases and eventually surpasses this limit during evaporation, part of the atoms are ejected out of the BEC [Don01], leaving the remnant behind to form a stable BEC again. This cycle continues throughout evaporation, until the remaining atom

number is smaller than N_0 or the elastic collision rate is too low to reduce the temperature further and add atoms to the BEC. Consequently, one would expect a random atom number $N < N_0$ in the BEC at the end of evaporation. This is precisely the observation of Ref. [Mic10]: for a large number of experimental realizations, the BEC atom numbers were evenly distributed between $\sim 0.4\,N_0$ and N_0. In view of the application of degenerate ^{88}Sr in precision measurements, we will now show how the shot-to-shot variation in BEC atom number can be reduced.

In the work presented here, we deliberately start with a low initial number of ^{87}Sr atoms to perform inefficient evaporation. After 80% (or 3.5 s) of evaporation, only 12 000 ^{87}Sr atoms remain, and the scattering rate of a thermal ^{88}Sr atom with an ^{87}Sr atom has dropped from initially $250\,\mathrm{s}^{-1}$ to below $4\,\mathrm{s}^{-1}$. At this point, we do not expect any appreciable cooling to take place. Instead, further lowering of the trap depth removes all thermal atoms from the trap, leaving behind a pure BEC of 6000 atoms. The atom number of this BEC is certainly below $N_0 \approx 10\,000$ for our conditions of $\bar{\omega} = 70(1)\,\mathrm{Hz}$ and an assumed scattering length of $a = -1.4\,a_0$. The shot-to-shot variation in BEC atom number, however, is surprisingly small: We obtain a standard deviation of only 9% in the atom number. This value is certainly larger than our typical ^{84}Sr BEC atom number fluctuations of about 1%, but it constitutes a substantial improvement towards precision measurements with ^{88}Sr.

In conclusion, we have confirmed the ^{88}Sr BEC experiments by the Rice group, using very similar conditions. We observe a much smaller variation in BEC atom number at the end of evaporation, which might be attributed to a slightly different choice of initial conditions. We note that in our dipole trap with $\bar{\omega} = 70\,\mathrm{Hz}$, we never observe BECs with more than 7000 atoms. When identifying this number with N_0, we can deduce a scattering length of $-2.0\,a_0$, which is well within the uncertainty of the widely stated value of $-1.4\,a_0$.

8.6 Double-degenerate Bose-Bose mixtures of Sr

Many fascinating and fundamentally important systems can be studied with a mixture of two Bose-degenerate gases. These range from the (im)miscibility and phase separation of two quantum fluids [Hal98] to systems featuring quantum turbulence [Tak10]. A mixture of two BECs of different atomic species can be the starting point for the creation of ultracold heteronuclear molecules, which carry a large dipole moment if transferred to their singlet ground state [Ni10]. Within the alkalis, a number of Bose-Bose mixtures have been realized: ^{41}K + ^{87}Rb [Mod02], ^{85}Rb + ^{87}Rb [Pap08], and ^{87}Rb + ^{133}Cs [Ler11].

For a large and stable two-component mixture, the absolute value of all three intra- and interspecies scattering lengths must not be too large to avoid rapid decay. Further, the interspecies interaction should not induce phase separation, but still provide some degree of interaction. The scattering length of alkaline-earth systems cannot be tuned without introducing detrimental losses [Bla11b]. This limits the number of possible binary mixtures considerably, despite the large number of isotopes. In particular, all combination of bosonic Ca isotopes seem unfavorable, since all intraspecies scattering lengths of the most abundant Ca isotopes are quite large [Kra09, Dam11]. In Yb, two out of five bosonic isotopes have large negative scattering lengths [Kit08], excluding many possible combinations of isotopes.

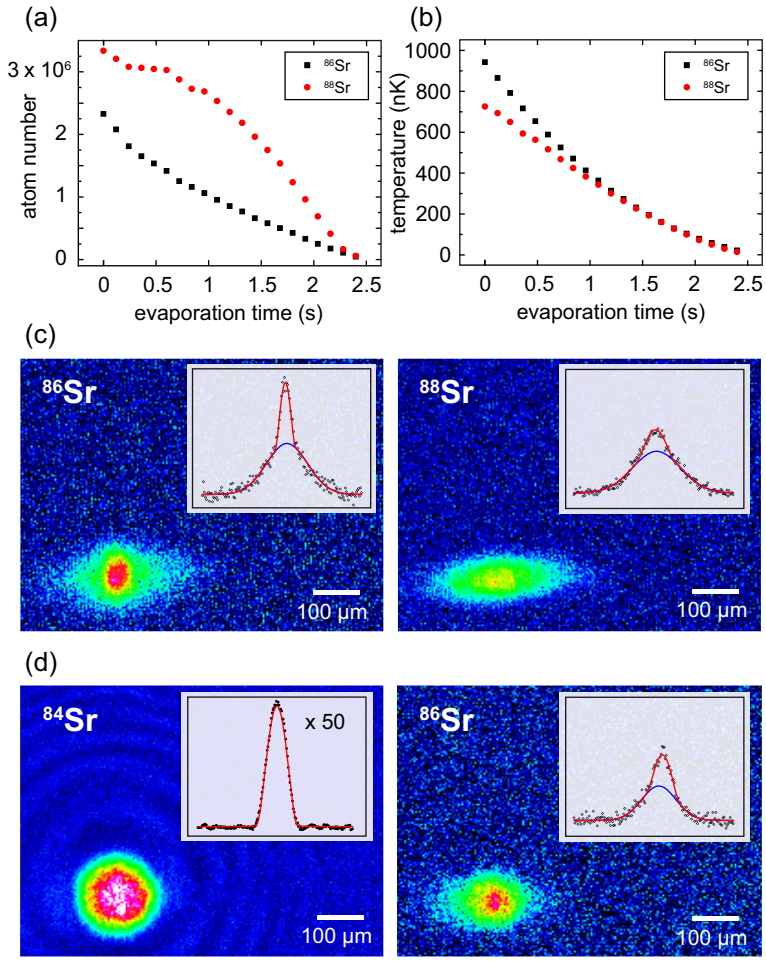

Figure 8.4: Creation of double-degenerate Bose-Bose mixtures. The development of atom number (a) and temperature (b) during evaporation are shown for the mixture of ^{86}Sr (black squares) and ^{88}Sr (red circles). Despite a significant temperature difference at the start of evaporation, the sample thermalizes within 1 s. Below, we show absorption images of the mixtures ^{86}Sr + ^{88}Sr (c) and ^{84}Sr + ^{86}Sr (d), taken after 26 ms of free expansion. The BEC of ^{84}Sr contains 2×10^6 atoms, and imaging is performed with a detuning of 1 Γ. The other three BECs are not pure. We show 2D integrations along the vertical direction, with bimodal fits to the data. The color palette of these three images is identical, and the integrated optical densities of the insets are to scale.

One remaining combination, ^{170}Yb + ^{174}Yb, has a large and negative interspecies scattering length of $-500a_0$. One of the two remaining combination, ^{168}Yb + ^{174}Yb, has been brought to double degeneracy very recently, with 9 000 atoms in the BEC of each species [Sug11]. The interspecies scattering length between these two isotopes is $2.4(3.4)a_0$ and provides only minuscule interaction between the two.

Here we report on double-degenerate Bose-Bose mixtures of the combinations ^{84}Sr + ^{86}Sr and ^{86}Sr + ^{88}Sr, which have sizeable interspecies scattering lengths of $32\,a_0$ and $98\,a_0$, respectively. The experimental realization is straightforward: We load the two isotopes into the

reservoir consecutively, repump them simultaneously on their respective $^3P_2 - {}^3D_2$ transitions, and operate two red MOTs simultaneously. The mixture is loaded into the dipole trap and subsequently evaporated to form two BECs. Imaging is performed on the blue $^1S_0 - {}^1P_1$ transition, and we image only one isotope per experimental run. The frequency shift between even isotopes is about $4.5\,\Gamma$, and we spatially separate the two clouds during TOF to avoid signal contributions from the unwanted isotope. The separation is obtained by acceleration of the unsought species with an 8-ms pulse of light from an upwards propagating beam on the red transition, which is very isotope-selective. The pulse of light is applied after 17 ms TOF, such that the density of the sample has decreased sufficiently and both atom number and momentum distribution of the imaged species remain unperturbed.

The experimental results are shown in Fig. 12.3. We will discuss the ^{86}Sr + ^{88}Sr combination first: 2.3×10^6 (3.3×10^6) atoms of ^{86}Sr (^{88}Sr) are loaded into the dipole trap, consisting of the horizontal beam and a weak vertical beam for additional axial confinement. The initial temperatures of the two species are quite different: 950 nK for ^{86}Sr and 720 nK for ^{88}Sr, which reflects the different intraspecies scattering behavior. The interspecies scattering length is around $100\,a_0$, and the two species clearly thermalize to reach equilibrium after 1 s of evaporation. As the trap depth is lowered further, we observe the onset of BEC in ^{86}Sr (^{88}Sr) after 2.0 s (2.3 s). At the end of our evaporation ramp, which lasts 2.4 s, we obtain 10 000 (3000) atoms of ^{86}Sr (^{88}Sr) in the condensate fraction, see Fig. 12.3(a). At this point, trap frequencies are 160 Hz (20 Hz) in the vertical (horizontal) directions, and further evaporation does not increase the BEC atom numbers.

In a second experiment, we investigate the ^{84}Sr + ^{86}Sr mixture with an interspecies scattering length of $32\,a_0$. Starting out with 10×10^6 (1.5×10^6) atoms of ^{84}Sr (^{86}Sr) in the dipole trap, we perform forced evaporation over 2 s, and the two species remain in perfect thermal equilibrium throughout this time. The phase transition of ^{84}Sr is observed already after 1.3 s, with about 2.5×10^6 atoms present at a temperature of 200 nK. Trap frequencies at this point are $\omega_{\mathrm{vert}} = 335$ Hz, $\omega_{\mathrm{trans}} = 29$ Hz, and $\omega_{\mathrm{ax}} = 5.0$ Hz. After 1.9 s, the BEC is essentially pure and contains up to 2×10^6 atoms. The atom number in ^{86}Sr is considerably lower to avoid three-body loss, and the phase transition occurs later: after 1.7 s, with 400 000 atoms at a temperature of 130 nK and trap frequencies ω_{vert} (ω_{trans}, ω_{ax}) of 160 Hz (20 Hz, 3.7 Hz). Until the end of evaporation, the BEC fraction grows to 8 000 atoms but remains accompanied by a large thermal fraction; see Fig. 12.3(b). Note that the remaining combination of two bosonic isotopes in Sr, ^{84}Sr + ^{88}Sr, is unstable due to the diverging interspecies scattering length.

In conclusion, we have presented two binary Bose-Bose mixtures of alkaline-earth atoms with appreciable interaction between the two species. These mixtures enjoy the property that isotope-selective optical traps can be operated close to one of the intercombination lines. The differential isotope shift between even isotopes of Sr, expressed in term of the linewidth, is about $\Delta_{(N+2)-N}/\Gamma = 25\,000$ for the $^1S_0 - {}^3P_1$ transition, and much larger for the $^1S_0 - {}^3P_0$ clock transition. This might allow for an individual addressing of the isotopes by a dipole trap operated close to these transition [Yi08], reminiscent of the case of Rb in its hyperfine states $|F = 1\rangle$ and $|F = 2\rangle$ [Man03] or nuclear substates in Yb and Sr [Tai10, Ste11].

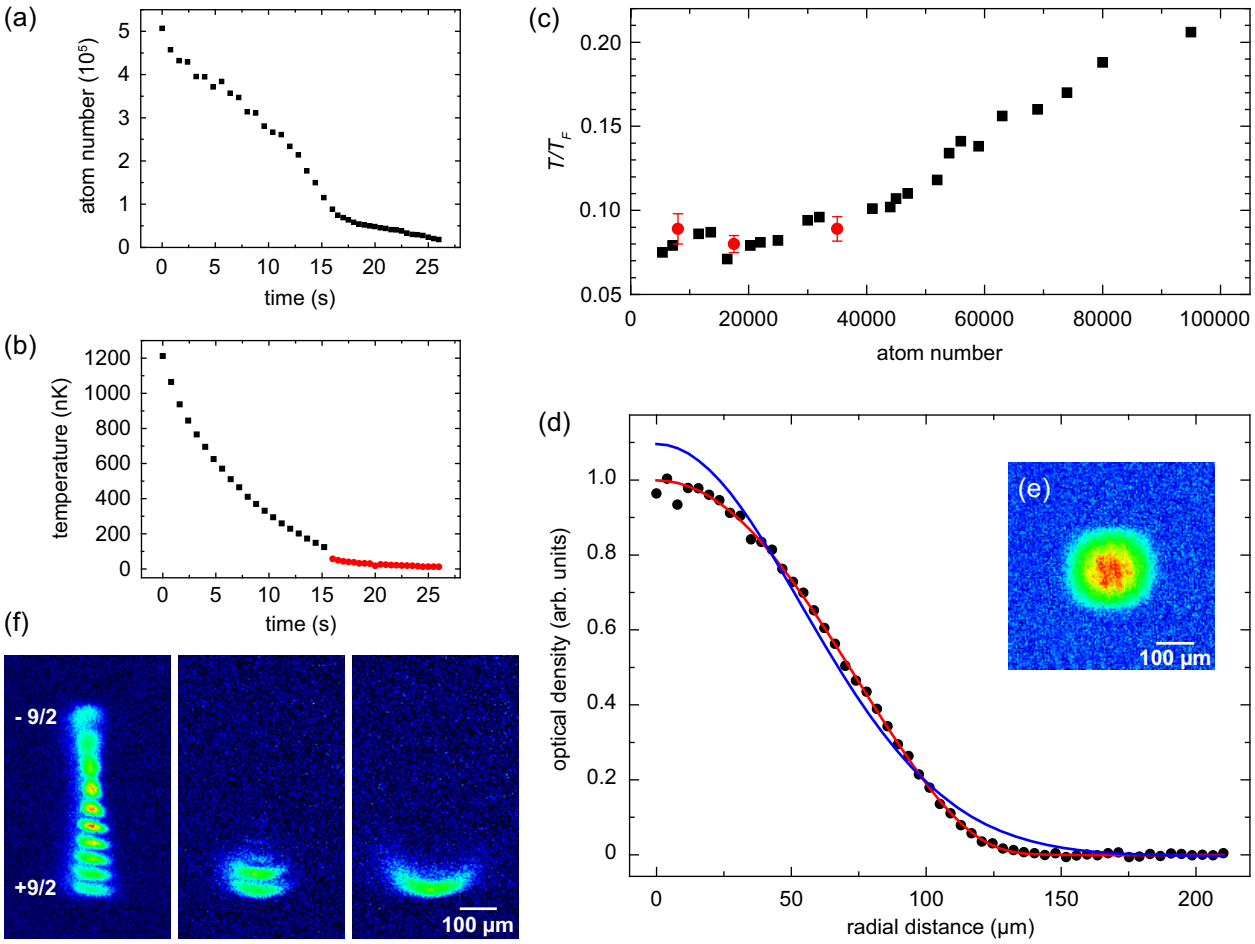

Figure 8.5: Deeply degenerate Fermi gases of ^{87}Sr. Panels (a) through (e) illustrate the evaporation of a balanced 10-state mixture. The temperature (b) is determined from Gaussian fits for high temperatures (black data), and from fits to the wing of the distribution for lower temperatures (red data). The value of T/T_F in dependence of atom number per spin state is shown in (c), where some data points have been taken multiple times (red data) to determine the statistical uncertainty. The value of T/T_F is extracted from Fermi fits (red line in (d)) to the momentum distribution, which describe the data (black circles) very well. A Gaussian fit (blue line) clearly disagrees with this sample of $T/T_F = 0.08(1)$. The corresponding absorption image (e) is taken after 25.4 ms TOF. Preparation of samples with a variable number of spin states N requires detection of individual spin states, which is done by the OSG technique and shown here for $N = 10$, $N = 2$ and $N = 1$ (f).

8.7 Deeply-degenerate Fermi gases of ^{87}Sr

A wealth of recent proposals suggest to employ the fermionic isotope of an alkaline-earth atom as a platform for the simulation of spin systems [Caz09, Gor10, Wu03, Wu06, FF10, Her09, Xu10, Hun11], for the generation of artificial gauge fields [Ger10, Coo11b, Bér11, Gór11a], or for quantum computation schemes [Dal08, Gor09]. Many schemes of quantum simulation

require the number of spin states N to be large. In addition, it is proposed that cooling in a lattice works best for large N [Bon12]. The largest nuclear spin of any alkaline-earth like atom is 9/2, and it occurs in the nuclei of ^{87}Sr and the two nobelium isotopes ^{253}No and ^{259}No, both of which have a lifetime on the order of only minutes. This makes ^{87}Sr with its ten spin states the prime candidate for many studies of quantum simulation.

These schemes also require the temperature of the sample to be below the super-exchange scale, t^2/U, where t is the tunneling rate in the lattice, and U is the on-site interaction [Bon12]. A high degree of degeneracy in the bulk would constitute a good starting point for subsequent loading of the lattice. A degeneracy of $T/T_F = 0.26(5)$ in a 10-state mixture [DeS10] and a degeneracy of $T/T_F = 0.30(5)$ in a single-spin state [Tey10] of ^{87}Sr were presented already, both with about 20 000 atoms in each Fermi sea. Neither of these two experiments had the means to set the number of spin states at will. Here, we present degenerate Fermi gases of Sr at considerably deeper degeneracy with an arbitrary number of spin states between 1 and 10.

About 5×10^6 atoms of ^{87}Sr are loaded into the optical dipole trap, where we measure a temperature of $1.2\,\mu$K. At this time, atoms are in a roughly even mixture of all spins. Optical pumping is then performed on the $^1S_0 - {}^3P_1, |F = 9/2\rangle \rightarrow |F' = 9/2\rangle$ transition at a small guiding field of 3 G, which splits adjacent m'_F-states by $35\,\Gamma = 260$ kHz. As we have shown before [Ste11], we can prepare any combination and relative population of the ten spin states. The optical pumping is optimized using the optical Stern-Gerlach (OSG) technique described in Ref. [Ste11], and quantified using state-selective absorption imaging on the intercombination line [Ste11]. With a detection threshold of 3 000 atoms, we can reduce the population of undesired spin states to below 0.1%. After the spin preparation, which does not heat the sample, we perform evaporative cooling. Evaporation proceeds in two stages: the first stage lasts 16 s, during which the power of the horizontal beam is reduced by a factor of five. At this point, the gas enters the degenerate regime with a typical temperature of around $0.3\,T_F$. Evaporation becomes less efficient due to the increased occupation of low momentum states. We compensate for this by reducing the ramp speed for the second evaporation stage, which lasts 10 s. Trap frequencies at the end of evaporation are about 120 Hz in the vertical and 40 Hz in the horizontal directions. The final trap depth is slightly modified, depending on the number of spin states used. The case $N = 1$ is unique as fermions in the same spin state do not collide at low temperatures due to the Pauli exclusion principle, impeding thermalization of the sample. In this case, we add ^{84}Sr atoms to the system to facilitate sympathetic cooling.

In all of these experiments, we determine the atom number and degeneracy T/T_F by 2D Fermi fits to the data using the same fitting routine as in our previous work [Tey10]. The width of the cloud σ is related to the temperature by $T = m\sigma^2/k_B t_{\mathrm{TOF}}^2$, and T_F is calculated from the atom number and average trap frequency as $T_F = \hbar\bar{\omega}(6N_{\mathrm{at}})^{1/3}/k_B$. The momentum distribution of a gas at small T/T_F strongly deviates from a Gaussian shape, which we show in azimuthally integrated profiles; see Fig. 8.5(d).

We will limit the presentation of our data to the cases of $N = 10$, $N = 2$, and $N = 1$. For the 10-state mixture, the fraction of Pauli-forbidden collisions is small, and evaporative cooling performs well to yield a stack of ten spatially overlapping Fermi seas. Figures 8.5(a) and (b) show the development of atom number per spin state and temperature along the

evaporation ramp. The degree of degeneracy T/T_F in dependence of atom number in shown in (c). With about 30 000 atoms per spin state, we obtain a degeneracy of $0.10(1)\,T/T_F$. We reach degeneracies as low as $0.08(1)\,T/T_F$ by further evaporation. The errors given here are statistical errors of multiple experimental realizations, and we assume systematic errors to be of similar magnitude.

For the 2-state mixture, we pump all atoms into a balanced population of $m_F = +9/2$ and $m_F = +7/2$ states. The total atom number, initial temperature, and evaporation trajectory are identical to the previous case of a 10-state mixture, but there is a crucial difference: Only half of all possible collisions are Pauli-allowed in the binary mixture, leading to a decreased thermalization rate. The reduced evaporation efficiency immediately manifests itself in the degree of degeneracy reached: Despite the higher atom number per spin state, we can reach only $0.20(1)T/T_F$ with 1.0×10^5 atom per spin state. The lowest degeneracies reached are $0.17(1)T/T_F$ with 60 000 atoms remaining. Further evaporation does not reduce T/T_F.

In the case of a single-spin sample of 2.5×10^6 fermionic atoms, we add 6.5×10^6 atoms of ^{84}Sr to the dipole trap. Evaporation is performed in one single exponential ramp over 8 s and results in a pure BEC of 7×10^5 atoms. Towards the end of evaporation, the fermionic cloud contains 1.0×10^5 atoms. The sample is not well thermalized in the axial direction of the trap, which we take into account by fitting the vertical and horizontal directions independently to obtain $T/T_F = 0.12$ and $T/T_F = 0.23$, respectively.

This result is an improvement by a factor of about five in atom numbers over our previous work [Tey10] and reaches a deeper degeneracy. However, we find it challenging to reach even lower degeneracies in this isotopic mixture, probably limited by rather poor thermalization towards the end of the evaporation. The interspecies scattering length of $-56\,a_0$ is rather small in itself. In addition, the bosons form a BEC quite early, which reduces the scattering cross section with the fermions further. Operating at a higher density might increase scattering between bosons and fermions, but also increase 3-body heating and losses within the bosons as $\sim n^2$. We conclude that the 10-state Fermi mixture performs much better than the Bose-Fermi pair.

8.8 Degenerate Bose-Fermi mixtures of Sr

Double-degenerate Bose-Fermi mixtures in ultracold gases have been realized in bi-alkali (e.g. [Sch01]), alkali/alkaline-earth [Har11] and bi-alkaline-earth systems [Fuk09b, Tey10]. The Bose-Fermi mixture of ^{84}Sr and a single spin state of ^{87}Sr has already been presented in Sec. 8.7. Here, we will introduce two other isotopic combinations: ^{86}Sr + ^{87}Sr and ^{88}Sr + ^{87}Sr. It might seem worthless to realize the same combination of elements with different isotopes of identical nuclear spin, but it is not: Given the absence of magnetic Feshbach resonances, the choice of isotopes can provide some coarse tuning of the interaction strength. The interspecies scattering lengths of the three combinations mentioned afore are $-56\,a_0$, $164\,a_0$, and $55\,a_0$, respectively, thus covering a broad range of values.

At first, we present the mixture of ^{84}Sr + ^{87}Sr. In contrast to the experiment in Sec. 8.7, we are now working with the entire 10-state mixture of ^{87}Sr. About 6×10^6 fermions at $1.15\,\mu$K and 2.1×10^6 bosons at $1.1\,\mu$K are loaded into the dipole trap. The first of two

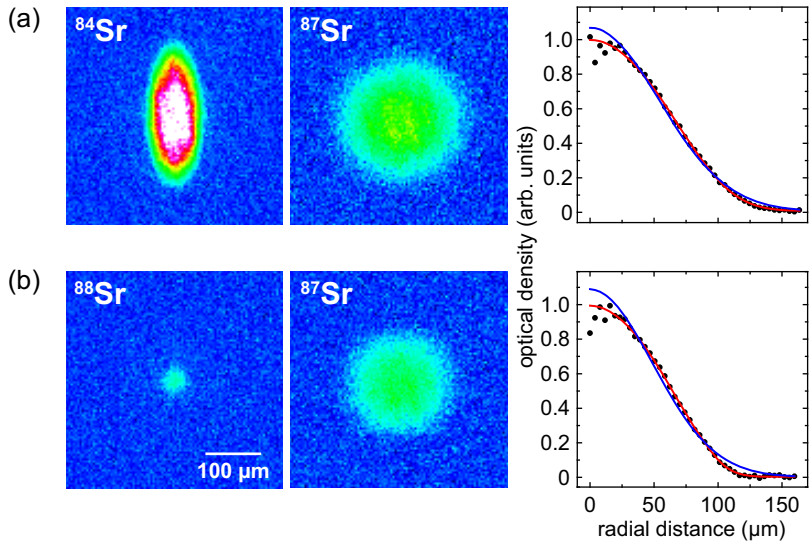

Figure 8.6: Eleven-fold degeneracy of Bose-Fermi mixtures. The two combinations shown here are ^{84}Sr + ^{87}Sr (a) and ^{88}Sr + ^{87}Sr (b). The absorption images of the bosonic (left column) and fermionic isotopes (middle column) are taken after 25.4 ms TOF; the color and length scales are identical for all four images. The fermionic cloud consists of ten spin states, where azimuthal integrations of the density after TOF are shown in right column. The final atom number and the degree of degeneracy depend on the scattering properties, which are different for every combination of isotopes.

exponential evaporation ramps takes 12 s, during which the onset of BEC in ^{84}Sr is observed already after 8 s. The BEC is essentially pure after 12 s, containing about 3×10^5 atoms. The fermions remain in perfect thermal equilibrium with the bosons. At the end of this first ramp, we obtain 7×10^4 atoms per spin state at a temperature of about 100 nK, but still well outside the degenerate regime. For further cooling, we add a very slow second evaporation ramp of 7.5 s duration. Such a slow ramp is required because Pauli blocking decreases the scattering rate between the fermions, and superfluidity of the BEC decreases the scattering rate between fermions and bosons. The final trap frequencies are 210 Hz (41 Hz and 32 Hz) in the vertical (horizontal) directions. The degree of Fermi degeneracy has increased substantially to $T/T_F = 0.15(1)$ with 15 000 atoms in each spin component at the end of evaporation. The BEC atom number has decreased slightly to 2×10^5 atoms; see Fig. 8.6(a). This experiment reaches an eleven-fold degeneracy of distinguishable particles, possibly the largest number of overlapping degenerate gases ever reported. It seems that the presence of the bosons reduces the evaporation efficiency of the fermions, as deeper degeneracies were achieved in absence of the bosons; see Sec. 8.7.

In a second experiment, we replace the bosonic isotope by ^{86}Sr. The bosonic intraspecies and the interspecies scattering lengths are much larger than in the previous case, which we account for by decreasing the density of the sample: we load less atoms (1.6×10^6 atoms of ^{86}Sr at 1.1 μK and 3.7×10^6 atoms of ^{87}Sr at 1.0 μK), and we keep the average trap frequency low by reducing the horizontal confinement. We maintain the concept of two sequential evaporation ramps of different time constants and evaporate slightly deeper than

is the previous case, but reduce the total evaporation time to 3.4 s. Final trap frequencies are 160 Hz, 23 Hz, and about 10 Hz in the vertical and horizontal directions. This isotopic combination performs worse than the previous one, yielding a bosonic sample with only 15% condensate fraction. The axial trap frequency, required to be small to inhibit 3-body losses of ^{86}Sr, does not ensure thermalization of the fermionic sample in this direction. We obtain $T/T_F = 0.15(5)$ for the vertical direction. The BEC contains 5 000 atoms, and each Fermi sea contains 10 000 atoms (not shown).

As a last experiment, we use the ^{88}Sr isotope as the boson. Starting out with 1.2×10^6 bosons and 6.5×10^6 fermions both at 1.2 μK, we reduce the trap depth in two ramps of 12 and 8 s. The atom number of the ^{88}Sr BEC is limited by the negative scattering length, and evaporation to this rather low trap depth is required to remove the thermal fraction. We finally obtain a pure BEC of 4000 atoms immersed in ten Fermi seas, each comprising 10 000 atoms at $0.11(1)\,T/T_F$; see Fig. 8.6(b).

8.9 Conclusion

In this chapter, we have presented a collection of experiments related to the creation of BECs and degenerate Fermi gases of strontium. We have shown how both electronic and collisional properties add to create a framework of unparalleled strength and diversity. Many key parameters of a quantum gas, such as the BEC atom number, the preparation time, the lifetime, and the fidelity of state preparation, have been improved by an order of magnitude over previous experiments. In particular, we have presented the largest BECs ever created in an optical trap, and we were able to reduce the cycle time to 2 s. Some of the techniques, such as the design of the dipole trap, might also be applicable to other systems, for example the recently condensed species Dy [Lu11a] and Er [Aik12].

Chapter 9

Reservoir spectroscopy of the $5s5p\,^3P_2 - 5s5d\,^3D_{1,2,3}$ transitions in Sr

Some transitions in strontium are very well explored, but some have not yet been investigated. We perform spectroscopy on the optical dipole transition $5s5p\,^3P_2 - 5s5d\,^3D_{1,2,3}$ for all stable isotopes of atomic strontium. We develop a new spectroscopy scheme, in which atoms in the metastable $^3P_2$ state are stored in a reservoir before being probed. Previous measurements have been performed in a magneto-optical trap or discharge. The method presented here increases the attained precision and accuracy by two orders of magnitude. We show how the state distribution and velocity spread of atoms in the reservoir can be tailored to increase the spectroscopy performance. The absolute transition frequencies are measured with an accuracy of 2 MHz, and the isotope shifts are given to within 200 kHz. We calculate the A and Q parameters for the hyperfine structure of the fermionic isotope with an error of about 1 MHz. Furthermore, we show that the $5s5p\,^3P_2 - 5s5d\,^3D_3$ transition is not completely cycling.

9.1 Introduction

The rich electronic structure of elements with two valence electrons, comprising long-lived metastable states and ultranarrow transitions, is of great interest for precision measurements, as demonstrated by optical clocks [Ido03, Ste04, Tak05, Hon05, Lud08b, Lem09a, Lem09b, Koh09, Nic12] or gravimeters [Pol11]. Quantum degenerate samples of Yb [Tak03, Fuk07a, Fuk07b, Fuk09b, Tai10, Sug11] and the alkaline-earth elements Ca [Kra09] and Sr [Ste09, Mar09a, Mic10, DeS10, Tey10, Ste10b] have opened new possibilities, such as the study of unique many-body phenomena [Wu03, Wu06, Caz09, Her09, Gor10, FF10, Xu10, Hun11], including the possibility to create strong artificial gauge fields [Ger10, Coo11b, Bér11, Gór11a], and novel schemes of quantum computation [Sto08, Dal08, Gor09, Rei09].

Many of these applications and proposals rely on broad optical transitions originating from the metastable triplet states. These transitions are essential for laser-cooling of Mg, Ca, and Sr [Reh07, Bin01, Kat99]. They can be used to drive Raman transitions between metastable states and for fluorescence read-out in quantum computation schemes [Dal08]. The $^3P_2 - {}^3D_3$ transition could be used for operation of a MOT and for absorption imaging.

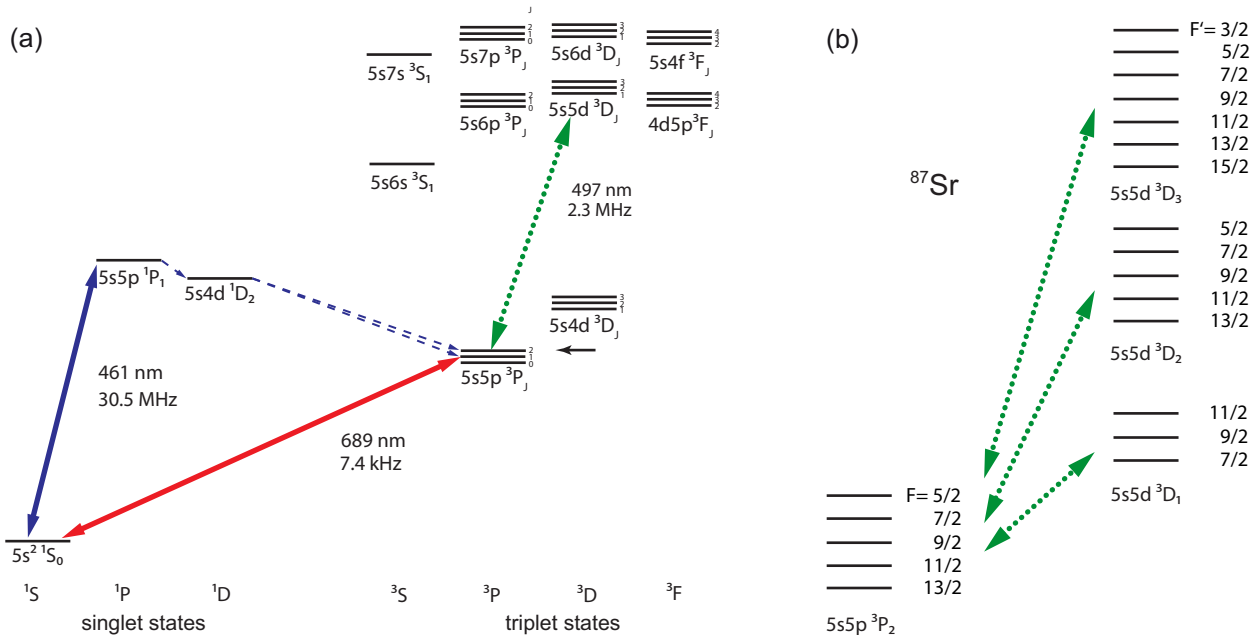

Figure 9.1: Schematic illustration of the energy levels and transitions in strontium relevant for this work. (a) Atoms in the metastable $5s5p\,^3P_2$ state (indicated by the small solid arrow) are repumped using the $5s5p\,^3P_2 - 5s5d\,^3D_{1,2,3}$ transitions (dotted line) around 497 nm. (b) Details of this transition for the fermionic ^{87}Sr isotope. Its nonzero nuclear spin introduces a rich hyperfine structure.

A good knowledge of these transitions is crucial for the calculation of the polarizability of the $^3P_2$ state, which is important for quantum computation schemes [Por08, Dal08].

So far, spectroscopic data is available for some of the dipole transitions within the triplet system of strontium. The $^3P_0 - {}^3S_1$ and $^3P_1 - {}^3S_1$ transitions, as well as the isotope shifts and hyperfine splittings involved, have been measured by Courtillot *et al.* to a precision of a few 100 kHz [Cou05]. The Rydberg series $5snd\,^3D_{1,2,3}$ for $n > 12$ has been investigated in a discharge [Bei82], and the $5s5p\,^3P_2 - 5s4d\,^3D_2$ transition has been investigated in a magneto-optical trap [Mic09], both with an accuracy of about 1 GHz and a precision of a few 10 MHz. The $5s5p\,^3P_2 - 5s5d\,^3D_{1,2,3}$ transitions have not been investigated so far, the hyperfine structure of the $^3P_2$ state, however, is very well known [Hei77].

In this chapter, we present spectroscopic data on the three $5s5p\,^3P_2 - 5s5d\,^3D_{1,2,3}$ transitions, which are separated by roughly 0.5 nm. Spectroscopy is performed for the three stable bosonic isotopes ^{84,86,88}Sr as well as the fermionic isotope ^{87}Sr. While the bosonic isotopes have zero nuclear spin, the fermionic one has a nuclear spin $I = 9/2$, which gives rise to a rich hyperfine structure. The wealth of hyperfine transitions requires a sophisticated spectroscopy scheme. For all isotopes, we use a magnetic trap as a reservoir to accumulate atoms in the metastable $^3P_2$ state, hence the name *reservoir spectroscopy*. Atoms in this trap are then probed, and we can populate or deplete certain states beforehand to improve measurement performance. Both precision and accuracy are improved by about two orders of magnitude compared to spectroscopy in a discharge or MOT.

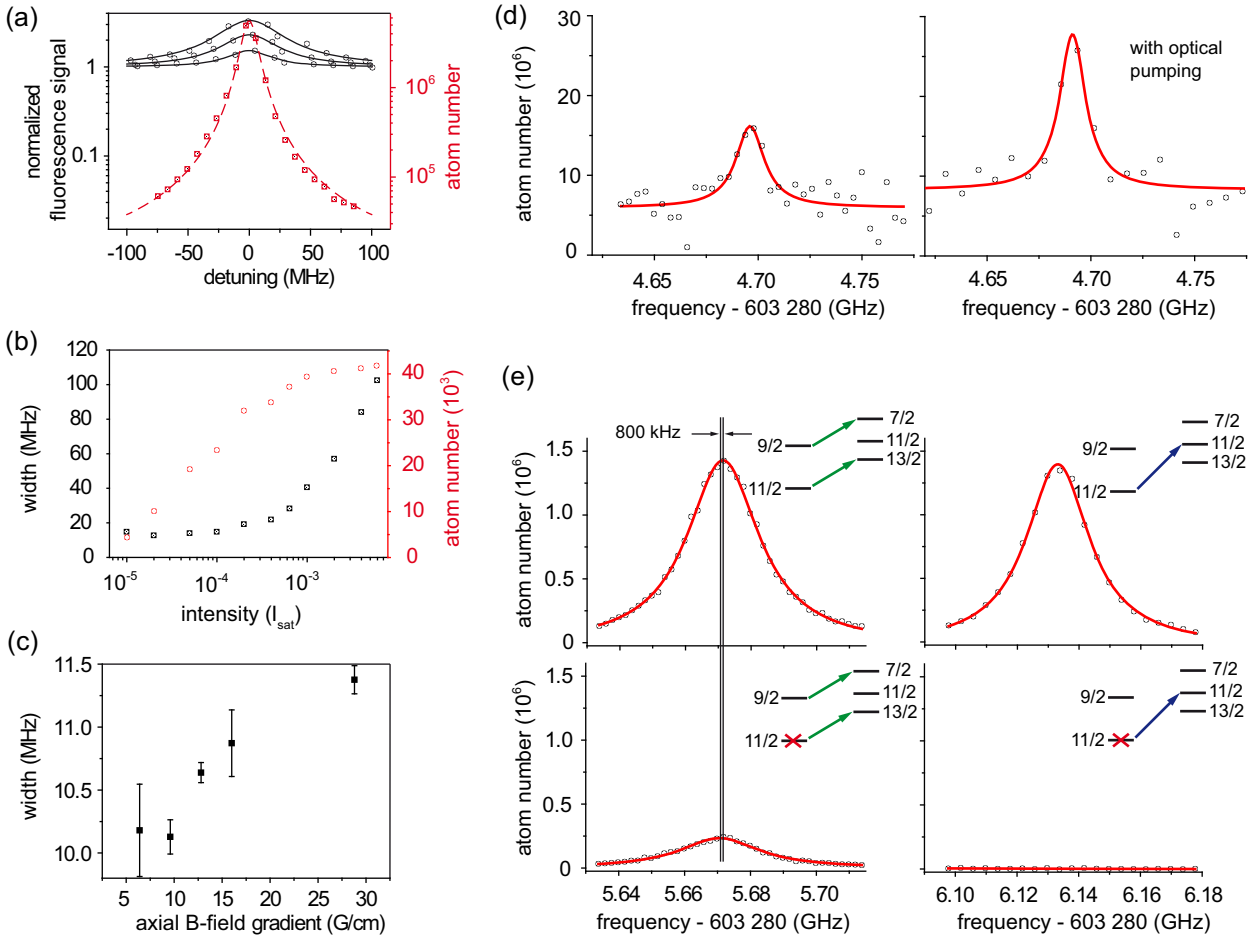

Figure 9.2: Reservoir spectroscopy scheme. (a) The amplitude of the reservoir spectroscopy signal (red squares) is much larger than comparable measurements in a MOT (black circles) with respect to the respective background. A Lorentzian profile is fit to each curve, and the fluorescence curves are taken at $I = 1,\ 3,\ 10 \times 10^{-3}\, I_{\mathrm{sat}}$, from below. (b) Width (black squares) and atom number (red circles) in dependence of repump intensity. (c) Dependence of the width of the transition on the depth of the magnetic trap. (d) Amplification of a certain hyperfine state by optical pumping increases the signal. (e) Depletion of certain hyperfine states allows for a separation of otherwise overlapping hyperfine transitions. All measurements are taken on the $5s5p\,^3P_2 - 5s5d\,^3D_2$ transition in ^{88}Sr ((a)-(d)) and ^{87}Sr ((e)); see the text for details.

9.2 Experimental procedure

The experimental sequence for the preparation of cold and dense samples of bosonic Sr atoms, as they are required for our spectroscopy scheme, is as follows: Atoms are Zeeman-slowed and cooled in a blue MOT using the broad $^1S_0 - {}^1P_1$ transition at 461 nm; see Fig. 9.1(a). This transition is not completely cycling, as atoms from the $^1P_1$ state can decay into the $^1D_2$ state. From here, they may decay further on two different pathways: One path leads into the $^3P_1$ triplet state, which has a lifetime of 21 μs and returns the atoms into the $^1S_0$

singlet ground state, back into the MOT cycle. The other pathway, which is relevant for this work, leads into the $^3P_2$ metastable state, which has a lifetime of about 500 s [Yas04]. Atoms in weak-field seeking m_F states of the $^3P_2$ manifold can be trapped in the quadrupole field of the MOT, which we refer to as the reservoir. The MOT is extinguished when about 10^7 atoms in the $^3P_2$ state have accumulated in the reservoir, where the loading time varies between 50 ms and 10 s, depending on the natural abundance of the respective isotope. A 1-s wait time ensures that only atoms in the magnetic trap remain in the probe volume. A mechanical shutter blocks the atomic beam.

A 50-ms flash of light with a wavelength near 497 nm pumps atoms from the $^3P_2$ into the $5s5p\,^3D_2$ state, from where they decay into the $^3P_1$ state and further into the $^1S_0$ state. Once in the $^1S_0$ ground state, they are further cooled and compressed in a red MOT on the narrow $^1S_0 - {}^3P_1$ transition at 689 nm. Up to 10^7 atoms are cooled to about 500 nK. Absorption imaging is then performed on the broad $^1S_0 - {}^1P_1$ transition, with a lower detection threshold of about 3000 atoms. While the $^3P_2 - {}^3D_2$ transition is commonly used for repumping, also the $^3P_2 - {}^3D_{1,3}$ transitions return atoms into the ground state, however with lower efficiency.

This sequence forms the basis of our reservoir spectroscopy scheme. We change the frequency of the repump laser in each experimental run and record the number of atoms in the red MOT.

9.3 Characterization of the spectroscopy scheme

We will now present the details of the spectroscopy scheme, discuss the optimization of all relevant parameters, and present different methods to increase the signal strength. We do this by comparing our reservoir spectroscopy scheme to a previously used approach, in which spectroscopy was performed directly in the blue MOT [Mic09]. The atom number of a continuously loaded blue MOT is reduced by the constant leakage of atoms into the $^3P_2$ state. This leak can be closed by continuously returning the atoms back into the MOT cycle using a laser on a suited repump transition. When on resonance, the number of atoms in the blue MOT increases significantly. The metastable states can also be populated by a discharge, however measurements using this technique have a precision of a few GHz and will not be considered further. We believe that reservoir spectroscopy is superior to spectroscopy in the blue MOT in three ways.

First, our measurement is intrinsically background-free. Far away from resonance, no atoms are captured in the red MOT. The small background noise on the absorption images stems from photon shot noise and residual fringes, which resemble atom clouds of at most a few thousand atoms. This background noise can be reduced by averaging over multiple images. On the other hand, spectroscopy in a MOT has the background of the MOT itself, possibly stray light and photo detector dark counts. The superior signal strength is shown in Fig. 9.2(a). Depending on the MOT loading rate and repump intensity used, the fluorescence of the MOT increases by a factor of up to about five, however at the expense of a large linewidth. The atom number increase for the fermions is at most a few 10% on resonance [Mic09] due to the involved hyperfine structure. The reservoir spectroscopy described here can yield a signal more than three orders of magnitude larger than the background noise.

Fig. 9.2(a) shows typical fluorescence spectra of a ^{88}Sr MOT at repump intensities of about 1×10^{-3}, 3×10^{-3}, and $1 \times 10^{-2}\, I_{\mathrm{sat}}$, starting from below (solid black lines, normalized to the fluorescence of a MOT without repumping). The dashed red curve shows the corresponding measurement using reservoir spectroscopy, taken at an intensity of $5 \times 10^{-5}\, I_{\mathrm{sat}}$. The amplitude of 5×10^6 atoms is more than three orders of magnitude above the background noise, and the width is smaller by a factor of four compared to the fluorescence curve at highest repump intensity.

To optimize our spectroscopy approach, we measure the linewidth of the transition and the amplitude of the signal in dependence of repump intensity. A larger repump intensity will yield a larger amplitude of the signal, but also a larger width, see Fig. 9.2(b). We find a region around $5 \times 10^{-4}\, I_{\mathrm{sat}}$ in which the width is not broadened by the intensity, but the amplitude has almost saturated. At this intensity, width and amplitude are almost independent of the repump time for times greater than about 10 ms. A distortion of the line shape can be observed at intensities lower than $2 \times 10^{-4}\, I_{\mathrm{sat}}$; see panel (a i) in Fig. 9.3. For higher intensities, we do not observe any intensity-dependent line shifts.

The second advantage of reservoir spectroscopy is the potential to reduce the Doppler broadening: the quadrupole field, which confines the metastable atoms, acts as a velocity filter, as it traps only atoms below a certain kinetic energy. A deeper trap will capture more atoms also at higher velocity classes, while the confinement can be reduced to deliberately select only the low-velocity atoms to reduce the Doppler-broadening, as shown in Fig. 9.2(c). In this measurement, the quadrupole field is ramped down after the blue MOT phase to allow high-energy atoms to escape.

As a third advantage, we can selectively populate the reservoir with the specific states of interest. This is important for the fermionic isotope with its large number of hyperfine levels. In particular, atoms can be pumped into the state of interest during or after the MOT phase. This is illustrated in Fig. 9.2(d): During the ^{87}Sr blue MOT, atoms in all $^3P_2$ hyperfine states are accumulated in the reservoir, however at different relative amounts. The $F = 7/2$ state has the lowest g_F factor, therefore only very few atoms are trapped. In addition, π-transitions into the $^3D_2$ states tend to be weaker than σ-transitions, making the $F = 7/2 \rightarrow F' = 7/2$ transition one of the weakest among all 13 $^3P_2 - {}^3D_2$ transitions. Constantly pumping atoms from the $F = 9/2$ into the $F = 7/2$ state by standard optical pumping can amplify the population of this state significantly.

Similarly, atoms from undesired states can be removed from the reservoir. This is shown in Fig. 9.2(e): The $F = 11/2 \rightarrow F' = 13/2$ and $F = 9/2 \rightarrow F' = 7/2$ hyperfine transitions of the $^3P_2 - {}^3D_2$ line in ^{87}Sr overlap entirely. The initial population of the $F = 11/2$ state is about ten times that of the $F = 9/2$ state, therefore the $F = 11/2 \rightarrow F' = 13/2$ transition completely covers the $F = 9/2 \rightarrow F' = 7/2$ transition. To selectively interrogate only the $F = 9/2 \rightarrow F' = 7/2$ transition, we remove all $F = 11/2$-state atoms during the blue MOT phase by optical pumping into the $F' = 11/2$ state. As an additional benefit, this also increases the $F = 9/2$ population. We first verify on the $F = 11/2 \rightarrow F' = 11/2$ (or alternatively the $F = 11/2 \rightarrow F' = 13/2$) transition that all $F = 11/2$ atoms have been removed, and then selectively probe the $F = 9/2$ state and determine the frequency difference between the $F = 11/2 \rightarrow F' = 13/2$ and $F = 9/2 \rightarrow F' = 7/2$ transitions to be 800 (200) kHz. This would not be possible by spectroscopy on a continuously operated

$^3D_1$	
Δ_{86}^{84}	45.7 (2) MHz
Δ_{88}^{86}	49.3 (2) MHz
A	227.3 (7) MHz
Q	0 (3) MHz

$^3D_2$	
Δ_{86}^{84}	45.3 (2) MHz
Δ_{88}^{86}	47.5 (2) MHz
A	−71.5 (5) MHz
Q	0 (30) MHz

$^3D_3$	
Δ_{86}^{84}	45.0 (2) MHz
Δ_{88}^{86}	46.6 (2) MHz

Table 9.1: Isotope shifts Δ and interaction constants A and Q of the three $5s5p\,^3P_2 - 5s5d\,^3D_{1,2,3}$ transitions.

MOT.

A detailed error analysis is given in Sec. **??**. In brief, the laser is locked to a stable cavity for short-term stability, and monitored on a wavemeter. The wavemeter is calibrated by a laser operating on the clock transition of a $^{40}Ca^+$ ion. The accuracy of the wavemeter is measured with a frequency comb. As a conservative estimate, the accuracy of the absolute frequencies given here is 2 MHz. Relative frequency differences, such as the isotope shifts, have an error of about 200 kHz. Compared to spectroscopy in a MOT or discharge, the scheme described here can improve both the precision and accuracy by at least two orders of magnitude.

9.4 Spectroscopy data

Our set of measurements is shown in Fig. 9.3, where parts (a), (b), and (c) show spectroscopy data of the $^3P_2 - {}^3D_{(1,2,3)}$ transitions, respectively. Panels (i) show the spectra of the three bosonic isotopes, where the isotope shift is about 20 MHz per mass unit. The loading time of the reservoir is adjusted to compensate for the different natural abundances of the bosonic isotopes. The three sets in (a) through (c) are taken at different intensities; (a) $1\times10^{-4}\,I_{\rm sat}$, (b) $5\times10^{-4}\,I_{\rm sat}$, and (c) $1\times10^{-3}\,I_{\rm sat}$. The lineshapes of different isotopes for a given intensity are very similar, which allows for a precise determination of the isotope shift despite the asymmetric shape.

Panels (ii) show measurements on the fermionic isotope, taken with a typical intensity of $1\times10^{-3}\,I_{\rm sat}$. Note that the spectrum spans many GHz in frequency, and that the amplitude of the signal rises up to two orders of magnitude above the background. Note also the two overlapping lines in panel (b ii), which were discussed in Fig. 9.2(e). The $^3P_2 - {}^3D_3$ transition has the lowest repumping efficiency, as the probability of atoms in the $^3D_3$ state to decay into the $^3P_1$ state is relatively low. Instead, atoms might decay into another $^3P_2$ hyperfine state and be dark for the repumping light. Despite a careful search over more than 8 GHz, only four out of 15 lines could be detected. One might speculate that two strongest ones are the cycling $F = 5/2 \to F' = 3/2$ and $F = 13/2 \to F' = 15/2$ transitions, which would imply that the hyperfine structure of the $^3D_3$ state is inverted with an interaction constant $A \approx -150$. For a complete scan of the $^3P_2 - {}^3D_3$ transition, it would be necessary to perform repumping of atoms that have decayed into hyperfine states other than the initial one.

For the $^3P_2 - {}^3D_{(1,2)}$ transitions, we can identify each of the resonances by their relative positions, and subsequently calculate the interaction constants A and Q of the $^3D_{1,2}$ states

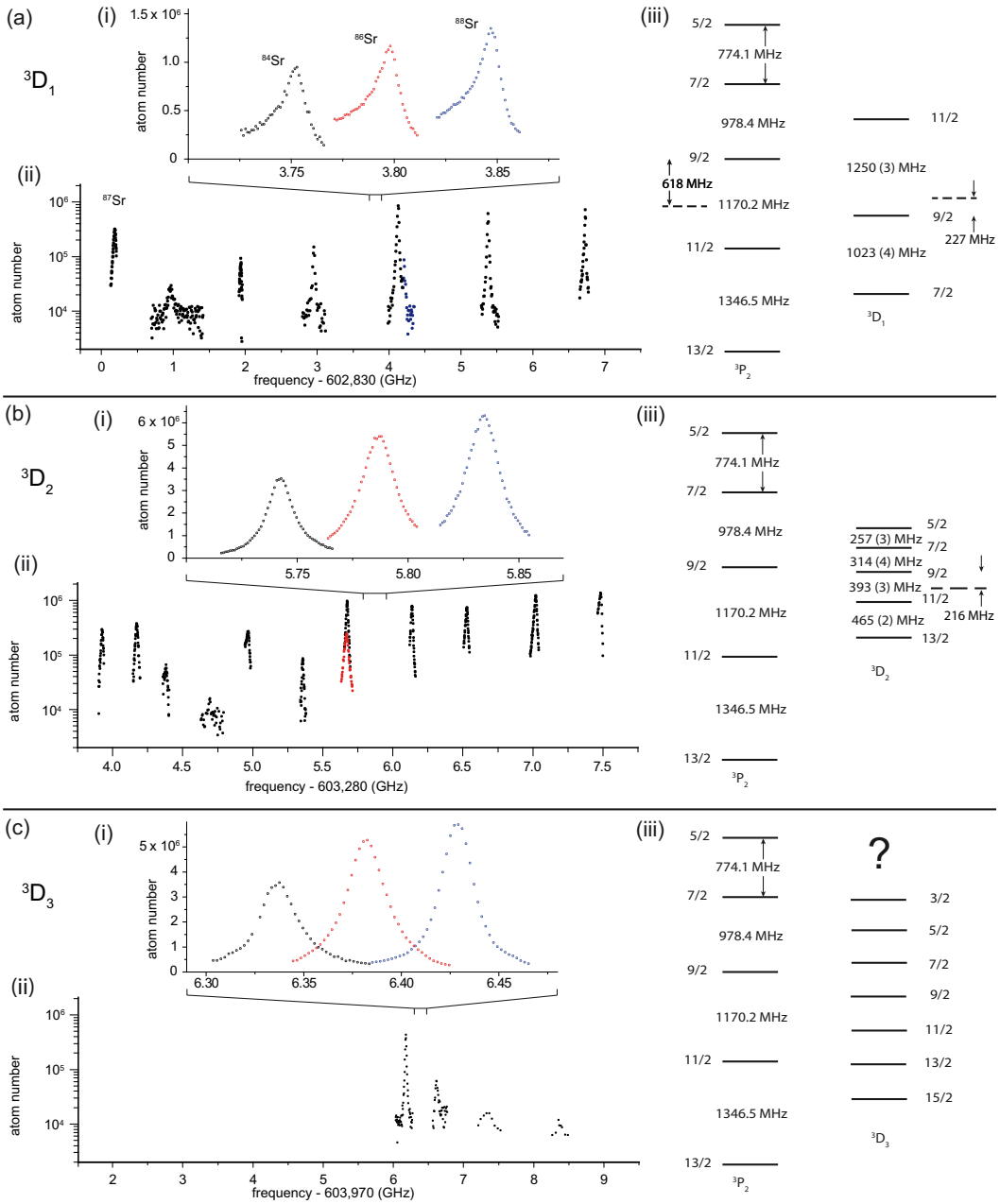

Figure 9.3: Spectroscopy data of the transitions from the $^3P_2$ to the (a) $^3D_1$, (b) $^3D_2$, and (c) $^3D_3$ states. Panels (i) show transitions of the bosonic isotopes ^{84}Sr (black symbols, left peak), ^{86}Sr (red, center), and ^{88}Sr (blue, right). Panels (ii) show scans of the fermionic ^{87}Sr isotope. Note that the feature around 4.1 GHz in panel (a ii) consists of two individual peaks. The separate measurement of the two overlapping lines in panel (b ii) around 5.67 GHz is discussed in Sec. 9.3. The frequency interval of panel (c ii) corresponds to the frequency range scanned in the measurement. For the two lines at highest frequency, the outcome of ten experimental runs have been averaged for each data point. Panels (iii) show the relative positions of the hyperfine states, where the dashed line indicates an assumed $I = 0$ state. The data in (c) is insufficient to determine the hyperfine structure.

using

$$\Delta E_{\mathrm{hfs}}/h = \frac{A}{2}K + \frac{Q}{2}\frac{\frac{3}{4}K(K+1) - I(I+1)J(J+1)}{I(2I-1)J(2J-1)}.$$

Here, $K = F(F+1) - I(I+1) - J(J+1)$, where $I = 9/2$ is the nuclear spin, J is the total angular momentum, and F denotes the hyperfine state, given by $\vec{F} = \vec{I} + \vec{J}$. The hyperfine structure of the $^3P_2$ state is known to the kHz-level [Hei77], and we fix these values for our calculation. The hyperfine structure is shown in panels (iii).

A compilation of the transition frequencies can be found in Tab. 9.2, and the deduced isotope shifts and interaction constants A and Q are compiled in Tab. 9.1. As discussed in Sec. 9.7, the absolute frequencies have an error of 2 MHz. The isotope shifts between the bosons can be measured to within 200 kHz. The measurement of the hyperfine structure of the fermionic isotope is more involved, leading to a larger error in the magnetic dipole and electric quadrupole interaction constants A and Q.

9.5 Is the $5s5p\,^3P_2 - 5s5d\,^3D_3$ transition cycling?

The $^3P_2 - {}^3D_3$ transitions are unique in that they are the only closed transitions originating from the ^3P manifold. There is an infinite ladder of $5snd\,^3D_3$ states reachable from the $5s5p\,^3P_2$ state, starting from $n = 4$. These transitions have been proposed as MOT transitions to cool atoms in the metastable $^3P_2$ state. Doppler cooling on one of them has been performed in calcium [Grü02], which has a very similar electronic structure to strontium. These transitions could potentially be used for fluorescence and absorption imaging as well. A recent publication on quantum computation with fermionic ^{87}Sr [Dal08] suggests the use of the $^3P_2, F = 13/2 \rightarrow {}^3D_3, F' = 15/2$ transition for fluorescence readout of atoms in the metastable states. For this application, the transition would need to be cycling. We will first determine the number of photons cycled on the $5s5p\,^3P_2 - 5s5p\,^3D_3$ transition, and comment on the potential usage of the other transitions later. The measurements presented in the following are performed with the bosonic isotope ^{88}Sr, since operation with the fermionic isotope is complicated by the hyperfine structure and multitude of m_F states.

The $^3P_2 - {}^3D_3$ transition is certainly not completely cycling, as can be inferred from the spectroscopy described in Sec. 9.4: obviously, some atoms are transferred into the $^1S_0$ ground state. One might consider various mechanisms, such as (i) direct decay into the $^3P_1$ state via higher-order processes, or (ii) decay along various dipole-allowed pathways. Case (ii) can be visualized by the level scheme in Fig. 9.1: There are various decay paths from the $5s5d\,^3D_3$ state into the adjacent $5s6p\,^3P_2$ state and further into either the $5s6s\,^3S_1$ or $5s4d\,^3D_{1,2,3}$ states and into the $5s5p\,^3P_{0,1,2}$ states. Additional channels are opened starting from the $4s5p\,^3F_{2,3}$ states. The decay from the $5s5d\,^3D_3$ state into states outside of the $5s5p\,^3P$ manifold should be small due to the large difference in the energy of the released photon, but coupling between the $5s5d\,^3D_3$ state and adjacent states could be enhanced by black-body radiation[1].

[1] As a coincidence, the energy difference of 1050 cm^{-1} between the $5s6p\,^3D_2$ and $5s5d\,^3D_3$ states corresponds exactly to the maximum intensity of the black body radiation spectrum at room temperature. It has been observed in other systems that black body radiation can redistribute population between near-degenerate levels [Gue07], and we assume a similar process here.

84		602,833,752.9 (2.0) MHz
86	$^3\mathbf{D_1}$	602,833,798.1 (2.0) MHz
88		602,833,846.9 (2.0) MHz
	$5/2 \rightarrow 7/2$	602,830,186.7 (2.0) MHz
	$7/2 \rightarrow 7/2$	602,830,963.6 (2.0) MHz
	$7/2 \rightarrow 9/2$	not observed
	$9/2 \rightarrow 7/2$	602,831,939.1 (2.0) MHz
87	$9/2 \rightarrow 9/2$	602,832,967.1 (2.0) MHz
	$9/2 \rightarrow 11/2$	602,834,213.5 (2.0) MHz
	$11/2 \rightarrow 9/2$	602,834,129.3 (2.0) MHz
	$11/2 \rightarrow 11/2$	602,835,381.1 (2.0) MHz
	$13/2 \rightarrow 11/2$	602,836,730.7 (2.0) MHz
84		603,285,688.0 (2.0) MHz
86	$^3\mathbf{D_2}$	603,285,733.3 (2.0) MHz
88		603,285,780.8 (2.0) MHz
	$5/2 \rightarrow 5/2$	603,284,178.9 (2.0) MHz
	$5/2 \rightarrow 7/2$	603,283,927.0 (2.0) MHz
	$7/2 \rightarrow 5/2$	not observed
	$7/2 \rightarrow 7/2$	603,284,694.0 (2.0) MHz
	$7/2 \rightarrow 9/2$	603,284,381.8 (2.0) MHz
	$9/2 \rightarrow 7/2$	603,285,670.6 (2.0) MHz
87	$9/2 \rightarrow 9/2$	603,285,358.5 (2.0) MHz
	$9/2 \rightarrow 11/2$	603,284,969.3 (2.0) MHz
	$11/2 \rightarrow 9/2$	603,286,530.8 (2.0) MHz
	$11/2 \rightarrow 11/2$	603,286,133.1 (2.0) MHz
	$11/2 \rightarrow 13/2$	603,285,671.5 (2.0) MHz
	$13/2 \rightarrow 11/2$	603,287,485.6 (2.0) MHz
	$13/2 \rightarrow 13/2$	603,287,021.1 (2.0) MHz
84		603,976,337.0 (2.0) MHz
86	$^3\mathbf{D_3}$	603,976,382.0 (2.0) MHz
88		603,976,428.6 (2.0) MHz
	?	603,976,180.8 (2.0) MHz
87	?	603,976,619.5 (2.0) MHz
	?	603,977,350 (10) MHZ
	?	603,978,375 (10) MHz

Table 9.2: Measured frequencies of the three $5s5p\,^3P_2 - 5s5d\,^3D_{1,2,3}$ transitions.

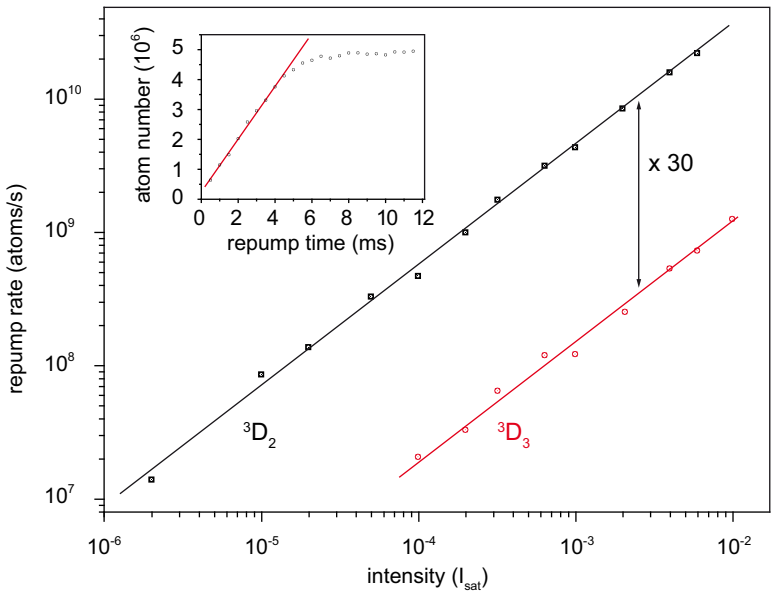

Figure 9.4: Repump rate in dependence of light intensity. The number of atoms repumped into the $^1S_0$ ground state is proportional to the repump time before reaching saturation (inset, taken on the $^3P_2 - {}^3D_3$ transition at $I = 1 \times 10^{-2}\, I_{\mathrm{sat}}$). This rate is measured for a large range of intensities on both the $^3P_2 - {}^3D_2$ and $^3P_2 - {}^3D_3$ transitions.

It is now our goal to estimate the branching ratio of atoms in the $5s5d\,^3D_3$ state to decay into the $^3P_2$ state, or to decay into other states. To do so, we first measure the number of atoms repumped on the $^3P_2 - {}^3D_2$ transition in dependence of repump time. For low intensities and short repumping times, there is a linear dependence of repumped atoms on repump time until the atom number saturates, see the inset of Fig. 9.4. We perform this measurement for a wide range of repumping intensities, and plot the rate of repumping vs intensity, as shown in Fig. 9.4. Next, we perform the same experiment on the $^3P_2 - {}^3D_3$ transition. We find that 30(1)-times the light intensity is needed to achieve the same repumping rate.

Let us now revisit the other transitions into the $5snd\,^3D_3$ states, with $n \geq 4$. The $5s5p\,^3P_2 - 5s4d\,^3D_3$ transition at $2.92\,\mu$m has a linewidth of only 50 kHz, making it well suited for operation of a MOT due to the combination of low Doppler and recoil limit. There are no intermediate states between the two, such that this transition is indeed cycling. It is also the only transition originating from the $^3P_2$ state (except for the open transition into the $5s6s\,^3S_1$ state) for which the absorption of two photons does not ionize the atom. Apart from the fact that lasers at this frequency and linewidth are difficult to operate, efficient MOT operation might be hindered by inelastic losses [Tra09]. The large wavelength brings about a substantial decrease in imaging resolution compared to the 497-nm transition, which might be relevant for single-atom detection. Further, CCD chips based on InGaAs technology do not operate at this wavelength range, but alternative technologies do exist.

The $5s5p\,^3P_2 - 5s5d\,^3D_3$ transition at 497 nm, which has been investigated in this chapter, is probably not well suited for MOT operation due to nonzero branching into other states

and ready ionization upon absorption of two photons. Using this transition for fluorescence detection might require the repumping of atoms that have decayed out of the fluorescence cycle.

The $5s5p\,^3P_2 - 5s6d\,^3D_3$ transition is situated at 403.15 nm, where suitable laser diodes with high output power are available, thus circumventing the need of frequency doubling[2]. The effect of nonzero branching ratio into states other than the $5s5p\,^3P_2$ state should be even larger than for the $5s6d\,^3P_3$ state, since further potential decay paths open up: the $5s7p\,^3P_2$ state is located only 245.73 cm^{-1}, the $5s4f\,^3F_{2,3,4}$ states are located about 950 cm^{-1} below the $5s6d\,^3P_3$ state, see Fig. 9.1. Going up the ladder of $5snd\,^3D_3$ states, this branching is likely to become more and more unfavorable.

9.6 Conclusion

In conclusion, we have perfomed spectroscopy on the $5s5p\,^3P_2 - 5s5d\,^3D_{1,2,3}$ transitions in strontium and determined the isotope shifts and A and Q hyperfine parameters. We have shown that the $5s5p\,^3P_2 - 5s5d\,^3D_3$ transition is not completely cycling, which might have implications for the usage of this transition for fluorescence detection.

The general scheme of performing spectroscopy on atoms stored in a metastable state can be applied to many other species as well. Elements such as magnesium, calcium [Han05], and ytterbium have an electronic structure very similar to strontium. More complex atoms, such as the rare-earth species [Han04] dysprosium [Lu11b], holmium, erbium [McC06, Aik12], and thulium [Suk10], which are currently under investigation, all have a wealth of metastable states which can be trapped in the magnetic field of a MOT.

9.7 Error analysis

The spectroscopy light at 497 nm is generated by a frequency-doubled diode laser, which delivers about 40 mW of green light. The IR laser is locked to a stable reference cavity, which has a drift of typically 100 kHz per hour, mainly due to piezo creep and possibly thermal drift. The absolute frequency is constantly monitored on a High Finesse WSU/2 wavemeter. The wavemeter is calibrated by a Ti:Saph laser at 729 nm. This laser is locked to a high-finesse cavity with a drift rate of 10 Hz per hour. The absolute frequency is determined by spectroscopy of the $4s\,^2S_{1/2} - 3d\,^2D_{5/2}$ transition in the $^{40}Ca^+$ ion at 432 042 129 776 393.2 (1.0) Hz [Chw09]. Calibration of the wavemeter has an (in)accuracy of 500 kHz, which can be reduced substantially by averaging over many calibrations. If not constantly re-calibrated, the wavemeter drifts by about 100 kHz per hour. A possible inaccuracy of the wavemeter, used about 250 nm away from the calibration wavelength, is not considered in this analysis.

The green light is passed through a cascade of four acousto-optic modulators (AOMs) in double-pass configuration. The AOMs have a design frequency of 350 MHz and a bandwidth of about 150 MHz, resulting an overall scan range of 1.2 GHz. The RF used to drive the

[2]It is worth mentioning that the $5s5p\,^3P_2 - 5s6d\,^3D_2$ transition at 403.15 nm should be well suited for repumping, where powerful and inexpensive laser diodes available. To our knowledge, this transition has not been used so far.

AOMs is generated by direct digital synthesizers (DDSs), which are referenced to the global positioning system (GPS) and have negligible error. The laser light itself has a linewidth on the order of 1 MHz, about 1 mW is available for the experiment and collimated to a beam of 18 mm diameter to interrogate the atoms.

The dominant uncertainty in our experiment stems from the accuracy and drift of the wavemeter. The accuracy of the absolute transition frequency is limited to the 10 MHz accuracy of the wavemeter. For the measurement of the isotope shifts between the bosons, the wavemeter is carefully calibrated and then left free-running. The complete spectroscopy scan is then performed within less than half an hour, in which the wavemeter drifts by much less than 100 kHz. A complete scan of all the hyperfine transitions of the fermionic isotope takes about one day, and the wavemeter might drift by up to 1 MHz in this period. Note that the error on the frequency of the green light is twice that of the IR light, which we monitor on the wavemeter. As a conservative estimate, the isotope shifts between the bosons can be measured with a precision of about 200 kHz, and the hyperfine splittings can be determined to about 4 MHz. We repetitively measure certain transitions over the course of many days to exclude any long-term drifts and find the scatter to be within less than 1 MHz.

The data is fit by a Lorentzian profile, where deviations from a Lorentzian lineshape are visible only for extremely low repumping intensities. The error in the determination of the centriod ranges between 50 kHz and a few MHz, depending on the signal strength. Only for weak transitions does this error dominate over the wavemeter uncertainty.

Chapter 10

The lattice

Many experiments targeted at the study of magnetism, topological phases, and related topics all take place on a lattice geometry. The sites of an optical lattice also form perfect cradles for the preparation of rovibronic ground-state molecules. In other words: the implementation of an optical lattice is absolutely necessary to pursue the proposals laid out in Chpt. 1. Optical lattices are usually formed by the interference of two counter-propagating laser beams, forming a standing wave. The light is red- or blue-detuned to the principal transition, thereby forming a periodic potential for the atoms, which accumulate in the potential wells.

The work on optical lattices has been pioneered by the MPQ group in Munich [Gre02], and many experiments around the world are now equipped with such lattices. As the first alkaline-earth species, both bosonic and fermionic Yb atoms have been loaded into the ground state of 3D optical lattices [Fuk09a, Tai10]. These systems are perfectly suited for the study and simulation of solid-state phenomena, where the light field takes the role of the ionic crystal and the atoms take the role of the electrons. In contrast to real solid materials, e.g. semi-conductors, the optical lattice is free of defects, and many parameters, such as interactions and lattice depth, can be tuned. The system is governed by the interplay between two energy contributions: the energy cost required to place two atoms on a common lattice site (on-site interaction energy U) and the energy required for an atom to hop from one lattice site to the next (hopping matrix element J). Together, we find the well-known Bose-Hubbard Hamiltonian

$$\mathbf{H} = -J \sum_{\langle i,j \rangle} a_i^\dagger a_j + \sum_i \epsilon_i a_i^\dagger a_i + \frac{U}{2} \sum_i n_i(n_i - 1), \tag{10.1}$$

where $n_i = a_i^\dagger a_i$ is the occupation of lattice site i, ϵ_i is the local energy on a lattice site, and $\langle i, j \rangle$ denotes the sum over all neighboring lattice sites. There exists extensive literature for further treatment, e.g. Ref. [Blo08] and references therein.

10.1 Experimental techniques

The experimental setup of our 3D lattice at 532 nm has already been described in Chpt. 3. We will start out by establishing some experimental techniques common to all lattice experiments.

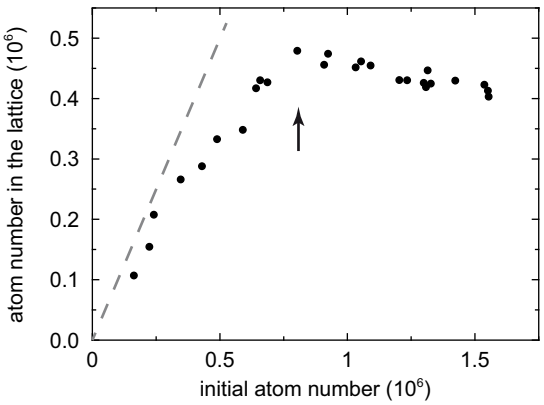

Figure 10.1: Evidence of triply occupied sites: We measure the number of atoms recovered after adiabatic loading into a deep lattice. A sharp drop in recovered atom number for samples of more than 7×10^5 atoms (indicated by the arrow) points to the formation of triply occupied sites, in which atoms undergo rapid 3-body recombination. The dashed grey curve is a guide to the eye indicating zero losses.

Loading of the lattice — While we observe only little heating when loading ^{84}Sr atoms into and out of the lattice, we do observe pronounced atom loss when attempting to increase the number of atoms in the lattice; see Fig. 10.1. For initial atom numbers below about 7×10^5, the number of recovered atoms is constantly lower than the initial one, which we attribute to 3-body losses in the superfluid bulk as the density increases through the additional confinement of the lattice beams, and possibly scattering of lattice photons. For higher atom number, however, there is dramatic and sudden break-down in atom number. We attribute this loss to the formation of triply occupied sites in the central region, which rapidly eliminate themselves through inelastic 3-body recombination. We verify that the loss appears already during loading of the lattice (i.e. on timescales below 10 ms), not during a hold time in the lattice. The lifetime of the remaining atoms in the lattice is up to 10 s, depending on the atom number.

We set up a simple model to calculate the "wedding cake" structure in dependence of atom number [DeM05, She10], and find the formation of the $n = 3$ Mott shell (i.e. *triply* occupied sites) to set in at an initial atom number of about 1.5×10^6 atoms, in rough agreement with the observation. As we will see in the next chapter, photoassociation can be used to determine the number of atoms on *doubly* occupied sites. All atoms surviving the lattice loading and subsequent exposure to photoassociation light must be located on a *singly* occupied site. These three values give a good and model-independent understanding of the atom distribution in the lattice. Note that our lattice sites are a factor of $2^3 = 8$ smaller than those of a 1064-nm lattice. This requires much higher initial densities to reach large occupation numbers, and it seems to reduce the lifetime of triply occupied sites tremendously.

Lattice depth calibration — We need a way to quantify the lattice depth, which is usually stated in units of the recoil energy $E_{\mathrm{rec}} = \hbar^2 k_L^2 / 2m$, where $k_L = 2\pi/\lambda_L$ is the lattice wave vector. This is done by measuring the energy gap ΔE between the zeroth and second

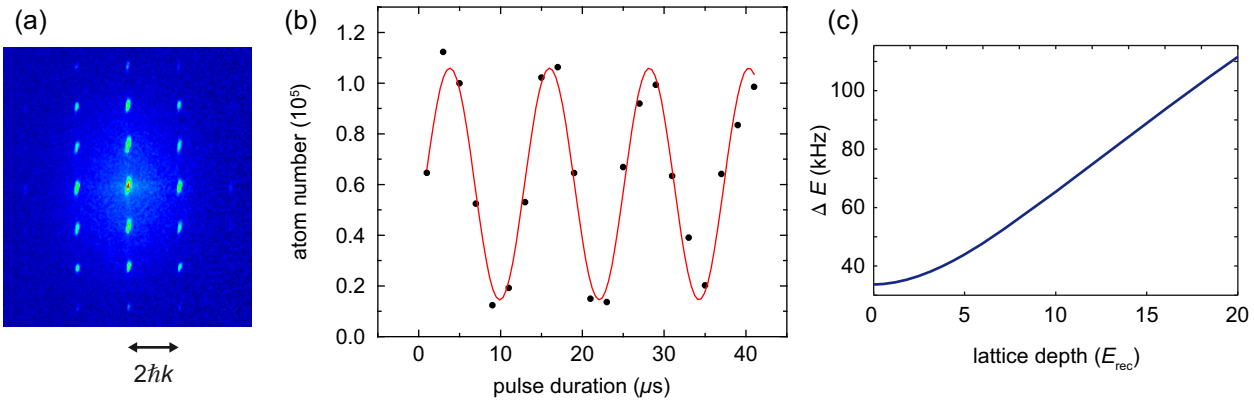

Figure 10.2: Lattice depth calibration. (a) Flashing the two lattice beams orthogonal to the imaging axis for a few μs reveals a beautiful diffraction pattern. (b) The population of the diffraction peaks is modulated with the duration of the pulse. The modulation frequency ω is directly related to the energy difference between the zeroth and second band as $\Delta E = \hbar\omega$, with only small contributions from higher bands for low enough lattice depths. (c) The lattice depth given in E_{rec} can be related to ΔE via a simple band structure calculation.

band, and relating this energy to the lattice depth via a simple band structure calculation [Ovc99, Den02]; see Fig. 10.2. The energy gap is measured well in the Kapitza-Dirac regime: the lattice is flashed on for a variable, very short time, and the population of the diffraction peaks is modulated at the frequency corresponding to ΔE [1]. The uncertainty in the measured ΔE is about 1%, and the uncertainty of the band structure calculation is about the same value, such that this simple method is accurate to within a few percent. The lattice depth is measured independently for all three lattice beams, and the power of the beams is set to obtain an equal depth in all directions.

Band mapping technique — An important technique for lattice experiments is band mapping. Here, the quasi-momentum of atoms in the lattice is mapped onto real momentum by a fast ramp-down of the lattice [Gre01, Köh05]. The ramping lasts a few ms and is adiabatic on the timescale of the individual lattice sites ($\mathcal{O}(10\,\mathrm{kHz})$), but fast on the timescale of the external confinement ($\mathcal{O}(10...100\,\mathrm{Hz})$). During the subsequent expansion, atoms of the nth band appear in the $(n+1)$th Brillouin zone. A sufficiently cold gas does not fill the lowest lattice band, and the TOF image looks unspectacular. A thermal gas however, which fills a good part of the lowest band, results in an entirely filled first Brillouin zone, as shown in Fig. 10.3(b). Even hotter atoms might breach the band gap and populate the first excited band, visible as the second Brillouin zone in Fig. 10.3(c).

When imaging our atoms, we are looking at an edge of the lattice unit cell, not onto a face as in most lattice experiments. While this is true for both of our imaging axes, we will present only images from the horizontal imaging system here. Figure 10.3(a) clarifies the geometry.

[1] The short pulse is analogous to a thin grating for a beam of photons or massive particles.

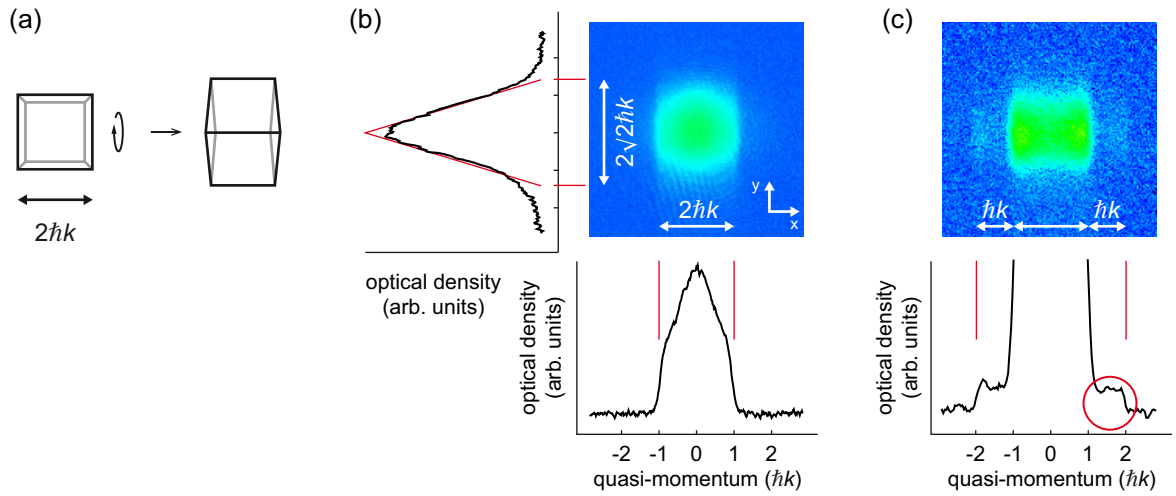

Figure 10.3: The band mapping technique. (a) Most experiments image the atoms looking at the face of a cubic unit cell (left), whereas we are looking at an edge (right). (b) An evenly filled first Brillouin zone would not appear as a square, but as a box-shaped density distribution of width $2\hbar k$ in the x-direction and as a triangle of width $2\sqrt{2}\hbar k$ in the y-direction. The Brillouin zone shown here is not completely filled. (c) Thermal atoms might populate the first excited band, visible here as a faint population of the second Brillouin zone, which extends between $\hbar k$ and $2\hbar k$ in the x-direction and is indicated by the red circle. Some of the atoms in this image were located on doubly occupied sites and formed repulsively bound pairs; see Fig. 12.4 for a much clearer signal. The TOF, color scale, and scale of the optical density are different to (b) in order to increase the contrast of small signals. Both images are averaged over 20 experimental runs.

10.2 Mott-insulator transition

As a first experiment using the lattice, we will present the famous superfluid-to-Mott insulator transition, observed for the first time in strontium. We start out with a pure ^{84}Sr BEC in a crossed dipole trap. The lattice depth is adiabatically increased from zero to $19\,E_{\mathrm{rec}}$, held there for a short time, and decreased to zero again. Snapshots of the momentum distribution are taken at various times throughout the cycle and shown in Fig. 10.4. For small lattice depths, the BEC remains superfluid, and the periodic potential is a small perturbation. Particles seek to minimize their kinetic energy by spreading out over the lattice, establishing a fixed phase relation across the sample. We observe the appearance of diffraction peaks, caused by the constructive interference of atoms from all lattice sites; equivalent to the diffraction of light from a periodic structure. As the lattice depth increases, atoms begin to localize on individual lattice sites, and the phase relation dwindles away: the visibility of the diffraction pattern drops. For the very deep lattice, the atom number on each lattice site is a well-defined Fock state, and the atomic wavepacket is tightly confined to a specific lattice site; all phase coherence between lattice sites is lost. This is called the Mott-insulator (MI) regime, detected by the complete disappearance of interference peaks upon release from the trap. The external potential leads to a wedding-cake structure with plateaus of uniform

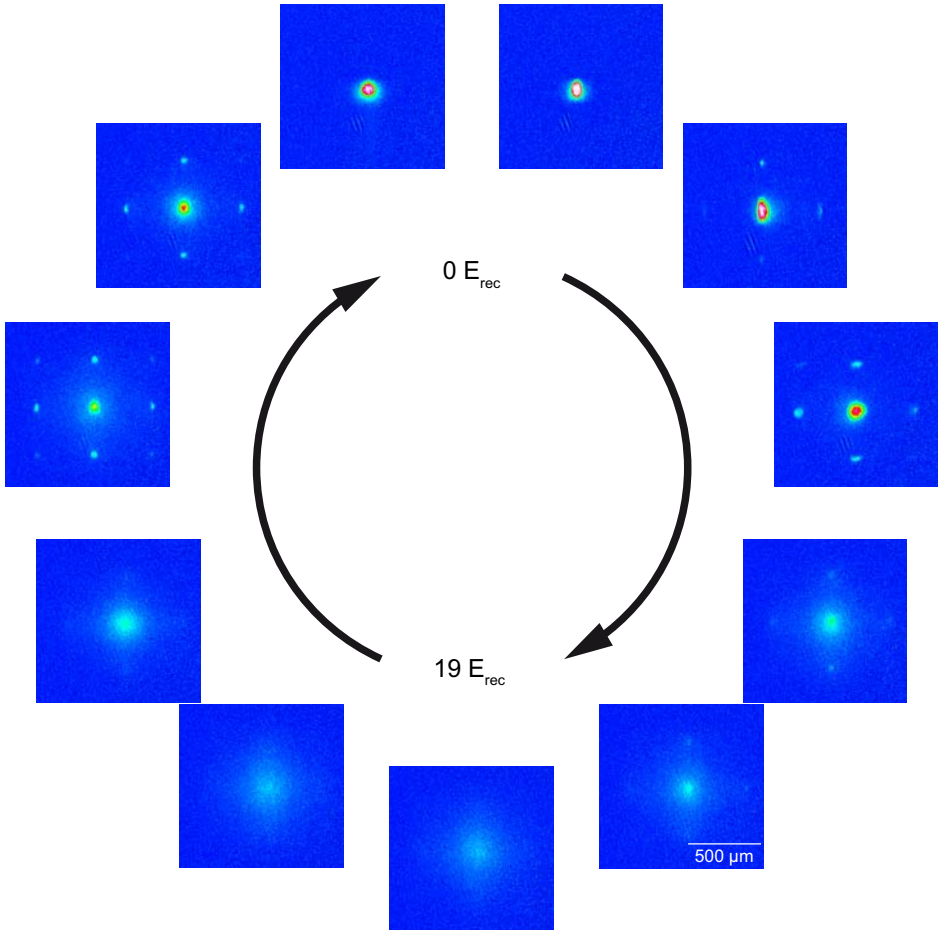

Figure 10.4: The MI transition in ^{84}Sr. Starting from the top right, the lattice depth is adiabatically increased, and we observe the appearance of superfluid diffraction peaks. For deep lattices (bottom), the visibility of diffraction peaks vanishes, and the atoms are in the insulating state. The rebirth of a BEC upon lowering of the lattice (top left) shows that the heating of the lattice is indeed small. The TOF is 24 ms.

filling n and superfluid layers in between.

As the lattice depth is lowered again, the sample becomes superfluid again, and phase coherence across the sample is regained: the original BEC forms again, provided the ramping was adiabatic and insignificant heating was applied to the system.

The images shown in Fig. 10.4 are strong evidence, but not sufficient proof of the MI transition. The Mott state is characterized by large regions of lattice sites with equal (i.e. at least unity) filling, but corresponding information is not contained in these images. We can, however, deduce the existence of a dense central region in an indirect way. We observe the formation of triply occupied sites by strong atom loss, and the occupation of doubly occupied sites by photoassociation measurements. The detection of such multiply occupied sites affirms the existence of large $n = 1$ and $n = 2$ Mott shells.

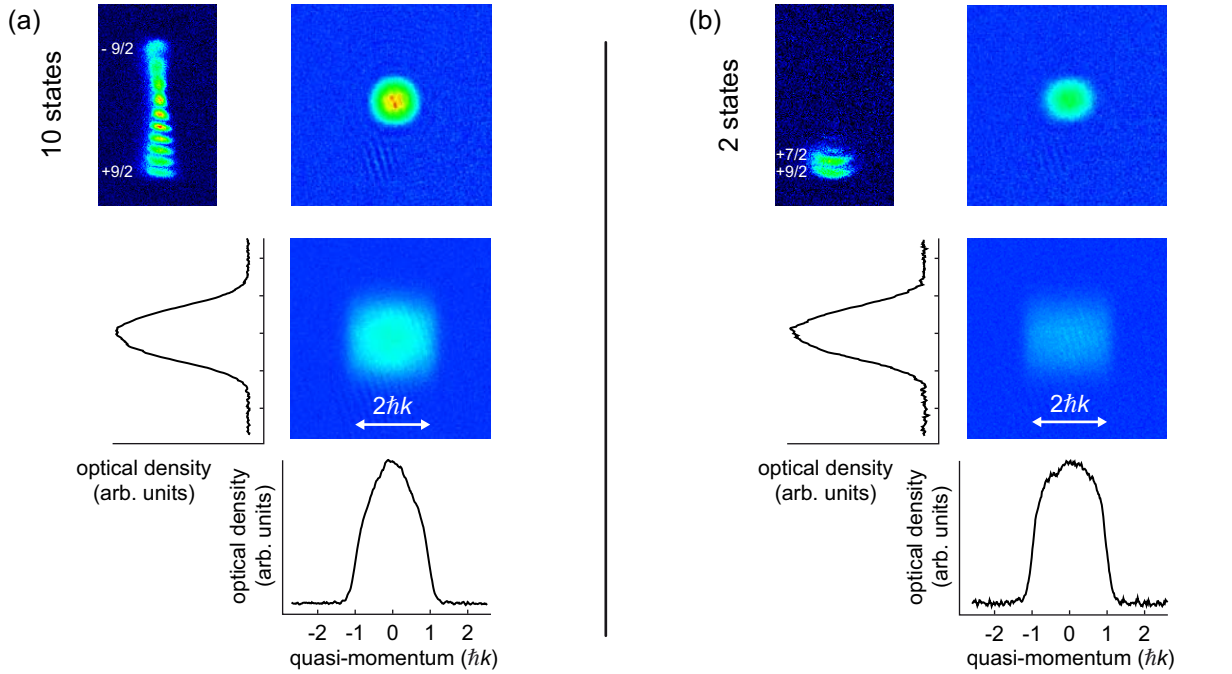

Figure 10.5: Fermions in a lattice with (a) 10 spin states and (b) only 2 spin states. The number of occupied spin states is visualized by the OSG technique. Absorption images of the Fermi gases prior to loading into the lattice are shown in the top row and indicate a similar degree of degeneracy of around $0.15\,T/T_F$. The band mapping technique reveals a population of the lowest Bloch band. There are about twice as many atoms per spin state in case (b) than in case (a), giving rise to a more uniform filling of the first Brillouin zone. All images except for the OSG ones are taken after 24 ms TOF and have the same color scale, the band mapping images are averaged over five experimental runs.

10.3 Fermions on a lattice

An ultracold gas of fermions loaded into an optical lattice allows for a realization of the famous Fermi-Hubbard model. Ground-breaking experiments with alkali atoms have been performed, establishing fundamental techniques such as the determination of the doublon occupancy, and measuring basic properties like the incompressibility of a fermionic lattice gas (see Refs. [Jör08, Sch08] and Refs. [Blo08, Ess10] for reviews and further references). All of the proposals for alkaline-earth systems outlined in Chpt. 1.1 utilize fermions on a lattice as the underlying structure. First experiments with alkaline-earth atoms have been performed with Yb [Tai10] and recently demonstrated Pomeranchuk cooling, an important step towards the envisioned SU(N) Hubbard systems [Tai12].

For the first time, we will now present the loading of degenerate fermionic ^{87}Sr atoms into a lattice. The maximum number of spin states in Sr is larger than in Yb, which extends the SU(N) systems up to $N = 10$ and might allow to reach lower temperatures [Bon12].

In a first experiment, we evaporate a mixture of $N = 10$ spin states to a degeneracy of $T/T_F = 0.14(2)$ and load the sample of 28 000 atoms per spin state into a lattice with a

depth of about 16 E_{rec}. We perform band mapping [Köh05] and observe a partially-filled first Brillouin zone; see Fig. 10.5(a). The occupation of higher momenta is not caused by thermal atoms, but a beautiful signature of the finite Fermi momentum even for $T \to 0$. The loading into and out of the lattice is not entirely adiabatic, and we observe a decrease in degeneracy to $T/T_F = 0.30(5)$ as the lattice is ramped down again. This heating is comparable to previous experiments with alkali atoms, and the sample remains in the degenerate regime throughout the sequence.

In a second experiment, we optically pump the atoms into a mixture of only $N = 2$ spin states before evaporation. All other experimental parameters, such as the final trap depth, the lattice depth, and the timing are identical to the previous case. Evaporation proceeds a little less efficient, and we obtain 62 000 atoms per spin state at $T/T_F = 0.17(3)$. The larger atom number per spin state leads to an increased filling of the first Brillouin zone, as nicely seen by a comparison of Figs. 10.5(a) and (b). The heating during the sequence seems to be smaller than in the case of $N = 10$, and we measure a degeneracy of $T/T_F = 0.20(2)$ after the lattice ramp-down. While our two measurements are not exactly identical, we note that recent experiments by the Kyoto group have shown larger heating rates for larger N as well.

10.4 Spatial Pauli blocking

One of the first experiments we performed in the lattice was an attempt to directly observe spatial Pauli blocking, as suggested recently [San11]. In very simplified words, the idea is the following: two fermionic atoms are prepared on the same lattice site: one is in an excited state $|e\rangle$, the other in the ground state $|g\rangle$, both in the lowest band $|0\rangle$. The excited atom sure wants to decay, but the ground state $|g, 0\rangle$ is already occupied, and it eventually has to decay into the first excited band $|g, 1\rangle$, but this decay is reduced by a factor η^2; see Fig. 10.6(a). Here, η is the Lamb-Dicke parameter and compares the harmonic oscillator length with the wavelength of the probe light, $\eta = 2\pi l_{ho}/\lambda$. In essence, this experiment is a modification of the question "What does an excited fermion do if all states of the Fermi sea it seeks to decay into are already occupied?", raised in Ref. [Bus98] for fermions in the bulk.

The original proposal suggests the $^3P_0$ clock state as the excited state. The extremely long lifetime could be quenched to experimentally accessible timescales by coupling to the $^1P_1$ state. The lattice would be operated on the magic wavelength, such that the lattice potential is identical for the $^1S_0$ and $^3P_0$ states. In our present experimental setup, we lack both the magic wavelength lattice and the clock laser to coherently excite atoms into the $^3P_0$ state. Instead, we chose the $^3P_1$ state as $|e\rangle$, and we work at a moderate depth of about 15 E_{rec} in our 532-nm lattice.

The experimental sequence is as follows: A sample of a few 10^6 atoms of ^{87}Sr is prepared in an incoherent mixture of $m_F = 7/2$ and $m_F = 9/2$ states, evaporated into degeneracy, and loaded into the 3D lattice. We then optically pump the $m_F = 9/2$ atoms into the $^3P_1, |F' = 9/2, m_{F'} = 9/2\rangle$ state with a short pulse. The natural lifetime of this state is 21 μs, and we measure the re-appearance of these atoms in the $^1S_0$ state using red absorption imaging; see Chpt. 7. The excited atom can decay into the $m_F = 7/2$ and $m_F = 9/2$ ground states, and provided that this atom sits on a doubly-occupied lattice site with the companion

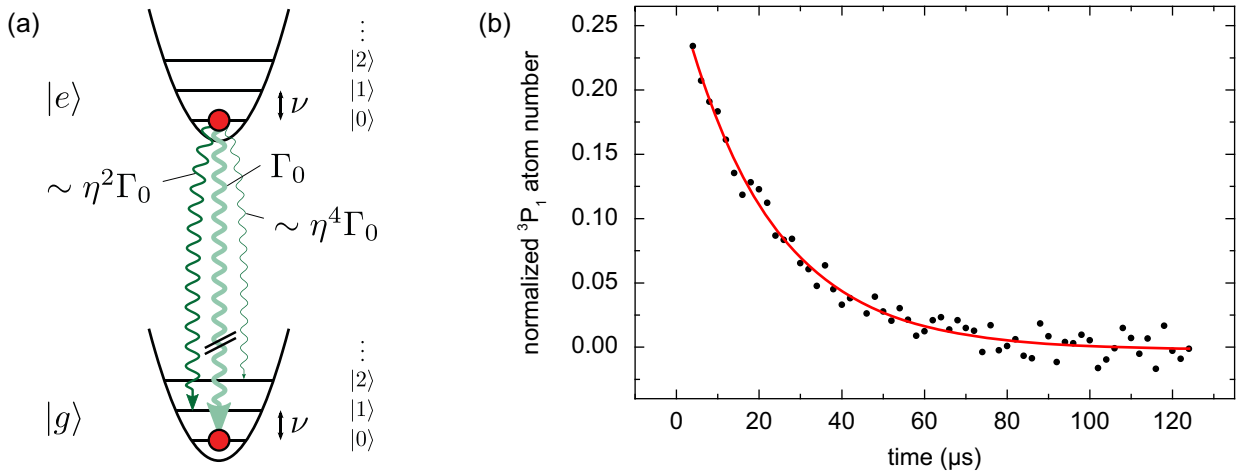

Figure 10.6: (a) Scheme to observe spatial Pauli blocking: Two identical fermionic atoms prepared in the internal excited state $|e\rangle$ and the internal ground state $|g\rangle$ experience the same external harmonic oscillator potential. In the Lamb-Dicke limit ($\eta \ll 1$), the dominant decay channel for a single particle $|e,0\rangle \rightarrow |g,0\rangle$ with a rate Γ_0 is now blocked by the ground-state atom due to the Pauli exclusion principle. The excited atom decays under change of its motional state with a rate that is reduced of order η^2. The decay rate Γ_0 is smaller than the vibrational spacing ν. (Image and caption adapted from [San11].) (b) Typical lifetime measurement of atoms in the $^3P_1, |F' = 9/2, m_{F'} = 9/2\rangle$ state. Here, the lifetime is $22.1(9)\,\mu$s. The data is obtained by measuring the appearance of atoms $N(t)$ in the $^1S_0$ state, normalizing it to the reference value N_0 for long wait times, and plotting $(1 - N/N_0)$ as the decay of the $^3P_1$ state.

atom in the $m_F = 7/2$ state, then this decay path would be blocked and might lead to an increased lifetime in the $^3P_1$ state. It is this increase in lifetime of a fraction of the $^3P_1$ atoms that we seek to measure.

Experimentally, we measure the time evolution in the number of atoms in the $^1S_0, |m_F = 9/2\rangle$ state following the optical pumping, and from these values deduce the number of atoms in the $^3P_1$ state; see Fig. 10.6(b). In addition, we perform reference measurements with a spin-polarized sample of thermal $m_F = 9/2$ atoms in the bulk. About 400 data points are taken to reduce the statistical uncertainty. Indeed, we find the lifetime of the excited atoms in the lattice configuration to be increased by about 1.5%. This value, however, is significantly smaller than our uncertainty of about 15%, and future experiments with a proper setup are required for a solid investigation.

10.5 Momentum state crystals revisited

In Chpt. 2.7, we looked into momentum state crystals, formed by multiple cycles of absorption and spontaneous emission of photons close to the $^1S_0 - {}^3P_1$ intercombination line. The position of the atoms after TOF resembled the corners of a cubic unit cell. Earlier in this chapter (Sec. 10.1), we worked in a very different regime, and observed the formation of

a different type of lattice: an extended lattice with lattice spacing $2\hbar k$, formed upon short flashing of the lattice beams.

Here, we are working again in the Kapitza-Dirac regime, very different to the measurements of Chpt. 2.7. A BEC is released from the dipole trap and immediately subjected to a very short and strong pulse of light red-detuned to the ${}^1S_0 - {}^3P_1$ transition by 500 kHz. The light impinges on the atoms from three retroreflected, mutually orthogonal "lattice" beams, which are our standard circularly polarized MOT beams. The intensity is a few $1000\, I_{\mathrm{sat}}$, and the duration is $10\,\mu$s. All beams are derived from the same master laser and have the same frequency, such that the atoms can absorb photons from and re-emit them into the mode of any beam.

We can vary the number of beam axes used: with only one beam orthogonal to the imaging axis (here the y-axis; see Fig. 10.7(a)), atoms gain momenta $\pm\, n_y\, 2\,\hbar k\, \vec{e}_y$ ($n_i \in \mathbb{N}$) along the direction of the beam. As we add another beam in the x-axis, we obtain an unfamiliar diffraction pattern: not only the $\pm\, n_x\, 2\,\hbar k\, \vec{e}_x \,\pm\, n_y\, 2\,\hbar k\, \vec{e}_y$ momenta are found, but also the $\pm\, m_x\, \hbar k\, \vec{e}_x \,\pm\, m_y\, \hbar k\, \vec{e}_y$ momenta for even values of $(m_x + m_y)$; see Fig. 10.7(b).

This observation can be generalized to three dimensions by adding a beam along the imaging axis; see Fig. 10.7(c). Besides the well-known momenta $\sum_{i=x,y,z} n_i\, 2\,\hbar k\, \vec{e}_i$, also the momenta $\sum_{i=x,y,z} m_i\, \hbar k\, \vec{e}_i$ with even values of $\sum_{i=x,y,z} m_i$ are assumed. The reasons that these additional peaks are not observed in conventional lattices are the frequency difference and the orthogonal polarization between orthogonal lattice beams, which do not allow the atoms to absorb a photon from one beam and emit it into another beam. One can also take the perspective of atoms being diffracted from the standing wave: in this view, orthogonal beams with a frequency difference of many MHz form a fast-moving interference pattern that cannot be resolved by the atoms. This experiment is again reminiscent of the seminal work on superradiance in elongated BECs [Ino99], which also showed well-defined momentum peaks upon scattering of photons. In that case, however, the preferential direction of photon emission was entirely given by the density distribution of the BEC.

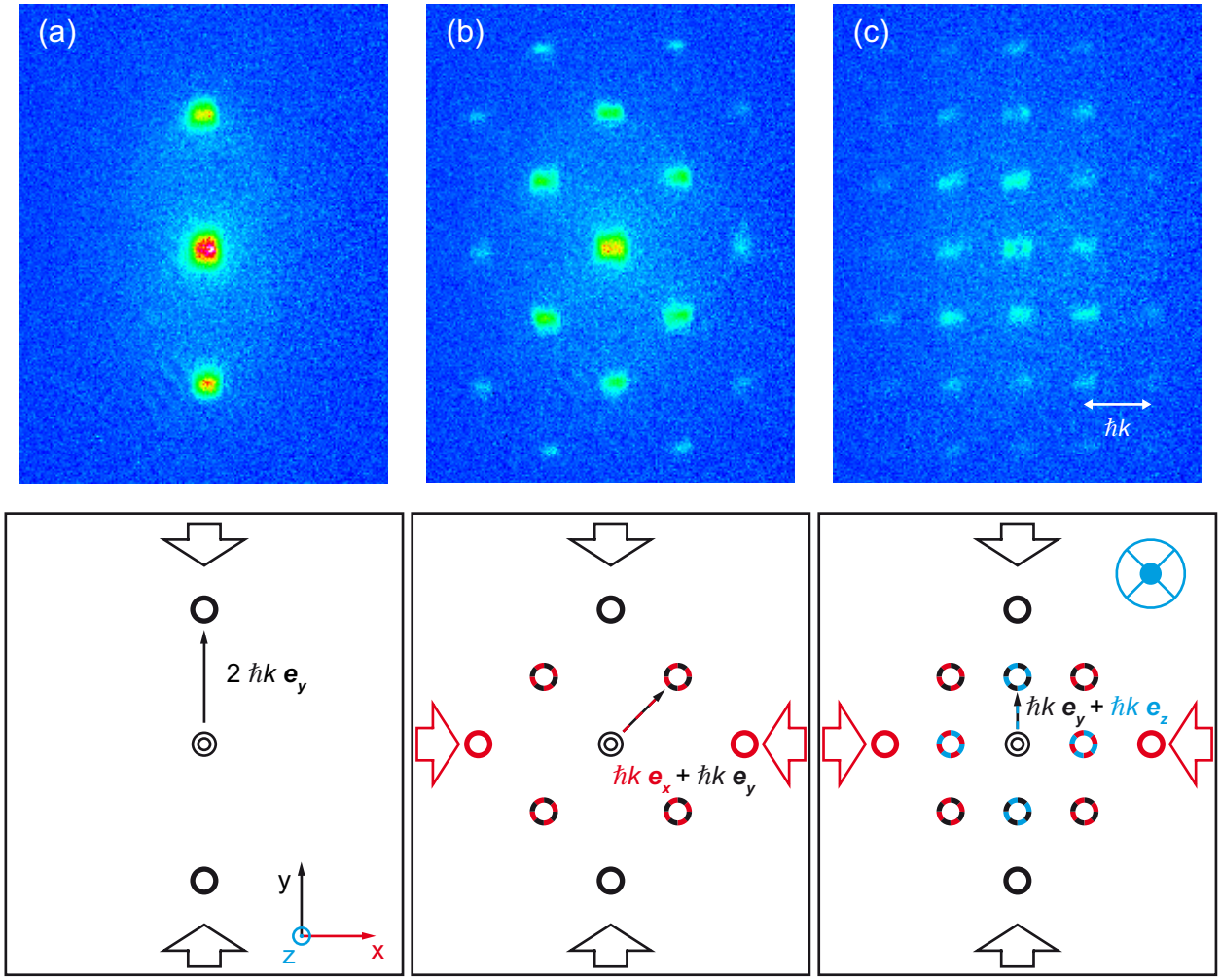

Figure 10.7: Momentum state crystals in the regime of short laser pulses. Absorption images (top) and corresponding schematic drawings (bottom) for scenarios with (a) one, (b) two, and (c) three orthogonal lattice beams of the same frequency. All six beams interfere pairwise, giving rise to additional diffraction peaks that are not present in usual lattice experiments. Note that the atoms do not form a simple cubic crystal with lattice spacing $\hbar k$, but a crystal with face-centered cubic structure and a unit cell size of $2\hbar k$.

Chapter 11

Publication: Creation of ultracold Sr_2 molecules in the electronic ground state[†]

Phys. Rev. Lett **109**, 115302 (2012)

Simon Stellmer,[1] Benjamin Pasquiou,[1] Rudolf Grimm,[1,2] and Florian Schreck,[1]

[1] *Institut für Quantenoptik und Quanteninformation, Österreichische Akademie der Wissenschaften, 6020 Innsbruck, Austria*
[2] *Institut für Experimentalphysik, Universität Innsbruck, 6020 Innsbruck, Austria*

We report on the creation of ultracold $^{84}Sr_2$ molecules in the electronic ground state. The molecules are formed from atom pairs on sites of an optical lattice using stimulated Raman adiabatic passage (STIRAP). We achieve a transfer efficiency of 30% and obtain 4×10^4 molecules with full control over the external and internal quantum state. STIRAP is performed near the narrow $^1S_0 - {}^3P_1$ intercombination transition, using a vibrational level of the $1(0_u^+)$ potential as intermediate state. In preparation of our molecule association scheme, we have determined the binding energies of the last vibrational levels of the $1(0_u^+)$, $1(1_u)$ excited-state, and the $X^1\Sigma_g^+$ ground-state potentials. Our work overcomes the previous limitation of STIRAP schemes to systems with magnetic Feshbach resonances, thereby establishing a route that is applicable to many systems beyond bi-alkalis.

The creation of ultracold molecular gases has made rapid progress over the last years. The rich internal structure of molecules combined with low translational energy enables pre-

[†]The author constructed and characterized the optical lattice and build the laser systems required for the PA spectroscopy and STIRAP. He performed the spectroscopy measurements and analyzed the data. He developed the experimental sequence and characterized the novel scheme of molecule association, and he acquired and partially analyzed the corresponding data. Calculations of the molecular potentials were performed by B. P. The author wrote the manuscript of the supplemental material and contributed to the writing of the main article.

cision measurements of fundamental constants, realizations of novel quantum phases, and applications for quantum computation [Kre09]. A very successful route to large samples of ultracold molecules with complete control over the internal and external quantum state is association of molecules from ultracold atoms. Early experiments used magnetic Feshbach resonances to form weakly bound bi-alkali molecules, some of which have even been cooled to quantum degeneracy [Fer]. Stimulated Raman adiabatic passage (STIRAP) [Vit01] has enabled the coherent transfer of these Feshbach molecules into the vibrational ground state [Dan08, Lan08, Ni08]. In particular, heteronuclear molecules in the vibrational ground state have received a lot of attention, because they possess a strong electric dipole moment, leading to anisotropic, long-range dipole-dipole interactions, which will enable studies of fascinating many-body physics [Pup]. Efforts are underway to create samples of completely state-controlled molecules beyond bi-alkalis [Har11, Han11, Nem09], which will widen the range of applications that can be reached experimentally.

So far, the key step in the efficient creation of ultracold molecules has been molecule association using magnetic Feshbach resonances. This magnetoassociation technique cannot be used to form dimers of alkaline-earth atoms or ytterbium, because of the lack of magnetic Feshbach resonances in these nonmagnetic species. An example is Sr_2, which has been proposed as a sensitive and model-independent probe for time variations of the proton-to-electron mass ratio [Zel08, Kot09, Bel11]. Another class of molecules for which magnetoassociation is difficult, are dimers containing an alkali atom and a nonmagnetic atom, since in these cases magnetic Feshbach resonances are extremely narrow [Zuc10, Bru12]. This difficulty occurs in current experimental efforts to create LiYb, RbYb, or RbSr molecules [Har11, Han11, Nem09]. Other molecule creation techniques that are suitable for dimers containing nonmagnetic atoms have been proposed. Examples are molecule formation by STIRAP from a Bose-Einstein condensate (BEC) [Mac00, Dru02, Mac05, Dru05] or from atom pairs in a deep optical lattice [Tom11], as well as two-color photoassociation (PA) of atom pairs in a Mott insulator [Jak02].

In this Letter, we show that ultracold Sr_2 molecules in the electronic ground state can be efficiently formed, despite the lack of a magnetic Feshbach resonance. Instead of magnetoassociation, we combine ideas from [Mac00, Dru02, Mac05, Dru05, Tom11, Jak02] and use optical transitions to transform pairs of atoms into molecules by STIRAP. The molecule conversion efficiency is enhanced by preparing pairs of atoms in a Mott insulator on the sites of an optical lattice [Jak98, Gre02]. We achieve an efficiency of 30% and create samples of 4×10^4 $^{84}Sr_2$ molecules. We perform PA spectroscopy to identify the vibrational levels and optical transitions used for molecule creation.

STIRAP coherently transfers an initial two-atom state $|a\rangle$ into a molecule $|m\rangle$ by optical transitions; see Fig. 11.1. In our case, the initial state $|a\rangle$ consists of two ^{84}Sr atoms occupying the ground state of an optical lattice well. The final state $|m\rangle$ is a Sr_2 molecule in the second-to-last ($\nu = -2$) vibrational level of the $X^1\Sigma_g^+$ ground-state molecular potential without rotational angular momentum. The molecules have a binding energy of 645 MHz and are also confined to the ground state of the lattice well. States $|a\rangle$ and $|m\rangle$ are coupled by laser fields L_1 and L_2, respectively, to state $|e\rangle$, the third-to-last ($\nu' = -3$) vibrational level of the metastable $1(0_u^+)$ state, dissociating to $^1S_0 + {}^3P_1$.

We use the isotope ^{84}Sr for molecule creation, since it is ideally suited for the creation

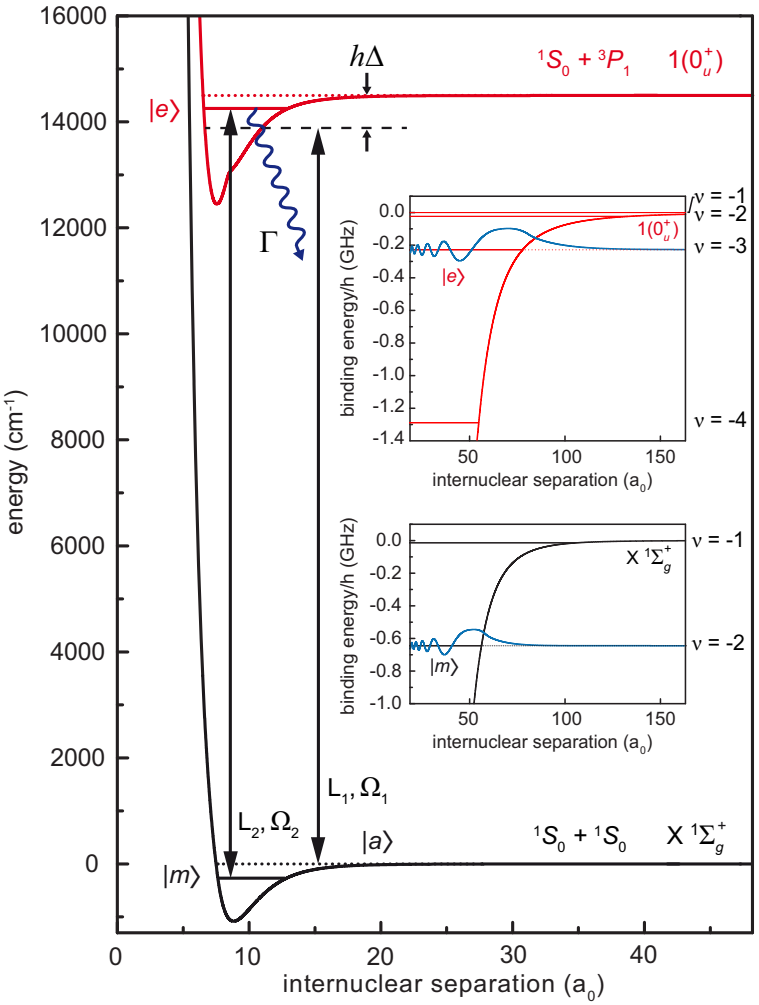

Figure 11.1: Molecular potentials and vibrational levels of $^{84}Sr_2$ involved in STIRAP. The initial state $|a\rangle$, an atom pair in the ground state of an optical lattice well, and the final molecular state $|m\rangle$, are coupled by laser fields L_1 and L_2 to the excited state $|e\rangle$ with Rabi frequencies Ω_1 and Ω_2, respectively. The parameter Δ is the detuning of L_1 from the $^1S_0 - {}^3P_1$ transition and Γ is the decay rate of $|e\rangle$. The insets show the last vibrational levels of the molecular potentials and the wavefunctions of states $|m\rangle$ and $|e\rangle$. For comparison, the wavefunction of atomic state $|a\rangle$ (not shown) has its classical turning point at a radius of 800 a_0, where a_0 is the Bohr radius. The potentials are taken from [Ste08, Sko12] and the wavefunctions are calculated using the WKB approximation. The energies of states $|m\rangle$ and $|e\rangle$ are not to scale in the main figure.

of a BEC [Ste09, Mar09a], and formation of a Mott insulator. The binding energies of the vibrational levels involved in our STIRAP scheme are only known for the isotope ^{88}Sr [Zel06, Mar08] and can be estimated for ^{84}Sr by mass-scaling [Gri93, Gao00]. An essential task in preparation for molecule creation is therefore to spectroscopically determine the binding energies of relevant $^{84}Sr_2$ levels.

We perform PA spectroscopy on a ^{84}Sr BEC, produced similarly to our previous work

ν	$1(0_u^+)$ (MHz)	$1(1_u)$ (MHz)	$X^1\Sigma_g^+$ $(l=0)$ (MHz)	$X^1\Sigma_g^+$ $(l=2)$ (MHz)
-1	$-0.32(1)$	$-351.45(2)$	$-13.7162(2)$	-
-2	$-23.01(1)$		$-644.7372(2)$	$-519.6177(5)$
-3	$-228.38(1)$			
-4	$-1288.29(1)$			

Table 11.1: Binding energies of the highest vibrational levels of the $1(0_u^+)$, $1(1_u)$, and $X^1\Sigma_g^+$ $(l=0,2)$ states, where l is the rotational angular momentum quantum number. The levels are labeled by ν, starting from above with $\nu=-1$. Measurement procedure and error discussion are given in Sec. 11.1.1.

[Ste09]; see Sec. 11.1.1. The BEC is confined in an oblate crossed-beam optical dipole trap with oscillation frequencies of 55 Hz in the horizontal plane and 180 Hz in the vertical direction, based on two 5-W laser sources operating at 1064 nm with a linewidth of 3 nm. Laser fields L_1 and L_2, which are used for spectroscopy and STIRAP, have linewidths of $\sim$ 2 kHz and are referenced with an accuracy better than 1 kHz to the ${}^1S_0-{}^3P_1$ intercombination line, which has a natural width of $\Gamma/2\pi = 7.4$ kHz. To achieve the coherence of the laser fields required for STIRAP, L_1 and L_2 are derived from the same master laser by means of acousto-optical modulators. These laser beams are copropagating in the same spatial mode with a waist of $100(25)\,\mu$m on the atoms and are linearly polarized parallel to a guiding magnetic field of 120 mG.

One-color PA spectroscopy is used to determine the binding energies of the last four vibrational levels of the $1(0_u^+)$ state. To record the loss spectrum, we illuminate the BEC for 100 ms with L_1 for different detunings Δ with respect to the ${}^1S_0-{}^3P_1$ transition. The binding energies derived from these measurements are presented in Tab. 12.1.

We then use two-color PA spectroscopy to determine the binding energies of the last vibrational levels of the $X^1\Sigma_g^+$ ground-state potential. The loss spectra are recorded in the same manner as for one-color PA spectroscopy, just with the additional presence of L_2. Figure 11.2 shows two spectra, for which L_2 is on resonance with the transition from state $|m\rangle$ to state $|e\rangle$. The difference between the spectra is the intensity of L_2. The spectrum shown in Fig. 11.2(a) was recorded at high intensity and displays an Autler-Townes splitting [Aut55]. In this situation, the coupling of states $|m\rangle$ and $|e\rangle$ by L_2 leads to a doublet of dressed states, which is probed by L_1. The data of Fig. 11.2(b) was recorded at low intensity and shows a narrow dark resonance at the center of the PA line. Here, a superposition of states $|a\rangle$ and $|m\rangle$ is formed, for which excitation by L_1 and L_2 destructively interfere. The binding energies of the ground-state vibrational levels derived from measurements of dark resonances are given in Tab. 12.1.

The Rabi frequencies $\Omega_{1,2}$ of our coupling lasers are determined by fitting a three-mode model to the spectra [Win05]; see Fig. 11.2. The free-bound Rabi frequency Ω_1 scales with intensity I_1 of L_1 and atom density ρ as $\Omega_1 \propto \sqrt{I_1}\sqrt{\rho}$ [Dru02]. The bound-bound Rabi frequency $\Omega_2 \propto \sqrt{I_2}$ depends only on the intensity I_2 of L_2. We obtain $\Omega_1/(\sqrt{I_1}\sqrt{\rho/\rho_0}) = 2\pi\times 10(4)\,\mathrm{kHz}/\sqrt{\mathrm{W/cm^2}}$ at a peak density of $\rho_0 = 4\times10^{14}\,\mathrm{cm^{-3}}$ and $\Omega_2/\sqrt{I_2} = 2\pi\times 50(15)\,\mathrm{kHz}/\sqrt{\mathrm{W/cm^2}}$, where the error is dominated by uncertainty in the

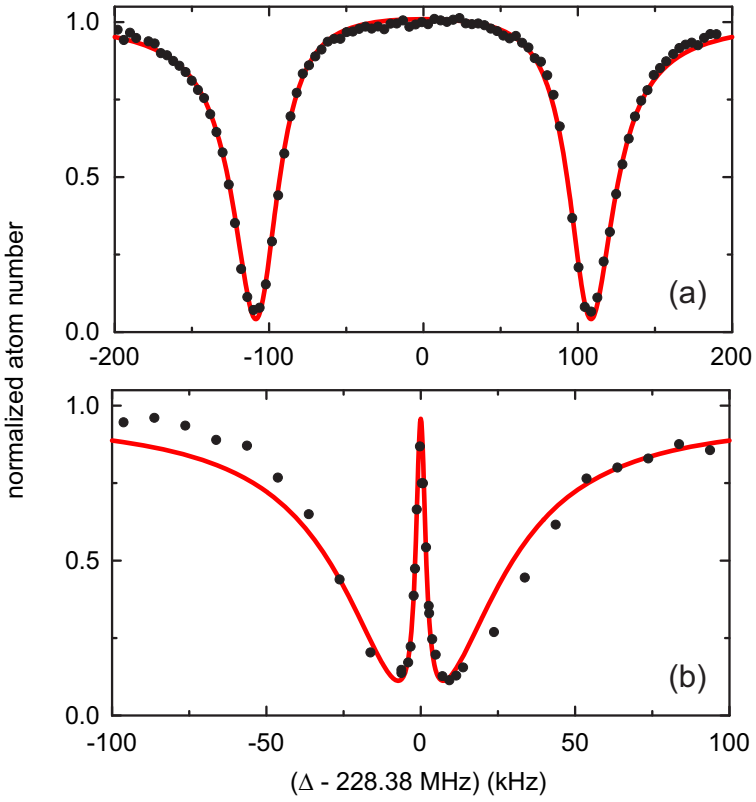

Figure 11.2: Two-color PA spectra near state $|e\rangle$ for two intensities of L_2. (a) For high intensity ($20\,W/cm^2$) the spectrum shows an Autler-Townes splitting. (b) For low intensity ($80\,mW/cm^2$) a narrow dark resonance is visible. For both spectra, the sample was illuminated by L_1 for 100 ms with an intensity of $7\,mW/cm^2$ at varying detuning Δ from the ${}^1S_0$-${}^3P_1$ transition. The lines are fits according to a three-mode model [Win05].

laser beam intensity.

To enhance molecule formation, we create a Mott insulator by loading the BEC into an optical lattice; see Chpt. 10. The local density increase on a lattice site leads to an increased free-bound Rabi frequency Ω_1. Furthermore, molecules are localized on lattice sites and thereby protected from inelastic collisions with each other. The lattice is formed by three nearly orthogonal retroreflected laser beams with waists of $100\,\mu m$ on the atoms, derived from an 18-W single-mode laser operating at a wavelength of $\lambda = 532\,nm$. Converting the BEC into a Mott insulator is done by increasing the lattice depth during 100 ms to $16.5\,E_{rec}$, where $E_{rec} = \hbar^2k^2/2m$ is the recoil energy with $k = 2\pi/\lambda$ and m the mass of a strontium atom. After lattice ramp-up, the 1064-nm dipole trap is ramped off in 100 ms.

To estimate the number of doubly occupied sites, which are the sites relevant for molecule formation, we analyze the decay of the lattice gas under different conditions. After loading a BEC with less than $\sim 3 \times 10^5$ atoms into the lattice, the lifetime of the lattice gas is 10(1) s. For higher BEC atom numbers, we observe an additional, much faster initial decay on a timescale of 50 ms, which removes a fraction of the atoms. We attribute this loss to three-body decay of triply occupied sites, which are formed only if the BEC peak density

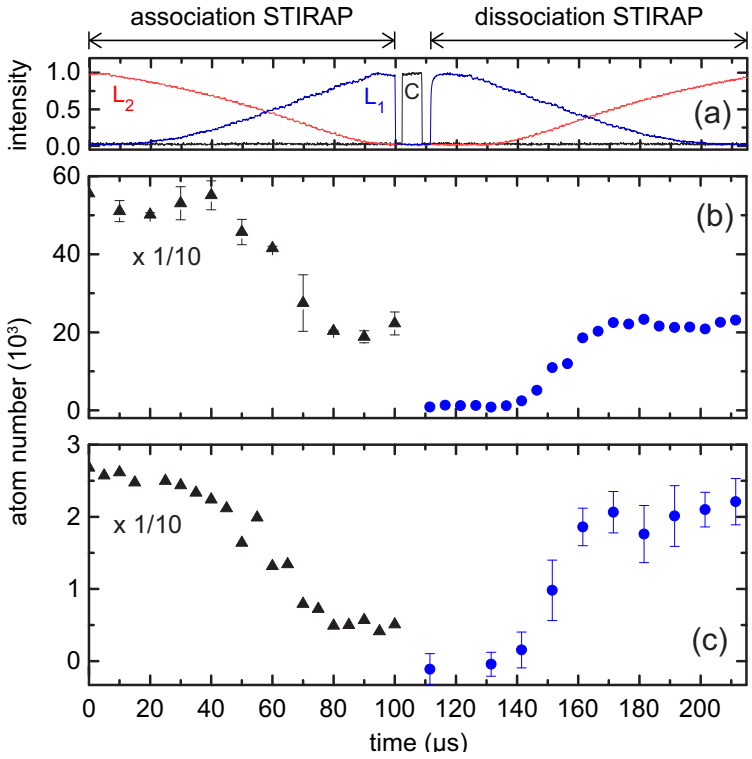

Figure 11.3: Time evolution of STIRAP transfers from atom pairs to Sr_2 molecules and back. (a) Intensities of L_1, L_2, and cleaning laser C, normalized to one. (b), (c) Atom number evolution. For these measurements, L_1 and L_2 are abruptly switched off at a given point in time and the atom number is recorded on an absorption image after 10 ms free expansion. Note the scaling applied to data taken during the first 100 μs (triangles). The starting point for the time evolution shown in (b) is a Mott insulator, whereas the starting point for (c) is a sample for which 80% of the atoms occupy lattice sites in pairs.

is high enough. To obtain a high number of doubly occupied sites, we load a large BEC of 1.5×10^6 atoms into the lattice. After the initial decay, 6×10^5 atoms remain. By inducing PA loss using L_1, we can show that half of these atoms occupy sites in pairs.

We are now ready to convert the atom pairs on doubly occupied sites into molecules by STIRAP. This method relies on a counterintuitive pulse sequence [Vit01], during which L_2 is pulsed on before L_1. During this sequence, the atoms populate the dark state $|\Psi\rangle = (\Omega_1 |m\rangle + \Omega_2 |a\rangle)/(\Omega_1^2 + \Omega_2^2)^{1/2}$, where Ω_1 and Ω_2 are the time-dependent Rabi frequencies of the two coupling laser fields as defined in [Vit01], which can reach up to $\Omega_1^{\max} \sim 2\pi \times 150$ kHz and $\Omega_2^{\max} = 2\pi \times 170(10)$ kHz in our case [1]. Initially the atoms are in state $|a\rangle$, which is

[1] Note that [Win05] and [Vit01, Win07] use different definitions of Ω_1, which we note here as Ω_1^{BEC} and Ω_1^{MI}. We use the three-mode model of [Win05] to determine Ω_1^{BEC} from two-color PA spectroscopy of a BEC. This model is not able to describe STIRAP starting from an atom pair on a lattice site. Suitable models are given in [Vit01, Win07] and use Ω_1^{MI}, which we approximate by $\Omega_1^{\mathrm{MI}} \sim \sqrt{2}\sqrt{\rho_0^{\mathrm{MI}}/\rho_0^{\mathrm{BEC}}}\sqrt{I_1^{\mathrm{STIRAP}}/I_1^{\mathrm{PA}}}\Omega_1^{\mathrm{BEC}}$. Here $\rho_0^{\mathrm{BEC}} = 4 \times 10^{14}\,\mathrm{cm}^{-3}$ is the peak density of the BEC, $\rho_0^{\mathrm{MI}} = 5 \times 10^{15}\,\mathrm{cm}^{-3}$ the peak density of an atom pair on a lattice site, I_1^{PA} the intensity of L_1 used for PA spectroscopy, and I_1^{STIRAP} the intensity of L_1 used during STIRAP, which is maximally $10\,\mathrm{W/cm}^2$. The factor $\sqrt{2}$ is discussed in [Dru05].

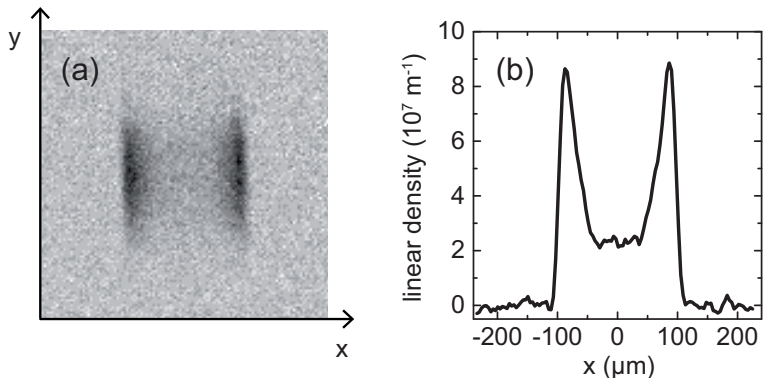

Figure 11.4: Quasi-momentum distribution of repulsively bound pairs. (a) Average of 20 absorption images recorded 10 ms after release of the atoms from the lattice. (b) Integral of the distribution along y.

the dark state after L_2 is suddenly switched on, but L_1 kept off. During the pulse sequence, which takes $T = 100\,\mu$s, L_1 is ramped on and L_2 off; see association STIRAP in Fig. 11.3(a). This adiabatically evolves the dark state into $|m\rangle$ if $\Omega_{1,2}^{\max} \gg 1/T$, a condition, which we fulfill. To end the pulse sequence, L_1 is suddenly switched off. During the whole process, state $|e\rangle$ is only weakly populated, which avoids loss of atoms by spontaneous emission if $\Omega_{1,2}^{\max} \gg \Gamma$. This condition is easily fulfilled with a narrow transition as the one used here. The association STIRAP transfer does not lead to molecules in excited lattice bands, since T is long enough for the band structure to be spectrally resolved.

We now characterize the molecule creation process. To detect molecules, we dissociate them using a time-mirrored pulse sequence (dissociation STIRAP in Fig. 11.3(a)) and take absorption images of the resulting atoms. The atom number evolution during molecule association and dissociation is shown in Fig. 11.3(b). After the molecule association pulse sequence, 2×10^5 atoms remain, which we selectively remove by a pulse of light resonant to the ${}^1S_0 - {}^1P_1$ atomic transition, out of resonance with any molecular transition[2]; see "cleaning" laser C in Fig. 11.3(a). The recovery of 2×10^4 atoms by the dissociation STIRAP confirms that molecules have been formed. Further evidence that molecules are the origin of recovered atoms is that 80% of these atoms occupy lattice sites in pairs. Quantitatively this is shown by removing atom pairs using PA and measuring the loss of atoms. Qualitatively we illustrate this fact by creating and detecting one-dimensional repulsively bound pairs along the x-direction [Win06]. The pairs were created by ramping the x-direction lattice beam to a value of $10\,E_{\rm rec}$ before ramping all lattice beams off, which propels the pairs into free atoms with opposite momenta along x. Figure 11.4 shows the characteristic momentum space distribution of these pairs.

To estimate the STIRAP efficiency and subsequently the number of molecules, we perform another round of molecule association and dissociation on such a sample of atoms with large fraction of doubly occupied sites; see Fig. 11.3(c). We recover $f = 9\%$ of the atoms, which corresponds to a single-pass efficiency of $\sqrt{f} = 30\%$. The largest sample of atoms

[2]The pulse of light (duration $7\,\mu$s, intensity $250\,\mathrm{mW/cm^2}$) separates the atoms in momentum space from the molecules, which leads to a spatial separation on absorption images recorded after 10 ms free expansion.

created by dissociating molecules contains $N_a = 2.5 \times 10^4$ atoms, which corresponds to $N_m = N_a/(2\sqrt{f}) = 4 \times 10^4$ molecules.

We measure the lifetime of molecules in the lattice, by varying the hold time between molecule creation and dissociation. We obtain $\sim 60\,\mu$s, nearly independent of the lattice depth. Executing the cleaning laser pulse after the hold time instead of before, does not change the lifetime. This time is surprisingly short and can neither be explained by scattering of lattice photons nor by tunneling of atoms or molecules confined to the lowest band of the lattice and subsequent inelastic collisions. By band mapping [Gre01], we observe that 3×10^4 of the initial 6×10^5 atoms are excited to the second band during the association STIRAP, and more atoms have possibly been excited to even higher bands. We speculate that these atoms, which move easily through the lattice, collide inelastically with the molecules, resulting in the observed short molecule lifetime. The cleaning laser pulse is not able to push these atoms out of the region of the molecules fast enough to avoid the loss. The short lifetime can explain the 30%-limit of the molecule conversion efficiency. Without the loss, the high Rabi frequencies and the good coherence of the coupling lasers should result in a conversion efficiency close to 100%. The excitation of atoms to higher bands cannot be explained by off-resonant excitation of atoms by L_1 or L_2. Incoherent light of the diode lasers on resonance with the atomic transition might be the reason for the excitation. Further investigation of the excitation mechanism is needed in order to circumvent it.

In conclusion, we have demonstrated that it is possible to use STIRAP to coherently create Sr_2 molecules from atom pairs on the sites of an optical lattice. The advantage of this technique compared to the traditional magnetoassociation approach is that it can be used for systems that do not possess a suitable magnetic Feshbach resonance. This new approach might be essential for the formation of alkali/alkaline-earth molecules.

We thank Manfred Mark for helpful discussions. We gratefully acknowledge support from the Austrian Ministry of Science and Research (BMWF) and the Austrian Science Fund (FWF) through a START grant under Project No. Y507-N20. As member of the project iSense, we also acknowledge financial support of the Future and Emerging Technologies (FET) programme within the Seventh Framework Programme for Research of the European Commission, under FET-Open grant No. 250072.

11.1 Supplemental material

11.1.1 One-color PA spectroscopy

We use one-color PA spectroscopy to measure the binding energies of the last vibrational levels of the $1(0_u^+)$ and $1(1_u)$ states. A pure BEC of 10^6 atoms is illuminated by L_1 for 100 ms, and the number of remaining atoms is measured by absorption imaging. The detuning Δ of L_1 with respect to the atomic ${}^1S_0 - {}^3P_1$ transition is changed for consecutive experimental runs, generating loss spectra as the ones shown in Fig. 11.5. To compensate the difference in line strength for the different vibrational levels, we adjust the intensity of L_1 to obtain a large, but not saturated signal. Intensities used for the last four levels ($\nu' = -1, -2, -3, -4$) of the $1(0_u^+)$ state and the last level ($\nu' = -1$) of the $1(1_u)$ state are 0.005, 1.8, 3.7, 260, and 260 mW/cm^2, respectively.

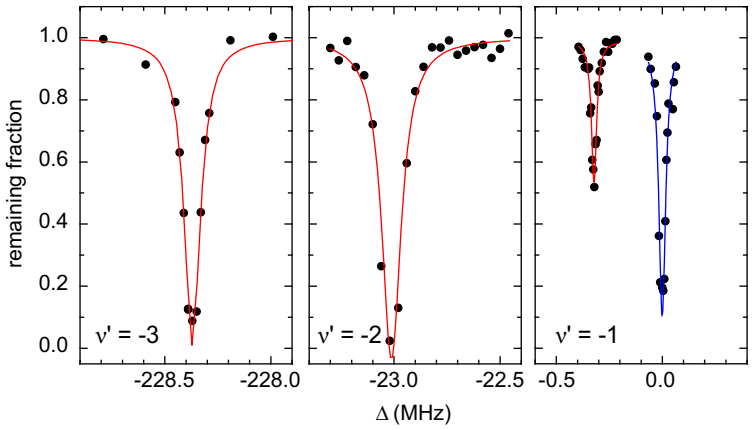

Figure 11.5: One-color PA spectra. A BEC is illuminated by L_1, and the fraction of remaining atoms is recorded (black circles). Various loss features are observed in the dependence on the L_1 frequency. Except for the atomic transition feature near zero, these features correspond to vibrational levels of the $1(0_u^+)$ state.

The lineshapes of the resonances are very symmetric and can be described by a simple Lorentz profile. This is in contrast to similar measurements performed in a thermal gas of ^{88}Sr, where the inhomogeneous broadening of the line had to be considered [Zel06]. The uncertainty in the position of the resonances amounts to 1, 2, 2, 6, and 20 kHz for the five levels mentioned above, and to 1 kHz for the atomic transition. Systematic errors arise from light shifts and mean-field shifts; see Tab. 11.2. We measure these shifts for the $\nu' = -3$ level and find that they are on the kHz scale; see Fig. 11.7(a) and (b). The strength of the magnetic field does not influence the resonance position, since we use π-polarized light for spectroscopy and drive a magnetic field insensitive $m_J = 0$ to $m'_J = 0$ transition. We do not measure light shifts and mean-field shifts for the other vibrational levels, and therefore give a rather conservative total uncertainty of 10 kHz in Tab. I of the article.

11.1.2 Two-color PA spectroscopy

We use two-color PA spectroscopy to determine the binding energies of the last vibrational levels of the ground-state potential. The two laser fields L_1 and L_2 couple three states in a Λ-scheme. Laser field L_1 couples two BEC atoms to a molecular state $|e'\rangle$, which is a vibrational level of the $1(0_u^+)$ state. Laser field L_2 couples $|e'\rangle$ to a molecular state $|m'\rangle$ in the ground-state potential. The frequency difference between L_1 and L_2 gives the binding energy of $|m'\rangle$.

As an example, we present the determination of the binding energy of the last bound level $\nu = -1$ of the $X^1\Sigma_g^+$ ground-state. Here we choose the excited vibrational level $\nu' = -3$ as the intermediate state $|e'\rangle$. A pure BEC of 6×10^5 atoms is prepared in an optical dipole trap and illuminated by L_1 and L_2 for 100 ms. Afterwards, the number of remaining atoms is measured using absorption imaging. The frequency of L_1 is always set to be resonant with the free-bound transition, and the intensity is chosen such that almost all atoms are ejected from the trap. To search for the molecular state $|m'\rangle$, the frequency of L_2 is increased from

error source				uncertainty kHz
position free-free				1
position free-bound				2
master laser				< 1
total				2
error source	shift Hz/mW	shift Hz/(mW/cm^2)	mW	shift kHz
L_1 Stark	$2.2(1) \times 10^4$	300	0.06	1.3
vert DT Stark	170(10)	0.003	4	0.6
	mHz/atom		atoms	
mean field	2.4(5)		$\leq 10^6$	≤ 2.5

Table 11.2: Uncertainties and systematic shifts for the binding energy of the $\nu' = -3$ vibrational level of the $1(0_u^+)$ state.

effect	shift $\frac{\text{Hz}}{\mu\text{W}}$	shift $\frac{\text{Hz}}{\text{mW/cm}^2}$	mW	shift Hz	uncert. Hz
L_1 Stark	16.4(4)	2.8(1)	4.5×10^{-4}	3	<1
L_2 Stark	$-10.2(4)$	$-1.7(1)$	6×10^{-4}	-6	<1
hor DT Stark	$4(1) \times 10^{-4}$	50(10)	320	120	30
vert DT Stark	$1.1(3) \times 10^4$	90(40)	27	300	100
fitting					5
RF					1
shot-to-shot					80
total				420	130

Table 11.3: Error budget for the binding energy of the $\nu = -2\,(l = 0)$ level of the $X^1\Sigma_g^+$ state.

one experimental run to the next. If L_2 is on resonance with the bound-bound transition, an atom-molecule dark state is created. Light from L_1 is no longer absorbed and no photoassociative loss occurs. We are searching for this dark resonance as a signature of state $|m'\rangle$ while we change the frequency of L_2.

Without initial knowledge about the rough position of the resonance, many 100 MHz need to be scanned; see Fig. 11.6(a). Once the resonance is found, we can reduce the intensity of L_2, which reduces the width of the resonance considerably. Consecutive scans with decreasing intensity allow for a very precise determination of the resonance position, shown in Fig. 11.6(a) through (f). The data can be fitted nicely with a Lorentz profile. For the smallest L_2 intensity used here, we obtain a linewidth of 1.0 kHz and an uncertainty in the position of the resonance of 5 Hz. We find the lineshapes to be very symmetric, which is in contrast to [Mar08], where the measurements were performed in a thermal gas.

In the search presented, we had no initial knowledge about the position of the resonance.

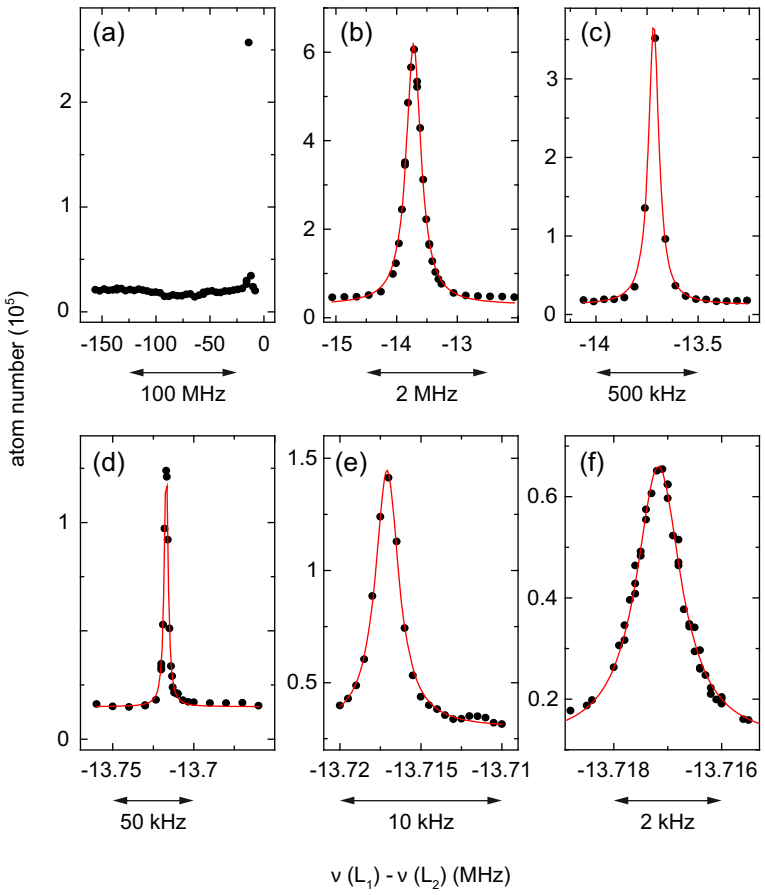

Figure 11.6: Search for a dark resonance. A BEC is illuminated by laser fields L_1 and L_2, where the frequency of L_1 is kept fixed as the frequency of L_2 is varied. The number of atoms remaining after a 100 ms pulse is recorded (black circles). The resonance feature is described by a Lorentz profile (red line). The intensity of L_2 is continuously reduced from (a) through (f), assuming values of 110, 13, 3.2, 0.084, 0.038, and 0.013 $\mathrm{mW/cm^2}$, respectively, thereby drastically reducing the linewidth of the resonance.

The search can be simplified if the rough position is calculated beforehand. We can estimate the energy of the last bound level from the known s-wave scattering length of ^{84}Sr [Mar08, Ste10a] using a simple analytical model [Gri93]. Using general properties of van der Waals potentials [Gao00], this estimation is extended to more deeply bound levels. This estimation guides our search for two other bound levels of the $X^1\Sigma_g^+$ state: the $\nu = -2$ level for $l = 0$ and the $\nu = -1$ level for $l = 2$.

We will now investigate the systematic errors and uncertainties of our measurement. The dominant systematic errors are caused by light shifts induced by the light fields involved: L_1 and L_2, as well as the horizontal and vertical dipole trap beams. For a systematic analysis, we vary each parameter independently, and record the resonance position. We fit the data with a straight line and extrapolate to zero; examples are shown in Fig. 11.7(c) and (d).

Uncertainties in the laser frequencies are small, since L_1 and L_2 are generated by injection-

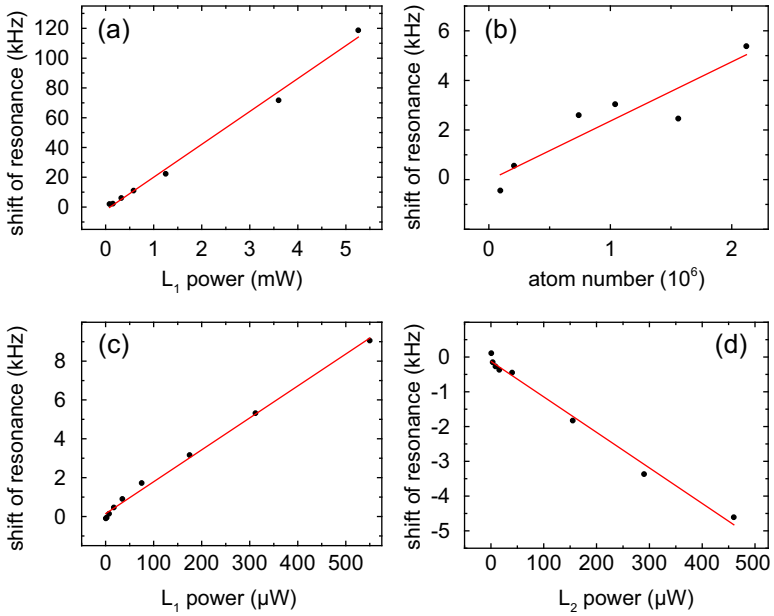

Figure 11.7: Systematic shifts of the binding energies. Panels (a) and (b) show the shift of the excited-state $\nu' = -3$ level with varying power of L_1 and varying atom number, whereas panels (c) and (d) show shifts of the ground-state $\nu = -2$ level.

locking two slave lasers with light from the same master laser. The light is frequency-shifted using acousto-optical modulators, where the radiofrequency source is referenced to the global positioning system (GPS). Frequency drifts of the master laser do not affect the measurement. For scans taken at the maximum resolution, there is an unexplained jitter of at most 80 Hz between scans taken some time apart. This is the dominant contribution to the overall uncertainty. In Tab. 11.3, we present a compilation of all systematic and statistical errors for the case of the $\nu = -2$ level, which is the one used for STIRAP. Note that our measurements are a factor 1000 more precise than previously reported data for the ^{88}Sr isotope [Mar08].

Chapter 12

Laser cooling to quantum degeneracy

We laser cool a gas of strontium atoms to Bose-Einstein condensation (BEC). The condensate is formed within a sample that is continuously Doppler cooled to below one microkelvin on a narrow-linewidth transition. The critical phase-space density for BEC is reached in a central region of the sample, in which atoms are rendered transparent for laser cooling photons and the number density is locally enhanced. Thermal equilibrium between the gas in this central region and the surrounding laser cooled part of the cloud is established by elastic collisions. Condensates of up to 10^5 atoms can be repeatedly formed on a timescale of 100 ms, with prospects for the generation of a continuous atom laser.

12.1 Laser cooling to quantum degeneracy

Laser cooling has revolutionized contemporary atomic and molecular physics in many respects, for example pushing the precision of clocks by orders of magnitude, and enabling ion quantum computation [Ari92]. Since the early days of laser cooling, the question has been asked if this efficient method would allow to cool atomic gases to the quantum degenerate regime. Despite significant experimental and theoretical effort this goal has been elusive. So far, laser cooling had to be followed by evaporative cooling to reach quantum degeneracy [Ing99].

A gas of bosonic atoms with number density n and temperature T enters the quantum-degenerate regime and forms a Bose-Einstein condensate if its phase-space density $n\lambda_{dB}^3$ exceeds a value of 2.612. Here $\lambda_{dB} = h/(2\pi m k_B T)^{1/2}$ is the thermal de Broglie wavelength, where h and k_B are Planck's and Boltzmann's constant, respectively, and m is the mass of an atom. Since $n\lambda_{dB}^3 \propto nT^{-3/2}$, low temperatures in combination with high densities have to be reached to obtain quantum degeneracy. Numerous studies, mainly carried out in the 1980's and 90's, have paved the ground to the present state of the art of laser cooling and have identified the limitations of the technique [Chu].

The longstanding goal of reaching the quantum degenerate regime by laser cooling [Dum94, Wis95, Spr95, Ols96, Bor96, Cir96, Mor98, Cas98, San99] can be discussed in terms of three main experimental challenges. First, temperatures in the low microkelvin regime have to be reached. Only here, quantum degeneracy can be obtained at a density that is low enough to avoid fast decay of the gas by molecule formation. This challenge has been

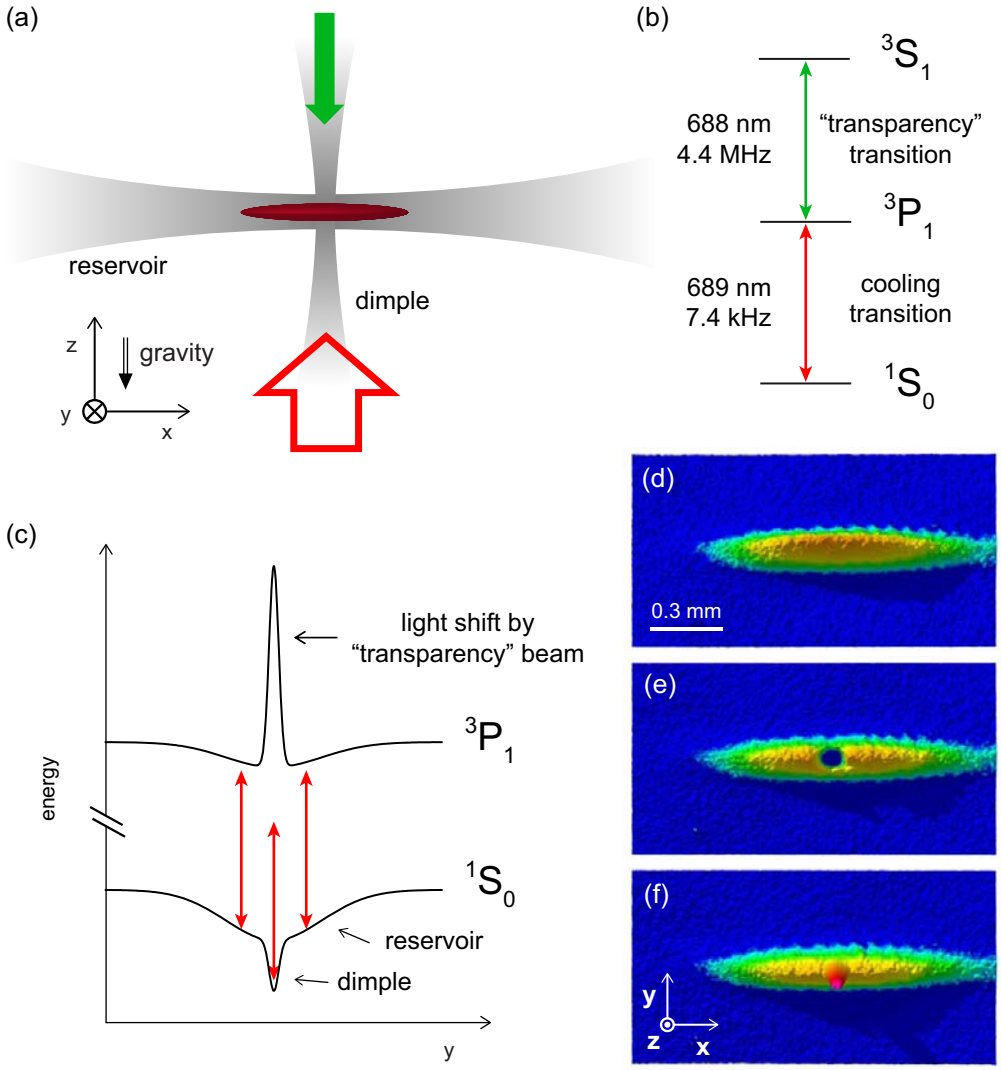

Figure 12.1: Scheme to reach quantum degeneracy by laser cooling. (a) A cloud of atoms is confined in a deep reservoir dipole trap and exposed to a single laser cooling beam (red arrow). Atoms are rendered transparent by a "transparency" laser beam (green arrow) and accumulate in a dimple dipole trap by elastic collisions. (b) Level scheme showing the laser cooling transition and the transparency transition. (c) Potential experienced by $^1S_0$ ground-state atoms and atoms excited to the $^3P_1$ state. The transparency laser induces a light shift on the $^3P_1$ state, which tunes the atoms out of resonance with laser cooling photons. (d) through (f) Absorption images of the atomic cloud recorded using the laser cooling transition. The images show the cloud from above and demonstrate the effect of the transparency laser (e) and the dimple (f). (d) is a reference image without these two laser beams.

met with several laser cooling techniques, as for example Sisyphus cooling [Let88, Dal89], velocity selective coherent population trapping [Asp88], Raman cooling [Kas92], Raman sideband cooling [Ham98], or Doppler cooling on narrow lines [Ido00]. The second challenge is an efficient trapping scheme that allows to accumulate atoms at high density at a certain location [SK98b, Web03]. The third, and most severe challenge is to avoid the detrimental effects of the laser cooling photons, which impede the required density increase. One such effect are light-assisted inelastic collisions, which lead to loss [Jul92, Wal97]. Another is the reabsorption of photons scattered during laser cooling [Ses91], which leads to an effective repulsion between the atoms and to heating of atoms in the lowest energy states. Both effects increase with density and make it impossible to reach quantum degeneracy. For low phase-space density samples, this challenge has been overcome by rendering the atoms transparent to laser cooling photons [Ket93, Gri06, Cle09] or by decreasing the photon scattering rate below the frequency of a confining trap [Cir96, Cas98, Wol00]. It has also been proposed to reduce reabsorption by dimensional reduction of the sample [Cas98]. The solutions to the three challenges implemented so far are insufficient to reach quantum degeneracy. The highest phase-space densities ever attained are one order of magnitude too low [Han00, Ido00]. Surprisingly, this last order of magnitude has been an insurmountable obstacle for a decade.

Our experiment overcomes all three challenges and creates a BEC of strontium by laser cooling. Our scheme essentially relies on the combination of three techniques, favored by the properties of this element. Strontium possesses a transition with such a narrow linewidth ($\Gamma/2\pi = 7.4\,\mathrm{kHz}$) that simple Doppler cooling can reach temperatures down to 350 nK [Ido00]. Using this transition, we prepare a laser cooled sample of 10^7 ^{84}Sr atoms in a large "reservoir" dipole trap. To avoid the detrimental effects of laser cooling photons, we render atoms transparent for these photons in a small spatial region within the laser cooled cloud. Transparency is induced by a light shift on the optically excited state of the laser cooling transition. In the region of transparency, we are able to increase the density of the gas, by accumulating atoms in an additional, small "dimple" dipole trap [SK98b, Web03]. Atoms in the dimple thermalize with the reservoir of laser cooled atoms by elastic collisions and form a BEC.

The details of our scheme are shown in Fig. 12.1. Based on our previous work [Ste09], we use several stages of laser cooling to prepare a sample of ^{84}Sr atoms in the reservoir trap; see Sec. 12.2.1 for details. The trap consists of an infrared laser beam (wavelength 1065 nm) propagating horizontally (x-direction). The beam profile is strongly elliptic, with a beam waist of 300 μm in the horizontal direction (y-direction) and 17 μm along the field of gravity (z-direction). The depth of the reservoir trap is kept constant at $k_B \times 9\,\mu\mathrm{K}$. After preparation of the sample, a further laser cooling stage is performed on the narrow $^1S_0 - ^3P_1$ intercombination line, using a single laser beam propagating vertically upwards. The detuning of the laser cooling beam from resonance is $\sim -2\,\Gamma$ and the peak intensity is $0.15\,\mu\mathrm{W/cm^2}$, which is 0.05 of the transition's saturation intensity. These parameters result in a photon scattering rate of $\sim 70\,\mathrm{s^{-1}}$. At this point, the ultracold gas contains 9×10^6 atoms at a temperature of 900 nK.

To render the atoms transparent to cooling light in a central region of the laser cooled cloud, we induce a light shift on the $^3P_1$ state, using a "transparency" laser beam 15 GHz blue detuned to the $^3P_1 - ^3S_1$ transition; see Sec. 12.5 for details. This beam propagates

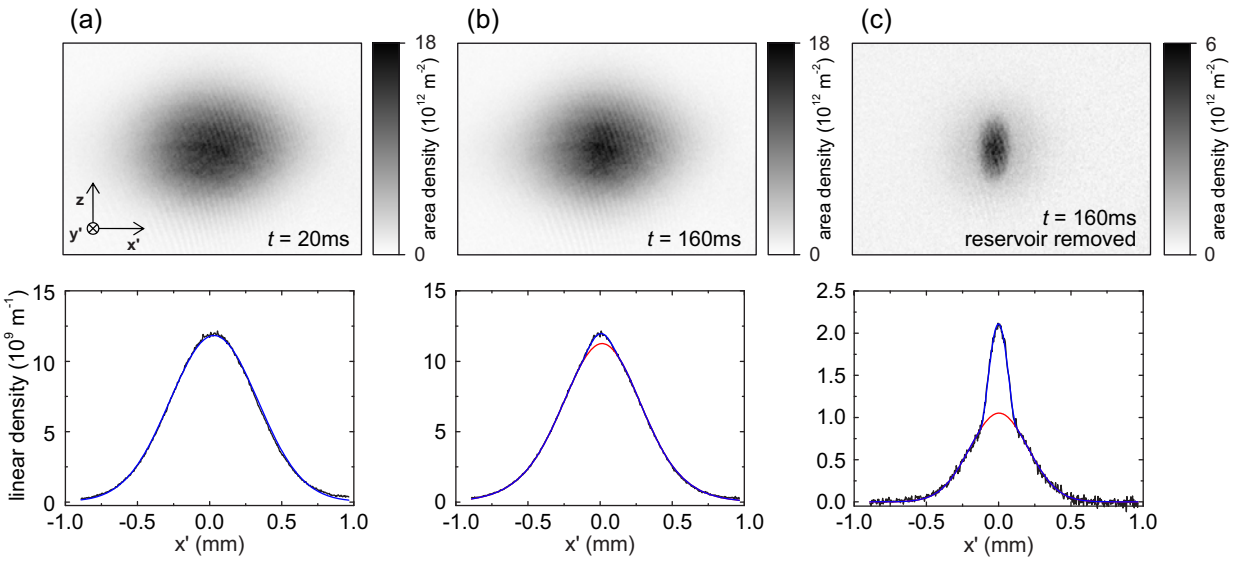

Figure 12.2: Creation of a BEC by laser cooling. Shown are time-of-flight absorption images and integrated density profiles of the atomic cloud for different times t after the transparency laser has been switched on, recorded after 24 ms of free expansion. (a) and (b) The appearance of an elliptic core at $t = 160$ ms indicates the creation of a BEC. (c) Same as in (b), but to increase the visibility of the BEC, atoms in the reservoir trap were removed before the image was taken. The fits (blue lines) consist of Gaussian distributions to describe the thermal background and an integrated Thomas-Fermi distribution describing the BEC. The red lines show the component of the fit corresponding to the thermal background. The $x'y'$-plane is rotated by 45° around the z-axis with respect to the xy-plane and the field of view of the absorption images is 2 mm × 1.4 mm.

downwards under a small angle of 15° to vertical and has a beam waist of 26 μm in the plane of the reservoir trap (xy-plane). The beam has a peak intensity of 0.7 kW/cm^2 and upshifts the $^3P_1$ state by more than 10 MHz. Related schemes of light-shift engineering were used to image the density distribution of atoms [Tho95, Bra08], to improve spectroscopy [Kap02], or to enhance loading of dipole traps [Gri06, Cle09]. To demonstrate the effect of the transparency laser beam, we take absorption images of the cloud on the laser cooling transition. Figure 12.1(d) shows a reference image without the transparency beam. In presence of this laser beam, atoms in the central part of the cloud are transparent for the probe beam, as can be seen in Fig. 12.1(e).

To increase the density of the cloud, the dimple trap is added to the system. It consists of an infrared laser beam (wavelength 1065 nm) propagating upwards under a small angle of 22° to vertical and crossing the laser cooled cloud in the region of transparency. In the plane of the reservoir trap, the dimple beam has a waist of 22 μm. The dimple is ramped to a depth of $k_B \times 2.6\,\mu$K, where it has trap oscillation frequencies of 250 Hz in the horizontal plane. Confinement in the vertical direction is only provided by the reservoir trap and results in a vertical trap oscillation frequency of 600 Hz. Figure 12.1(f) shows a demonstration of the dimple trap in absence of the transparency beam. The density in the region of the dimple

increases substantially. However, with the dimple alone no BEC is formed because of photon reabsorption.

The combination of the transparency laser beam and the dimple trap leads to BEC. Starting from the laser cooled cloud held in the reservoir trap, we switch on the transparency laser beam and ramp the dimple trap to a depth of $k_B \times 2.6\,\mu$K. The potentials of the $^1S_0$ and $^3P_1$ states in this situation are shown in Fig. 12.1(c). Atoms accumulate in the dimple without being disturbed by photon scattering. Elastic collisions thermalize atoms in the dimple with the laser cooled reservoir. The phase-space density in the dimple increases and a BEC emerges.

We detect the BEC by taking absorption images 24 ms after switching off all laser beams; see Fig. 12.2. Figure 12.2(a) shows the momentum distribution 20 ms after switching on the transparency beam, which is well described by a thermal distribution. By contrast, we observe that 140 ms later, an additional, central elliptical feature has developed; see Fig. 12.2(b). This is the hallmark of the BEC. Although clearly present, the BEC is not very well visible in Fig. 12.2(b), because it is shrouded by 8×10^6 thermal atoms originating from the reservoir. To show the BEC with higher contrast, we have developed a background reduction technique. We remove the reservoir atoms by an intense flash of light on the $^1S_0 - ^3P_1$ transition applied during 10 ms. Atoms in the region of transparency remain unaffected by this flash. Only 5×10^5 thermal atoms in the dimple remain and the BEC stands out clearly; see Fig. 12.2(c). We use this background reduction technique only for demonstration purposes, but not for measuring atom numbers or temperatures.

Quantitative data on our experiment are obtained by two-dimensional fits to time-of-flight absorption images; see Sec. 12.2.5 for details. The atom number of the thermal cloud and of the BEC are extracted from fits to 24-ms expansion images, consisting of Gaussian distributions describing the thermal background and an integrated Thomas-Fermi distribution describing the BEC. Further absorption images taken after 4 ms expansion time are used to determine atom number and temperature of the gas in the reservoir and the dimple, respectively.

We now analyze the dynamics of the system after the transparency laser beam has been switched on. As we increase the dimple strength to its final depth in 10 ms, 10^6 atoms accumulate in it (Fig. 12.3(a)) and the temperature of the dimple gas increases; see Fig. 12.3(b). During the next $\sim$ 100 ms the dimple gas thermalizes with the reservoir gas by elastic collisions. The temperature of the reservoir gas is hereby not increased, since the energy transferred to it is dissipated by laser cooling. We carefully check that evaporation is negligible even for the highest temperatures of the gas; see Sec. 12.4 for details. Already after 60 ms a BEC is detected. Its atom number saturates at 1.1×10^5 after 150 ms (Fig. 12.3(c)). The atom number in the reservoir decreases slightly, initially because of migration into the dimple and on longer timescales because of light assisted loss processes in the laser cooled cloud (Fig. 12.3(a)).

To demonstrate the power of our laser cooling scheme, we repeatedly destroy the BEC and let it reform; see Fig. 12.4. To destroy the BEC, we pulse the dimple trap depth to $k_B \times 15\,\mu$K for 2 ms, which increases the temperature of the dimple gas by a factor two. We follow the evolution of the BEC atom number while the heating pulse is applied every 200 ms. A new BEC starts forming a few 10 ms after each heating pulse for more than 30

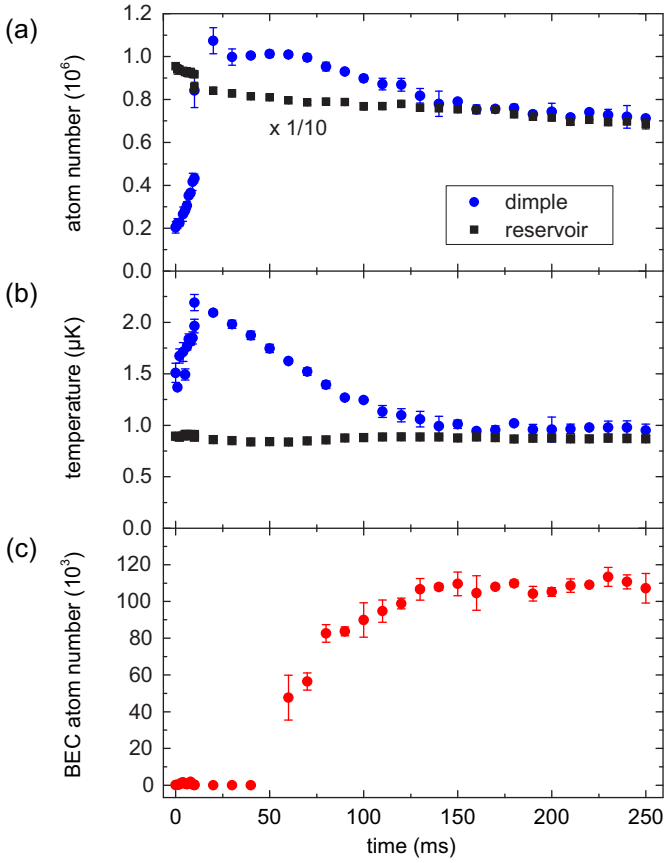

Figure 12.3: Characterization of the BEC formation process after the transparency laser is switched on. Shown are the evolution of the atom number in the dimple and the reservoir (a), the evolution of temperature in these regions (b) and the BEC atom number (c). During the first 10 ms of this evolution, the dimple trap is ramped on. After 60 ms a BEC is detected.

pulses. We find that the observed decrease in the BEC size from pulse to pulse stems from the reduction of the total atom number in the system.

To clarify the role laser cooling plays in our scheme, we perform a variation of the experiment. Here, we switch off the laser cooling beam before ramping up the dimple and we do not use the transparency beam. Heat released while ramping up the dimple or after a heating pulse is again distributed from the dimple to the whole system by elastic collisions, but this time not dissipated by laser cooling. Since the reservoir gas has a ten times higher atom number than the dimple gas, the temperature after thermalization is only increased by a small amount. If the final temperature in the dimple is below the critical temperature, a BEC is formed. This scheme resembles the formation of a BEC by trap deformation, as demonstrated in [SK98b] using a sample of atoms cooled by evaporation. We test the performance of this BEC creation scheme again by repeated heating pulses. We can detect a BEC after at most five pulses. For more pulses, the temperature of the gas in the dimple remains too high to allow the formation of a BEC. This poor behavior stands in stark contrast to the resilience of BEC formation to heating, if the system is continuously laser cooled.

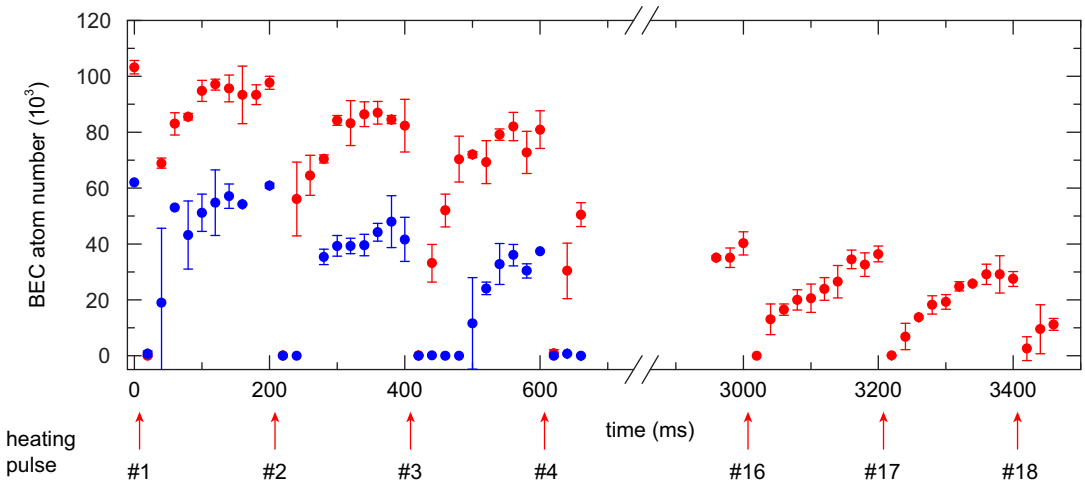

Figure 12.4: Repeated destruction and reformation of the BEC. Shown is the evolution of BEC atom number while the BEC is destroyed every 200 ms (arrows) by suddenly increasing the depth of the dimple trap. If the system is laser cooled, the BEC atom number quickly increases again, which is shown here for up to 18 cycles (red). Without laser cooling, a BEC is detectable for at most five heating cycles, of which the first three are shown here (blue).

The ability to reach the quantum degenerate regime by laser cooling has many exciting prospects. This method can be applied to any element possessing a laser cooling transition with a linewidth in the kHz range and suitable collision properties. Besides strontium this encompasses several lanthanides [Lu11a, Aik12]. The technique can also cool fermions to quantum degeneracy and it can be extended to sympathetic cooling in mixtures of isotopes or elements. Another tantalizing prospect enabled by variations of our techniques, is the realization of a continuous atom laser, which converts a thermal beam into a laser-like beam of atoms. To realize such a device, our scheme needs to be extended in two ways. First, the reservoir of laser cooled atoms needs to be replenished, for example by sending a thermal beam of atoms onto a part of the reservoir with sufficiently high cooling laser intensity to allow capture of these atoms. Second, a continuous beam of condensed atoms needs to be outcoupled. Using magnetic species such as dysprosium or erbium, outcoupling from the BEC is possible by changing the internal state and thereby the magnetic force on the atoms [Mew97, Blo99]. Alternatively, the reservoir can be connected to a outcoupling dipole trap, creating a narrow channel where atoms can escape without further interaction with the cooling light [Lah05].

In the following sections, we will present in-depth information about our approach to reach quantum degeneracy by laser cooling. In Sec. 12.2 we give details on the experimental sequence. In Sec. 12.3 we discuss the parameter dependence of BEC creation and properties of the BEC. In Sec. 12.4 we show that evaporative cooling does not play a role in reaching quantum degeneracy. In Sec. 12.5 we analyze the shifting of atomic and molecular transitions by the transparency beam. In Sec. 12.6 we model the density distributions of the BEC and the thermal cloud.

12.2 Experimental sequence

In the following, we discuss in detail the experimental sequence with which we obtain BEC by laser cooling. We first describe the preparation of a sample of ultracold ^{84}Sr atoms in the reservoir dipole trap, which follows closely the procedure used in our previous work [Ste09]. Then we give details on the additional steps we take to produce a BEC. These details include information on the transparency beam, the dimple dipole trap and the conditions of the final laser cooling stage. We end with a discussion of our data acquisition and analysis method.

12.2.1 Sample preparation

Isotope choice — Of the three bosonic strontium isotopes, ^{84}Sr is best suited for our experiment, since its scattering length of $a_{84} = 124\,a_0$ (with a_0 the Bohr radius) allows efficient thermalization by elastic collisions. The other bosonic isotopes are unsuitable for our task. ^{88}Sr has a negligible scattering length of $a_{88} = -1.4\,a_0$ and therefore does not thermalize. ^{86}Sr suffers from three-body inelastic loss because of a very large scattering length $a_{86} = 800\,a_0$. Unfortunately ^{84}Sr has a low natural abundance of only 0.56%. To obtain a large sample, we accumulate metastable state atoms in a magnetic trap, as described below.

Atomic beam and blue MOT — A sample of strontium metal with natural isotopic composition is heated in an oven under vacuum to about 600 °C in order to sublimate strontium atoms. The atoms form an atomic beam after escaping the oven through a bundle of microtubes. ^{84}Sr atoms in the atomic beam are transversally cooled, Zeeman-slowed, and captured in a "blue" magneto-optical trap (MOT) with laser light red-detuned to the ^{84}Sr $^1S_0 - {}^1P_1$ transition at 461 nm; see Fig. 12.5. This transition has a linewidth of $\Gamma_{\mathrm{blue}}/2\pi = 30.5\,\mathrm{MHz}$, corresponding to a Doppler temperature of $T_{D,\mathrm{blue}} = \hbar\Gamma_{\mathrm{blue}}/(2k_B) = 720\,\mu\mathrm{K}$. The MOT uses a quadrupole magnetic field with vertically oriented axis and a vertical field gradient of 55 G/cm. The MOT beams have waists of 5 mm and peak intensities of $10\,\mathrm{mW/cm^2}$, which is a quarter of the saturation intensity $I_{\mathrm{sat,blue}} = \pi hc\Gamma_{\mathrm{blue}}/3\lambda^3_{\mathrm{blue}} = 40.7\,\mathrm{mW/cm^2}$. The detuning of the MOT light to resonance is −30 MHz.

Metastable state reservoir — The blue MOT cycle is not completely closed, as atoms in the excited $^1P_1$ state can decay into the metastable and magnetic $^3P_2$ state with a branching ratio of 1:150 000. Atoms in this state can be trapped in the quadrupole magnetic field of the MOT. Since the lifetime of magnetically trapped $^3P_2$-state atoms of ~ 30 s is about three orders of magnitude longer than the leak time scale of the blue MOT, metastable state atoms accumulate in the magnetic trap. We operate the MOT until about 10^8 atoms are accumulated in this "metastable state reservoir", which takes ~ 10 s. This accumulation of atoms allows us to use the ^{84}Sr isotope, despite its low natural abundance.

Red MOT — To increase the phase-space density of the sample, we use a narrow-line "red" MOT operated on the $^1S_0 - {}^3P_1$ intercombination line, which has a wavelength of $\lambda_{\mathrm{red}} = 689\,\mathrm{nm}$ and a linewidth of $\Gamma_{\mathrm{red}}/2\pi = 7.4\,\mathrm{kHz}$. Our red MOT laser has a linewidth of about 2 kHz and an absolute stability better than 500 Hz. The horizontal (upward, down-

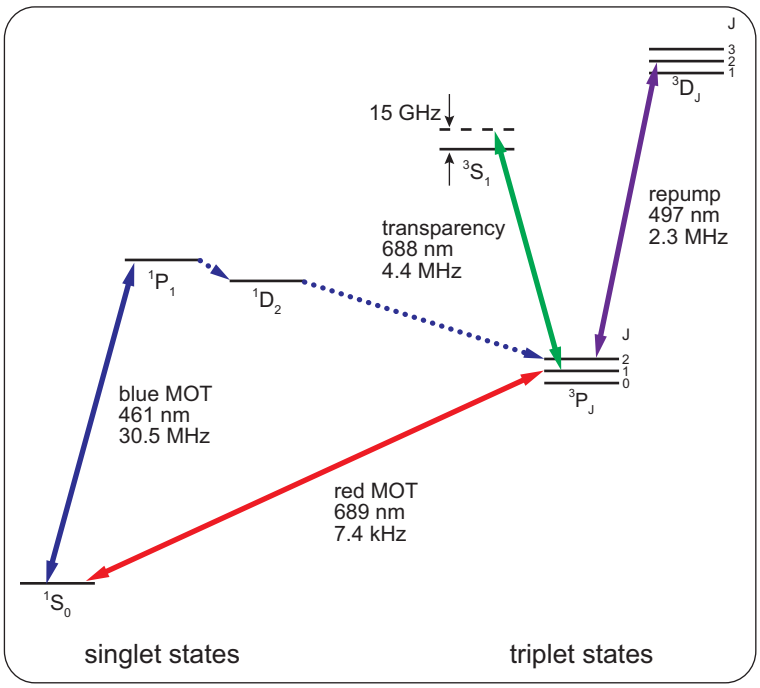

Figure 12.5: Level scheme of strontium with all relevant states and transitions. The dotted arrows show the decay path of atoms from the $^1P_1$ state into the $^3P_2$ state.

ward propagating) red MOT beams have waists of 3.1 mm (2.9 mm, 3.1 mm). The Doppler temperature of the red MOT $T_{D,\mathrm{red}} = 180\,\mathrm{nK}$ is comparable to the recoil temperature $T_r = \hbar^2 k^2/(k_B m) = 460\,\mathrm{nK}$, where $k = 2\pi/\lambda_{\mathrm{red}}$ is the wave vector of the cooling light, and m is the atom's mass. The temperature can approach $T_r/2$ when reducing the cooling light intensity to the saturation intensity $I_{\mathrm{sat,red}} = 3\,\mu\mathrm{W/cm^2}$ [Lof04b]. Not only the temperature but also the atom number decreases, when decreasing the cooling light intensity, and a compromise between atom number and temperature has to be chosen [Sor06]. We typically reach temperatures of 800 nK with samples of about 10^7 atoms.

To load the red MOT, metastable state atoms are transferred into the $^1S_0$ ground state by optical pumping via the $5s5d\,^3D_2$ state. The temperature of the sample recovered from the metastable state reservoir is on the order of the Doppler temperature of the blue MOT $T_{D,\mathrm{blue}} = 720\,\mu\mathrm{K}$, which is three orders of magnitude higher than the final temperature reached with the red MOT. We initially use red MOT parameters that allow to capture such a high temperature sample and then ramp these parameters to conditions in which a high phase space density is reached. The intensity and frequency of the MOT light during the capture phase and the subsequent ramps are given in Figs. 12.6(a) and (b). During the capture phase, the red MOT laser beams are frequency-modulated to increase the capture velocity of the MOT. In addition, the quadrupole magnetic field gradient is suddenly lowered to 1.15(5) G/cm in the vertical direction, which increases the capture volume, and then maintained at this value for the remainder of the experimental sequence. The detuning of the MOT light is reduced to compress the atomic cloud, and the intensity is reduced to lower the temperature. This provides optimal conditions for loading the reservoir dipole trap.

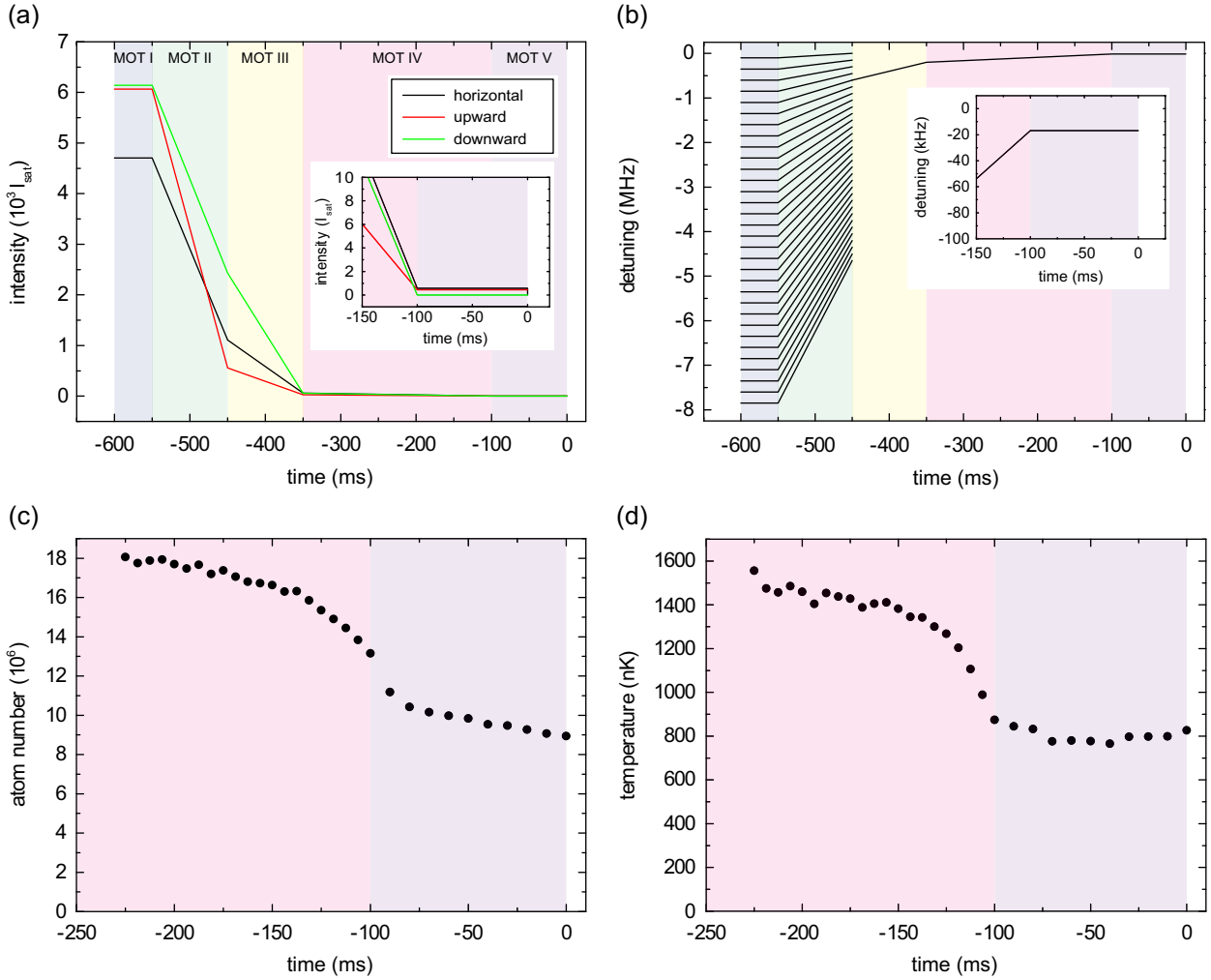

Figure 12.6: Narrow-line MOT and dipole trap loading. The narrow-line cooling consists of five consecutive stages, labeled MOT I through V: a 50-ms capture MOT, during which the repumping of atoms from the $^3P_2$ to the $^1S_0$ state takes place, a compression MOT of 100 ms, two cooling MOT stages of 100 ms and 250 ms, and a 100-ms hold time at final parameters. The end of the MOT phase is chosen as the origin of the time axis. (a) Intensity of the MOT beams in units of the saturation intensity $I_{\mathrm{sat}} = 3\,\mu\mathrm{W/cm^2}$. The intensity of the horizontal, upward, and downward MOT beams can be set independently. The downward MOT beam has little effect and is turned off before the other ones (see inset). (b) Frequency of the MOT beams, given as detuning from the Zeeman-shifted σ^+ transition. The light is frequency-modulated in the first two MOT stages. For clarity, only every tenth line of the resulting frequency comb is shown here. (c) and (d): Atom number (c) and temperature (d) drop significantly during the end of MOT stage IV. The drop in atom number happens as the restoring force of the MOT becomes too weak to support atoms against gravity, and all atoms outside the dipole trap are lost. The last 100 ms of hold time do not reduce the temperature further, but this stage is crucial to increase the density of atoms in the dipole trap.

Reservoir dipole trap — The reservoir dipole trap is a large-volume dipole trap consisting of a horizontally propagating beam. This beam is derived from a 5-W fiber laser operating at a wavelength of 1065 nm with a linewidth of 0.5 nm (IPG ytterbium fiber laser, model YLD-5-1064-LP). The beam contains up to 2 W of power and is linearly polarized in the vertical direction. Cylindrical lenses are used to create a horizontally elongated beam profile. The beam has a vertical (horizontal) waist of 17.3(2) μm (298(3) μm), yielding an aspect ratio of about 1:17. The trap frequencies are 600(6) Hz (35.3(4) Hz, 5.78(6) Hz) in the vertical (transverse horizontal, axial horizontal) direction at a power of 1760(35) mW as used in the experiment. Including gravitational sagging, the potential depth in the vertical direction is $\sim k_B \times 9\,\mu$K. The errors given here are dominated by the uncertainty in the measurement of the laser beam powers, which we assume to be 2%. The uncertainty in the trap oscillation frequencies is much smaller, and other effects, such as transmission losses of the glass cell and gravitational sagging in the dipole trap, are accounted for.

We increase the axial frequency slightly by a second, near-vertical beam with 297(3) μm waist and circular polarization, using a second fiber laser of the same model as mentioned above as source. At the power of 740(15) mW used in the experiment it has a trap depth of only $k_B \times 0.29(1)\,\mu$K and increases the trap frequency in the x-direction to 8.14(8) Hz. This increased axial trap frequency slightly increases the density of the sample and reduces the timescale of BEC formation. It has no further effects, and otherwise identical results are obtained without this additional beam.

Loading of the reservoir dipole trap — When the intensity of the MOT beams is low, gravity plays an important role in the MOT dynamics. The atoms are pulled towards the lower part of an ellipsoid of equal magnetic field magnitude located around the quadrupole magnetic field center. On this ellipsoid, the atoms are in resonance with the cooling light and levitated by it, giving the MOT a pancake shape, roughly matched to the shape of the reservoir dipole trap. The dipole trap is located 600(100) μm below the center of quadrupole field, where the B-field has a magnitude of 70(10) mG and is oriented nearly vertically. To overlap the MOT with the dipole trap, we carefully adjust the MOT laser detuning. Figures 12.6(c) and (d) show temperature and atom number evolution of the atomic cloud, while it is loaded into the reservoir dipole trap. At the endpoint of the ramp, the intensities of the horizontal (upward, downward propagating) MOT beams are $0.6\,I_{\mathrm{sat}}$ ($0.5\,I_{\mathrm{sat}}$, $0\,I_{\mathrm{sat}}$). The detuning from the σ^+-cooling transition is about -20 kHz. With the given nonzero B-field at the position of the atoms, this corresponds to a detuning of about -150 kHz from the unperturbed π-transition.

Laser cooling of the atoms in the dipole trap is influenced by Zeeman and light shifts. The vertical gradient of 1.15 G/cm translates to a negligible shift of 600 μG across the sample, assuming an estimated vertical size of 5 μm. The horizontal gradient is 0.63 G/cm, and the horizontal radius of the cloud is rather large: about 200 μm, giving a shift of 12 mG between the center and the outsides, which corresponds to a significant frequency shift of 25 kHz. The dipole trap induces a non-negligible differential AC Stark shift on the $^1S_0$ and $^3P_1$ states. We can reduce this shift by choosing the optimized polarizations for the horizontal and vertical dipole trap beams mentioned above, such that the magnitude of the shift is about 10 kHz [Boy07a]. Assuming that the atoms explore one tenth of the trap depth, we obtain a shift

beam	waist x (μm)	waist y (μm)	waist z (μm)	P (mW)	U/k_B (μK)	f_x (Hz)	f_y (Hz)	f_z (Hz)
horizontal		298(3)	17.3(2)	1760(35)	9.2(2)	5.78(6)	35.3(4)	600(6)
vertical	297(3)	297(3)		740(15)	0.29(1)	5.73(6)	5.73(6)	~ 0
dimple	22.4(2)	22.4(2)		38.3(8)	2.6(1)	228(2)	228(2)	~ 0

Table 12.1: Parameters of the dipole trap beams used for the experiments described in the report. Gravitational sagging is taken into account in the calculation of the horizontal dipole trap depth.

across the sample of about 1 kHz, which is negligible.

About 9×10^6 atoms are captured in the reservoir dipole trap at a temperature of 830 nK. The achievable temperature is density dependent. A reduction of the atom number by a factor two leads to a temperature reduction of $\sim$ 100 nK. Over the course of one hour, the variation of atom number between experimental cycles is about 1% and the temperature variation is below 10 nK. After loading of the dipole trap, the intensity of the upward cooling beam is reduced by a factor of 10, and the horizontal beams are turned off. Such a sample is the starting point for the subsequent laser cooling into quantum degeneracy.

12.2.2 Transparency beam

Immediately after completion of the dipole trap loading, the transparency beam is turned on. This beam is derived from a free-running master diode laser with a frequency stability of order 100 MHz/day. The frequency is blue detuned by 15 GHz from the $^3P_1 - {}^3S_1$ transition, and constantly monitored by a wavemeter. The beam is circularly polarized and focused onto the center of the atomic cloud with a waist of $26.2(3)\,\mu$m, again calculated from trap frequency measurements. The power used is 7.5(2) mW, translating to a peak intensity of $7 \times 10^5\,\mathrm{mW/cm^2} = 7\,\mathrm{MW/m^2}$. The beam propagates downwards, at an angle of 15° to vertical due to geometrical restrictions.

The transparency beam has a strong influence on the $^3P_1$ state. The differential AC Stark shift of the $^1S_0 - {}^3P_1$ cooling transition is on the order of +10 MHz, such that the cooling light is red-detuned by $> 1000\,\Gamma_{\mathrm{red}}$ for atoms at the center of the transparency beam. In this way, atoms illuminated by the transparency beam are transparent to laser cooling photons. Note that this scheme is drastically different to a scenario in which the cooling beam would contain a small dark spot imaged onto the dimple region: in this case, atoms in the dimple region could still absorb cooling light scattered by atoms in the reservoir. Our method differs also from the dark spot MOT technique, since we do not change the internal state of the atom in the region of transparency. A careful analysis of the magnitude of the AC Stark shift of the $^3P_1$ state is given in Sec. 12.5.

The transparency beam also creates an attractive trapping potential for the $^1S_0$ state with a depth of $k_B \times 0.5\,\mu$K. Because of similar beam orientation and waists, the potential created by the transparency beam resembles the potential created by the dimple beam, but has only about 20% of its depth.

12.2.3 Cooling light

The cooling light consists of an upward propagating, circularly polarized beam, red detuned by about 15 kHz from the σ^+ $^1S_0$ $-^3$ P_1 transition. It has a power of 20 nW and a peak intensity of $0.15\,\mu\mathrm{W/cm}^2$, corresponding to $0.05\,I_{\mathrm{sat}}$. The light has the same source as the light used for the narrow-line MOT. Any desired cooling rate of up to many 100 nK/ms can be achieved by a suitable combination of detuning and intensity, where a larger detuning can be compensated by an increased intensity. We find a fixed relation between cooling rate and induced decay rate, which is independent on the combination of detuning and intensity. There is a low temperature limit of about 450 nK, below which cooling is accompanied by rapidly increasing loss rates. For the experiments described in the report, we use only one upward propagating cooling beam, and we find that the addition of further cooling beams from other directions does not improve the performance.

12.2.4 Dimple

The local increase in density is facilitated by the dimple beam. This beam is aligned almost vertically, with an angle of 22° (37°) towards vertical (the transparency beam) due to geometrical restrictions. It is derived from the same laser source as the vertical dipole trap, has circular polarization and a waist of $22.4(2)\,\mu$m. The dimple beam is centered in the plane of the reservoir trap with the transparency beam to within $5\,\mu$m. At a power of 38.3(8) mW, the dimple provides horizontal trap frequencies of 228(2) Hz and has negligible trap frequencies in the vertical direction. In presence of the dimple, we refer only to the region outside of the dimple as the reservoir.

The dimple trap is set to a small depth of $k_B \times 0.15\,\mu$K at the beginning of the experimental sequence and ramped in 10 ms to a depth of $k_B \times 2.6\,\mu$K after the transparency beam is switched on. The ramp speed is not adiabatic with respect to the horizontal trap frequencies of the reservoir trap and atoms from the reservoir continue to accumulate in the dimple for 10 ms after the ramp. At this point, the temperature of the gas in the dimple is twice the temperature of the reservoir gas. Thermal contact with the laser cooled reservoir lowers the temperature on a timescale of ~ 100 ms. In thermal equilibrium, the dimple leads to a peak density increase of a factor of 30 compared to the reservoir. This density increase is the origin of the gain in phase-space density.

The BEC phase transition is observed 50 ms after ramping the dimple to high power. The BEC grows to slightly more than 10^5 atoms after another 100 ms. The local harmonic potential confining the BEC is dominated horizontally by the dimple trap and vertically by the horizontal dipole trap, leading to trap frequencies of 228(2) Hz in the horizontal plane and 600(6) Hz in the vertical direction. The BEC is pancake-shaped with a horizontal (vertical) Thomas-Fermi radius of $5\,\mu$m ($2\,\mu$m).

12.2.5 Absorption imaging and data analysis

We use time-of-flight absorption images to deduce all relevant information from our atomic samples. We are interested in the following quantities: atom number in the dimple and in

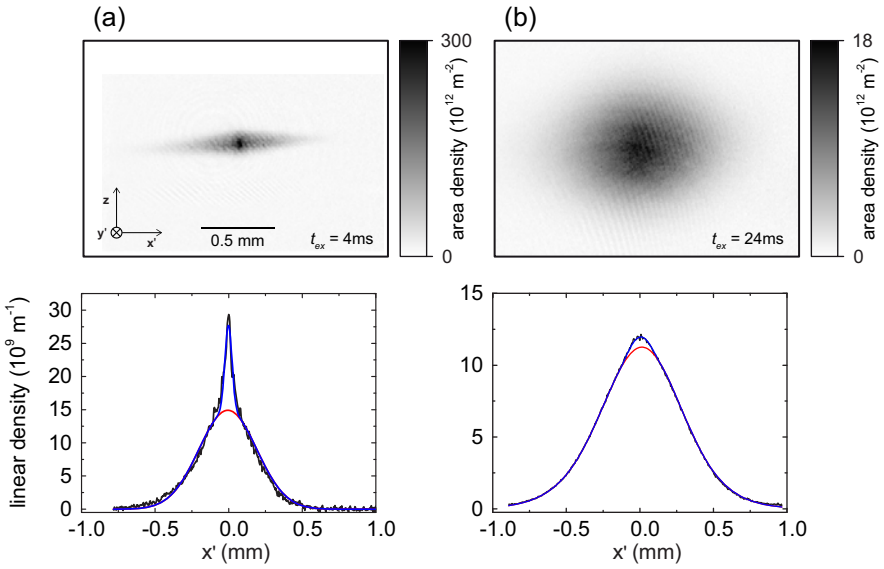

Figure 12.7: Typical absorption images used to determine temperatures and atom numbers. (a) Absorption image after a short expansion time $t_{\mathrm{ex}} = 4\,\mathrm{ms}$. A two-dimensional double Gaussian fit is used to extract atom number and temperature individually for dimple and reservoir. (b) Absorption image after a long expansion time $t_{\mathrm{ex}} = 24\,\mathrm{ms}$. A tri-modal two-dimensional fit, consisting of two Gaussians and an integrated Thomas-Fermi distribution are used to extract the atom number of the thermal component and the BEC. The panels below the absorption images show the density distribution (black) and the fits integrated along the z-direction (blue). The red curves show the Gaussian component of the fits.

the reservoir, temperature of the dimple and of the reservoir, and number of atoms in the condensate.

The temperature and atom number of the dimple and reservoir regions are measured in absorption images taken after 4 ms of free expansion; see Fig. 12.7(a). After this short time, the clouds from the two regions can still be clearly distinguished in the horizontal direction (x'-direction), but have expanded well beyond their initial size in the vertical direction (z-direction) to allow thermometry. Since the atomic clouds are very dense and nearly opaque to resonant imaging light, we image at a detuning of $48\,\mathrm{MHz} \approx 1.5\,\Gamma$, which reduces the absorption cross section by a factor of about twelve. We employ a 2D bi-Gaussian fit to the data. The temperature is derived from the vertical expansion only.

The overall atom number and the BEC atom number are determined from absorption images taken after a free expansion time of 24 ms; see Fig. 12.7(b). We fit the data with a 2D distribution consisting of two Gaussians for thermal atoms and an integrated Thomas-Fermi distributions for the BEC. Two Gaussians are used to take into account the two different sources of thermal atoms, the reservoir and the dimple. If only one Gaussian is employed to describe all thermal atoms, the BEC atom number deduced from the Thomas-Fermi part of the fit increases by about 50%.

All measurements are performed three times, and the average values and statistical error bars of atom number and temperature are given in Figs. 3 and 4 of Sec. 12.1.

12.3 Characterization of laser-cooled BECs

The BEC formation depends on various parameters. In this section, we will explore the influence of these parameters on the system and show that our method of laser cooling to quantum degeneracy works in a very broad range of parameters.

12.3.1 BEC atom number

Total atom number and temperature — The lowest achievable temperature depends on the total atom number in the system as a consequence of red-MOT dynamics. We measure the BEC atom number N_{BEC} in dependence of the total atom number N, at these lowest achievable temperatures. We find that $N_{\mathrm{BEC}} \propto N$. This behavior can be explained by the model described in Sec. 12.6.

Trap depth — We independently vary the trap depth of horizontal beam and dimple around the values presented in the report. A variation in trap depth of the horizontal beam by a factor of 1.7 changes the BEC atom number by at most 15%, and a variation of dimple power by a factor of 2.5 changes the atom number by at most 30%. A broad, global maximum of the BEC atom number exists, which is where we perform our experiments.

An important constraint on the trap depth is the desire to avoid evaporation. This constraint is fulfilled by the conditions chosen; see Sec. 12.4 for details.

Dimple — We find that the BEC atom number depends only weakly on the dimple size. We vary the waist of the dimple beam between 20 and 50 μm, but find no appreciable change in BEC atom number. The BEC formation time, however, is increased for larger waists. We also vary the ramp-up time of the dimple between 0 and 100 ms, but find no influence on temperature or BEC atom number after a 250-ms equilibration time.

12.3.2 Transparency beam

The transparency beam is the key novelty of our work. A detailed study of the non-trivial shifting of the laser cooling transition can be found in Sec. 12.5.

Frequency — The transparency beam is employed to locally shift the energy of the $^3P_1$ state by about +10 MHz. This would in principle be possible with light blue-detuned to any transition originating from the $^3P_1$ state. We chose to work in the vicinity of the $^3P_1 - {}^3S_1$ transition at 688 nm for two reasons: The availability of diode lasers, and the negligible influence on the $^1S_0$ state.

In our experiment, the transparency beam is blue-detuned by about 15 GHz from the $^3P_1 - {}^3S_1$ transition. In a series of measurements, we set the detuning to different values and vary the intensity of the transparency beam while searching for the appearance of a BEC. We never observe BEC formation for frequencies around or red-detuned to the $^3P_1 - {}^3S_1$ transition. We observe BEC formation only in a frequency range between 6 and 30 GHz blue detuning, where the upper bound of 30 GHz is probably limited by the available laser power of 10 mW.

Intensity — We observe the formation of a BEC only above a certain critical intensity I_c of the transparency beam, which depends on its frequency. The BEC atom number quickly grows for larger intensities, and saturates at about $2\,I_c$. The experiment is performed at around $10\,I_c$, corresponding to a peak intensity of $0.7\,\mathrm{kW/cm^2}$.

Spectral filtering — The ${}^3P_1 - {}^3S_1$ transition is 1.428 nm (or 902 GHz or $30\,\mathrm{cm^{-1}}$) away from the ${}^1S_0 - {}^3P_1$ intercombination transition, and off-resonant excitation of the intercombination transition is negligible. The light originating from the laser diode, however, contains incoherent fluorescence light, also known as residual amplified spontaneous emission (ASE). This light covers a broad spectrum with a width of about 20 THz, which includes the ${}^1S_0 - {}^3P_1$ transition. A spectrometer is used to estimate the spectral power of the incoherent background P_{ASE} to be on the order of $10^{-12} P_0$ in a 1 kHz wide band 1 THz away from the laser line, where P_0 is the power in the laser line. The scattering of these incoherent photons limits the lifetime of a BEC to 800 ms when illuminated by unfiltered transparency light. Spectral filtering of the light allows us to reduce the amount of resonant light by a factor of 500, leading to an increased lifetime of 10 s. The lifetime measurement is performed with a pure BEC obtained by standard evaporation, and its lifetime is limited to 10 s by inelastic collisions.

Waist — The transparency beam needs to be well-aligned with the dimple beam, and it needs to cover the BEC entirely. We vary the waist of the transparency beam between 10 and 55 μm. For comparison, the dimple waist is 22 μm and the Thomas-Fermi radius of the BEC in the xy-plane is 5 μm. Given an appropriate adjustment of the intensity, we can create laser-cooled BECs within the entire range of transparency beam waists examined. The purification method, during which reservoir atoms are selectively removed (see Fig. 12.2(c)), becomes increasingly inefficient for larger beam sizes, as also parts of the reservoir are shielded. A larger beam size makes the system insensitive to misalignments of the beams, which we verify experimentally.

Local density increase — One might speculate that the transparency beam leads to an increase in atom density purely by elimination of photon emission and re-absorption cycles, which act as an effective repulsion. This is not the case. We do observe a small density increase induced by the transparency beam, but it can be explained entirely by its trapping potential for atoms in the ${}^1S_0$ state.

12.3.3 Timescales

Collision rate and thermalization — The peak scattering rate of thermal atoms in the dimple region is $3100\,\mathrm{s^{-1}}$, found at the edge of the BEC (see Sec.12.6). The scattering rate decreases with distance from the center of the dimple, down to $50\,\mathrm{s^{-1}}$ outside of the dimple region. We observe that thermalization happens on a timescale of about 100 ms (compare Fig. 12.3(b)), which corresponds to about five collisions. This number matches well with the expectation of about three collisions required for thermalization [Mon93].

BEC formation time — We study the time required for the BEC to form after the dimple has been ramped up. For a BEC to be created, the atom number in the dimple has to be high enough and the temperature below a critical temperature for the given atom number. We find that the timescale required to accumulate atoms in the dimple is much shorter than the timescale required to thermalize the dimple gas with the reservoir; see Fig. 12.3. Thus, the BEC formation time is limited by the thermalization time scale. This time scale is linked to the elastic collision rate, which depends on the density of the sample. To test this relation, we vary the density by two means, changing the reservoir atom number and changing the reservoir trap frequency. We observe an increase in formation time as we decrease the atom number, down to a minimum atom number of about 1×10^6 atoms, below which no BEC forms in our trap geometry. Using the trap parameters of the experiment described in the report, the fastest formation time is about 50 ms for the maximum achievable atom number of 10×10^6 . An increase of the axial frequency from 8 Hz to 40 Hz reduces the formation time to about 20 ms. The timescale of BEC formation (following abrupt changes of the thermal distribution) was studied in previous experiments [Köh02, Rit07] and found to depend on the scattering rate, in agreement with our measurements.

Reservoir lifetime — A sample of 9×10^6 atoms at 800 nK confined in the horizontal dipole trap has a lifetime of ~ 30 s. When adding the dimple beam to obtain settings identical to the ones used in the experiment described in the report, the lifetime is reduced to 3.4(1) s. We believe that this lifetime is mainly limited by 3-body collisions in the dimple region, as the reservoir constantly replenishes the dimple population. The cooling light induces an additional decay, which is strongly dependent on intensity and detuning. For the values used in the experiment, the lifetime of the reservoir is reduced to about 2.5 s.

BEC lifetime — We observe that the lifetime of our BEC is linked to the lifetime of the reservoir gas. The reason is that any atom loss from the BEC is quickly and continuously replaced by atoms from the reservoir. A BEC exists as long as the total atom number in the system is above $\sim 10^6$ atoms. In order to measure the bare lifetime of the BEC without constant replenishment, we create a BEC, remove the atoms in the reservoir, and turn off the cooling light and the transparency light. The lifetime of this BEC is 1.0(1) s, probably limited by heating and loss resulting from inelastic 3-body collisions. The same result is obtained for an identical BEC created by conventional evaporation and re-compressed into the dimple. By contrast, the lifetime of a BEC in presence of the reservoir, the transparency light and the cooling light corresponds to the reservoir lifetime of 2.5 s.

Performance of the transparency beam — The transparency beam is absolutely necessary to protect the BEC from destruction by the cooling light. With the transparency beam turned off and the BEC subjected to cooling light, we measure a decay rate of about 1 ms, and the BEC is completely destroyed in less than 3 ms.

To demonstrate the ability of the transparency light to protect the BEC from resonant photons, we measure the lifetime of a BEC after removal of the reservoir and in presence or absence of both, the transparency and the laser cooling light. The lifetime is the same in both cases, 1 s. We conclude that the BEC lifetime is not limited by scattering of laser

cooling photons if the transparency light is present. We give an upper bound of $1\,\mathrm{s}^{-1}$ for the scattering rate of laser cooling photons, which is consistent with measurements presented in Sec. 12.5.

The transparency beam itself has no negative effect on the BEC: lifetime measurements let us deduce an absorption rate of photons from this light field to be well below $0.1\,\mathrm{s}^{-1}$.

Vacuum lifetime — Limitations to the lifetime of ultracold atoms in a dipole trap (beyond 3-body losses and residual evaporation) are off-resonant scattering of dipole trap photons, background gas collisions, and resonant stray light. We measure the lifetime of atoms at low density in a deep dipole trap to be 120 s, much longer than any other timescale. Note that all of the lifetimes evaluated here are between one and three orders of magnitude larger than the BEC formation time.

12.4 Absence of evaporation

The novelty of our work lies in the fact that BEC is achieved purely by laser cooling and thermalization between atoms, and not by evaporation and associated loss to the outside environment. Standard evaporative cooling of ^{84}Sr has been used in past experiments and can be very efficient: for a factor of 10 loss in atom number, more than three orders of magnitude in phase space density can be gained [Ste09]. Thus, already little evaporative atom loss can increase the phase space density considerably. It would require an infinitely deep trap to rigorously exclude evaporation. Here, we quantify the flux of evaporated atoms and ensure that evaporation is reduced to a negligible level.

We observe an overall atom loss that leads to a lifetime of the sample of about 3 s. This loss is not a measure of evaporation, as it includes various other loss processes as well: 3-body recombination, loss by scattering of cooling photons, light-assisted collisions, and off-resonant optical pumping into the $^3P_{0,2}$ states by the transparency light. We therefore need a specific probe for evaporated atoms.

It is also important to understand that the temperature of atoms in the reservoir is set entirely by the cooling light. This is true even if efficient evaporation would be taking place in the reservoir: in this case, the cooling light would heat the sample. In the following, we will be concerned only about evaporation in the dimple region, where the sample is transparent to cooling light.

The atoms are supported against gravity by the horizontal trap, and further confined by the dimple beam, which does not support the atoms against gravity. Atoms from the horizontal beam will preferentially evaporate downwards, aided by gravity. If they do so within the dimple region, they are attracted by and guided in the dimple beam. This beam provides superb confinement of evaporated atoms and enables us to detect even minute atom numbers in absorption imaging. The dimple beam has a potential depth of $k_B \times 2.6\,\mu\mathrm{K}$ and therefore selectively guides only low-energy atoms from evaporation, but not atoms originating from inelastic collisions.

The amount of atoms leaking from the dimple region into the dimple beam will depend on the sample temperature, the power of the horizontal beam, and the power of the dimple

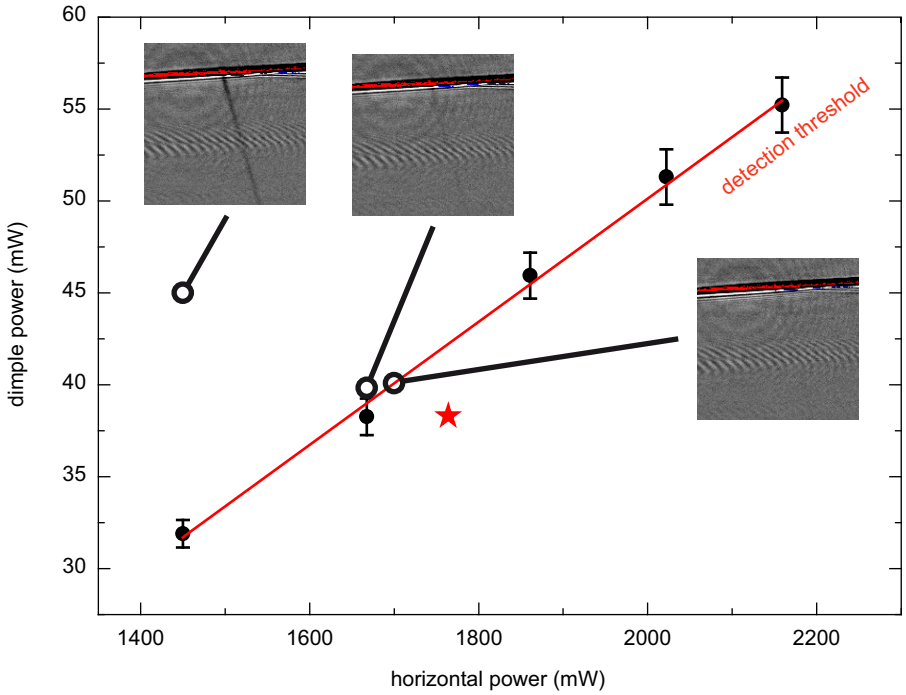

Figure 12.8: Detection of residual evaporation. Hot atoms from the dimple region might leave the dipole trap along gravity. When doing so, they are funneled into the dimple beam and can be detected by absorption imaging (insets). The amount of evaporation depends on the power in the horizontal and dimple trap beams, illustrated by the three insets showing atom fluxes of 350, 120, and < 50 atoms/ms. Our detection limit is about 50 atoms/ms, and conditions with atom fluxes that touch this limit are indicated by the black data points. The straight line is a linear fit to the data. Experiments are performed in the region below this line, indicated by the star. The images are averages of 10 experimental realizations, and the color scale is adjusted to maximize contrast of small signals.

beam. We set the temperature to the one used in the experiment, vary the power of the horizontal and the dimple beam independently, and measure the atom leakage. The result of such a measurement is shown in Fig. 12.8. The data points denote combinations of parameters where the atom flux is about 50 atoms/ms, which is our detection threshold. The straight line is a linear fit to the data. Note that for a leakage of 50 atoms/ms and a BEC formation time below 60 ms, less than 3000 out of 9×10^6 atoms evaporate in the dimple region. For the experiments described in the report, we verify that no discernable evaporation takes place at any time during the optical cooling.

We explore the entire parameter region shown in Fig. 12.8 and find no dramatic difference in BEC formation time or final BEC atom number, again indicating that any residual evaporation has no measurable contribution to the BEC formation.

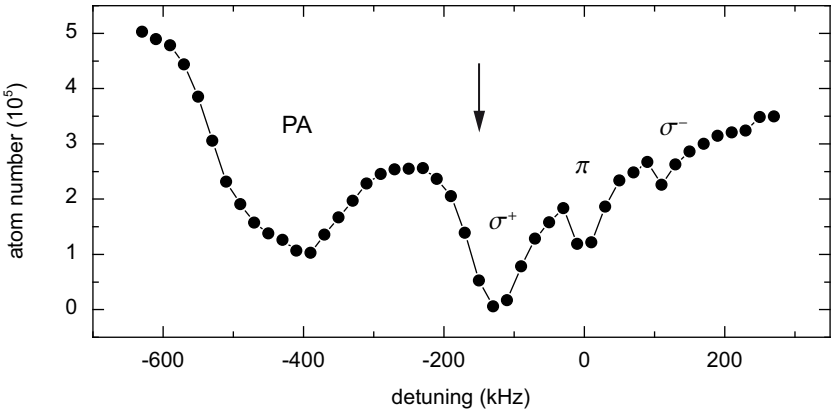

Figure 12.9: Loss spectrum of atoms confined in a dipole trap and illuminated by σ^+-polarized cooling light. A small guiding field of 90 mG splits the $^3P_1$ state into three clearly visible m_J states. The broad feature around -400 kHz is due to photoassociation (PA). The visibility of π and σ^- transitions indicates that the cooling light is not perfectly circularly polarized. In the experiment described in the report, cooling is performed on the red side of the σ^+ transition, indicated by the arrow. The line is a guide to the eye. Note that the detuning here is calculated from the resonance position at zero B-field, which is determined to better than 10 kHz.

12.5 Shifting atomic and molecular transitions

12.5.1 Introduction

We intend to cool atoms in the dipole trap with light resonant to the $^1S_0 - {}^3P_1$ transition, but only in the region outside the dimple. To do so, we render the atoms in the dimple region transparent for the cooling light by locally shifting the $^3P_1$ state out of resonance. Cooling of atoms in the reservoir is performed on the red side of the $^1S_0 - {}^3P_1$ transition, so we need to locally shift the $^3P_1$ state towards higher energies by at least a few 10 linewidths. This is done with the transparency beam, which spatially overlaps with the dimple region.

To characterize the system, we work in similar conditions as used in the experiment described in Sec. 12.1. Atoms are tightly confined in a crossed-beam dipole trap, consisting of the horizontal trap and the dimple, and we evaporate into a pure BEC to reach both high densities (to enhance possible photoassociative loss) and low trap depths (such that atoms can leave the trap with very few photon recoils). We then illuminate the atoms with circularly polarized cooling light, using only an upward propagating beam. The intensity of the cooling light is $1.2\, I_{\mathrm{sat}}$ and the duration of illumination is 10 ms. A magnetic field of 90 mG magnitude and vertical orientation is present. A typical loss spectrum is shown in Fig. 12.9; note the broad photoassociation (PA) feature, which corresponds to the $\nu = -1$ state of the $1(0_u^+)$ potential [Ste12].

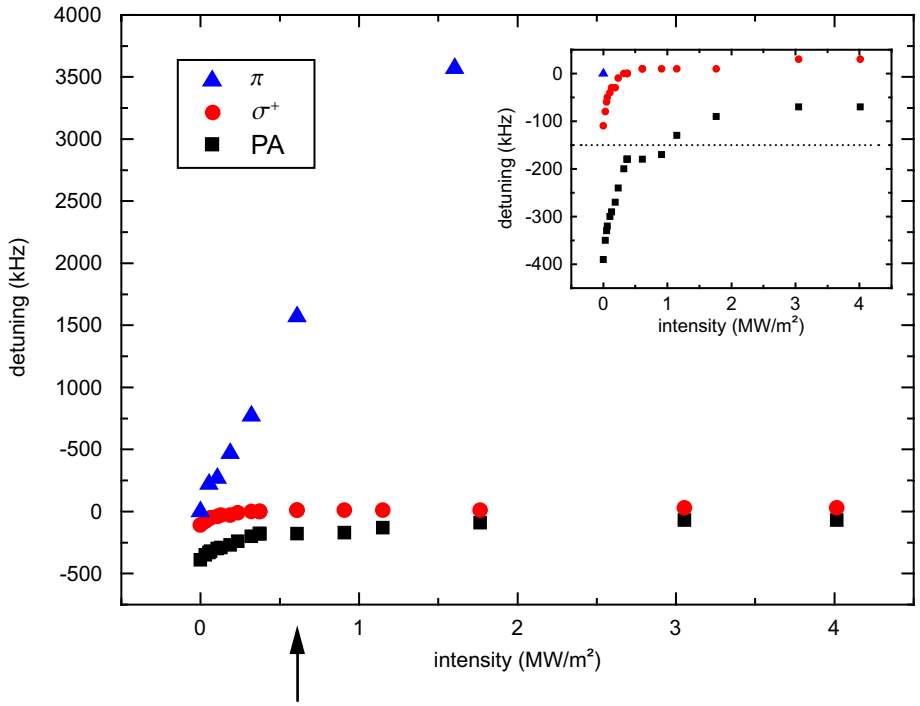

Figure 12.10: Resonance positions in dependence of transparency light intensity. Spectra as the one shown in Fig. 12.9 are taken for various intensities of the transparency beam, and the resonance positions recorded. The σ^- transition is too weak to be tracked. Inset: a magnification of the region around the cooling frequency, denoted by the dotted line. An intensity of $0.6\,\mathrm{MW/m^2}$ (arrow) is used to take the data presented in Fig. 12.11.

12.5.2 Shifting of resonances

In a next step, we illuminate the atoms with transparency light tuned 15 GHz blue to the ${}^3P_1 - {}^3S_1$ transition. The light is linearly polarized, propagating at an angle of 15° to vertical. The waist is set to $35\,\mu$m to ensure a uniform light intensity across the sample. We take loss spectra as the one shown in Fig. 12.9 for various intensities and observe that the four loss features experience different Stark shifts and move differently with intensity; see Fig. 12.10. The π-transition moves rapidly towards blue detuning, whereas the σ^+ and PA lines approach asymptotic values less than 100 kHz from resonance.

For our cooling strategy, we intend to work at a detuning of about $-150\,$kHz from the resonance frequency at zero B-field. It seems possible to move the σ^+ transition a few 100 kHz away from this frequency. Unfortunately, the broad PA transition moves into exactly this region, potentially causing undesired losses given the high density in the dimple region. The transitions broaden considerably with increased transparency beam intensity.

12.5.3 Polarization dependence

So far, we have not considered the polarization of the transparency beam, which was linear in the previous measurement. This beam is almost co-aligned with the magnetic quantization

axis, such that its field can be decomposed into equal amounts of σ^+ and σ^--light (but no π-light) in the reference frame of the atoms. The three m_J-states of the $^3P_1$ manifold, as well as the PA line tied to the $m_J = +1$ state, couple differently to the $^3S_1$ states; see Fig. 12.11(a). This helps to understand the different shifts of the π- and σ^+-transitions in Fig. 12.10, and we expect the shifting of the individual states to strongly depend on the polarization of the transparency light.

In a next step, we fix the intensity of the transparency light intensity to $0.6\,\mathrm{MW/m^2}$ and take scans at various polarizations. The results are shown in Figs. 12.11(b) and (c). The loss features change dramatically in position, width, and amplitude depending on the polarization of the transparency beam. The σ^+-transition and its associated PA line are maximally shifted by a σ^--polarized transparency beam. This can easily be understood from the fact that σ^+-polarized light cannot couple the $m_J = +1$ state to the $^3S_1$ manifold. We find that already small variations in the polarization decrease the performance considerably. Note that in the experiment described in the report, we use an intensity of the transparency light that is larger by a factor of about ten.

We will now focus on the region of interest around the cooling frequency and highlight the importance of the polarization of the transparency light under conditions close to the ones used in the experiment described in the report. We increase the intensity of the transparency beam to $7\,\mathrm{MW/m^2}$ and make the cooling pulse 25-times stronger (five times longer and five times more intense) to amplify even small losses. Two spectra for σ^- and near-linear polarization are shown in Fig. 12.11(d). Not only does the loss feature move to positive detuning with increasing circular polarization, also its width and amplitude decrease dramatically. The small remaining loss feature is about $250\,\mathrm{kHz} = 35\,\Gamma$ away from the desired cooling frequency. We speculate that this is the $m_J = -1$ state, which is unaffected by transparency light of σ^--polarization and driven by small σ^--polarization components in the cooling light.

12.5.4 Conclusion

We have shown that the magnetic substates of the $^3P_1$ state, as well as the highest molecular level of the $1(0_u^+)$ potential, can be shifted by a light field slightly detuned from the $^3P_1 - {}^3S_1$ transition. In particular, we find that the three Zeeman lines and the first PA line move very differently in dependence of the polarization of the transparency laser. We find that all lines can be moved at least 250 kHz away from the desired cooling transition, reducing the photon scattering rate by at least three orders of magnitude. The strongest lines are even moved by a few MHz. This transparency beam allows us to cool atoms in the reservoir, while keeping the photon scattering rate of atoms in the dimple below the rate of 3-body collisions, which eventually determine the lifetime of the BEC. Further investigations are needed to gain a quantitative understanding of the AC Stark shifts in dependence on transparency laser frequency, intensity, and polarization.

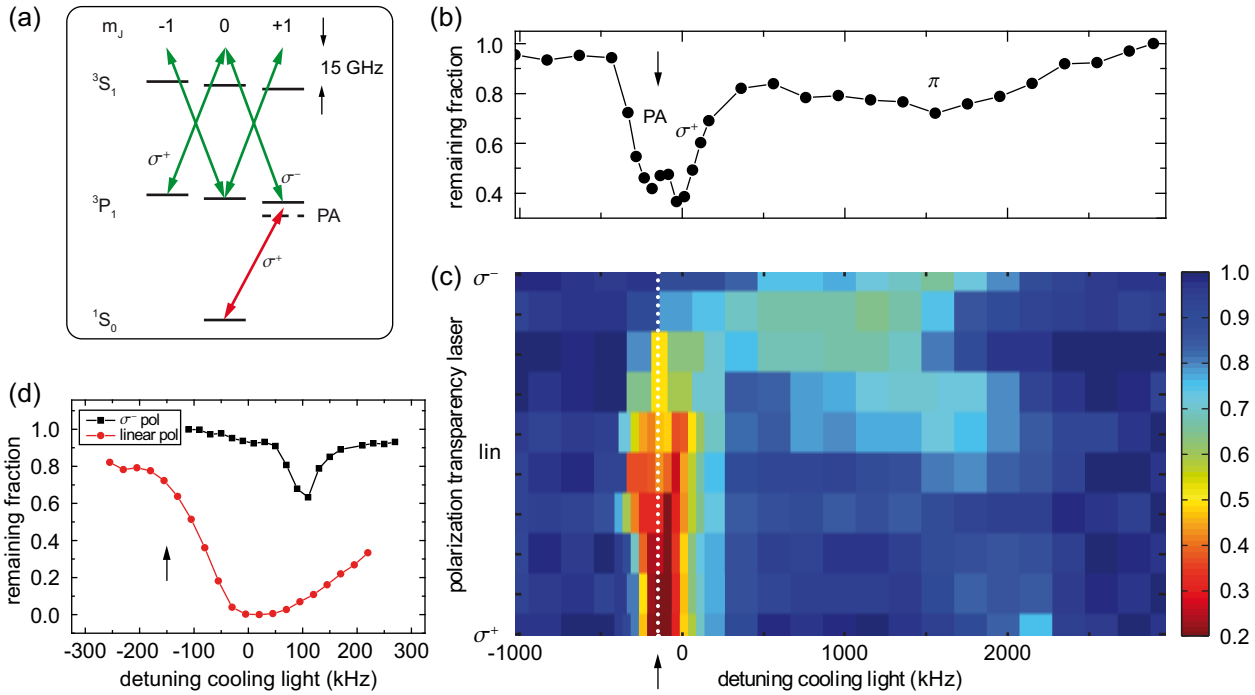

Figure 12.11: Resonance positions in dependence of the polarization of the transparency light. (a) The three m_J states of the $^3P_1$ manifold couple differently to light on the $^3P_1 - {}^3S_1$ transition (green arrows). The $m_J = +1$ state, for example, does not couple at all to σ^+-polarized light due to the absence of any $m_J = +2$ state in the $^3S_1$ manifold. The cooling light (red arrow) is always σ^+-polarized, with small admixtures of other components due to experimental imperfections. (b) A loss spectrum of atoms illuminated by the transparency light and subjected to a pulse of cooling light. The frequency of the cooling light is scanned, and the number of remaining atoms is recorded. The three loss features correspond to the PA-, σ^+-, and π-transitions. This spectrum is taken with a near-linear polarization of the transparency light and corresponds to the data set indicated by an arrow in Fig. 12.10. (c) We take spectra at various polarizations, covering the complete range between σ^+-circular (bottom) to linear and σ^--circular polarization (top). The fraction of remaining atoms is encoded in the color, with red color denoting high atom loss. The dotted white line indicates the frequency of the cooling light. (d) Loss spectra for two extreme values of the polarization, taken with the intensity of the transparency light used in the experiment described in the report, and applying a 25-times stronger cooling pulse compared to the measurements shown in (b) and (c). The spectra taken with intermediate polarizations (not shown) smoothly interconnect between these two curves. The cooling frequency is again indicated by an arrow.

12.6 Density distribution models

We now determine the density distributions of our samples by a numerical model and by a simple analytical model. Both models assume that the gas is in thermal equilibrium and neglect the influence of laser cooling light on the density distribution in the reservoir. The models are compared to the experiment and used to determine important quantities, such as the elastic collision rate.

12.6.1 Self-consistent mean-field equations

We use a self-consistent mean-field model [Dal99] to describe the density distribution of the BEC $n_0(\mathbf{r})$ and of the thermal gas $n_{\rm th}(\mathbf{r})$. The thermal gas is described as a gas of non-interacting particles residing in the potential $U_{\rm th}(\mathbf{r}) = U_{\rm ext}(\mathbf{r}) + 2g(n_0(\mathbf{r}) + n_{\rm th}(\mathbf{r}))$, which is the sum of the external trapping potential $U_{\rm ext}$ and the mean-field potential of all atoms. Here $g = 4\pi\hbar^2 a/m$, where a is the scattering length and m the mass of the atoms. The potential $U_{\rm ext}$ is assumed to be zero at its deepest point. In the semiclassical approximation, the thermal density distribution in dependence of the potential is given by

$$n_{\rm th}(U) = \lambda_{\rm th}^{-3} g_{3/2}(e^{-[U-\mu]/k_B T}),$$

where $\lambda_{\rm th} = h/\sqrt{2\pi m k_B T}$ is the thermal de Broglie wavelength and μ the chemical potential. The function $g_{3/2}(z)$ is a polylogarithm function, $g_\alpha(z) = \sum_{n=1}^{\infty} z^n/n^\alpha$. The spatial density distribution is then

$$n_{\rm th}(\mathbf{r}) = n_{\rm th}(U_{\rm th}(\mathbf{r})). \tag{12.1}$$

The BEC distribution is obtained in the Thomas-Fermi (TF) approximation

$$n_0(\mathbf{r}) = \max[(\mu - U_0(\mathbf{r}))/g, 0], \tag{12.2}$$

where the potential $U_0(\mathbf{r}) = U_{\rm ext}(\mathbf{r}) + 2g n_{\rm th}(\mathbf{r})$ is the sum of external potential and the mean-field potential of the thermal atoms.

12.6.2 Numerical model

To determine the density distributions n_0 and $n_{\rm th}$, we self-consistently solve Eqns. 12.1 and 12.2. The solution is obtained by a numerical calculation for given values of the chemical potential μ and the temperature T. The calculation starts from initial density distributions that are zero everywhere, and obtains better and better approximations for the distributions by iterating Eqns. 12.1 and 12.2 [1]. The potential is described by a sum of the gravitational

[1] To speed up calculations, we first calculate tables containing $n_0(U)$ and $n_{\rm th}(U)$ for a range of relevant potential depths U. We then interpolate these tables to obtain $n_0(U)$ and $n_{\rm th}(U)$ for any U. The spatial density distributions $n_0(\mathbf{r})$ and $n_{\rm th}(\mathbf{r})$ are obtained in the local density approximation using realistic potentials $U(\mathbf{r})$. To avoid numerical artifacts, the self-consistent solution of Eqns. 12.1 and 12.2 is obtained in two stages. During the first stage, the mean-field of the thermal atoms is not included in the potential that the thermal atoms experience. After 20 rounds of iteratively solving Eqns. 12.1 and 12.2, we linearly ramp-on

potential and the potentials created by the dipole trapping beams, which we assume to be Gaussian.

In the experiment we determine the atom number in the reservoir N_{res} and the atom number in the dimple N_{dimple} by performing a double-Gauss fit to the density distribution recorded after a short expansion time. To determine similar values from the numerical calculation, we define the reservoir density distribution $n_{\mathrm{th,res}}(\mathbf{r}) = n_{\mathrm{th}}(U_{\mathrm{res}}(\mathbf{r}))$, where $U_{\mathrm{res}}(\mathbf{r})$ is a potential without the contribution of the dimple, but the same potential values outside the dimple region. The atom numbers in BEC and reservoir are determined by integrating $n_0(\mathbf{r})$ and $n_{\mathrm{th,res}}(\mathbf{r})$, respectively. The thermal atom number in the dimple is obtained by integrating $n_{\mathrm{th,dimple}}(\mathbf{r}) = n_{\mathrm{th}}(\mathbf{r}) - n_{\mathrm{th,res}}(\mathbf{r})$. The radii R_i ($i \in \{x, y, z\}$) of the BEC are defined by the locations at which the BEC density drops to zero.

An important quantity which we want to extract from our model is the elastic collision rate of the thermal gas. It is given by $\Gamma_{\mathrm{el,th}}(n) = nv\sigma$, where $v = 4\sqrt{k_B T/\pi m}$ and $\sigma = 8\pi a^2$ [Dal98]. The peak collision rate of the thermal gas $\Gamma_{\mathrm{el,th,peak}}$ is reached at the edge of the BEC, where the gas has the critical density. The timescale of thermalization between the gas in the dimple and the reservoir gas is limited by the elastic collision rate in the reservoir, outside the dimple region. This rate is highest just to the side of the dimple in the xy-plane, and determined from n_{th} at that location, which we denote as $n_{\mathrm{th,edge}}$. Assuming a Gaussian reservoir density profile in the z-direction and a homogeneous distribution in the xy-plane, the average elastic collision rate in the reservoir close to the dimple is $\Gamma_{\mathrm{el,th,res}} = n_{\mathrm{th,edge}} v\sigma/\sqrt{2}$.

12.6.3 Analytical model

Before we present the results of the numerical model, we discuss a simple analytical model. We neglect the mean-field of the thermal atoms and approximate the dimple potential by a harmonic potential with trap oscillation frequencies f_i. The BEC resides entirely in the dimple and has the usual TF inverted parabola shape. The chemical potential is determined from the BEC atom number N_0 by

$$\mu = \frac{\hbar\omega}{2}\left(\frac{15N_0 a}{a_{\mathrm{ho}}}\right)^{2/5},$$

where $a_{\mathrm{ho}} = \sqrt{\hbar/m\omega}$ and $\omega = 2\pi(f_x f_y f_z)^{1/3}$. The radii of the BEC are given by the TF radii $R_{\mathrm{TF},i} = \sqrt{2\mu/m(2\pi f_i)^2}$ and the peak density is $n_0(0) = \mu/g$.

Because of different correlations in the BEC and the thermal gas, the BEC mean-field is twice as strong for thermal atoms than for atoms in the BEC. Thermal atoms in the center of the trap experience a "Mexican hat" potential, created by the external confinement combined with the BEC mean-field. In the center of the BEC, this mean-field reaches $2gn_0(0) = 2\mu$. For our typical parameters (see Tab. 12.3), the chemical potential is on

this potential contribution in a second stage consisting of 25 rounds. In every round, the minimum $U_{\mathrm{th}}^{\mathrm{min}}$ of U_{th} is determined. Since the presence of a BEC is assumed, $n_{\mathrm{th}}(U_{\mathrm{th}}^{\mathrm{min}}) = n_c$ and is used as boundary condition in the determination of $n_{\mathrm{th}}(\mathbf{r})$. To avoid oscillations in the calculation, we low pass filter $U_{\mathrm{th}}^{\mathrm{min}}$ and use the filtered value in the calculation of $n_{\mathrm{th}}(\mathbf{r})$.

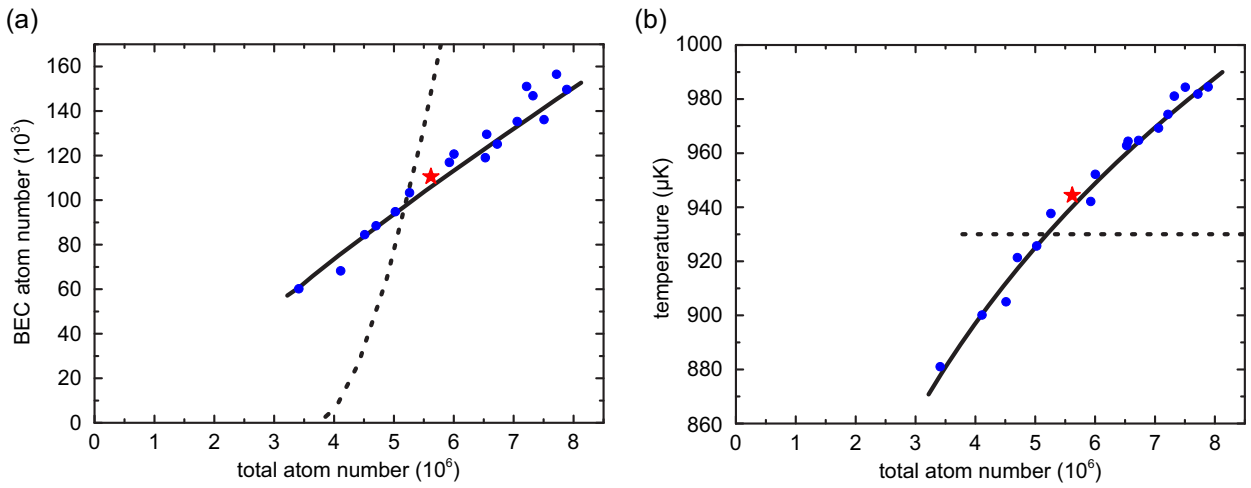

Figure 12.12: Comparison of experiment (blue data points) and numerical model (solid lines). Shown are BEC atom number (a) and temperature (b) in dependence of the total atom number. Experiment and calculation agree well. A peculiar feature is that the BEC atom number is nearly proportional to the total atom number. An important contribution to this behavior is the increase in temperature with the atom number observed in the experiment. For comparison, a calculation for constant temperature is shown as dashed line. Here, the BEC atom number increases much more steeply with total atom number. Results of the models matched to the star-shaped data point are given in Tab. 12.3 and Fig. 12.13.

the order of half the temperature, $\mu \sim 0.5 k_B T$, which means that the thermal distribution is strongly modified by the BEC mean-field. The density of the thermal gas reaches the critical density $n_c = n_{\mathrm{th}}(\mu) = 2.612/\lambda_{\mathrm{th}}^3$ at the edge of the BEC. The dimple potential has a finite size in the xy-plane and a finite depth $U_{\mathrm{dimple}}^{\mathrm{max}}$. At the edge of the dimple, the density is $n_{\mathrm{th,edge}} = n_{\mathrm{th}}(U_{\mathrm{dimple}}^{\mathrm{max}})$. The elastic collision rate in the reservoir is given by $\Gamma_{\mathrm{el,th,res}} = \Gamma_{\mathrm{el,th}}(n_{\mathrm{th,edge}})$ and the peak elastic collision rate of the thermal gas is again $\Gamma_{\mathrm{el,th,peak}} = \Gamma_{\mathrm{el,th}}(n_c)$.

We can estimate the atom number in the reservoir N_{res}, by describing the reservoir as a harmonic potential with trap oscillation frequencies $f_{\mathrm{res},i}$. The central density of the reservoir is about $n_{\mathrm{th,edge}}$, which is much lower than the critical density. Therefore the gas in the reservoir is well described by a classical thermal distribution. With this approximation we obtain $N_{\mathrm{res}} = n_{\mathrm{th,edge}}(2\pi k_B T/m)^{3/2}/\omega_{\mathrm{res}}^3$, where $\omega_{\mathrm{res}} = 2\pi(f_{\mathrm{res},x} f_{\mathrm{res},y} f_{\mathrm{res},z})^{1/3}$.

12.6.4 Comparison to the experiment

We now compare the experiment and the numerical model. Since the model can only describe a thermalized sample without the influence of the laser cooling beams, we perform experiments corresponding to this situation. The experimental sequence is identical to the one described in the report, up to the moment before the dimple is ramped on. Here, we switch off laser cooling and we do not use the transparency laser. After ramping on the

beam	waist x (μm)	waist y (μm)	waist z (μm)	P (mW)	U/k_B (μK)
reservoir		298.2	17.32	1748	11.73
vertical	297	297		743	0.29
dimple	22.41	22.41		39.6	2.73

Table 12.2: Parameters of the dipole trap beams used for the experiments described in this section.

dimple, we wait 200 ms to let the system thermalize. Then we record as usual time-of-flight absorption images with 24 ms expansion time, from which we extract temperature, total atom number and BEC atom number. We perform this measurement for different loading times of the metastable state reservoir at the beginning of the experimental sequence. A longer loading time leads to a higher atom number and, as a consequence of the laser cooling process, to a higher temperature. The result of the experiment is shown in Fig. 12.12. In the examined range from 3.5×10^6 to 8×10^6 atoms, the temperature changes from 880 nK to 990 nK. The atom number in the condensate is nearly proportional to the total number of atoms N_{tot} and is well described by $N_0 = 0.02 N_{\mathrm{tot}}$.

The numerical model needs the potential as input. To describe the potential, we sum the contributions of gravity and of the potentials of the three Gaussian optical dipole trap beams used in this experiment. The parameters of the beams, determined from trap oscillation and beam power measurements, are given in Tab. 12.2. The precision with which we know the potential shape is not quite enough to give a good match between the model and the experiment. We therefore vary one potential parameter, here the dimple depth, and match the model to the experiment around $N_{\mathrm{tot}} = 6 \times 10^6$. Experiment and model agree for a dimple depth that is 10% larger than the measured one. A good match between model and experiment could have alternatively been achieved by varying other parameters or by correcting a possible systematic error in the experimental data. A candidate systematic measurement error, which would be sufficient to bring the numerical model and the experiment into agreement, is an overestimation of the temperature by 5%. This hypothetical systematic shift is smaller than our experimental uncertainty.

After matching the model to the data in a single point, we can now explore the whole range of data. The model requires as input parameters the chemical potential and the temperature. For two data points near 3.5×10^6 and 8×10^6 atoms, we determine the chemical potential that corresponds to the measured BEC atom number. This procedure results automatically in a good match for the total atom number, which already shows that the model describes the data well. Instead of determining the chemical potential for each measurement point, we now simply linearly interpolate temperature and chemical potential between these two extreme points and calculate N_0 and N_{tot} for many values in between. The result is the solid line in Fig. 12.12 and shows a good overall match between experiment and calculation. In a second calculation, we keep the temperature always at 930 nK and vary only the chemical potential; see dashed line in Fig. 12.12. The mismatch between calculation and data shows the importance of the small temperature change observed in the experiment between low and high atom number.

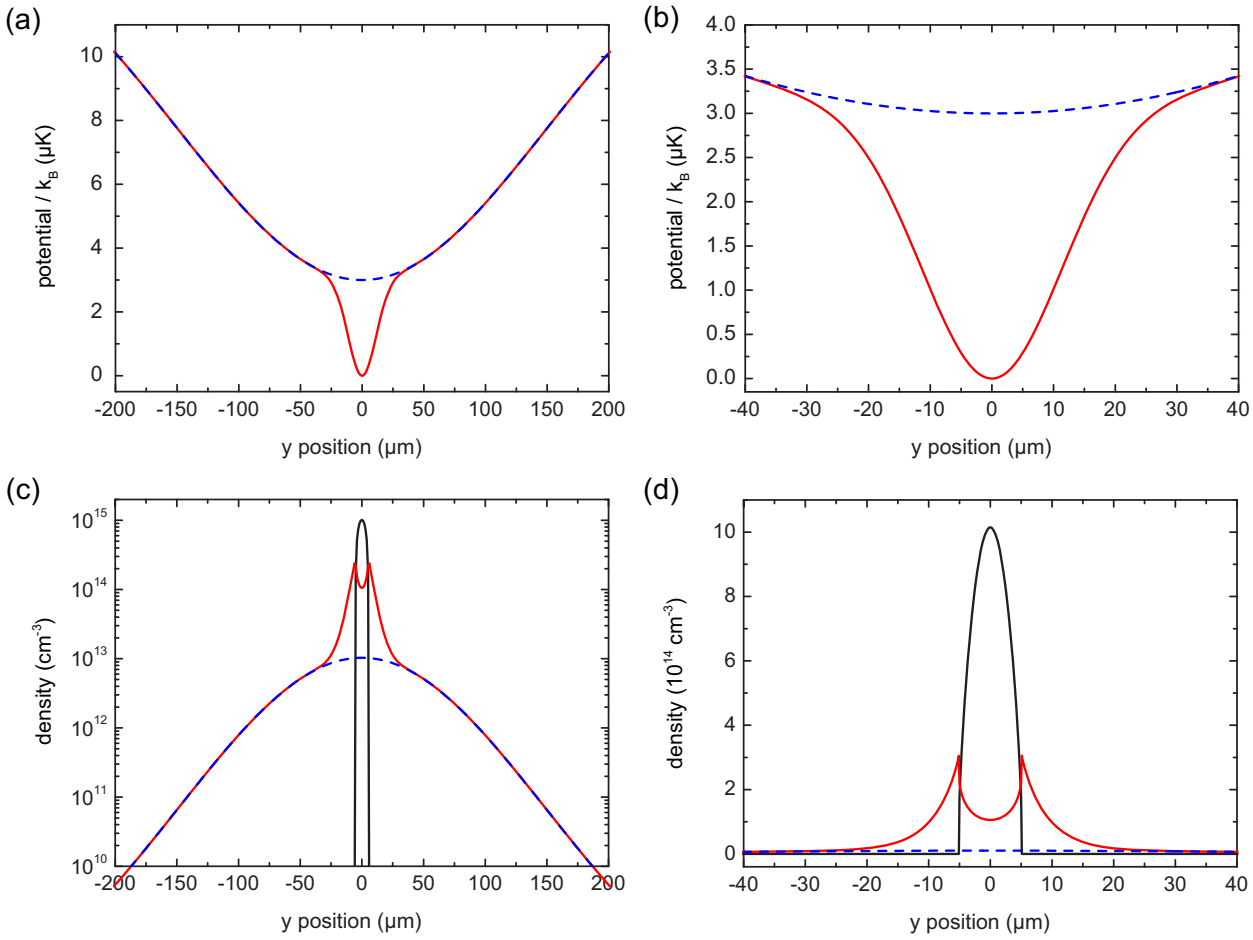

Figure 12.13: Potential (a) and (b) and density (c) and (d) along the y-direction determined by the numerical model, using parameters that correspond to the star-shaped data point of Fig. 12.12. In (a) and (b) the reservoir potential is shown as blue, dashed line and the full potential, including the dimple, as red line. Panels (c) and (d) show the density distributions of the thermal gas n_{th} (red line) and of the BEC n_0 (black line). The dashed blue line shows the density of thermal atoms in absence of the dimple potential $n_{\mathrm{th,res}}$.

We now examine the data point marked by a star in Fig. 12.12 in more detail. We chose this data point because the atom number in the BEC is comparable to the one achieved in the experiments discussed in the report. As input for the models, we use the measured temperature and BEC atom number and adapt the chemical potential accordingly. Figure 12.13 shows the potential and the density profiles of BEC and thermal gas along the x-direction as determined by the numerical calculation. The BEC mean-field clearly has a strong effect on the thermal distribution, pushing thermal atoms outwards. Table 12.3 compares experimental data with the two models and shows a general good agreement.

Some information extracted from the models is worth further discussion. We expect that the conditions in the experiments presented in the report are comparable to the experiments presented here within the volume illuminated by the transparency laser. Only outside this

quantity	experiment	numerical	analytical
T	944(50) nK	944 nK	944 nK
μ/k_B		478 nK	405 nK
N_{BEC}	111×10^3	111×10^3	111×10^3
N_{dimple}		654×10^3	
$N_{\mathrm{reservoir}}$		5.0×10^6	2.6×10^6
N_{total}	5.8×10^6	5.8×10^6	
$n_0(0)$		$1.0 \times 10^{15}\,\mathrm{cm}^{-3}$	$8.6 \times 10^{14}\,\mathrm{cm}^{-3}$
n_c		$3.5 \times 10^{14}\,\mathrm{cm}^{-3}$	$3.5 \times 10^{14}\,\mathrm{cm}^{-3}$
$n_{\mathrm{th,edge}}$		$9.9 \times 10^{12}\,\mathrm{cm}^{-3}$	$8.7 \times 10^{12}\,\mathrm{cm}^{-3}$
v		$21.8\,\mu$m/ms	$21.8\,\mu$m/ms
$\Gamma_{\mathrm{el,th,peak}}$		$2700\,\mathrm{s}^{-1}$	$2700\,\mathrm{s}^{-1}$
$\Gamma_{\mathrm{el,th,res}}$		$50\,\mathrm{s}^{-1}$	$50\,\mathrm{s}^{-1}$
$R_{\mathrm{TF},x}$		$5.1\,\mu$m	$5.8\,\mu$m
$R_{\mathrm{TF},y}$		$5.0\,\mu$m	$5.8\,\mu$m
$R_{\mathrm{TF},z}$		$1.9\,\mu$m	$2.3\,\mu$m

Table 12.3: Comparison of the experiment and the models. The values given correspond to the star-shaped data point in Fig. 12.12. The trap oscillation frequencies of dimple and reservoir are $f_x = 244\,\mathrm{Hz}$, $f_y = 247\,\mathrm{Hz}$, $f_z = 624\,\mathrm{Hz}$, $f_{\mathrm{res},x} = 8.4\,\mathrm{Hz}$ $f_{\mathrm{res},y} = 37\,\mathrm{Hz}$, and $f_{\mathrm{res},z} = 622\,\mathrm{Hz}$.

volume, laser cooling will change the conditions and make a comparison more complicated. An indication for this is that the atom number in the dimple, which was not measured here, is comparable to the one observed in the experiment of the report.

Since the reservoir contains nearly an order of magnitude more atoms than the dimple, the density distribution of the gas in the reservoir and the temperature of the system will barely change when ramping the dimple on. Therefore the ratio of $n_{\mathrm{th,edge}}/n_c$, which is 35, gives an idea of the thermal gas density increase and the phase-space density increase provided by the dimple.

Finally we note that the average elastic collision rate in the reservoir close to the dimple corresponds to about five collisions during the $\sim 100\,\mathrm{ms}$ required for thermalization. This number compares well with the ~ 3 collisions required to obtain thermal equilibrium as determined from Monte Carlo simulations [Mon93].

Chapter 13

Outlook: On and behind the horizon

During the course of this thesis, we went from an empty lab to the first degenerate gases of Sr, and later developed a collection of techniques to handle our new and beloved atomic species. The reader might ask "Are we there yet?" or "Cool, where do we go next?", depending on his or her attitude.

Predicting the future of this experiment will inevitably fail, and in a few years' time, the community is likely to move into a direction no one can anticipate today. Still, we will try to sketch a few ideas of experiments that could be performed in the near and not-so-far future. We will divide them into three categories: (i) the "homework" we still have to do in order to better understand Sr, (ii) work along the lines of quantum simulation, and (iii) work along the lines of RbSr molecules.

13.1 Further investigation of strontium

Part of this thesis was dedicated to the investigation of atomic and many-body properties of strontium. Some quite obvious and important questions, however, have not been addressed.

- **3-body decay coefficients** We have not yet succeeded in measuring the 3-body decay coefficient K_3 of the different isotopes, most prominently ^{84}Sr, with a satisfying precision. We identified a trapping geometry of two horizontal dipole trap beams to be advantageous for this measurement. Some quantum simulations require three distinguishable fermions to be located on the same lattice site, and it would be valuable to assess the lifetime of such a system.

- **SU(N) character** In Chpt. 7, we were able to put an upper bound on the ratio of spin-changing to elastic collisions in a spin mixture of the fermionic isotope. This value can be converted into a deviation of less than 5×10^{-4} from the assumed SU(N) symmetry [Bon12]. These measurements were performed in a dipole trap that did not allow for strong compression or long hold times. With our improved laser cooling capability and an increased oven flux, we should be able to improve the phase space density by a factor of ten. Pumping atoms into two carefully-chosen states (instead of depleting only one state) will increase the number of relevant collisions by a factor

of about five. The confinement can certainly be increased as well. With improved statistics, we might be able to improve our sensitivity of spin-changing collisions by three orders of magnitude. To rigorously prove SU(N) symmetry, one would have to show that the scattering lengths of all combinations of two different m_F states are identical.

- **Inelastic scattering in the $^3P_0$ state** Some proposals for quantum simulation require two distinguishable fermions in the metastable $^3P_0$ state to be located on the same 3D lattice site. Large inelastic decay rates are expected and were indeed measured in a thermal gas [Bis11]. Expanding these measurements into the regime of lower temperatures would certainly be helpful. This measurement requires a clock laser to drive the $^1S_0 - {}^3P_0$ transition, which will soon be available in our laboratory [Vog12].

- $5s5d\,^3D_3$ **hyperfine structure** In Chpt. 9, we determined the hyperfine interaction constants A and Q of the $5s5d\,^3D_{1,2}$ states, but lacked sufficient information on the $^3D_3$ state. Adding the repumpers at 679 and 707 nm will increase the signal strength sufficiently. Alternatively, spectroscopy can be performed starting from the $^3P_{0,1}$ states.

- **Lifetime of the $^3D_1$ states** The frequency of the $^1S_0 - {}^3P_0$ clock transition is perturbed by black-body radiation. A quantification of the black-body shift requires good knowledge of the lifetime of all states that are coupled to the clock states. Such a measurement has been performed very recently for Yb [Bel12] and could be performed for Sr as well.

- **Simplified repumping** The $5s6d\,^3D_2$ state has not yet been considered for repumping. Using this state would require light at 403.15 nm, which is available from the available Blu-ray technology. If the branching ratio into the $^3P_0$ state turns out to be tolerable, then these diode lasers would be an inexpensive and simple replacement for lasers at 497 nm or 2.7 μm.

13.2 Quantum simulation

The investigation of non-trivial spin models, possibly possessing topological order, is challenging to both theoretical and experimental approaches. An adequate starting point would be a fermionic Mott-insulator state with variable spin number N. Attainment of this state would be verified e.g. by measurement of double occupancy via photoassociation. This method could also be used to quantify the entropy of the sample. The heating rate during lattice loading, as well as the attainable entropy, depend on N, and a determination of the variation with N would connect to similar work in Yb [Tai12]. The attained entropy might not allow for antiferromagnetic ordering, calling for novel schemes to remove or re-distribute entropy. The amount of entropy still present in the system will select the class of possible experiments.

The detection of magnetic order is also not trivial, and the measurement of correlations from TOF absorption images seems a possible yet challenging approach. Eventually, one would desire spin-selective, *in-situ* fluorescence imaging with single-site resolution, which

might not be feasible with the present glass cell. This glass cell might also hinder the implementation of lattice geometries envisioned for quantum computation [Dal08], which require supreme control of beams at non-standard lattice beam angles. The investigation of optical flux lattices [Coo11b] seems less challenging from a technological perspective and might thus be pursued on a shorter time scale.

13.3 Rb-Sr mixtures and molecules

The creation of RbSr ground state molecules seems straightforward, since all necessary techniques have already been demonstrated in similar systems. Our experiment is augmented with an additional Rb oven, a standard Rb laser system together with the necessary optics, and with a more powerful dipole trap laser. The metastable state reservoir of Sr suggests a sequential MOT operation. There is considerable hope that the Sr red MOT can be used to sympathetically cool Rb to μK temperatures. The large choice of isotopes guarantees the existence of a Rb-Sr pair with a scattering length suitable for evaporative cooling, allowing to the formation of two overlapping BECs. These would constitute the starting point of two-color PA measurements, aiming for a characterization of the ground-state potential and a determination of all Rb-Sr interspecies scattering lengths. The sample would then be loaded into an IR lattice. Molecules can be associated via STIRAP from two free atoms on the same lattice site, closely following the scheme for Sr_2 molecules presented in Chpt. 11. The final STIRAP into the rovibronic ground state would be the subsequent step, where suitable intermediate potentials and states have been identified already. Such molecules have a sizable dipole moment and could be used to study lattice spin models with long-range, spin-dependent interactions. In some sense, this work follows studies on the Li-Yb mixture [Har11]; a system which, in stark contrast to Rb-Sr, features a large mass imbalance but only a midget dipole moment in the molecular ground state. At the time of writing this thesis, two-species Rb-Sr MOTs have been realized in our laboratory.

Appendix A

Construction of a simple high-finesse cavity

Optical resonators are of utmost importance for the field of laser technology. They are found as the resonator around the lasing medium, for intensity enhancement (e.g. around a doubling crystal for frequency conversion or for large-volume optical dipole traps), for mode cleaning, frequency selection, monitoring of the performance of a laser (in the form of common Fabry-Pérot cavities), precision measurements, for the reduction of a laser linewidth, for the detection of gravitational waves (such as in LIGO), or as an absolute frequency reference. The type of cavity described below is by no means aimed at the small linewidth or absolute frequency stability realized in groups within the optical clock community (see e.g. the work of the JILA/NIST, MPQ, or PTB groups), which have reached sub-Hz linewidths and absolute frequency drifts of less than 100 mHz/s. Instead, we are optimizing the cavity design for simplicity, such that it can be constructed within two days at a cost of about 5000 €. A laser locked to such a cavity has a linewidth below 10 kHz and a drift on the order of 1 MHz/day.

In the following, we will describe the set-up of the cavity, give some advice for the assembly, and evaluate the performance. A thorough treatment of optical resonators recently appeared in our group [Tre07] and includes relevant references. Some information on the design described here can be found in Ref. [Hua09].

Design — A horizontally mounted 100 mm Zerodur® spacer is used. It has a square front facet of $30 \times 30\,\mathrm{mm}^2$, a longitudinal bore of 10 mm diameter and an additional side bore to vent the central bore. The mirrors are 12.7 mm in diameter and have a center thickness of 3 mm. They are glued to the spacer using 353 ND two-component heat-curing epoyx. This epoxy is certified by NASA and has very low outgassing. We also tried UV-curing epoxy, but found no advantage. The mirrors have a radius of curvature of 150 mm. This ensures stable operation of the resonator and sufficient mode separation. The reflectivity of the mirrors depends on the desired finesse and ranges from 99% for the green cavity to 99.95% for the red and blue cavities[1].

[1]The spacer is custom-made from Hellma (Jena, Germany). The epoxy can be obtained e.g. from Epoxy Technology, Inc. The coating of all our resonator mirrors is done by Layertec (Mellingen, Germany).

If the length of the cavity is to be actively controlled, a pair of piezos is glued to one side of the cavity[2]. The use of two piezos has two advantages: the tuning range is doubled for a certain voltage applied, and possible temperature drifts due to thermal expansion of the piezos cancel. The outer piezo has a diameter of 24.5 mm, a thickness of 1 mm and a height of 5 mm. It is glued to the spacer. On the other side, it is attached to a Macor® ring of thickness 2 mm, which has a slit to allow for wires to be guided outwards[3]. A smaller piezo of same height and thickness, but outer diameter 18.5 mm is glued to the same side of the Macor® ring. It carries another Macor® ring, to which the mirror is attached with its curved surface. Capton wires of 500 μm diameter are soldered to the two sides of the piezos using standard solder. The use of special vacuum-compatible solder might however be desired. The wires are connected to the vacuum feedthroughs using standard vacuum connectors.

The spacer is placed inside a massive stainless steel block of 175 mm length and 74 mm by 74 mm width. The block is chosen as a large thermal capacitor, as well as for vibration dampening. Steel is preferred over other materials because of its large density and heat capacity. The length is limited by the capability of our wire erosion machine, and the width is maximized to fit into a CF 100 vacuum tube. The steel block features an inner bore to accommodate the spacer. The bore is machined at an angle of 4° with respect to the longitudinal axis of the block. This angle ensures that reflections from the cavity do not coincide with reflections from the vacuum window. This angle is way too large and is reduced to 1° in an improved design.

The spacer is mounted inside the steel block with rubber rods of 5.7 mm diameter made of Viton®. It is essential to use Viton® as the material. Nitrile, a similar substance, has outgassing rates that are about three orders of magnitude higher. It is not possible to heat a cavity chamber equipped with nitrile to 50 °C and maintain vacuum conditions. Other materials, such as silicone and Teflon®, have similar high outgassing rates. The Viton® needs be heated to 175 °C for at least four hours to free large amounts of water immersed in the material. The size of the material shrinks substantially during this process (about 2% of the diameter), which needs to be taken into account for tight fitting. After this baking, which does not harm the material, it can be used in high vacuum conditions. The steel block itself is set into the vacuum tube with Viton® rods of 8.5 mm diameter. The steel block features notches to securely hold the Viton® rods, and care is taken to avoid bubbles of air being trapped. To reduce the outgassing surface of the Viton®, we do not use the entire length of the spacer for clamping. The end facets of the steel block are covered by simple sheets of 2.5 mm aluminium to prevent black-body radiation from entering the spacer. They are clamped to the spacer at four points, again preventing the formation of air bubbles. A drawing of the assembly is shown in Fig. A.1.

[2]We use ring piezos from the Chinese company Annon Piezo. Similar piezos at comparable costs are now available from Ferroperm, a Danish company that spares certain annoyances. The piezos are designed to operate between −30 and +150 V, but have been found to routinely operate between −200 and +300 V without damage. They can be stored at ambient temperature and humidity conditions over many years without damage. The piezos are driven by home-built HV amplifiers.

[3]The Macor® rings are home-built. Machining of this material works surprisingly well, given the small thickness of only 2 mm.

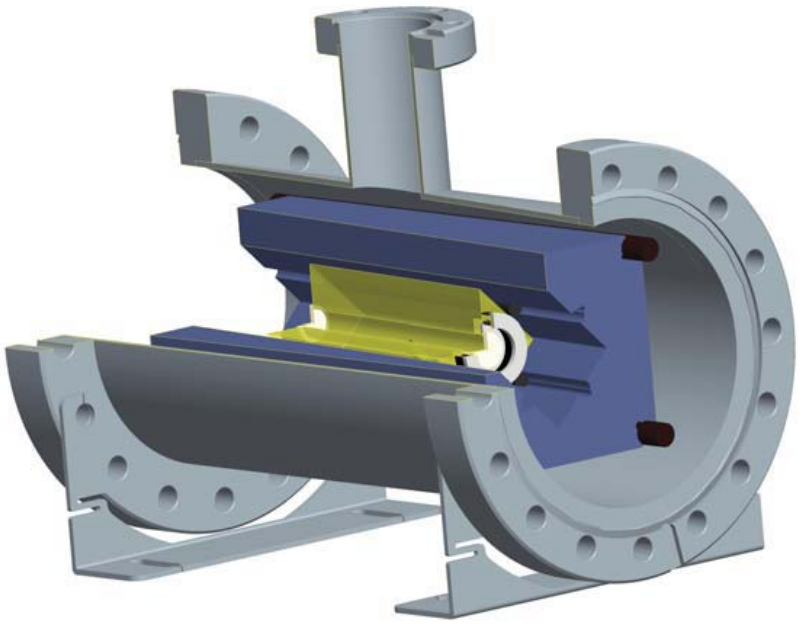

Figure A.1: Technical drawing of the cavity assembly. The spacer (yellow) holds two mirrors (white), one of which is supported by two piezos (black) and two Macor® rings (white). The spacer is clamped into a stainless steel block (blue) with Viton® rods (brown).

The CF 100 tube is equipped with a large viewport on both sides and mounted horizontally. The two CF 100 flanges are not rotatable and oriented such that no M8 hole lies on the vertical symmetry axis. This way, the support structures can be designed such that dual nuts can be used throughout. Two support structures attach to the M8 bolts and are made of a simple 3 mm aluminum sheet. The support structure is shaped to act as a spring. This design reduces heat conduction and provides some vibrational insulation, but can surely be improved. The height of the optical axis of the cavity can be set by the design of the support structure and is at least 80 mm.

The CF 100 tube features two (or three, if an electrical feedthroughs is needed) CF 40 or 16 flanges on the top. These flanges are welded very close to the tube to make the whole device as compact as possible. The flanges connect to a valve, a 2 l/s ion pump, and possibly the feedthroughs[4].

The CF 100 tube is wrapped with about 60 turns of standard lacquered copper wire of 200 μm diameter, amounting to a resistance of about 6 Ω. The wire is mainly wound around the sides of the tube, as most heat loss is expected through the support structure and the windows. Two 10 kΩ NTCs are glued to the tube. A Wheatstone bridge is used to

[4]Most of our vacuum parts are from Vacom (Jena, Germany), the CF 100 tube is custom-made. Capton wire, connectors, and 4-pin feedthroughs are from MDC Caburn. We tested both the 2 l/s and 8 l/s ion pumps from Varian, Inc. (now with Agilent), and found the small model to be superior due to its extremely small size (120 cm^3) and weight. This pumps starts operation at 10^{-3} mbar and securely pumps the cavity into and below the 10^{-7} mbar range. The lifetime of the pump is tens of years. The current is less than 2 μA at a voltage of 5 kV, amounting to less than 10 mW of heating.

convert the resistance of the NTCs into a voltage, and a slow home-built PID is used for temperature stabilization. About 50 mm of thermal insulation are tightly wrapped around the vessel, where we choose a high-quality foam mainly used in plumbing[5]. A wooden box is built around the cavity, and insulated with foam on the inside. Three-layered wood is chosen to provide dampening over a wide range of acoustic frequencies.

Assembly procedure — The assembly of the cavity is very straightforward. At first, we bake the Viton® rods for a few hours at up to 200 °C. During this time, the mirrors (and possibly the piezos, to which the capton wires have been soldered) are glued to the spacer with a cure time of 45 min at around 80 °C, where a few steps are necessary. The piezos should be short-circuited when heated. Some pressure should be exerted during curing to ensure that no air bubbles form and no large amounts of glue accumulate between the surfaces. The cavity itself might be tested before mounting into the vacuum. Next, we assemble the complete vacuum chamber with all parts except for the actual cavity. Normal copper gaskets are used for the viewports, as annealed gaskets are found to be too soft for handling. The vessel is pumped down by an external turbo pump, moderately baked for a few hours, and leak tested. The ion pump should also be tested: after a few minutes, it should be able to maintain a vacuum in the 10^{-6} mbar range. In a next step, one of the vacuum windows is removed again, and the steel block including the spacer is placed inside the vacuum tube. The wires are connected to the feedthroughs, the vacuum is closed again, and pumping is performed over night at a moderate temperature of around 80 °C. On the next day, we turn on the ion pump, evaluate the vacuum quality, and then remove the turbo pump. We add the heating wires, NTCs, and thermal insulation to the cavity, and maybe build a wooden box around it.

Piezo vs AOM — One main question that needs to be addressed before the construction of the cavity is whether piezos should be used or not. With piezos in place, it is very easy to tune the cavity into resonance with the laser. It is also very convenient to scan the cavity during initial set-up. On the other hand, piezos are the major source of outgassing in the vacuum, of misalignment of the cavity, and of temperature drifts. They are susceptible to RF getting into the cavity, and to electronic noise eventually changing the length of the cavity at all possible frequencies. They require feedthroughs, which add to complexity of the vacuum system. And finally, they require a very stable HV amplifier.

On the other hand, an AOM placed between the laser and the cavity can be used to shift the frequency of the laser onto the cavity's resonance. A cavity of length $L = 100$ mm has a free spectral range (FSR) $\nu_{\mathrm{FSR}} = c/2L$ of 1.5 GHz, and AOMs with such a bandwidth do not exist. In an improved design, we now use spacers of 150 mm length, reducing the FSR to 1.0 GHz. A 350 MHz AOM in double-pass configuration can cover a large part of this FSR[6].

Evaluation — A total of six cavities of the type described above have been constructed

[5] The insulation material is Armaflex from Armacell.

[6] The diffraction efficiency of AOMs at large RF frequencies tends to decrease when going to larger wavelengths. A new model (3350-125 from Crystal Technology) has been developed partially for our application, showing decent efficiencies up to 850 nm.

and are successfully used in our lab. A linewidth of below 2 kHz has been measured for one of them. We observe a drift of up to 10 MHz/day without active temperature stabilization. The price of one such cavity amounts to about 5000 €, where the coating run for the mirrors and the ion pump take by far the largest share.

A major improvement might come from a new way of mounting the spacer: in the current design, it is mechanically *squeezed* rather than *supported*. It would be fairly simple to adapt the design such that the spacer is nicely hosted onto two horizontal Viton® rods. Furthermore, it might be noteworthy that cavities of similar design are now commercially available from Stable Lasers Inc.

Appendix B

Construction of a spectroscopy cell for the $^1S_0 - {}^3P_1$ transition

The 689 nm laser is locked to a cavity for linewidth reduction and for short-term frequency stability. The atomic transition is only 7.4 kHz wide, and the absolute frequency of the laser needs to be stabilized to less than this value. This cannot be done by our cavity, since long-term drifts are expected to be substantially larger than ~ 1 kHz/hour, which could be tolerated in the experiment. Therefore, the piezos in the cavity are used to lock the cavity to a spectroscopy signal. The spectroscopy cell should fulfill two requirements: it should give a large and stable spectroscopy signal, and it should operate for about a year without maintenance. Only a small disturbance of the environment due to heat dissipation would also be desirable.

In the following, we will describe the concept of a simple and robust spectroscopy cell that gives a large signal with only 30 W of power consumption, a lifetime of many years and costs of less than 1500 €.

Basic considerations — Unlike the strong D-line transitions in the alkalis, the intercombination lines in the alkaline earth elements are very weak. Therefore, a rather large vapor pressure is needed to generate enough absorption of the probe beam for a sufficiently large signal. The alkaline-earth elements and lanthanides have rather high melting points, very much unlike the alkalis. This might pose a challenge to the construction of a spectroscopy cell.

The dependence of vapor pressure on temperature in Sr is given e.g. in Ref. [Pol05a], while slightly conflicting numbers are found in the literature as well. Given the experimentally determined coefficients [Vog99], the Clausius-Clapeyron equation reads

$$P(T) = 10^{-9450/T+10.62-1.31\,\log(T)} \tag{B.1}$$

with the temperature T given in units of K and the pressure P obtained in mbar. The dependence is plotted in Fig. B.1. Our spectroscopy cell will operate at a temperature of about 450 °C, corresponding to a pressure of about 10^{-6} mbar. By contrast, the spectroscopy cell for the broad transition at 461 nm operates at about 340 °C, where the vapor pressure is roughly three orders of magnitude smaller.

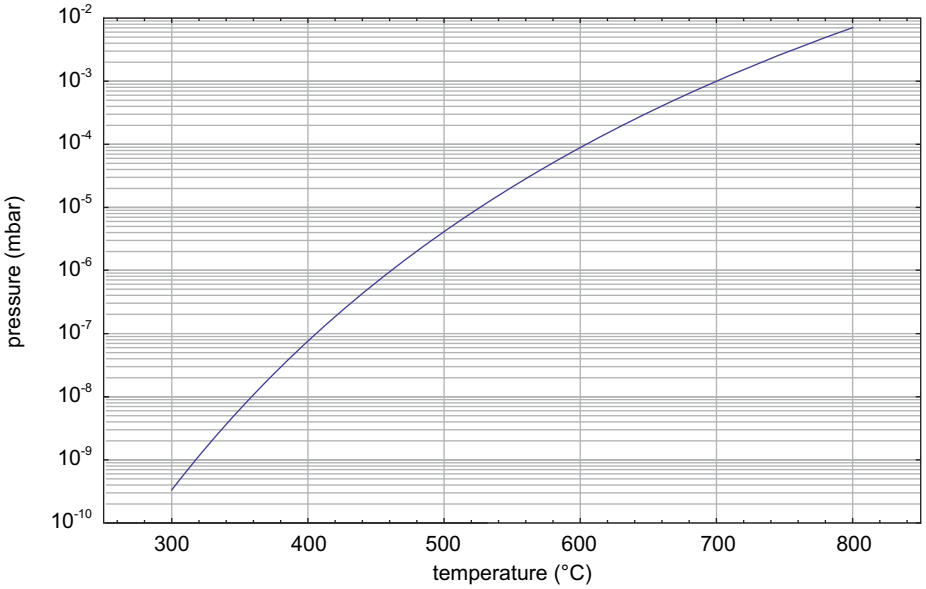

Figure B.1: Vapor pressure of Sr in dependence on temperature. The density of the Sr vapor can be calculated using the ideal gas law, $n(T) = P(T)/k_B T$. The melting point of Sr is at 777 °C.

We will now discuss a few aspects relevant for the design: transient and collisional broadening, as well as two different measures to avoid coating of the spectroscopy cell windows.

Let us begin with a look at the atom's kinematics. Given a linewidth of 7.4 kHz, the lifetime of the excited state is 21 μs. At a temperature of 450 °C, the mean velocity of an atom is obtained from equating its kinetic energy $E_{\text{kin}} = \frac{1}{2}mv_0{}^2$ and the energy of a particle in an ideal gas $E_{\text{gas}} = \frac{3}{2}k_B T$, yielding $v_0 = 460\,\text{m/s}$. The distance traveled during 21 μs is 10 mm. Transient broadening follows from Heisenberg's uncertainty principle and occurs if the atom does not spend enough time in the probe light to entirely resolve its linewidth. To avoid such broadening, the diameter of the probe beams needs to be sufficiently large, about 10 mm in our case. A large probe beam has another advantage: the saturation intensity of the transition is very small, $I_{\text{sat}} = 3\,\mu\text{W/cm}^2$, and power-broadening of the transition inevitably occurs. The larger the probe beam, the more power can be used for a given intensity, which improves the S/N on the detection photodiode.

Another possible broadening mechanism stems from collisions: if the time between consecutive collisions is shorter than the lifetime of the excited state, the linewidth cannot be resolved, similar to the previous case. The mean free path l of a particle is given by

$$l = \frac{k_B T}{\sqrt{2}\pi d^2 P} \tag{B.2}$$

with the particle diameter d and pressure P. There are a number of different approaches to determine the effective diameter of an atom. For simplicity, we will use the covalent radius [Sla64], which is about 200 pm for strontium. For a temperature of 450 °C and a pressure of 10^{-6} mbar, we obtain a mean free path of $l = 140\,\text{m}$ and a corresponding timescale of $\tau = l/v_0 = 300\,\text{ms}$. Clearly, collisions between Sr atoms do not play a role. Strontium also

acts as a supreme getter and will quickly remove all chemically reactive elements to establish a high vacuum. Further details can be found in Ref. [Bid02].

A major complication of working with heat pipes is the degradation of the windows: Hot Sr atoms attach to the cold viewports and form a reflective layer that can only be removed by exposure to oxygen. A widely used solution is the addition of a small amount of buffer gas into the heat pipe. Any hot atom travelling towards a window should collide with a buffer gas atom and be deflected to the cold end of the heat pipe, where it attaches to the wall. In an early trial, we found that a buffer gas pressure of less than 10^{-6} mbar will lead to a coating of the windows within hours, while a pressure of about 10^{-3} mbar will prevent coating for years. In the current setup, 8×10^{-4} mbar of nitrogen are added as buffer gas. This was actually a bad choice, as Sr reacts with N_2 to form strontium nitrite Sr_3N_2 at temperatures above 380 °C. A better choice would be argon. At a buffer gas pressure of 10^{-3} mbar and assuming a covalent radius of 70 pm, we calculate a mean free path of 400 mm, which is about the size of our cell.

Another approach to reduce the flux of atoms impinging on the windows is an optimized geometry of the spectroscopy cell. Atoms are heated to high temperatures only in the center of the cell, and the smaller the solid angle under which they can hit a window in a direct flight, the smaller the flux. In other words: the longer the cell, the better.

With a length of the spectroscopy cell L and an inner diameter of the tube D, the solid angle of the windows as seen from a hot Sr atom in the center is $\Omega = 2\pi(D/L)^2$ sr. In our case of $L = 600$ mm and $D = 8$ mm, we obtain $\Omega \approx 10^{-3}$ sr or about 10^{-4} of the total solid angle. Decreasing the tube diameter and building the tube as long as possible is therefore beneficial.

Let us now summarize our findings. The desire for a large probe beam (> 10 mm) competes with the requirement of a narrow tube, which reduces the solid angle for atoms hitting the windows. There is no disadvantage to making the cell longer, except for limitations in available space. The temperature could safely be increased to about 700 °C before observing collisional broadening from Sr-Sr collisions. The amount of buffer gas should be chosen such that the mean free path of Sr atoms is much larger than the diameter of the probe beam, but much smaller than the length of the tube, $D < l < L$. A few 10^{-3} mbar of Ar seem reasonable. A systematic determination of the broadening and shifting of the ${}^1S_0 - {}^3P_1$ transition in Sr by various buffer gases has been performed by the Tokyo group [Shi09] and compared to earlier results of other groups. Broadening and shifts are at most a few kHz/10^{-3} mbar pressure and went unnoticed in all of our experiments.

Design — The spectroscopy cell consists of a 600 mm long stainless steel tube of 12 mm outer diameter and 8 mm inner diameter. The thickness is chosen to be large enough to prevent the tube from bending at high temperatures, while being small enough to minimize heat conduction. Two CF 40 flanges are welded to the sides and will support the viewports. The metallic Sr is contained in a barrel welded into the center of the tube. This barrel has a height of 60 mm and an outer diameter of 30 mm. It is oriented vertically, with the bottom of the barrel situated 45 mm below the axis of the horizontal tube. This barrel forms a nice cup to hold 10 g of strontium. Initial pumping is performed through a short 6 mm tube welded to one side of the long tube and equipped with a CF 16 flange. A heating wire is wound

around the barrel, and two thermocouples are attached for temperature measurement. The entire length of the long tube is tightly wrapped in 80 mm of thermal insulation, which is capped with multiple layers of aluminum foil[1].

About 30 W of power are needed to heat the central region to 450 °C. We use a simple DC power supply, which is very convenient as it spares the annoyances of 50 Hz noise, high voltages, or noise from pulse-width modulation. Water-cooling of the cell is provided through small copper blocks clamped to the ends of the long tube, about 50 mm away from the viewports. These copper blocks are internally flushed with cooling water. Two simple support structures attach to the CF 40 viewports and hold the cell at a height of 100 mm. The entire structure is set inside a 2 mm aluminum box to decouple it from the environment. The air inside this box heats up considerably and is cooled by a commercial water cooler radiator.

Assembly procedure — The tube is equipped with heating wires, thermocouples, and some provisional insulation, and heated to about 300 °C to remove any contamination from the welding process. The viewports and valve are attached. The valve is connected to a T, which goes to the valve used to inject the buffer gas in a controlled way, and the turbo pump. The cell is pumped, baked, and leak-tested. The controlled flushing of buffer gas is tested as well. As a next step, the vacuum is opened again, the insulation and viewports are removed, and the cell is placed in an atmosphere of argon. About 5 to 10 g of metallic Sr are filled into the barrel. This can nicely be done by placing small pieces of up to 3 mm size into the long tube and sliding them one-by-one into the center. Attempting to forcefully shove larger pieces into the center will unavoidably clog the tube. It takes about an hour to complete the task. Afterwards, the viewports are attached again.

In a last step, the cell is pumped, moderately heated to about 200 °C for an hour, and leak-tested. Excess heating under high vacuum at this stage will coat the windows. The buffer gas is slowly flushed into the system up to a pressure of about 1 mbar, and then turned off. The pressure is reduced to the desired value of about 10^{-3} mbar by the turbo pump, and the valve of the cell is closed. Care should be taken when reading the pressure from the vacuum pump's gauge: the values are usually given for diatomic gases and differ significantly for argon. The cell can now be tested: at about 450 °C, a resonant probe beam of moderate intensity should be absorbed almost entirely.

Evaluation — The design of our spectroscopy cells undergoes a steady improvement. The version described above operates already for more than 2 years at around 420 °C, without

[1] The CF 16 valve is a VAT model 54024. Our heating wire is model SEI 10/50 from Thermocoax (France). The hot part has a length of 50 cm and an outer diameter of 1 mm, its resistance is about 6 Ω, and the maximum heating capability is about 200 W. The smaller version SEI 10/25 of half the length could be used as well. We use standard K-type thermocouples, which can be purchased from a range of companies. We tried different types of thermal insulation material suited for high temperatures, and found Superwool® PLUS™ most satisfying, obtained from Contherm (Germany). This is a ceramic wool optimized for small volumes of confined air and reduced knots. This wool comes in different shapes (paper, blankets, bulk, ...) and is developed for high temperatures of up to 1500 °C. It is also supposed to be less harmful than glass fiber, which comes apart much more easily. We use blankets of 25 mm and 50 mm thickness. The entire spectroscopy cell is home-built in our workshop, employing vacuum parts from Vacom (Germany). We use metallic Sr from Alfa Aesar, delivered in dendritic pieces under Ar atmosphere.

degradation of the absorption signal or coating of the windows, and has not been touched ever since. From previous experiments, we know that the cell can be heated to above 700 °C, leaving a large security margin should the absorption signal ever drop. We are able to stabilize the laser to better than 500 Hz over a 1-hour period, and we did not detect any drifts of more than a few kHz over years. A few 100 μW of power are used in the pump and probe beams, which is certainly sufficient for a suitable photodiode. We estimate that this design can also be used for atomic species with substantially smaller linewidth (such as Ca) or much higher boiling point (such as Er).

Appendix C

Construction of an oven for strontium

The design of our oven follows the design of the FeLiKx multi-species oven, which has been described in Ref. [Wil09]. We will summarize the basic concept here, elaborate on different heating strategies, and then evaluate the oven design in view of future improvements. Afterwards, we will briefly review our unsuccessful efforts to work with an enriched source. The vapor pressure of Sr, as well as all relevant information on the required materials, can be found in the preceding Appendix B.

Design — We follow the FeLiKx design not only because of the possibility to later add a different element such as Rb to Sr, but also to be able to use a natural and an enriched source of atoms. A common Zeeman-slower should be used for the chemically different elements, which are potentially reactive and have to be heated to different temperatures. Therefore, the reservoirs need to be spatially separated sufficiently to establish a temperature difference of up to 500 °C, and migration between the reservoirs must be avoided. Each element is devoted its own oven segment; see Fig. 3.1 for an image and Ref. [Wil09] for details. The metal is contained and evaporated in a reservoir tube, and the atoms are directed towards the MOT region by a bundle of microtubes. The area of the microtubes formes a segment of a circle (typically 1/3) around the longitudinal axis of the oven. Up to three ovens can be stacked one after the other. They are rotated around the common axis such that the flux of the rear oven can pass through the front ones, which provide a suitable "fly-by" channel. This compact design establishes a high flux of atoms very close to the axis of the Zeeman-slower. In the setup used for the work of this thesis, the front oven and two-thirds of the available cross section were reserved for an enriched source of strontium. This segment was never used, and we worked with only one third of the available cross section.

Heating of the oven — Two 25 cm heating wires are used for each oven segment, and one 50 cm wire is wrapped around each reservoir. Some of the flanges connecting two oven segments are heated as well, and each heating wire is driven independently. Close to a dozen of thermocouples are used to read out the temperature of different spots of the oven. We use a ceramic wool for insulation and cast the oven into a solid double-walled 6 mm aluminum box, where the air enclosed between the two walls of the box is constantly exchanged for cooling.

The choice of the power supplies and the concept of temperature control are guided by the following criteria: The power supplies need to deliver about 200 W, but they must not be powerful enough to melt the entire oven. For safety reasons, they should not operate at hazardous voltages. DC power supplies are preferred over AC ones to avoid 50 Hz emission in the vicinity of the experiment. Similarly, pulse-width modulation should be avoided to reduce time-varying fields. The heating of the oven could be turned off during the crucial stage of the experiment to avoid influences on the B-field.

In the beginning, we used an 35 V AC transformer as power source, and control was achieved via pulse-width modulation using a set of solid state relays, one for each heating wire. After about two years, we had to increase the temperature of our oven to maintain the same atom flux, we found that the heating wires broke more frequently. The heating wires have a limited lifetime, where rapid changes in the temperature as well as mechanical and thermal stress lead to degradation. In an attempt to reduce the stress on the heating wires, we opted for DC power supplies with a manually adjusted current output. We reduced the oven temperature only when not operating the machine for more than a few days. None of the heating wires broke during about one year of such operation.

Evaluation — After about three years of operation, the oven flux had decreased substantially, and we exchanged the oven. We disassembled the old oven completely and found that the stainless steel structure and flanges showed no signs of degradation, despite operation at temperatures of up to 750 °C for years. To our surprise, we found that the reservoir was completely empty, and a large chunk of Sr had deposited in the "fly-by" channel of the front oven, entirely blocking this section. This now explained the reduced flux and poorer collimation which we had observed. Astonishingly, the microtubes were as clean as at the time of installation, with no Sr deposited in or around the tubes.

A future design might consider a slightly different distribution of heating wires around the oven segments to increase the temperature at the front ends of the microtubes. It is recommended to use only the long 50 cm heating wires to reduce thermal stress and increase their lifetime. Great care should be taken to heat the front oven segment to a higher temperature than the rear ones in order to avoid deposition in the "fly-by" channels.

Enriched source — Out of the four stable isotopes of strontium, the ones of most interest to us are ^{84}Sr (because of its moderate scattering length, rendering it ideal for efficient evaporative cooling to form large BECs sympathetically cool ^{87}Sr and possibly other elements) and ^{87}Sr (because of its fermionic nature and nonzero nuclear spin). Ironically, ^{84}Sr has the lowest natural abundance of all isotopes, 0.5%. The natural abundance of ^{87}Sr is roughly 10%, but the rich hyperfine structure decreases the efficiency of the blue MOT, the repumping, and the red MOT. Despite being 20-times more abundant, an optimized red MOT of ^{87}Sr contains only about one third of the atom number of the ^{84}Sr isotope, given the same reservoir loading time. Thus, it would be beneficial to use enriched sources of these two isotopes.

A few years ago, metallic ^{84}Sr enriched to 70% was available from Eurisotopes. Unfortunately, this is not the case any more. Instead, enriched strontium in the chemical compound strontium carbonate $^{84}SrCO_3$ is easily and readily available from various companies, at a

price of roughly 70 $/mg. The task of converting the carbonate into a pure metal is highly nontrivial, and despite considerable effort, we were not able to find a company able and willing to perform this purification. A collaboration with two chemists, Prof. Huppertz and Dr. Heymann from the University of Innsbruck, was aimed to explore possible ways of purification.

An *aluminothermic reaction* is the most straightforward process. The $SrCO_3$ would be heated to more than 1268 °C, where it would form an oxide: $SrCO_3 \rightarrow SrO + CO_2$. The oxide can be reduced further by aluminum: $3SrO + 2Al \rightarrow 3Sr + Al_2O_3$. Two major problems occurred: First, the carbonate turned out to be very reactive and penetrate into the glass container, which was made of quartz. The high temperatures made it impossible to use another material, thus some new material would have to be engineered. Second, the wettability of the SrO by the aluminum melt turned out to be unexpectedly low, making reaction times very long.

Because of these difficulties, we turned to *fused-salt electrolysis*. This process is common to remove chlorene or fluorene from all alkalis and most alkaline-earths. The idea is to turn the strontium carbonate into a chloride: $SrCO_3 + 2HCl \rightarrow SrCl_2 + H_2CO_3$. Afterwards, the strontium chloride would be heated and decomposed into its constituents by electrolysis. Again, we found that currently available types of glass cannot stand the temperatures present during the reaction.

In order not to rely on any glass container for the reaction process, one might consider doing the chemistry not *in vitro* and later transferring an ampoule with metallic strontium into the oven, but to do everything *in situ* within our vacuum chamber. This approach was successfully followed in an experiment with barium [De09], where Ba follows Sr in the second column of the periodic table. Here, the oven was filled with both $BaCO_3$ and Zr powder and heated to about 700 °C. At this temperature, the carbonate bond breaks to from barium oxide, $BaCO_3 \rightarrow BaO + CO_2$. Afterwards, the oven is operated at a lower temperature of roughly 500 °C, where *reduction by zirconium* removes the oxygen atom. The atomic Ba has a sufficient vapor pressure at this temperature to form a proper atomic beam [De08]. An adaption of this scheme to Sr would require a much higher temperature for the calcination process, as stated above. The thermite reaction might also employ silicon, but the necessary temperature is generally expected to be higher than in the case of barium. Nevertheless, it would be interesting to test this approach.

Research was far from completion when we found that accumulation of laser-cooled atoms in the metastable $^3P_2$ state allows for large enough samples and large BECs, so we discontinued further studies. With the advent of space missions employing ^{87}Sr clocks, there is new interest in the production of pure metallic ^{87}Sr. In applications that require a good vacuum in the experimental chamber, but could tolerate a high oven temperature, isotopic post-selection by optical means is also possible: an atomic beam emerging from the source could be deflected and guided into the experimental chamber by light resonant on the $^1S_0 - {}^1P_1$ transition, which is fairly isotope-selective.

Bibliography

[Aid11] M. Aidelsburger, M. Atala, S. Nascimbène, S. Trotzky, Y.-A. Chen, and I. Bloch, *Experimental Realization of Strong Effective Magnetic Fields in an Optical Lattice*, Phys. Rev. Lett. **107**, 255301 (2011).

[Aik12] K. Aikawa, A. Frisch, M. Mark, S. Baier, A. Rietzler, R. Grimm, and F. Ferlaino, *Bose-Einstein Condensation of Erbium*, Phys. Rev. Lett. **108**, 210401 (2012).

[And95] M. Anderson, J. Ensher, M. Matthews, C. Wieman, and E. Cornell, *Observation of Bose-Einstein condensation in dilute atomic vapor*, Science **269**, 198 (1995).

[And06] A. André, D. DeMille, J. Doyle, M. Lukin, S. Maxwell, P. Rabl, R. Schoelkopf, and P. Zoller, *A coherent all-electrical interface between polar molecules and mesoscopic superconducting resonators*, Nature Phys. **2**, 636 (2006).

[Ari92] E. Arimondo, W. D. Phillips, and F. Strumia (Eds.), *Laser Manipulation of Atoms and Ions*, North Holland, Amsterdam (1992), Proceedings of the International School of Physics "Enrico Fermi", Course CXVIII, Varenna, 9-19 July 1991.

[Asp88] A. Aspect, E. Arimondo, R. Kaiser, N. Vansteenkiste, and C. Cohen-Tannoudji, *Laser Cooling below the One-Photon Recoil Energy by Velocity-Selective Coherent Population Trapping*, Phys. Rev. Lett. **61**, 826 (1988).

[Aut55] S. Autler and C. Townes, *Stark Effect in Rapidly Varying Fields*, Phys. Rev. **100**, 703 (1955).

[Bak09] W. S. Bakr, J. I. Gillen, A. Peng, S. Fölling, and M. Greiner, *A quantum gas microscope for detecting single atoms in a Hubbard-regime optical lattice*, Nature **462**, 74 (2009).

[Bar01] M. D. Barrett, J. A. Sauer, and M. S. Chapman, *All-Optical Formation of an Atomic Bose-Einstein Condensate*, Phys. Rev. Lett. **87**, 010404 (2001).

[Bar02] M. Baranov, L. Dobrek, K. Góral, L. Santos, and M. Lewenstein, *Ultracold Dipolar Gases - a Challenge for Experiments and Theory*, Physica Scripta **T102**, 74 (2002).

[Bar08] M. A. Baranov, *Theoretical progress in many-body physics with ultracold dipolar gases*, Physics Reports **464**, 71 (2008).

[Bec10] C. Becker, P. Soltan-Panahi, J. Kronjäger, S. Dörscher, K. Bongs, and K. Sengstock, *Ultracold quantum gases in triangular optical lattices*, New Journal of Physics **12**, 065025 (2010).

[Bed00] P. F. Bedaque, E. Braaten, and H.-W. Hammer, *Three-body recombination in Bose gases with large scattering length*, Phys. Rev. Lett. **85**, 908 (2000).

[Bei82] R. Beigang, K. Lücke, D. Schmidt, A. Timmermann, and P. J. West, *One-Photon Laser Spectroscopy of Rydberg Series from Metastable Levels in Calcium and Strontium*, Physica Scripta **26**, 183 (1982).

[Bel08] K. Beloy, A. Derevianko, and W. R. Johnson, *Hyperfine structure of the metastable* $^3P_2$ *state of alkaline-earth-metal atoms as an accurate probe of nuclear magnetic octupole moments*, Phys. Rev. A **77**, 012512 (2008).

[Bel11] K. Beloy, A. W. Hauser, A. Borschevsky, V. V. Flambaum, and P. Schwerdtfeger, *Effect of* α *variation on the vibrational spectrum of* Sr_2, Phys. Rev. A **84**, 062114 (2011).

[Bel12] K. Beloy, J. A. Sherman, N. D. Lemke, N. Hinkley, C. W. Oates, and A. D. Ludlow, *Determination of the* $5d6s\,^3D_1$ *state lifetime and blackbody radiation clock shift in Yb*, arXiv:1208.0552v1 (2012).

[Bér11] B. Béri and N. Cooper, $\mathbb{Z}_2$ *Topological Insulators in Ultracold Atomic Gases*, Phys. Rev. Lett. **107**, 145301 (2011).

[Bev89] N. Beverini, F. Giammanco, E. Maccioni, F. Strumia, and G. Vissani, *Measurement of the calcium* $^1P_1 - ^1D_2$ *transition rate in a laser-cooled atomic beam*, JOSA B **6**, 2188 (1989).

[Bid02] Y. Bidel, *Piégeage et refroidissement laser du strontium; Etude de l'effet des interférences en diffusion multiple*, Ph.D. thesis, Université de Nice, Nice, France (2002).

[Bin01] T. Binnewies, G. Wilpers, U. Sterr, F. Riehle, J. Helmcke, T. E. Mehlstäubler, E. M. Rasel, and W. Ertmer, *Doppler Cooling and Trapping on Forbidden Transitions*, Phys. Rev. Lett. **87**, 123002 (2001).

[Bis11] M. Bishof, M. J. Martin, M. D. Swallows, C. Benko, Y. Lin, G. Quéméner, A. M. Rey, and J. Ye, *Inelastic collisions and density-dependent excitation suppression in a* ^{87}Sr *optical lattice clock*, Phys. Rev. A **84**, 052716 (2011).

[Bla08] S. Blatt, A. D. Ludlow, G. K. Campbell, J. W. Thomsen, T. Zelevinsky, M. M. Boyd, J. Ye, X. Baillard, M. Fouché, R. Le Targat, A. Brusch, P. Lemonde, M. Takamoto, F.-L. Hong, H. Katori, and V. V. Flambaum, *New Limits on Coupling of Fundamental Constants to Gravity Using* ^{87}Sr *Optical Lattice Clocks*, Phys. Rev. Lett. **100**, 140801 (2008).

[Bla11a] S. Blatt, *Ultracold Collisions and Fundamental Physics with Strontium*, Ph.D. thesis, University of Colorado, Boulder, USA (2011).

[Bla11b] S. Blatt, T. L. Nicholson, B. J. Bloom, J. R. Williams, J. W. Thomsen, P. S. Julienne, and J. Ye, *Measurement of Optical Feshbach Resonances in an Ideal Gas*, Phys. Rev. Lett. **107**, 073202 (2011).

[Blo99] I. Bloch, T. W. Hänsch, and T. Esslinger, *Atom Laser with a cw Output Coupler*, Phys. Rev. Lett. **82**, 3008 (1999).

[Blo05] I. Bloch, *Ultracold quantum gases in optical lattices*, Nature Phys. **1**, 23 (2005).

[Blo08] I. Bloch, J. Dalibard, and W. Zwerger, *Many-body physics with ultracold gases*, Rev. Mod. Phys. **80**, 885 (2008).

[Blo12] I. Bloch, J. Dalibard, and S. Nascimbène, *Quantum simulations with ultracold quantum gases*, Nature Phys. **8**, 267 (2012).

[Bon12] L. Bonnes, K. R. A. Hazzard, S. R. Manmana, A. M. Rey, and S. Wessel, *Adiabatic loading of one-dimensional SU(N) alkaline earth fermions in optical lattices*, arXiv:1207.3900v1 (2012).

[Bor96] C. Bordé, *Amplification of atomic waves by stimulated emission of atoms*, in M. Inguscio, M. Allegrini, and A. Sasso (Eds.), *Proceedings of the 12th International Conference on Laser Spectroscopy*, 208, World Scientific, Singapore (1996).

[Bos24] S. N. Bose, *Plancksches Gesetz und Lichtquantenhypothese*, Zeitschrift für Physik **26**, 178 (1924).

[Boy07a] M. M. Boyd, *High Precision Spectroscopy of Strontium in an Optical Lattice: Towards a New Standard of Frequency and Time*, Ph.D. thesis, University of Colorado, Boulder, USA (2007).

[Boy07b] M. M. Boyd, A. D. Ludlow, S. Blatt, S. M. Foreman, T. Ido, T. Zelevinsky, and J. Ye, *^{87}Sr lattice clock with inaccuracy below 10^{-15}*, Phys. Rev. Lett. **98**, 083002 (2007).

[Boy07c] M. M. Boyd, T. Zelevinsky, A. D. Ludlow, S. Blatt, T. Zanon-Willette, S. M. Foreman, and J. Ye, *Nuclear spin effects in optical lattice clocks*, Phys. Rev. A **76**, 022510 (2007).

[Bra08] J. P. Brantut, J. F. Clément, M. Robert-de-Saint-Vincent, G. Varoquaux, R. A. Nyman, A. Aspect, T. Bourdel, and P. Bouyer, *Light-shift tomography in an optical-dipole trap for neutral atoms*, Phys. Rev. A **78**, 031401 (2008).

[Bre07] G. K. Brennen, A. Micheli, and P. Zoller, *Designing spin-1 lattice models using polar molecules*, New J. Phys. **9**, 138 (2007).

[Bri07] K.-A. Brickman, M.-S. Chang, M. Acton, A. Chew, D. Matsukevich, P. C. Haljan, V. S. Bagnato, and C. Monroe, *Magneto-optical trapping of cadmium*, Phys. Rev. A **76**, 043411 (2007).

[Bru12] D. A. Brue and J. M. Hutson, *Magnetically Tunable Feshbach Resonances in Ultracold Li-Yb Mixtures*, Phys. Rev. Lett. **108**, 043201 (2012).

[Büc07] H. P. Büchler, A. Micheli, and P. Zoller, *Three-body interactions with cold polar molecules*, Nature Phys. **3**, 726 (2007).

[Bus98] T. Busch, J. R. Anglin, J. I. Cirac, and P. Zoller, *Inhibition of spontaneous emission in Fermi gases*, EPL **44**, 1 (1998).

[Cas89] Y. Castin, H. Wallis, and J. Dalibard, *Limit of Doppler cooling*, J. Opt. Soc. Am. B **6**, 2046 (1989).

[Cas98] Y. Castin, J. I. Cirac, and M. Lewenstein, *Reabsorption of Light by Trapped Atoms*, Phys. Rev. Lett. **80**, 5305 (1998).

[Caz09] M. A. Cazalilla, A. Ho, and M. Ueda, *Ultracold Gases of Ytterbium: Ferromagnetism and Mott States in an SU(6) Fermi System*, New J. Phys. **11**, 103033 (2009).

[Cen03] G. Cennini, G. Ritt, C. Geckeler, and M. Weitz, *Bose-Einstein condensation in a CO_2-laser optical dipole trap*, Appl. Phys. B **77** (2003).

[Chi00] A. P. Chikkatur, A. Görlitz, D. M. Stamper-Kurn, S. Inouye, S. Gupta, and W. Ketterle, *Suppression and Enhancement of Impurity Scattering in a Bose-Einstein Condensate*, Phys. Rev. Lett. **85**, 483 (2000).

[Chi10] C. Chin, R. Grimm, P. S. Julienne, and E. Tiesinga, *Feshbach resonances in ultracold gases*, Rev. Mod. Phys. **82**, 1225 (2010).

[Cho10] C. W. Chou, D. B. Hume, J. C. J. Koelemeij, D. J. Wineland, and T. Rosenband, *Frequency Comparison of Two High-Accuracy* Al^+ *Optical Clocks*, Phys. Rev. Lett. **104**, 070802 (2010).

[Chu] S. Chu and C. Wieman, eds., *Laser Cooling and Trapping of Atoms*, Special issue of J. Opt. Soc. Am. B, **6**, Issue 11, (1989).

[Chw09] M. Chwalla, J. Benhelm, K. Kim, G. Kirchmair, T. Monz, M. Riebe, P. Schindler, A. S. Villar, W. Hänsel, C. F. Roos, R. Blatt, M. Abgrall, G. Santarelli, G. D. Rovera, and P. Laurent, *Absolute Frequency Measurement of the* $^{40}Ca^+$ $4s\,^2S_{1/2} - 3d\,^2D_{5/2}$ *Clock Transition*, Phys. Rev. Lett. **102**, 023002 (2009).

[Cir96] J. I. Cirac, M. Lewenstein, and P. Zoller, *Collective laser cooling of trapped atoms*, Europhys. Lett. **35**, 647 (1996).

[Ciu] R. Ciuryło, private communication.

[Ciu04] R. Ciuryło, E. Tiesinga, S. Kotochigova, and P. S. Julienne, *Photoassociation spectroscopy of cold alkaline-earth-metal atoms near the intercombination line*, Phys. Rev. A **70**, 062710 (2004).

[Ciu05] R. Ciuryło, E. Tiesinga, and P. Julienne, *Optical tuning of the scattering length of cold alkaline-earth-metal atoms*, Phys. Rev. A **71**, 030701 (2005).

[Cle09] J.-F. Clement, J.-P. Brantut, M. Robert-de-Saint-Vincent, R. A. Nyman, A. Aspect, T. Bourdel, and P. Bouyer, *All-optical runaway evaporation to Bose-Einstein condensation*, Phys. Rev. A **79**, 061406 (2009).

[Con] Control system homepage, `http://iqoqi.at/control`.

[Coo09] N. Cooper and G. Shlyapnikov, *Stable topological superfluid phase of ultracold polar fermionic molecules*, Phys. Rev. Lett. **103**, 155302 (2009).

[Coo11a] N. Cooper and J. Dalibard, *Optical flux lattices for two-photon dressed states*, EPL **95**, 66004 (2011).

[Coo11b] N. R. Cooper, *Optical Flux Lattices for Ultracold Atomic Gases*, Phys. Rev. Lett. **106**, 175301 (2011).

[Cou05] I. Courtillot, A. Quessada-Vial, A. Brusch, D. Kolker, G. D. Rovera, and P. Lemonde, *Accurate spectroscopy of Sr atoms*, Eur. Phys. J. D **33**, 161 (2005).

[Cra90] A. Crawford, Medical Communications (London) **2**, 301 (1790).

[Dal89] J. Dalibard and C. Cohen-Tannoudji, *Laser cooling below the Doppler limit by polarization gradients: simple theoretical models*, J. Opt. Soc. Am. B **6**, 2023 (1989).

[Dal98] J. Dalibard, *Bose-Einstein condensation in atomic gases*, chapter Collisional dynamics of ultra-cold atomic gases, North Holland, Amsterdam (1998), Proceedings of the International School of Physics "Enrico Fermi", Course CXL, Varenna, 7-17 July 1998.

[Dal99] F. Dalfovo, S. Giorgini, L. P. Pitaevskii, and S. Stringari, *Theory of Bose-Einstein condensation in trapped gases*, Rev. Mod. Phys. **71**, 463 (1999).

[Dal04] A. J. Daley, P. O. Fedichev, and P. Zoller, *Single-atom cooling by superfluid immersion: A nondestructive method for qubits*, Phys. Rev. A **69**, 022306 (2004).

[Dal08] A. J. Daley, M. M. Boyd, J. Ye, and P. Zoller, *Quantum computing with alkaline-earth-metal atoms*, Phys. Rev. Lett. **101**, 170504 (2008).

[Dal11] J. Dalibard, F. Gerbier, G. Juzeliunas, and P. Öhberg, *Artificial gauge potentials for neutral atoms*, Rev. Mod. Phys. **83**, 1523 (2011).

[Dam11] U. Dammalapati, L. Willmann, and S. Knoop, *Scattering lengths of calcium and barium isotopes*, Phys. Rev. A **84**, 054703 (2011).

[Dan08] J. G. Danzl, E. Haller, M. Gustavsson, M. J. Mark, R. Hart, N. Bouloufa, O. Dulieu, H. Ritsch, and H.-C. Nägerl, *Quantum Gas of Deeply Bound Ground State Molecules*, Science **321**, 1062 (2008).

[Dav08] H. Davy, *Electro-chemical researches on the decomposition of the earths; with observations on the metals obtained from the alkaline earths, and on the amalgam procured from ammonia*, Philosophical Transactions of the Royal Society of London **98**, 333 (1808).

[Dav95] K. B. Davis, M. O. Mewes, M. R. Andrews, N. J. van Druten, D. S. Durfee, D. M. Kurn, and W. Ketterle, *Bose-Einstein condensation in a gas of sodium atoms*, Phys. Rev. Lett. **75**, 3969 (1995).

[De08] S. De, *Laser Cooling and Trapping of Barium*, Ph.D. thesis, University of Groningen, Groningen, The Netherlands (2008).

[De09] S. De, U. Dammalapati, K. Jungmann, and L. Willmann, *Magneto-optical trapping of barium*, Phys. Rev. A **79**, 041402(R) (2009).

[DeM99] B. DeMarco and D. S. Jin, *Onset of Fermi Degeneracy in a Trapped Atomic Gas*, Science **285**, 1703 (1999).

[DeM01a] B. DeMarco, *Quantum Behavior of an Atomic Fermi Gas*, Ph.D. thesis, University of Colorado, Boulder, USA (2001).

[DeM01b] B. DeMarco, S. B. Papp, and D. S. Jin, *Pauli Blocking of Collisions in a Quantum Degenerate Atomic Fermi Gas*, Phys. Rev. Lett. **86**, 5409 (2001).

[DeM02] D. DeMille, *Quantum Computation with Trapped Polar Molecules*, Phys. Rev. Lett. **88**, 067901 (2002).

[DeM05] B. DeMarco, C. Lannert, S. Vishveshwara, and T.-C. Wei, *Structure and stability of Mott-insulator shells of bosons trapped in an optical lattice*, Phys. Rev. A **71**, 063601 (2005).

[Den02] J. H. Denschlag, J. E. Simsarian, H. Häffner, C. McKenzie, A. Browaeys, D. Cho, K. Helmerson, S. L. Rolston, and W. D. Phillips, *A Bose-Einstein condensate in an optical lattice*, Journal of Physics B: Atomic, Molecular and Optical Physics **35**, 3095 (2002).

[Der01] A. Derevianko, *Feasibility of Cooling and Trapping Metastable Alkaline-Earth Atoms*, Phys. Rev. Lett. **87**, 023002 (2001).

[Der11] A. Derevianko and H. Katori, *Colloquium: Physics of optical lattice clocks*, Rev. Mod. Phys. **83**, 331 (2011).

[DeS10] B. J. DeSalvo, M. Yan, P. G. Mickelson, Y. N. Martinez de Escobar, and T. C. Killian, *Degenerate Fermi Gas of* ^{87}Sr, Phys. Rev. Lett. **105**, 030402 (2010).

[Die08] S. Diehl, A. Micheli, A. Kantian, B. Kraus, H. Büchler, and P. Zoller, *Quantum states and phases in driven open quantum systems with cold atoms*, Nature Phys. **4**, 878 (2008).

[Don01] E. A. Donley, N. R. Clausen, S. L. Cornish, J. L. Roberts, E. A. Cornell, and C. E. Wieman, *Dynamics of Collapsing and Exploding Bose-Einstein Condensates*, Nature **412**, 295 (2001).

[Dru02] P. D. Drummond, K. V. Kheruntsyan, D. J. Heinzen, and R. H. Wynar, *Stimulated Raman adiabatic passage from an atomic to a molecular Bose-Einstein condensate*, Phys. Rev. A **65**, 063619 (2002).

[Dru05] P. D. Drummond, K. V. Kheruntsyan, D. J. Heinzen, and R. H. Wynar, *Reply to "Comment on 'Stimulated Raman adiabatic passage from an atomic to a molecular Bose-Einstein condensate' "*, Phys. Rev. A **71**, 017602 (2005).

[Dum94] R. Dum, P. Marte, T. Pellizzari, and P. Zoller, *Laser Cooling to a Single Quantum State in a Trap*, Phys. Rev. Lett. **73**, 2829 (1994).

[Ein24] A. Einstein, *Quantentheorie des einatomigen idealen Gases I*, Sitzungsberichte der Preussischen Akademie der Wissenschaften **21**, 261 (1924).

[Ein25] A. Einstein, *Quantentheorie des einatomigen idealen Gases II*, Sitzungsberichte der Preussischen Akademie der Wissenschaften **1**, 3 (1925).

[End12] M. Endres, T. Fukuhara, D. Pekker, M. Cheneau, P. Schauß, C. Gross, E. Demler, S. Kuhr, and I. Bloch, *The 'Higgs' amplitude mode at the two-dimensional superfluid/Mott insulator transition* **487**, 454 (2012).

[Eno08] K. Enomoto, K. Kasa, M. Kitagawa, and Y. Takahashi, *Optical Feshbach Resonance Using the Intercombination Transition*, Phys. Rev. Lett. **101**, 203201 (2008).

[Ess10] T. Esslinger, *Fermi-Hubbard Physics with Atoms in an Optical Lattice*, Annual Review of Condensed Matter Physics **1**, 129 (2010).

[Far10] D. M. Farkas, K. M. Hudek, E. A. Salim, S. R. Segal, M. B. Squires, and D. Z. Anderson, *A compact, transportable, microchip-based system for high repetition rate production of Bose–Einstein condensates*, Applied Physics Letters **96**, 093102 (2010).

[Fed96a] P. O. Fedichev, Y. Kagan, G. V. Shlyapnikov, and J. T. M. Walraven, *Influence of nearly resonant light on the scattering length in low-temperature atomic gases*, Phys. Rev. Lett. **77**, 2913 (1996).

[Fed96b] P. O. Fedichev, M. W. Reynolds, and G. V. Shlyapnikov, *Three-Body recombination of ultracold atoms to a weakly bound s level*, Phys. Rev. Lett. **77**, 2921 (1996).

[Fer] F. Ferlaino, S. Knoop, and R. Grimm, chap. 9 in [Kre09].

[Fer06a] G. Ferrari, R. E. Drullinger, N. Poli, F. Sorrentino, and G. M. Tino, *Cooling of Sr to high phase-space density by laser and sympathetic cooling in isotopic mixtures*, Phys. Rev. A **73**, 023408 (2006).

[Fer06b] G. Ferrari, N. Poli, F. Sorrentino, and G. M. Tino, *Long-lived Bloch oscillations with bosonic Sr atoms and application to gravity measurement at the micrometer scale*, Phys. Rev. Lett. **97**, 060402 (2006).

[Fey82] R. Feynman, *Simulating Physics with Computers*, International Journal of Theoretical Physics **21**, 467 (1982).

[FF10] M. Foss-Feig, M. Hermele, and A. M. Rey, *Probing the Kondo lattice model with alkaline-earth-metal atoms*, Phys. Rev. A **81**, 051603 (2010).

[Flo] Private homepage of Florian Schreck, `http://iqoqi006.uibk.ac.at/users/c704250/lab/GlasscellMountingCompressed.pdf`.

[Föl05] S. Fölling, F. Gerbier, A. Widera, O. Mandel, T. Gericke, and I. Bloch, *Spatial quantum noise interferometry in expanding ultracold atom clouds*, Nature **434**, 481 (2005).

[Föl07] S. Fölling, S. Trotzky, P. Cheinet, M. Feld, R. Saers, A. Widera, T. Müller, and I. Bloch, *Direct observation of second-order atom tunnelling*, Nature **448**, 1029 (2007).

[Fri11] J. Friebe, M. Riedmann, T. Wübbena, A. Pape, H. Kelkar, W. Ertmer, O. Terra, U. Sterr, S. Weyers, G. Grosche, H. Schnatz, and E. Rasel, *Remote frequency measurement of the* $^1S_0 \rightarrow {}^3P_1$ *transition in laser-cooled* ^{24}Mg, New Journal of Physics **13**, 125010 (2011).

[Fri12] A. Frisch, K. Aikawa, M. Mark, A. Rietzler, J. Schindler, E. Zupanič, R. Grimm, and F. Ferlaino, *Narrow-line magneto-optical trap for erbium*, Phys. Rev. A **85**, 051401 (2012).

[Fuk07a] T. Fukuhara, S. Sugawa, and Y. Takahashi, *Bose-Einstein condensation of an ytterbium isotope*, Phys. Rev. A **76**, 051604(R) (2007).

[Fuk07b] T. Fukuhara, Y. Takasu, M. Kumakura, and Y. Takahashi, *Degenerate Fermi gases of ytterbium*, Phys. Rev. Lett. **98**, 030401 (2007).

[Fuk09a] T. Fukuhara, S. Sugawa, M. Sugimoto, S. Taie, and Y. Takahashi, *Mott insulator of ultracold alkaline-earth-metal-like atoms*, Phys. Rev. A **79**, 041604(R) (2009).

[Fuk09b] T. Fukuhara, S. Sugawa, Y. Takasu, and Y. Takahashi, *All-optical formation of quantum degenerate mixtures*, Phys. Rev. A **79**, 021601(R) (2009).

[Gao00] B. Gao, *Zero-energy bound or quasibound states and their implications for diatomic systems with an asymptotic van der Waals interaction*, Phys. Rev. A **62**, 050702 (2000).

[Ger22] W. Gerlach and O. Stern, *Der experimentelle Nachweis des magnetischen Moments des Silberatoms*, Z. Phys. **8**, 110 (1922).

[Ger10] F. Gerbier and J. Dalibard, *Gauge fields for ultracold atoms in optical superlattices*, New J. Phys. **12**, 033007 (2010).

[Gio96] S. Giorgini, L. P. Pitaevskii, and S. Stringari, *Condensate fraction and critical temperature of a trapped interacting Bose gas*, Phys. Rev. A **54**, R4633 (1996).

[Gio08] S. Giorgini, L. P. Pitaevskii, and S. Stringari, *Theory of ultracold atomic Fermi gases*, Rev. Mod. Phys. **80**, 1215 (2008).

[Gór02] K. Góral, L. Santos, and M. Lewenstein, *Quantum Phases of Dipolar Bosons in Optical Lattices*, Phys. Rev. Lett. **88**, 170406 (2002).

[Gor08] A. V. Gorshkov, P. Rabl, G. Pupillo, A. Micheli, P. Zoller, M. D. Lukin, and H. P. Büchler, *Suppression of Inelastic Collisions Between Polar Molecules With a Repulsive Shield*, Phys. Rev. Lett. **101**, 073201 (2008).

[Gor09] A. V. Gorshkov, A. M. Rey, A. J. Daley, M. M. Boyd, J. Ye, P. Zoller, and M. D. Lukin, *Alkaline-earth-metal atoms as few-qubit quantum registers*, Phys. Rev. Lett. **102**, 110503 (2009).

[Gor10] A. Gorshkov, M. Hermele, V. Gurarie, C. Xu, P. Julienne, J. Ye, P. Zoller, E. Demler, M. D. Lukin, and A. M. Rey, *Two-orbital $SU(N)$ magnetism with ultracold alkaline-earth atoms*, Nature Phys. **6**, 289 (2010).

[Gór11a] A. Górecka, B. Grémaud, and C. Miniatura, *Synthetic magnetic fluxes on the honeycomb lattice*, Phys. Rev. A **84**, 023604 (2011).

[Gor11b] A. V. Gorshkov, S. R. Manmana, G. Chen, E. Demler, M. D. Lukin, and A. M. Rey, *Quantum magnetism with polar alkali-metal dimers*, Phys. Rev. A **84**, 033619 (2011).

[Gra02] S. R. Granade, M. E. Gehm, K. M. O'Hara, and J. E. Thomas, *All-Optical Production of a Degenerate Fermi Gas*, Phys. Rev. Lett. **88**, 120405 (2002).

[Gre01] M. Greiner, I. Bloch, O. Mandel, T. W. Hänsch, and T. Esslinger, *Exploring Phase Coherence in a 2D Lattice of Bose-Einstein Condensates*, Phys. Rev. Lett. **87**, 160405 (2001).

[Gre02] M. Greiner, O. Mandel, T. Esslinger, T. W. Hänsch, and I. Bloch, *Quantum phase transition from a superfluid to a Mott insulator in a gas of ultracold atoms*, Nature **415**, 39 (2002).

[Gri93] G. F. Gribakin and V. V. Flambaum, *Calculation of the scattering length in atomic collisions using the semiclassical approximation*, Phys. Rev. A **48**, 546 (1993).

[Gri00] R. Grimm, M. Weidemüller, and Y. B. Ovchinnikov, *Optical dipole traps for neutral atoms*, Adv. At. Mol. Opt. Phys. **42**, 95 (2000).

[Gri05] A. Griesmaier, J. Werner, S. Hensler, J. Stuhler, and T. Pfau, *Bose-Einstein condensation of chromium*, Phys. Rev. Lett. **94**, 160401 (2005).

[Gri06] P. F. Griffin, K. J. Weatherill, S. G. MacLeod, R. M. Potvliege, and C. S. Adams, *Spatially selective loading of an optical lattice by light-shift engineering using an auxiliary laser field*, New J. Phys. **8**, 11 (2006).

[Gri08] R. Grimm, *Proceedings of the International School of Physics "Enrico Fermi", Course CLXIV, Varenna, 20-30 June 2006*, chapter Ultracold Fermi gases in the BEC-BCS crossover: a review from the Innsbruck perspective (2008).

[Grü02] J. Grünert and A. Hemmerich, *Sub-Doppler magneto-optical trap for calcium*, Phys. Rev. A **65**, 041401 (2002).

[Gue07] J. R. Guest, N. D. Scielzo, I. Ahmad, K. Bailey, J. P. Greene, R. J. Holt, Z.-T. Lu, T. P. O'Connor, and D. H. Potterveld, *Laser Trapping of* ^{225}Ra *and* ^{226}Ra *with Repumping by Room-Temperature Blackbody Radiation*, Phys. Rev. Lett. **98**, 093001 (2007).

[Gué10] R. Guérout, M. Aymar, and O. Dulieu, *Ground state of the polar alkali-metal-atom-strontium molecules: Potential energy curve and permanent dipole moment*, Phys. Rev. A **82**, 042508 (2010).

[Hac08] H. Hachisu, K. Miyagishi, S. G. Porsev, A. Derevianko, V. D. Ovsiannikov, V. G. Pal'chikov, M. Takamoto, and H. Katori, *Trapping of Neutral Mercury Atoms and Prospects for Optical Lattice Clocks*, Phys. Rev. Lett. **100**, 053001 (2008).

[Had02] Z. Hadzibabic, C. A. Stan, K. Dieckmann, S. Gupta, M. W. Zwierlein, A. Görlitz, and W. Ketterle, *Two-Species Mixture of Quantum Degenerate Bose and Fermi Gases*, Phys. Rev. Lett. **88**, 160401 (2002).

[Häf08] H. Häffner, C. Roos, and R. Blatt, *Quantum computing with trapped ions*, Physics Reports **469**, 155 (2008).

[Hal98] D. S. Hall, M. R. Matthews, J. R. Ensher, C. E. Wieman, and E. A. Cornell, *Dynamics of Component Separation in a Binary Mixture of Bose-Einstein Condensates*, Phys. Rev. Lett. **81**, 1539 (1998).

[Hal12] P. Halder, C.-Y. Yang, and A. Hemmerich, *Alternative route to Bose-Einstein condensation of two-electron atoms*, Phys. Rev. A **85**, 031603 (2012).

[Ham98] S. E. Hamann, D. L. Haycock, G. Klose, P. H. Pax, I. H. Deutsch, and P. S. Jessen, *Resolved-Sideband Raman Cooling to the Ground State of an Optical Lattice*, Phys. Rev. Lett. **80**, 4149 (1998).

[Han00] D.-J. Han, S. Wolf, S. Oliver, C. McCormick, M. T. DePue, and D. S. Weiss, *3D Raman Sideband Cooling of Cesium Atoms at High Density*, Phys. Rev. Lett. **85**, 724 (2000).

[Han03] D. P. Hansen, J. R. Mohr, and A. Hemmerich, *Magnetic trapping of metastable calcium atoms*, Phys. Rev. A **67**, 021401(R) (2003).

[Han04] C. I. Hancox, S. C. Doret, M. T. Hummon, L. Luo, and J. M. Doyle, *Magnetic trapping of rare-earth atoms at millikelvin temperatures*, Nature **431**, 281 (2004).

[Han05] D. Hansen and A. Hemmerich, *Doppler-free spectroscopy of metastable calcium in a discharge heat pipe*, Phys. Rev. A **72**, 022502 (2005).

[Han06] D. Hansen and A. Hemmerich, *Observation of Multichannel Collisions of Cold Metastable Calcium Atoms*, Phys. Rev. Lett. **96**, 073003 (2006).

[Han11] A. H. Hansen, A. Khramov, W. H. Dowd, A. O. Jamison, V. V. Ivanov, and S. Gupta, *Quantum degenerate mixture of ytterbium and lithium atoms*, Phys. Rev. A **84**, 011606 (2011).

[Har11] H. Hara, Y. Takasu, Y. Yamaoka, J. M. Doyle, and Y. Takahashi, *Quantum Degenerate Mixtures of Alkali and Alkaline-Earth-Like Atoms*, Phys. Rev. Lett. **106**, 205304 (2011).

[Hay07] D. Hayes, P. S. Julienne, and I. H. Deutsch, *Quantum Logic via the Exchange Blockade in Ultracold Collisions*, Phys. Rev. Lett. **98**, 070501 (2007).

[Haz12] K. R. A. Hazzard, V. Gurarie, M. Hermele, and A. M. Rey, *High-temperature properties of fermionic alkaline-earth-metal atoms in optical lattices*, Phys. Rev. A **85**, 041604 (2012).

[Hei77] S. M. Heider and G. O. Brink, *Hyperfine structure of* ^{87}Sr *in the* $^3P_2$ *metastable state*, Phys. Rev. A **16**, 1371 (1977).

[Her09] M. Hermele, V. Gurarie, and A. M. Rey, *Mott Insulators of Ultracold Fermionic Alkaline Earth Atoms: Underconstrained Magnetism and Chiral Spin Liquid*, Phys. Rev. Lett. **103**, 135301 (2009).

[Hof76] D. R. Hofstadter, *Energy levels and wave functions of Bloch electrons in rational and irrational magnetic fields*, Phys. Rev. B **14**, 2239 (1976).

[Hon05] T. Hong, C. Cramer, E. Cook, W. Nagourney, and E. N. Fortson, *Observation of the* $^1S_0$ - $^3P_0$ *transition in atomic ytterbium for optical clocks and qubit arrays*, Optics Letters **30**, 2644 (2005).

[Hop98] T. C. Hope, Transactions of the Royal Society of Edinburgh **IV**, no. II, 3 (1798).

[Hor06] M. Horikoshi and K. Nakagawa, *Atom chip based fast production of BoseEinstein condensate*, Applied Physics B: Lasers and Optics **82**, 363 (2006).

[Hua09] B. Huang, *Linewidth Reduction of a Diode Laser by Optical Feedback for Strontium BEC Applications*, Master's thesis, University of Innsbruck, Austria (2009).

[Hud06] E. R. Hudson, H. J. Lewandowski, B. C. Sawyer, and J. Ye, *Cold Molecule Spectroscopy for Constraining the Evolution of the Fine Structure Constant*, Phys. Rev. Lett. **96**, 143004 (2006).

[Hun11] H.-H. Hung, Y. Wang, and C. Wu, *Quantum magnetism in ultracold alkali and alkaline-earth fermion systems with symplectic symmetry*, Phys. Rev. B **84**, 054406 (2011).

[Ido00] T. Ido, Y. Isoya, and H. Katori, *Optical-dipole trapping of Sr atoms at a high phase-space density*, Phys. Rev. A **61**, 061403 (2000).

[Ido03] T. Ido and H. Katori, *Recoil-free spectroscopy of neutral Sr atoms in the Lamb-Dicke regime*, Phys. Rev. Lett. **91**, 053001 (2003).

[Ido05] T. Ido, T. H. Loftus, M. M. Boyd, A. D. Ludlow, K. W. Holman, and J. Ye, *Precision Spectroscopy and Density-Dependent Frequency Shifts in Ultracold Sr*, Phys. Rev. Lett. **94**, 153001 (2005).

[Ing99] M. Inguscio, S. Stringari, and C. Wieman (Eds.), *Bose-Einstein condensation in atomic gases*, North Holland, Amsterdam (1999), Proceedings of the International School of Physics "Enrico Fermi", Course CXL, Varenna, 7-17 July 1998.

[Ing08] M. Inguscio, W. Ketterle, and C. Salomon (Eds.), *Ultracold Fermi gases*, IOS Press, Amsterdam (2008), Proceedings of the International School of Physics "Enrico Fermi", Course CLXIV, Varenna, June 2006.

[Ino99] S. Inouye, A. P. Chikkatur, D. M. Stamper-Kurn, J. Stenger, D. E. Pritchard, and W. Ketterle, *Superradiant Rayleigh Scattering from a Bose-Einstein Condensate*, Science **285**, 571 (1999).

[Jak98] D. Jaksch, C. Bruder, J. I. Cirac, C. W. Gardiner, and P. Zoller, *Cold Bosonic Atoms in Optical Lattices*, Phys. Rev. Lett. **81**, 3108 (1998).

[Jak02] D. Jaksch, V. Venturi, J. I. Cirac, C. J. Williams, and P. Zoller, *Creation of a Molecular Condensate by Dynamically Melting a Mott Insulator*, Phys. Rev. Lett. **89**, 040402 (2002).

[Jak03] D. Jaksch and P. Zoller, *Creation of effective magnetic fields in optical lattices: the Hofstadter butterfly for cold neutral atoms*, New J. Phys. **5**, 56 (2003).

[Jen11] B. B. Jensen, H. Ming, P. G. Westergaard, K. Gunnarsson, M. H. Madsen, A. Brusch, J. Hald, and J. W. Thomsen, *Experimental Determination of the* ^{24}Mg I $(3s3p)^3P_2$ *Lifetime*, Phys. Rev. Lett. **107**, 113001 (2011).

[Jo12] G.-B. Jo, J. Guzman, C. K. Thomas, P. Hosur, A. Vishwanath, and D. M. Stamper-Kurn, *Ultracold Atoms in a Tunable Optical Kagome Lattice*, Phys. Rev. Lett. **108**, 045305 (2012).

[Jör08] R. Jördens, N. Strohmaier, K. Günter, H. Moritz, and T. Esslinger, *A Mott insulator of fermionic atoms in an optical lattice*, Nature **455**, 204 (2008).

[Jul] P. S. Julienne, private communication.

[Jul92] P. Julienne, A. Smith, and K. Burnett, *Theory of Collisions between Laser Cooled Atoms*, Adv. At. Mol. Opt. Phys. **30**, 141 (1992).

[Kag97] Y. Kagan, E. L. Surkov, and G. V. Shlyapnikov, *Evolution of a Bose gas in anisotropic time-dependent traps*, Phys. Rev. A **55**, R18 (1997).

[Kap02] A. Kaplan, M. Fredslund Andersen, and N. Davidson, *Suppression of inhomogeneous broadening in rf spectroscopy of optically trapped atoms*, Phys. Rev. A **66**, 045401 (2002).

[Kas92] M. Kasevich and S. Chu, *Laser cooling below a photon recoil with three-level atoms*, Phys. Rev. Lett. **69**, 1741 (1992).

[Kat99] H. Katori, T. Ido, Y. Isoya, and M. Kuwata-Gonokami, *Magneto-optical trapping and cooling of strontium atoms down to the photon recoil temperature*, Phys. Rev. Lett. **82**, 1116 (1999).

[Kat01] H. Katori, T. Ido, Y. Isoya, and M. Kuwata-Gonokami, *Laser cooling of strontium atoms toward quantum degeneracy*, in E. Arimondo, P. DeNatale, and M. Inguscio (Eds.), *Atomic Physics 17*, 382–396, American Institute of Physics, Woodbury (2001).

[Ket93] W. Ketterle, K. B. Davis, M. A. Joffe, A. Martin, and D. E. Pritchard, *High densities of cold atoms in a dark spontaneous-force optical trap*, Phys. Rev. Lett. **70**, 2253 (1993).

[Ket96] W. Ketterle and N. J. van Druten, *Evaporative Cooling of Trapped Atoms*, Adv. Atom. Mol. Opt. Phys. **37**, 181 (1996).

[Kil07a] T. C. Killian, *Ultracold Neutral Plasmas*, Science **316**, 705 (2007).

[Kil07b] T. C. Killian, T. Pattard, T. Pohl, and J. M. Rost, *Ultracold neutral plasmas*, Phys. Rep. **449**, 77 (2007).

[Kin05] T. Kinoshita, T. Wenger, and D. S. Weiss, *All-optical Bose-Einstein condensation using a compressible crossed dipole trap*, Phys. Rev. A **71**, 011602 (2005).

[Kir95] R. Kirwan, Crell's Annalen 1795 **II**, 119, 205 (1795).

[Kit08] M. Kitagawa, K. Enomoto, K. Kasa, Y. Takahashi, R. Ciuryło, P. Naidon, and P. S. Julienne, *Two-color photoassociation spectroscopy of ytterbium atoms and the precise determinations of s-wave scattering lengths*, Phys. Rev. A **77**, 012719 (2008).

[Kla93] M. H. Klaproth, Crell's Annalen 1793 **II**, 189 (1793).

[Kla94] M. H. Klaproth, Crell's Annalen 1794 **I**, 99 (1794).

[Kla07] M. H. Klaproth, *Chemisches Wörterbuch*, Wollische Buchhandlung, Berlin (1807).

[Koc08] C. P. Koch, *Perspectives for coherent optical formation of strontium molecules in their electronic ground state*, Phys. Rev. A **78**, 063411 (2008).

[Köh02] M. Köhl, M. J. Davis, C. W. Gardiner, T. W. Hänsch, and T. Esslinger, *Growth of Bose-Einstein Condensates from Thermal Vapor*, Phys. Rev. Lett. **88**, 080402 (2002).

[Köh05] M. Köhl, H. Moritz, T. Stöferle, K. Günter, and T. Esslinger, *Fermionic Atoms in a Three Dimensional Optical Lattice: Observing Fermi Surfaces, Dynamics, and Interactions*, Phys. Rev. Lett. **94**, 080403 (2005).

[Koh09] T. Kohno, M. Yasuda, K. Hosaka, H. Inaba, Y. Nakajima, and F.-L. Hong, *One-Dimensional Optical Lattice Clock with a Fermionic* ^{171}*Yb Isotope*, Appl. Phys. Express **2**, 072501 (2009).

[Kot09] S. Kotochigova, T. Zelevinsky, and J. Ye, *Prospects for application of ultracold* Sr_2 *molecules in precision measurements*, Phys. Rev. A **79**, 012504 (2009).

[Koz99] M. Kozuma, Y. Suzuki, T. Yoshio, T. Sugiura, T. Kuga, E. W. Hagley, and L. Deng, *Phase-Coherent Amplification of Matter Waves*, Science **286**, 2309 (1999).

[Kra09] S. Kraft, F. Vogt, O. Appel, F. Riehle, and U. Sterr, *Bose-Einstein condensation of alkaline earth atoms:* ^{40}*Ca*, Phys. Rev. Lett. **103**, 130401 (2009).

[Kre08] R. Krems, *Cold controlled chemistry*, Phys. Chem. Chem. Phys. **10**, 4079 (2008).

[Kre09] R. V. Krems, B. Friedrich, and W. C. Stwalley (Eds.), *Cold Molecules: Theory, Experiment, Applications*, Taylor & Francis (2009).

[Kur90] T. Kurosu and F. Shimizu, *Laser cooling and trapping of calcium and strontium*, Jpn. J. Appl. Phys. **29**, L2127 (1990).

[Lae06] J. R. de Laeter and N. Bukilic, *The isotopic composition and atomic weight of ytterbium*, Int. J. of Mass Spectrometry **252**, 222 (2006).

[Lah05] T. Lahaye, Z. Wang, G. Reinaudi, S. P. Rath, J. Dalibard, and D. Guéry-Odelin, *Evaporative cooling of a guided rubidium atomic beam*, Phys. Rev. A **72**, 033411 (2005).

[Lah08] T. Lahaye, J. Metz, B. Fröhlich, T. Koch, M. Meister, A. Griesmaier, T. Pfau, H. Saito, Y. Kawaguchi, and M. Ueda, *d-wave collapse and explosion of a dipolar Bose-Einstein condensate*, Phys. Rev. Lett. **101**, 080401 (2008).

[Lan08] F. Lang, K. Winkler, C. Strauss, R. Grimm, and J. Hecker Denschlag, *Ultracold Triplet Molecules in the Rovibrational Ground State*, Phys. Rev. Lett. **101**, 133005 (2008).

[Lem09a] N. D. Lemke, A. D. Ludlow, Z. W. Barber, T. M. Fortier, S. A. Diddams, Y. Jiang, S. R. Jefferts, T. P. Heavner, T. E. Parker, and C. W. Oates, *Spin*-1/2 *Optical Lattice Clock*, Phys. Rev. Lett. **103**, 063001 (2009).

[Lem09b] P. Lemonde, *Optical lattice clocks*, Eur. Phys. J. Special Topics **172**, 81 (2009).

[Ler11] A. Lercher, T. Takekoshi, M. Debatin, B. Schuster, R. Rameshan, F. Ferlaino, R. Grimm, and H. Nägerl, *Production of a dual-species Bose-Einstein condensate of Rb and Cs atoms*, EPJD **65**, 3 (2011).

[Let88] P. D. Lett, R. N. Watts, C. I. Westbrook, W. D. Phillips, P. L. Gould, and H. J. Metcalf, *Observation of Atoms Laser Cooled below the Doppler Limit*, Phys. Rev. Lett. **61**, 169 (1988).

[Lin09] Y.-J. Lin, R. L. Compton, K. Jimenez-Garcia, J. V. Porto, and I. B. Spielman, *Synthetic magnetic fields for ultracold neutral atoms*, Nature **462**, 628 (2009).

[Lin11] Y.-J. Lin, K. Jimenez-Garcia, and I. B. Spielman, *Spin-orbit-coupled Bose-Einstein condensates*, Nature **471**, 83 (2011).

[Lis09] C. Lisdat, J. S. R. Vellore Winfred, T. Middelmann, F. Riehle, and U. Sterr, *Collisional Losses, Decoherence, and Frequency Shifts in Optical Lattice Clocks with Bosons*, Phys. Rev. Lett. **103**, 090801 (2009).

[Llo96] S. Lloyd, *Universal Quantum Simulators*, Science **273**, 1073 (1996).

[Lof02] T. Loftus, J. R. Bochinski, and T. W. Mossberg, *Magnetic trapping of ytterbium and the alkaline-earth metals*, Phys. Rev. A **66**, 013411 (2002).

[Lof04a] T. H. Loftus, T. Ido, M. M. Boyd, A. D. Ludlow, and J. Ye, *Narrow line cooling and momentum-space crystals*, Phys. Rev. A **70**, 063413 (2004).

[Lof04b] T. H. Loftus, T. Ido, A. D. Ludlow, M. M. Boyd, and J. Ye, *Narrow Line Cooling: Finite Photon Recoil Dynamics*, Phys. Rev. Lett. **93**, 073003 (2004).

[Lu11a] M. Lu, N. Q. Burdick, S. H. Youn, and B. L. Lev, *Strongly Dipolar Bose-Einstein Condensate of Dysprosium*, Phys. Rev. Lett. **107**, 190401 (2011).

[Lu11b] M. Lu, S. H. Youn, and B. L. Lev, *Spectroscopy of a narrow-line laser-cooling transition in atomic dysprosium*, Phys. Rev. A **83**, 012510 (2011).

[Lud08a] A. D. Ludlow, *The Strontium Optical Lattice Clock: Optical Spectroscopy with Sub-Hertz Accuracy*, Ph.D. thesis, University of Colorado, Boulder, USA (2008).

[Lud08b] A. D. Ludlow, T. Zelevinsky, G. K. Campbell, S. Blatt, M. M. Boyd, M. H. G. de Miranda, M. J. Martin, J. W. Thomsen, S. M. Foreman, J. Ye, T. M. Fortier, J. E. Stalnaker, S. A. Diddams, Y. Le Coq, Z. W. Barber, N. Poli, N. D. Lemke, K. M. Beck, and C. W. Oates, *Sr Lattice Clock at* 1×10^{16} *Fractional Uncertainty by Remote Optical Evaluation with a Ca Clock*, Science **319**, 1805 (2008).

[Mac00] M. Mackie, R. Kowalski, and J. Javanainen, *Bose-Stimulated Raman Adiabatic Passage in Photoassociation*, Phys. Rev. Lett. **84**, 3803 (2000).

[Mac05] M. Mackie, A. Collin, and J. Javanainen, *Comment on "Stimulated Raman adiabatic passage from an atomic to a molecular Bose-Einstein condensate"*, Phys. Rev. A **71**, 017601 (2005).

[Mad00] K. W. Madison, F. Chevy, W. Wohlleben, and J. Dalibard, *Vortex Formation in a Stirred Bose-Einstein Condensate*, Phys. Rev. Lett. **84**, 806 (2000).

[Man03] O. Mandel, M. Greiner, A. Widera, T. Rom, T. W. Hänsch, and I. Bloch, *Coherent Transport of Neutral Atoms in Spin-Dependent Optical Lattice Potentials*, Phys. Rev. Lett. **91**, 010407 (2003).

[Man11] S. R. Manmana, K. R. A. Hazzard, G. Chen, A. E. Feiguin, and A. M. Rey, $SU(N)$ *magnetism in chains of ultracold alkaline-earth-metal atoms: Mott transitions and quantum correlations*, Phys. Rev. A **84**, 043601 (2011).

[Mar] M.J. Martin, private communication.

[Mar08] Y. N. Martinez de Escobar, P. G. Mickelson, P. Pellegrini, S. B. Nagel, A. Traverso, M. Yan, R. Côté, and T. C. Killian, *Two-photon photoassociative spectroscopy of ultracold* ^{88}Sr, Phys. Rev. A **78**, 062708 (2008).

[Mar09a] Y. N. Martinez de Escobar, P. G. Mickelson, M. Yan, B. J. DeSalvo, S. B. Nagel, and T. C. Killian, *Bose-Einstein Condensation of* ^{84}Sr, Phys. Rev. Lett. **103**, 200402 (2009).

[Mar09b] Y. N. Martinez de Escobar, P. G. Mickelson, M. Yan, and T. C. Killian, *Modification of atom scattering using an intercombination-line optical Feshbach resonance at large detuning*, arXiv:0906.1837v1, v3 (2009).

[Mat98] M. R. Matthews, D. S. Hall, D. S. Jin, J. R. Ensher, C. E. Wieman, E. A. Cornell, F. Dalfovo, C. Minniti, and S. Stringari, *Dynamical Response of a Bose-Einstein Condensate to a Discontinuous Change in Internal State*, Phys. Rev. Lett. **81**, 243 (1998).

[Mat99] M. R. Matthews, B. P. Anderson, P. C. Haljan, D. S. Hall, C. E. Wieman, and E. A. Cornell, *Vortices in a Bose-Einstein Condensate*, Phys. Rev. Lett. **83**, 2498 (1999).

[McC06] J. J. McClelland and J. L. Hanssen, *Laser Cooling without Repumping: A Magneto-Optical Trap for Erbium Atoms*, Phys. Rev. Lett. **96**, 143005 (2006).

[McK11] D. McKay and B. DeMarco, *Cooling in strongly correlated optical lattices: prospects and challenges*, Reports on Progress in Physics **74**, 054401 (2011).

[McN06] J. M. McNamara, T. Jeltes, A. S. Tychkov, W. Hogervorst, and W. Vassen, *Degenerate Bose-Fermi Mixture of Metastable Atoms*, Phys. Rev. Lett. **97**, 080404 (2006).

[Med11] P. Medley, D. M. Weld, H. Miyake, D. E. Pritchard, and W. Ketterle, *Spin Gradient Demagnetization Cooling of Ultracold Atoms*, Phys. Rev. Lett. **106**, 195301 (2011).

[Met99] H. J. Metcalf and P. van der Straten, *Laser Cooling and Trapping*, Springer, New York (1999).

[Mew97] M.-O. Mewes, M. R. Andrews, D. M. Kurn, D. S. Durfee, C. G. Townsend, and W. Ketterle, *Output Coupler for Bose-Einstein Condensed Atoms*, Phys. Rev. Lett. **78**, 582 (1997).

[Mic05] P. G. Mickelson, Y. N. Martinez, A. D. Saenz, S. B. Nagel, Y. C. Chen, T. C. Killian, P. Pellegrini, and R. Côté, *Spectroscopic Determination of the s-Wave Scattering Lengths of* ^{86}Sr *and* ^{88}Sr, Phys. Rev. Lett. **95**, 223002 (2005).

[Mic06] A. Micheli, G. K. Brennen, and P. Zoller, *A toolbox for lattice-spin models with polar molecules*, Nature Phys. **2**, 341 (2006).

[Mic07] A. Micheli, G. Pupillo, H. P. Büchler, and P. Zoller, *Cold polar molecules in two-dimensional traps: Tailoring interactions with external fields for novel quantum phases*, Phys. Rev. A **76**, 043604 (2007).

[Mic09] P. G. Mickelson, Y. N. Martinez de Escobar, P. Anzel, B. J. DeSalvo, S. B. Nagel, A. J. Traverso, M. Yan, and T. C. Killian, *Repumping and spectroscopy of laser-cooled Sr atoms using the* $(5s5p)^3P_2 - (5s4d)^3D_2$ *transition*, J. Phys. B: At. Mol. Opt. Phys. **42**, 235001 (2009).

[Mic10] P. G. Mickelson, Y. N. Martinez de Escobar, M. Yan, B. J. DeSalvo, and T. C. Killian, *Bose-Einstein condensation of* ^{88}Sr *through sympathetic cooling with* ^{87}Sr, Phys. Rev. A **81**, 051601 (2010).

[Mid12] T. Middelmann, S. Falke, C. Lisdat, and U. Sterr, *High accuracy correction of blackbody radiation shift in an optical lattice clock*, arXiv:1208.2848v1 (2012).

[Mil10] J. Millen, G. Lochead, and M. P. A. Jones, *Two-Electron Excitation of an Interacting Cold Rydberg Gas*, Phys. Rev. Lett. **105**, 213004 (2010).

[Mod02] G. Modugno, M. Modugno, F. Riboli, G. Roati, and M. Inguscio, *Two Atomic Species Superfluid*, Phys. Rev. Lett. **89**, 190404 (2002).

[Mon93] C. R. Monroe, E. A. Cornell, C. A. Sackett, C. J. Myatt, and C. E. Wieman, *Measurement of Cs-Cs elastic scattering at T =30 μK*, Phys. Rev. Lett. **70**, 414 (1993).

[Mor98] G. Morigi, J. I. Cirac, K. Ellinger, and P. Zoller, *Laser cooling of trapped atoms to the ground state: A dark state in position space*, Phys. Rev. A **57**, 2909 (1998).

[Muk03] T. Mukaiyama, H. Katori, T. Ido, Y. Li, and M. Kuwata-Gonokami, *Recoil-limited laser cooling of ^{87}Sr atoms near the Fermi temperature*, Phys. Rev. Lett. **90**, 113002 (2003).

[Nag03] S. B. Nagel, C. E. Simien, S. Laha, P. Gupta, V. S. Ashoka, and T. C. Killian, *Magnetic trapping of metastable $^3P_2$ atomic strontium*, Phys. Rev. A **67**, 011401(R) (2003).

[Nag05] S. B. Nagel, P. G. Mickelson, A. D. Saenz, Y. N. Martinez, Y. C. Chen, T. C. Killian, P. Pellegrini, and R. Côté, *Photoassociative Spectroscopy at Long Range in Ultracold Strontium*, Phys. Rev. Lett. **94**, 083004 (2005).

[Nem09] N. Nemitz, F. Baumer, F. Münchow, S. Tassy, and A. Görlitz, *Production of heteronuclear molecules in an electronically excited state by photoassociation in a mixture of ultracold Yb and Rb*, Phys. Rev. A **79**, 061403 (2009).

[Ni08] K.-K. Ni, S. Ospelkaus, M. H. G. de Miranda, A. Pe'er, B. Neyenhuis, J. J. Zirbel, S. Kotochigova, P. S. Julienne, D. S. Jin, and J. Ye, *A High Phase-Space-Density Gas of Polar Molecules*, Science **322**, 231 (2008).

[Ni10] K. K. Ni, S. Ospelkaus, D. Wang, G. Quemener, B. Neyenhuis, M. H. G. de Miranda, J. L. Bohn, J. Ye, and D. S. Jin, *Dipolar collisions of polar molecules in the quantum regime*, Nature **464**, 1324 (2010).

[Nic12] T. Nicholson, M. Martin, J. Williams, B. Bloom, M. Bishof, M. Swallows, S. Campbell, and J. Ye, *Comparison of Two Independent Sr Optical Clocks with 1×10^{-17} Stability at 10^3 s*, arXiv:1210.0064v1 (2012).

[NIS] The National Institute of Standards and Technology (NIST) database, available online at `http://www.nist.gov/pml/data`.

[Ols96] M. Olshanii, Y. Castin, and J. Dalibard, *A model for an atom laser*, in M. Inguscio, M. Allegrini, and A. Sasso (Eds.), *Proceedings of the 12th International Conference on Laser Spectroscopy*, 7, World Scientific, Singapore (1996).

[Ovc99] Y. B. Ovchinnikov, J. H. Müller, M. R. Doery, E. J. D. Vredenbregt, K. Helmerson, S. L. Rolston, and W. D. Phillips, *Diffraction of a Released Bose-Einstein Condensate by a Pulsed Standing Light Wave*, Phys. Rev. Lett. **83**, 284 (1999).

[Pap08] S. B. Papp, J. M. Pino, and C. E. Wieman, *Tunable Miscibility in a Dual-Species Bose-Einstein Condensate*, Phys. Rev. Lett. **101**, 040402 (2008).

[Par] Chang Yong Park *et al.*, *Optical repumping of triplet-P states enhances magneto-optical trapping of ytterbium atoms*, Poster at ICAP 2012.

[Pol05a] N. Poli, *Raffreddamento ed intrappolamento di atomi di stronzio: verso un nuovo standard di frequenza nella regione ottica*, Ph.D. thesis, Universita degli studi di Firenze, Florence, Italy (2005).

[Pol05b] N. Poli, R. E. Drullinger, G. Ferrari, J. Léonard, F. Sorrentino, and G. M. Tino, *Cooling and trapping of ultracold strontium isotopic mixtures*, Phys. Rev. A **71**, 061403 (2005).

[Pol09] S. E. Pollack, D. Dries, and R. G. Hulet, *Universality in three- and four-body bound states of ultracold atoms*, Science **326**, 1683 (2009).

[Pol11] N. Poli, F.-Y. Wang, M. G. Tarallo, A. Alberti, M. Prevedelli, and G. M. Tino, *Precision Measurement of Gravity with Cold Atoms in an Optical Lattice and Comparison with a Classical Gravimeter*, Phys. Rev. Lett. **106**, 038501 (2011).

[Por08] S. G. Porsev, A. D. Ludlow, M. M. Boyd, and J. Ye, *Determination of Sr properties for a high-accuracy optical clock*, Phys. Rev. A **78**, 032508 (2008).

[Pup] G. Pupillo, A. Micheli, H. P. Büchler, and P. Zoller, chap. 12 in [Kre09].

[QV05] A. Quessada-Vial, *Developpement d'une horloge optique a atomes de strontium pieges: realisation d'un laser ultra-stabile et stabilite de frequence*, Ph.D. thesis, Universite de Paris VI, Paris, France (2005).

[Reh07] N. Rehbein, T. E. Mehlstäubler, J. Keupp, K. Moldenhauer, E. M. Rasel, W. Ertmer, A. Douillet, V. Michels, S. G. Porsev, A. Derevianko, C. Froese Fischer, G. I. Tachiev, and V. G. Pal'chikov, *Optical quenching of metastable magnesium*, Phys. Rev. A **76**, 043406 (2007).

[Rei09] I. Reichenbach, P. S. Julienne, and I. H. Deutsch, *Controlling nuclear spin exchange via optical Feshbach resonances in* ^{171}Yb, Phys. Rev. A **80**, 020701 (2009).

[Rei12] G. Reinaudi, C. B. Osborn, M. McDonald, S. Kotochigova, and T. Zelevinsky, *Optical Production of Stable Ultracold* $^{88}Sr_2$ *Molecules*, Phys. Rev. Lett. **109**, 115303 (2012).

[Rit07] S. Ritter, A. Öttl, T. Donner, T. Bourdel, M. Köhl, and T. Esslinger, *Observing the Formation of Long-Range Order during Bose-Einstein Condensation*, Phys. Rev. Lett. **98**, 090402 (2007).

[Roa02] G. Roati, F. Riboli, G. Modugno, and M. Inguscio, *Fermi-Bose Quantum Degenerate K-Rb Mixture with Attractive Interaction*, Phys. Rev. Lett. **89**, 150403 (2002).

[Rom01] M. V. Romalis, W. C. Griffith, J. P. Jacobs, and E. N. Fortson, *New Limit on the Permanent Electric Dipole Moment of* ^{199}Hg, Phys. Rev. Lett. **86**, 2505 (2001).

[Rup95] P. A. Ruprecht, M. J. Holland, K. Burnett, and M. Edwards, *Time-dependent solution of the nonlinear Schrödinger equation for Bose-condensed trapped neutral atoms*, Phys. Rev. A **51**, 4704 (1995).

[San67] P. G. H. Sandars, *Measurability of the Proton Electric Dipole Moment*, Phys. Rev. Lett. **19**, 1396 (1967).

[San99] L. Santos and M. Lewenstein, *Dynamical cooling of trapped gases. II: Many-atom problem*, Phys. Rev. A **60**, 3851 (1999).

[San00] L. Santos, G. V. Shlyapnikov, P. Zoller, and M. Lewenstein, *Bose-Einstein Condensation in Trapped Dipolar Gases*, Phys. Rev. Lett. **85**, 1791 (2000).

[San04] R. Santra, K. V. Christ, and C. H. Greene, *Properties of metastable alkaline-earth-metal atoms calculated using an accurate effective core potential*, Phys. Rev. A **69**, 042510 (2004).

[San11] R. M. Sandner, M. Müller, A. J. Daley, and P. Zoller, *Spatial Pauli blocking of spontaneous emission in optical lattices*, Phys. Rev. A **84**, 043825 (2011).

[Sch01] F. Schreck, L. Khaykovich, K. L. Corwin, G. Ferrari, T. Bourdel, J. Cubizolles, and C. Salomon, *Quasipure Bose-Einstein Condensate Immersed in a Fermi Sea*, Phys. Rev. Lett. **87**, 080403 (2001).

[Sch02] F. Schreck, *Mixtures of ultracold gases: Fermi sea and Bose-Einstein condensate of lithium isotopes*, Ph.D. thesis, Universite de Paris VI, Paris, France (2002).

[Sch04] V. Schweikhard, I. Coddington, P. Engels, V. P. Mogendorff, and E. A. Cornell, *Rapidly Rotating Bose-Einstein Condensates in and near the Lowest Landau Level*, Phys. Rev. Lett. **92**, 040404 (2004).

[Sch08] U. Schneider, L. Hackermüller, S. Will, T. Best, I. Bloch, T. A. Costi, R. W. Helmes, D. Rasch, and A. Rosch, *Metallic and Insulating Phases of Repulsively Interacting Fermions in a 3D Optical Lattice*, Science **322**, 204 (2008).

[Sen94] K. Sengstock, U. Sterr, J. H. Mller, V. Rieger, D. Bettermann, and W. Ertmer, *Optical Ramsey spectroscopy on laser-trapped and thermal Mg atoms*, App. Phys. B **59**, 99 (1994).

[Ses91] D. W. Sesko, T. G. Walker, and C. E. Wieman, *Behavior of neutral atoms in a spontaneous force trap*, J. Opt. Soc. Am. B **8**, 946 (1991).

[She10] J. F. Sherson, C. Weitenberg, M. Endres, M. Cheneau, I. Bloch, and S. Kuhr, *Single-atom-resolved fluorescence imaging of an atomic Mott insulator*, Nature **467**, 68 (2010).

[She12] J. A. Sherman, N. D. Lemke, N. Hinkley, M. Pizzocaro, R. W. Fox, A. D. Ludlow, and C. W. Oates, *High-Accuracy Measurement of Atomic Polarizability in an Optical Lattice Clock*, Phys. Rev. Lett. **108**, 153002 (2012).

[Shi09] N. Shiga, Y. Li, H. Ito, S. Nagano, T. Ido, K. Bielska, R. S. Trawiński, and R. Ciuryło, *Buffer-gas-induced collision shift for the* ^{88}Sr $^1S_0$-$^3P_1$ *clock transition*, Phys. Rev. A **80**, 030501 (2009).

[Shu10] E. S. Shuman, J. F. Barry, and D. DeMille, *Laser cooling of a diatomic molecule*, Nature **467**, 820 (2010).

[Sil05] C. Silber, S. Gunther, C. Marzok, B. Deh, P. W. Courteille, and C. Zimmermann, *Quantum-Degenerate Mixture of Fermionic Lithium and Bosonic Rubidium Gases*, Phys. Rev. Lett. **95**, 170408 (2005).

[Sim04] C. E. Simien, Y. C. Chen, P. Gupta, S. Laha, Y. N. Martinez, P. G. Mickelson, S. B. Nagel, and T. C. Killian, *Using Absorption Imaging to Study Ion Dynamics in an Ultracold Neutral Plasma*, Phys. Rev. Lett. **92**, 143001 (2004).

[SK98a] D. M. Stamper-Kurn, M. R. Andrews, A. P. Chikkatur, S. Inouye, H.-J. Miesner, J. Stenger, and W. Ketterle, *Optical Confinement of a Bose-Einstein Condensate*, Phys. Rev. Lett. **80**, 2027 (1998).

[SK98b] D. M. Stamper-Kurn, H.-J. Miesner, A. P. Chikkatur, S. Inouye, J. Stenger, and W. Ketterle, *Reversible Formation of a Bose-Einstein Condensate*, Phys. Rev. Lett. **81**, 2194 (1998).

[Sko12] W. Skomorowski, F. Pawlowski, C. P. Koch, and R. Moszynski, *Rovibrational dynamics of the strontium molecule in the* $A^1\Sigma_u^+$, $c^3\Pi_u$, *and* $a^3\Sigma_u^+$ *manifold from state-of-the-art ab initio calculations*, J. Chem. Phys. **136**, 194306 (2012).

[Sla64] J. C. Slater, *Atomic Radii in Crystals*, Journal of Chemical Physics **41**, 3199 (1964).

[Sle92] T. Sleator, T. Pfau, V. Balykin, O. Carnal, and J. Mlynek, *Experimental demonstration of the optical Stern-Gerlach effect*, Phys. Rev. Lett. **68**, 1996 (1992).

[Sor06] F. Sorrentino, G. Ferrari, N. Poli, R. Drullinger, and G. M. Tino, *Laser cooling and trapping of atomic strontium for ultracold atom physics, high precision spectrosopy and quantum sensors*, Modern Physics Letters B **20**, 1287 (2006).

[Spr95] R. J. C. Spreeuw, T. Pfau, U. Janicke, and M. Wilkens, *Laser-like Scheme for Atomic Matter Waves*, Europhys. Lett. **32**, 469 (1995).

[Ste] S. Stellmer et al., to be published.

[Ste04] U. Sterr, C. Degenhardt, H. Stoehr, C. Lisdat, H. Schnatz, J. Helmcke, F. Riehle, G. Wilpers, C. Oates, and L. Hollberg, *The optical calcium frequency standards of PTB and NIST*, C.R. Physique **5**, 845 (2004).

[Ste08] A. Stein, H. Knöckel, and E. Tiemann, *Fourier-transform spectroscopy of Sr_2 and revised ground-state potential*, Phys. Rev. A **78**, 042508 (2008).

[Ste09] S. Stellmer, M. K. Tey, B. Huang, R. Grimm, and F. Schreck, *Bose-Einstein condensation of strontium*, Phys. Rev. Lett. **103**, 200401 (2009).

[Ste10a] A. Stein, H. Knöckel, and E. Tiemann, *The $^1S+^1S$ asymptote of Sr_2 studied by Fourier-transform spectroscopy*, Eur. Phys. J. D **57**, 171 (2010).

[Ste10b] S. Stellmer, M. K. Tey, R. Grimm, and F. Schreck, *Bose-Einstein condensation of ^{86}Sr*, Phys. Rev. A **82**, 041602 (2010).

[Ste11] S. Stellmer, R. Grimm, and F. Schreck, *Detection and manipulation of nuclear spin states in fermionic strontium*, Phys. Rev. A **84**, 043611 (2011).

[Ste12] S. Stellmer, B. Pasquiou, R. Grimm, and F. Schreck, *Creation of Ultracold* Sr_2 *Molecules in the Electronic Ground State*, Phys. Rev. Lett. **109**, 115302 (2012).

[Sto08] R. Stock, N. S. Babcock, M. G. Raizen, and B. C. Sanders, *Entanglement of group-II-like atoms with fast measurement for quantum information processing*, Phys. Rev. A **78**, 022301 (2008).

[Str11] J. Struck, C. Ölschläger, R. Le Targat, P. Soltan-Panahi, A. Eckardt, M. Lewenstein, P. Windpassinger, and K. Sengstock, *Quantum Simulation of Frustrated Classical Magnetism in Triangular Optical Lattices* **333**, 996 (2011).

[Stu12] B. K. Stuhl, M. T. Hummon, M. Yeo, G. Quéméner, J. L. Bohn, and J. Ye, *Evaporative cooling of the dipolar radical OH*, arXiv:1209.6343v1 (2012).

[Sug11] S. Sugawa, R. Yamazaki, S. Taie, and Y. Takahashi, *Bose-Einstein condensate in gases of rare atomic species*, Phys. Rev. A **84**, 011610 (2011).

[Suk10] D. Sukachev, A. Sokolov, K. Chebakov, A. Akimov, S. Kanorsky, N. Kolachevsky, and V. Sorokin, *Magneto-optical trap for thulium atoms*, Phys. Rev. A **82**, 011405 (2010).

[Sul] F. G. Sulzer, *Über den Strontianit*, letter to J. F. Blumenbach (1791), printed e.g. in *Magazin für das Neueste aus der Physik und Naturgeschichte*, VII, 3. (1807).

[Tai10] S. Taie, Y. Takasu, S. Sugawa, R. Yamazaki, T. Tsujimoto, R. Murakami, and Y. Takahashi, *Realization of a $SU(2) \times SU(6)$ System of Fermions in a Cold Atomic Gas*, Phys. Rev. Lett. **105**, 190401 (2010).

[Tai12] S. Taie, R. Yamazaki, S. Sugawa, and Y. Takahashi, *An SU(6) Mott insulator of an atomic Fermi gas realized by large-spin Pomeranchuk cooling*, Nature Phys. (2012).

[Tak03] Y. Takasu, K. Maki, K. Komori, T. Takano, K. Honda, M. Kumakura, T. Yabuzaki, and Y. Takahashi, *Spin-singlet Bose-Einstein condensation of two-electron atoms*, Phys. Rev. Lett. **91**, 040404 (2003).

[Tak05] M. Takamoto, F.-L. Hong, R. Higashi, and H. Katori, *An optical lattice clock*, Nature **435**, 321 (2005).

[Tak10] H. Takeuchi, S. Ishino, and M. Tsubota, *Binary Quantum Turbulence Arising from Countersuperflow Instability in Two-Component Bose-Einstein Condensates*, Phys. Rev. Lett. **105**, 205301 (2010).

[Tar12] L. Tarruell, D. Greif, T. Uehlinger, G. Jotzu, and T. Esslinger, *Creating, moving and merging Dirac points with a Fermi gas in a tunable honeycomb lattice*, Nature **483**, 302 (2012).

[TE12] A. Trabesinger (Ed.), *Nature Physics Insight - Quantum Simulation*, in Nature Phys. **8**, no. 4 (2012).

[Tey10] M. K. Tey, S. Stellmer, R. Grimm, and F. Schreck, *Double-degenerate Bose-Fermi mixture of strontium*, Phys. Rev. A **82**, 011608 (2010).

[The04] M. Theis, G. Thalhammer, K. Winkler, M. Hellwig, G. Ruff, R. Grimm, and J. H. Denschlag, *Tuning the Scattering Length with an Optically Induced Feshbach Resonance*, Phys. Rev. Lett. **93**, 123001 (2004).

[Tho95] J. Thomas and L. Wang, *Precision position measurement of moving atoms*, Phys. Rep. **262**, 311 (1995).

[Tim98] E. Timmermans and R. Côté, *Superfluidity in Sympathetic Cooling with Atomic Bose-Einstein Condensates*, Phys. Rev. Lett. **80**, 3419 (1998).

[Tom11] M. Tomza, F. Pawłowski, M. Jeziorska, C. P. Koch, and R. Moszynski, *Formation of ultracold SrYb molecules in an optical lattice by photoassociation spectroscopy: theoretical prospects*, Phys. Chem. Chem. Phys. **13**, 18893 (2011).

[Tra09] A. Traverso, R. Chakraborty, Y. N. Martinez de Escobar, P. G. Mickelson, S. B. Nagel, M. Yan, and T. C. Killian, *Inelastic and elastic collision rates for triplet states of ultracold strontium*, Phys. Rev. A **79**, 060702(R) (2009).

[Tre07] A. Trenkwalder, *Design of a Resonator Enhanced Optical Dipole Trap for Fermionic Mixtures*, Master's thesis, University of Innsbruck, Austria (2007).

[Tre11] A. Trenkwalder, C. Kohstall, M. Zaccanti, D. Naik, A. I. Sidorov, F. Schreck, and R. Grimm, *Hydrodynamic Expansion of a Strongly Interacting Fermi-Fermi Mixture*, Phys. Rev. Lett. **106**, 115304 (2011).

[Tro08] S. Trotzky, P. Cheinet, S. Fölling, M. Feld, U. Schnorrberger, A. M. Rey, A. Polkovnikov, E. A. Demler, M. D. Lukin, and I. Bloch, *Time-Resolved Observation and Control of Superexchange Interactions with Ultracold Atoms in Optical Lattices*, Science **319**, 295 (2008).

[Tru01] A. G. Truscott, K. E. Strecker, W. I. McAlexander, G. B. Partridge, and R. G. Hulet, *Observation of Fermi Pressure in a Gas of Trapped Atoms*, Science **291**, 2570 (2001).

[Vil11] P. Villwock, S. Siol, and T. Walther, *Magneto-optical trapping of neutral mercury*, Eur. Phys. J. D **65**, 251 (2011).

[Vit01] N. V. Vitanov, T. Halfmann, B. W. Shore, and K. Bergmann, *Laser-Induced Population Transfer by Adiabatic Passage Techniques*, Annu. Rev. Phys. Chem. **52**, 763 (2001).

[Vog99] K. R. Vogel, *Laser Cooling on a narrow atomic transition and measurement of the two-body cold collision loss rate in a strontium magneto-optical trap*, Ph.D. thesis, University of Colorado, Boulder, USA (1999).

[Vog12] F. Vogl, Master's thesis, University of Innsbruck, Austria (2012).

[Wal97] T. Walker and P. Feng, *Measurements of Collisions Between Laser-Cooled Atoms*, Adv. At. Mol. Opt. Phys. **34**, 125 (1997).

[Web03] T. Weber, J. Herbig, M. Mark, H.-C. Nägerl, and R. Grimm, *Bose-Einstein condensation of cesium*, Science **299**, 232 (2003).

[Wil09] E. Wille, *Preparation of an Optically Trapped Fermi-Fermi Mixture of ^{6}Li and ^{40}K Atoms and Characterization of the Interspecies Interactions by Feshbach Spectroscopy*, Ph.D. thesis, University of Innsbruck, Innsbruck, Austria (2009).

[Win05] K. Winkler, G. Thalhammer, M. Theis, H. Ritsch, R. Grimm, and J. H. Denschlag, *Atom-Molecule Dark States in a Bose-Einstein Condensate*, Phys. Rev. Lett. **95**, 063202 (2005).

[Win06] K. Winkler, G. Thalhammer, F. Lang, R. Grimm, J. Hecker Denschlag, A. J. Daley, A. Kantian, H. P. Büchler, and P. Zoller, *Repulsively bound atom pairs in an optical lattice*, Nature **441**, 853 (2006).

[Win07] K. Winkler, F. Lang, G. Thalhammer, P. van der Straten, R. Grimm, and J. Hecker Denschlag, *Coherent optical transfer of Feshbach molecules to a lower vibrational state*, Phys. Rev. Lett. **98**, 043201 (2007).

[Wis95] H. Wiseman and M. Collett, *An atom laser based on dark-state cooling*, Phys. Lett. A **202**, 246 (1995).

[Wol00] S. Wolf, S. J. Oliver, and D. S. Weiss, *Suppression of Recoil Heating by an Optical Lattice*, Phys. Rev. Lett. **85**, 4249 (2000).

[Wu03] C. Wu, J.-P. Hu, and S.-C. Zhang, *Exact SO(5) Symmetry in the Spin-3/2 Fermionic System*, Phys. Rev. Lett. **91**, 186402 (2003).

[Wu06] C. Wu, *Hidden symmetry and quantum phases in spin-3/2 cold atomic systems*, Mod. Phys. Lett. B **20**, 1707 (2006).

[Xu03] X. Xu, T. H. Loftus, J. L. Hall, A. Gallagher, and J. Ye, *Cooling and trapping of atomic strontium*, J. Opt. Soc. Am. B **20**, 968 (2003).

[Xu10] C. Xu, *Liquids in multiorbital $SU(N)$ magnets made up of ultracold alkaline-earth atoms*, Phys. Rev. B **81**, 144431 (2010).

[Yam08] A. Yamaguchi, S. Uetake, D. Hashimoto, J. M. Doyle, and Y. Takahashi, *Inelastic Collisions in Optically Trapped Ultracold Metastable Ytterbium*, Phys. Rev. Lett. **101**, 233002 (2008).

[Yam10] R. Yamazaki, S. Taie, S. Sugawa, and Y. Takahashi, *Submicron Spatial Modulation of an Interatomic Interaction in a Bose-Einstein Condensate*, Phys. Rev. Lett. **105**, 050405 (2010).

[Yas04] M. Yasuda and H. Katori, *Lifetime Measurement of the $^3P_2$ Metastable State of Strontium Atoms*, Phys. Rev. Lett. **92**, 153004 (2004).

[Yas06] M. Yasuda, T. Kishimoto, M. Takamoto, and H. Katori, *Photoassociation spectroscopy of ^{88}Sr: Reconstruction of the wave function near the last node*, Phys. Rev. A **73**, 011403 (2006).

[Ye] J. Ye, private communication.

[Yel06] S. F. Yelin, K. Kirby, and R. Côté, *Schemes for robust quantum computation with polar molecules*, Phys. Rev. A **74**, 050301 (2006).

[Yi07] S. Yi, T. Li, and C. P. Sun, *Novel quantum phases of dipolar Bose gases in optical lattices*, Phys. Rev. Lett. **98**, 260405 (2007).

[Yi08] W. Yi, A. J. Daley, G. Pupillo, and P. Zoller, *State-dependent, addressable subwavelength lattices with cold atoms*, New Journal of Physics **10**, 073015 (2008).

[Yi11] L. Yi, S. Mejri, J. J. McFerran, Y. Le Coq, and S. Bize, *Optical Lattice Trapping of ^{199}Hg and Determination of the Magic Wavelength for the Ultraviolet $^1S_0 \leftrightarrow {}^3P_0$ Clock Transition*, Phys. Rev. Lett. **106**, 073005 (2011).

[Zac09] M. Zaccanti, B. Deissler, C. D'Errico, M. Fattori, M. Jona-Lasinio, S. Müller, G. Roati, M. Inguscio, and G. Modugno, *Observation of an Efimov spectrum in an atomic system*, Nature Phys. **5**, 586 (2009).

[Zel06] T. Zelevinsky, M. M. Boyd, A. D. Ludlow, T. Ido, J. Ye, R. Ciuryło, P. Naidon, and P. S. Julienne, *Narrow Line Photoassociation in an Optical Lattice*, Phys. Rev. Lett. **96**, 203201 (2006).

[Zel08] T. Zelevinsky, S. Kotochigova, and J. Ye, *Precision test of mass-ratio variations with lattice-confined ultracold molecules*, Phys. Rev. Lett. **100**, 043201 (2008).

[Zuc] P. S. Zuchowski, private communication.

[Zuc10] P. S. Zuchowski, J. Aldegunde, and J. M. Hutson, *Ultracold RbSr Molecules Can Be Formed by Magnetoassociation*, Phys. Rev. Lett. **105**, 153201 (2010).

Acknowledgements

The construction and operation of the strontium experiment has been a real adventure. Most of it has been hard work, and we have been rewarded with beautiful results. Especially the race for the first Sr BEC in September 2009 left fond memories. Since then, we set up what I believe is safe to call a very capable and versatile quantum gas machine. Although it might seem to be the achievement of only very few people, it is not. Indeed, the setup of such an experiment is a tremendous effort involving the help and advice of many people, and I feel privileged to be granted the company of many brilliant people. As I conclude my thesis, I would like to express my gratitude to everyone who contributed in one way or the other, and I ask everyone not mentioned here for forgiveness.

First and most of all, I would like to thank Florian Schreck for his supervision, advice, trust, and the great leeway he has given me. Florian's experience is amazing, ranging from software and hardware into all stretches of experimental physics, and is parallelled by his profound understanding of physics. I thank Florian for the careful reading of the manuscript, and, more importantly, for never ever accepting to come in second. We made a great team, and I wish him all the best for his future.

I would like to thank Rudi Grimm for giving me the opportunity to work in the Ultracold Group, and for his generous support in all respects. The Ultracold Group is his achievement, and it provides a fantastic environment for our research. Rudi had the right sense of when it would be appropriate to commence the strontium effort, and he got us started with a great deal of support and motivation. I acknowledge the continuous trust Rudi has in me and in our work.

Jun Ye agreed to be the external reviewer of this thesis, for which I would like to express my gratitude.

I would like to thank Meng Khoon Tey for setting up the red laser system and later getting the analysis of the first Fermi gases right. With his help, we were able to move fast enough towards the first BEC. Furthermore, I would like to thank Bo Huang for his work on the red cavity and laser lock. To my successors Benjamin Pasquiou, who contributed a lot during the last year, as well as to Alex Bayerle and Slava Tzanova, I wish all the best of luck. I am sure that they will make a great team and celebrate beautiful results.

Andreas Trenkwalder and I shared an office over all the years, and uncountable bike rides home, literally tons of bananas, discussions, hiking tours, skiing days, beers, and friendship. Andi knows right out *everything* about a quantum gas machine, and he will gratefully and patiently share his knowledge.

I would like to thank Eric Wille for piling up vast resources of optomechanics, optics, and myriads of useful gadgets in the cupboards of the FeLiKx lab, and I thank him and Devang

Naik for support in the early stages of the experiment. The company and friendship of the entire FeLiKx team has been a tremendous help.

Further, I would like to thank Gerhard Kirchmair, Florian Zähringer, Cornelius Hempel, and Michael Chwalla for valuable advice and for sharing of equipment. The spectroscopy measurements presented in Chpt. 9 could not have been performed without the help of Mike and Cornelius. Reaching beyond the premises of the IQOQI labs, I would like to thank the heros of the CsIII lab, Elmar Haller, Hans Danzl, and Manfred Mark, for dispensing all these little hints and tricks. Sure enough, I would like to thank the remainder of both the Ultracold and Rainer Blatt's group for making Innsbruck such a vivid and professional place to work in. In particular, I would like to thank Hanns-Christoph Nägerl for his care and hospitality when I visited Innsbruck for the first time. He convinced me that Innsbruck would be the right place to go.

Gerhard Hendl built endless numbers of electronics boxes, power supplies, and DDS racks. He mastered the construction of the coils and water cooling, and helped us out in countless occasions. I would like to thank our two guys from the mechanics workshop, Stefan Haslwanter and Andreas Strasser, for working so well so fast while never complaining about desired quantities or tight schedules. Regular working hours were meaningless when time was pressing.

I would like to thank Mr. Knabl for managing the institute in a very professional and effective manner. He deserves all respect for balancing the needs of so many people. Together with Doris Corona, we worked through hundreds of orders, and I always enjoyed coming into her office. Valentin Staubmann is a great help as our IT engineer, and he is always kind enough to overlook my ignorance of computers. Together with Elisabeth Huck and Christine Götsch-Obmascher, who took care of the necessary administrative paperwork, they provide a friendly and smoothly working environment. I would like to thank all of them for their trust in me.

During our work, we were able to greatly benefit from the expertise and knowledge accumulated by other groups. We especially acknowledge the work by the groups of Jun Ye, Hidetoshi Katori, Thomas Killian, and Yoshiro Takahashi, and we enjoyed discussions (and sometimes competition) with them. Furthermore, we would like to thank Roman Ciuryło and Eberhard Tiemann for calculations of the ^{84}Sr scattering length, as well as many other theoreticians for stimulating discussions, among them Alexey Gorshkov, Kaden Hazzard, Ana Maria Rey, Lars Bonnes, Andreas Läuchli, Andrew Daley, and Peter Zoller. Looking back, I would also like to thank the Hamburg group of Klaus Sengstock, especially Christoph Becker and Klaus, for drawing me into the field of ultracold atoms and providing me with a phenomenal training. The beauty of the Sr machine is a testimony of this education.

Constructing a quantum gas experiment, one finds oneself awfully dependent on external companies. Among many others, I remember very pleasant co-operation with and support from Jürgen Stuhler and Jan Schäfer from Toptica Photonics, Gerald Hegenbart and his exceptional team from Thorlabs, Kester Kroll from CVI, the entire team from Linos/Qioptiq, Sabine Hermann from VACOM, Michaela Böhme from Laser Components, Jaroslaw Sperling from Newport, and Alois Wiesböck and Franz Schwarzbauer from EQ Photonics.

Finally, I would like to thanks my parents Hartmut and Urte and my sister Franziska for their continuous support, and Hanna for her endless patience and love.